

Dual-mode photoacoustic and ultrasound imaging system based on a Fabry-Pérot scanner

Khoa Pham

A dissertation submitted in partial fulfillment
of the requirements for the degree of
Doctor of Philosophy
of
University College London.

Department of Medical Physics and Biomedical Engineering
University College London

11 November 2022

I, Khoa Pham, confirm that the work presented in this thesis is my own. Where information has been derived from other sources, I confirm that this has been indicated in the work.

Abstract

The planar Fabry-Pérot (FP) scanner is an ultrasound detector that simultaneously provides high sensitivity, a high density of small (sub-100 μm) acoustic elements, and a broad bandwidth (> 30 MHz). These features enable the FP scanner to acquire high-resolution 3D *in vivo* photoacoustic images of biological tissues up to depths of approximately 10 mm. The aim was to add complementary morphological ultrasound contrast to photoacoustic images to extend their clinical applicability. This was achieved by developing a dual-mode photoacoustic and ultrasound imaging system based on the FP scanner, which was modified to transmit optically generated ultrasound. The FP sensor head was coated with an optically absorbing polydimethylsiloxane (PDMS) composite layer, which was excited with nanosecond laser pulses to generate broadband planar ultrasound waves for pulse-echo imaging. First, an all-optical ultrasound system was developed using a highly absorbing carbon nanotube-PDMS composite coating. The system was characterised with a series of experiments, and its imaging performance was tested on tissue mimicking phantoms and *ex vivo* tissue samples. Second, the effect of the frequency content of the detected signals and the effect of spatial aliasing on the image quality were investigated in simulation. A broadband system was found to reduce the effect of spatial undersampling of high frequencies which results in a reduction of contrast due to the formation of grating lobe artefacts. Third, to improve the image quality, frequency and angle compounding were explored in simulations and experimentally. Coherent and incoherent compounding were considered, as well as the effect of the filter bandwidth on frequency compounded images, and the influence of the number and spread of angles used in angle compounded images. Finally, a dual-mode photoacoustic and ultrasound imaging system was demonstrated with a gold nanoparticle-PDMS composite which enabled wavelength-selective absorption of light. The system was shown to obtain high-resolution 3D dual-mode images providing complementary contrast from optically absorbing and acoustically scattering structures.

Impact

The planar Fabry-Pérot (FP) scanner has a number of applications in high-resolution photoacoustic imaging of superficial tissues. These include imaging of the skin, superficial tumours and lymph node disease in a clinical setting, and imaging of small animals in research settings. Extending the FP scanner with an ultrasound imaging modality would elevate the diagnostic value of the photoacoustic images further. Since clinicians are more used to seeing ultrasound images, a co-registered dual-mode image could help them interpret the photoacoustic image better. The added morphological ultrasound contrast could aid clinicians in the localisation of tissue structures, such as the skin, tumours, lymph nodes or bones. This could significantly help with the assessment of pathological conditions, including head and neck cancers and arthritis, which are highlighted in the photoacoustic vascular image. The system could be expanded to include multiple ultrasound transmissions to carry out ultrasound computed tomography. This would allow researchers to extract information about the spatially varying sound speed distribution in the tissue which could be used to improve the photoacoustic image reconstruction. With its broadband generation and detection capability, the optical ultrasound imaging system based on the FP scanner could serve as a research system. This could be to further develop broadband plane-wave imaging as a relatively unexplored ultrasound modality. The broad bandwidth of the system was exploited to study the effect of different frequency regimes on the image quality in plane-wave images. This could help researchers understand the underlying contrast mechanisms, which in turn could help contribute to research of conventional narrowband plane-wave systems.

Acknowledgements

First and foremost, I would like to thank my supervisors Paul Beard and Ben Cox for their continual guidance and support throughout my PhD. Without their enthusiasm and patience the completion of this thesis would not have been possible. In particular, I would like to thank Paul for his thorough attention to detail while always keeping the big picture in mind, and Ben for his unmatched ability to quickly understand a problem and find a practical solution.

My thanks extends to all members of the Photoacoustic Imaging Group and the Biomedical Ultrasound Group whom I had the pleasure to work with and could always come to for help. In particular, I would like to thank Trung Huynh and Edward Zhang who assisted with all scanner related issues, Olivia Wright who helped with the design and fabrication of 3D printed parts, Alissa Silva, Maxim Cherkashin and Morgan Roberts who helped immensely with the writing of this thesis, and Michael Brown who helped with almost everything.

I am lucky to have made so many friends at UCL over the years, the so-called BORL buddies and the not-so-called BUG buddies, thank you all. Thanks to Louis F.-H. for food and music related excursions. Thanks to Louis D., Robin, Eva and Ellie for being the best housemates and friends and an invaluable support network. Thanks to Morgan for all the times spent in the shed, it was a blast (sometimes literally). Thanks to Alissa, a friend, for anything from a sandwich to a trip to the airport. Special thanks to Michael and David Brown for putting a roof over my head in the last year. Thank you, Amélie, for always being there for me with a can of mustard.

At last, thanks to Khruangbin for the music, the universe smiles upon you.

Contents

Nomenclature	21
1 Introduction	23
1.1 Motivation	23
1.2 Aims	26
1.3 Structure	27
2 Background	29
2.1 Photoacoustic imaging	29
2.1.1 The photoacoustic effect	29
2.1.2 Optical ultrasound detectors	31
2.1.3 The planar FP scanner	33
2.2 Ultrasound imaging	34
2.2.1 Optical generation of ultrasound	35
2.2.2 Optical ultrasound imaging systems	37
2.2.3 Ultrasound image acquisition schemes	38
2.2.4 Plane-wave ultrasound imaging	40
2.3 Dual-mode imaging systems	42
2.4 Image property and image quality terms	44
3 Plane-wave ultrasound imaging with the FP scanner	49
3.1 Introduction	49
3.2 System working principle	51

3.2.1	Optical ultrasound generation	51
3.2.2	Optical ultrasound detection	52
3.2.3	Image reconstruction and processing	54
3.3	System characterisation	56
3.3.1	Mapping of optically generated ultrasound	56
3.3.2	Fabry-Pérot scanner bandwidth	66
3.3.3	Heating effects	66
3.3.4	Spatial resolution	76
3.3.5	Safety	80
3.4	Imaging experiments	81
3.4.1	3D imaging of arbitrarily shaped scatterers	83
3.4.2	Imaging of tissue mimicking phantoms	85
3.4.3	<i>Ex vivo</i> tissue imaging	87
3.4.4	Dynamic range and logarithmic compression	90
3.4.5	Frequency content of detected signal	91
3.4.6	Slice thickness	92
3.5	Conclusion	94
3.5.1	Summary	94
3.5.2	Outlook	95
4	Simulation of plane-wave ultrasound imaging	97
4.1	Introduction	97
4.2	Literature review	99
4.2.1	Representation of acoustically scattering medium	100
4.2.2	Forward model	101
4.3	Simulation platform	102
4.3.1	Simulated phantoms	105
4.3.2	Comparison of scattering media	108
4.4	Frequency dependence of image quality	110
4.4.1	Method and interpretation	110
4.4.2	Effect of simulation and imaging parameters	111

4.4.3	Experiment vs simulation	115
4.5	Spatial aliasing	117
4.5.1	Aliasing with the random scattering medium	118
4.5.2	Aliasing of a single point scatterer	121
4.5.3	Grating lobe artefacts	123
4.6	Spatial dependence	127
4.6.1	Spatial dependence of aliasing	128
4.6.2	Spatial dependence of image quality	131
4.7	Sensor directivity	138
4.8	Future work	141
4.8.1	Negative vs positive contrast.	141
4.8.2	Spatial dependence of grating lobes.	143
4.9	Conclusion	144
4.9.1	Summary	144
4.9.2	Outlook	145
5	Compounding methods for broadband plane-wave ultrasound imaging	147
5.1	Introduction	147
5.2	Frequency compounding	150
5.2.1	Coherent vs incoherent compounding	151
5.2.2	Frequency compounding with simulated data	153
5.2.3	Frequency compounding with FP scanner data	154
5.3	Angle compounding: reconstruction & methods	161
5.3.1	Derivation of the reconstruction algorithm	161
5.3.2	Data processing, reconstruction & compounding methods	169
5.4	Broadband angle compounding in simulation	172
5.4.1	Simulation set-up	172
5.4.2	Compounding results	174
5.5	Angle compounding with the FP scanner	180
5.5.1	System design	180
5.5.2	Optical generation of angled plane waves	184

5.5.3	Imaging with an angled transmitter coating	190
5.6	Future work	194
5.6.1	Frequency compounding	194
5.6.2	Angle compounding	195
5.6.3	Other compounding ideas	196
5.7	Conclusion	197
6	Dual-mode imaging with the FP scanner	201
6.1	Dichroic transmitter coating	203
6.2	Imaging experiments	204
6.2.1	Phantom imaging	204
6.2.2	Mode crosstalk	207
6.3	Future work	208
6.3.1	Simultaneous-excitation dual-mode imaging	208
6.3.2	Temporal separation of PA and US signals	211
6.4	Conclusion	211
7	Conclusion	213
	Appendices	217
A	Reconstruction code for normal plane-wave ultrasound imaging	219
B	Mapping of optically generated ultrasound from a CNT-PDMS film	223
C	Pulse duration variation of excitation laser	225
D	Screenshots from clinical ultrasound scanner	229
E	Dual-mode images on linear scale	233
	Publications	235
	Bibliography	237

List of Figures

1.1	Schematic of FP scanner system developed for photoacoustic imaging.	23
2.1	Photoacoustic effect explained in steps	29
2.2	Conventional focused ultrasound <i>vs</i> ultrafast angle compounded imaging	42
3.1	Schematic of the all-optical ultrasound imaging system	50
3.2	Concept of acoustic sensitivity of the FP scanner	53
3.3	Set-up for characterising optically generated ultrasound pulses	57
3.4	Profiling of the excitation beam used in the characterisation measurements	57
3.5	Characterisation of optically generated ultrasound produced by a CNT-PDMS composite transmitter coating on a PMMA slab	59
3.6	Characterisation of optically generated ultrasound produced by a SP coating on a PMMA slab	59
3.7	Characterisation of optically generated ultrasound produced by a CNT-PDMS composite transmitter coating on a FP sensor	61
3.8	Non-linear propagation of optical ultrasound produced by a CNT-PDMS transmitter coating for a range of ND filters to vary the fluence	63
3.9	Characteristics of optically generated ultrasound pulses	65
3.10	Heating effects on the sensitivity of the sensor	67
3.11	Timescale of long-term heating effects	68
3.12	Timescale of pulse-to-pulse heating effects	70

3.13	Schematic to demonstrate heating effects on pre-tuning	72
3.14	Heating effects on pre-tuning	74
3.15	Set-up used to estimate the line spread function of the system	77
3.16	Estimation of system line spread function.	78
3.17	Contour plot of lateral resolution in yz plane	79
3.18	Ultrasound imaging of arbitrarily shaped scattering structures	84
3.19	Ultrasound imaging of layered gel wax-based tissue-mimicking phantom	85
3.20	Ultrasound imaging of agar-based tissue-mimicking phantom	86
3.21	Ultrasound imaging of <i>ex vivo</i> pork belly	87
3.22	Ultrasound imaging of <i>ex vivo</i> mouse kidney	88
3.23	Ultrasound imaging of an <i>ex vivo</i> human lymph node	89
3.24	Comparison of <i>ex vivo</i> pork belly image on log and linear scales	90
3.25	Average frequency spectra of received data	91
3.26	Effect of slice thickness on <i>ex vivo</i> pork belly image	93
4.1	Band-pass frequency filtered images of agar-based tissue-mimicking phantom	99
4.2	Phantoms used in simulations	106
4.3	Definition of scattering SNR and CNR for a hole in a random scattering medium	107
4.4	Scattering SNR and CNR for hole phantom with different values of sound speed fluctuation Δc and density fluctuation $\Delta \rho$	109
4.5	Comparison of images of scattering media obtained from experiments and simulations	109
4.6	Effect of simulation grid size and medium granularity on frequency dependence of the image quality	112
4.7	Effect of sensor sampling step size and image voxel size on frequency dependence of the image quality	114
4.8	Effect of spatial aliasing on frequency dependence of the image quality	115

4.9	Frequency dependence of the image quality of scattering phantoms .	116
4.10	Effect of spatial aliasing on images of the random scattering medium	118
4.11	Effect of spatial aliasing on sensor data in frequency space	119
4.12	Map of angle of incidence associated with each spatial frequency k_x and temporal frequency ω value pair.	120
4.13	Effect of spatial aliasing on sensor data in frequency space and as a function of AOI and temporal frequency	122
4.14	Images of a point scatterer for narrowband frequency filtered data with increasing centre frequencies	124
4.15	Images of a point scatterer for frequency filtered data with increas- ing bandwidths	125
4.16	Positions of the point scatterers used to generate the 2D-FT and AOI plots in Figs. 4.17 and 4.18.	128
4.17	Spatial dependence of aliasing in frequency space	129
4.18	Spatial dependence of aliasing in angle-frequency space	130
4.19	Schematic to show difference in maximum AOI for point scatterers at different depths and different lateral positions relative to the sensor	130
4.20	Positions of the hole in a random scattering medium used for mea- suring spatial dependency of the scattering SNR and CNR	132
4.21	Spatial dependence of scattering SNR and CNR in an unfiltered broadband image of a hole in a random scattering medium	133
4.22	Images of a hole in a random scattering medium at different depths obtained with different sensor sampling step sizes, and recon- structed with or without applying a low-pass frequency filter	135
4.23	Spatial dependence of scattering SNR and CNR in a low-frequency image of a hole in a random scattering medium	136
4.24	Images of a point scatterer obtained with differently directional sen- sors	139
4.25	Images of a random scattering medium obtained with differently directional sensors	140

5.1	Flowchart of processing steps to obtain coherent and incoherent compound image, and compound filtered image.	151
5.2	Comparison of simulated frequency compounded images	154
5.3	Definition of image quality metrics for the agar-based tissue mimicking phantom	156
5.4	Frequency dependent image quality maps for agar-based tissue mimicking phantom	157
5.5	Comparison of frequency compounded images from experimental data	158
5.6	Comparison of coherently and incoherently frequency compounded images using narrowband or broadband frequency filters	160
5.7	Schematic for imaging an object function $f(\mathbf{r}_0)$	162
5.8	Transmit wave vector of a steered plane wave in 3D defined by steering angle ζ_T and rotation angle θ_T	167
5.9	Visualisation of data processing methods for angled plane wave reconstruction in 2D	170
5.10	Simulation setup for 2D ultrasound imaging with an angled plane wave	173
5.11	Simulated single plane wave images at different transmission angles	174
5.12	Simulated incoherent compound images	176
5.13	Simulated coherent compound images	177
5.14	Image quality of simulated angle compounded images	177
5.15	Coherent compound images with increasing number of transmission angles	178
5.16	Schematic for the set-up of the photoacoustic generation of an angled plane wave	181
5.17	Angle magnification system to amplify the rotation speed of a laser beam reflecting off of a rotating mirror	185
5.18	Excitation source set-up to generate variable excitation pulses . . .	188

5.19	Set-up for angled plane imaging with the FP scanner and a mechanically angled transmitter coating	190
5.20	Single plane wave ultrasound images of a 27 μm tungsten wire acquired with steering angles from -8° to 8°	191
5.21	Single plane wave ultrasound image of a polymer leaf phantom with a steering angle of approximately 3°	192
6.1	Schematic of system set-ups and example absorption spectra for US transmitter coatings	202
6.2	Absorption spectra of AuNP-PDMS composite samples.	203
6.3	Dual-mode imaging of a polymer leaf phantom to demonstrate 3D imaging capability of the dual-mode system.	205
6.4	Dual-mode imaging of ink-filled tube phantom to demonstrate complementary contrast provided by the dual-mode system.	206
6.5	Crosstalk reconstructions compared to normal reconstructions from dual-mode acquisition data of polymer leaf.	209
B.1	Characterisation of optically generated ultrasound produced by a CNT-PDMS composite transmitter coating on a PMMA slab	223
C.1	Non-linear propagation demonstrated with LUS from CNT on PMMA for a range of QS delays to vary the fluence	226
C.2	Acoustic pulse shape variation of LUS from CNT on PMMA for a range of long QS delays demonstrating optical pulse duration variation	227
D.1	Screenshot from clinical scanner imaging a layered gel-wax phantom	229
D.2	Screenshot from clinical scanner imaging an agar-based scattering phantom	230
D.3	Screenshot from clinical scanner imaging an <i>ex vivo</i> pork belly . . .	230
D.4	Screenshots from clinical scanner imaging an <i>ex vivo</i> human lymph node	231

E.1	Crosstalk reconstructions compared to normal reconstructions from dual-mode acquisition data of polymer leaf.	233
-----	--	-----

Nomenclature

AFG Arbitrary function generator

AOI Angle of incidence

AOM Acousto-optic modulator

AuNP Gold-nanoparticle

CMUT Capacitive micromachined ultrasound transducer

CNR Contrast-to-noise ratio

CNT Carbon-nanotube

CW Continuous-wave (laser)

EDFA Erbium-doped fibre amplifier

FP Fabry-Pérot

FT Fourier transform

FWHM Full-width-half-maximum

ITF Interferometer transfer function

LSF Line-spread function

MaxIP Maximum intensity projection

MeanIP Mean intensity projection

ND Neutral density (filter)

NEP Noise-equivalent pressure

PA Photoacoustic

PDMS Polydimethylsiloxane

PML Perfectly matched layer

PMMA Polymethylmethacrylate

PRF Pulse repetition frequency

ROI Region of interest

TMM Tissue mimicking material/phantom

TOA Time of arrival

US Ultrasound

Chapter 1

Introduction

1.1 Motivation

The planar Fabry-Pérot (FP) scanner, developed in the photoacoustic imaging group at UCL, is an ultrasound detector based on an interferometer [1], see Fig. 1.1. Acoustic pressures are detected by interrogating the sensor with a laser beam and measuring the reflected intensity, which changes in response to pressure-induced thickness changes of the interferometer spacer. The interrogation beam can be scanned across the sensor to build up a 3D data set of acoustic pressure-time series.

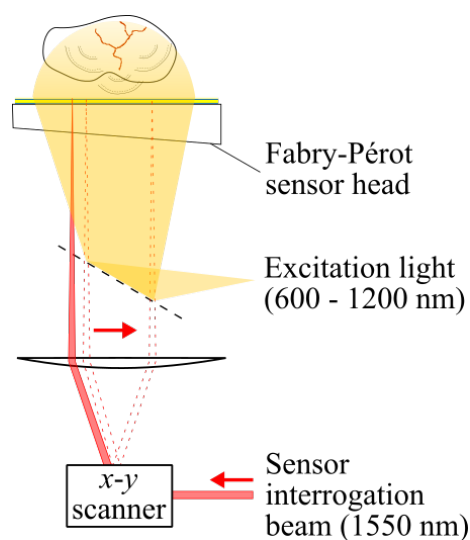


Figure 1.1: Schematic of FP scanner system developed for photoacoustic imaging.

The FP scanner was originally developed for photoacoustic (PA) imaging, which relies on optical absorption to create contrast [2]. During PA imaging a laser pulse is sent through the sensor into the tissue where it gets absorbed by some anatomical structures such as blood vessels, see Fig. 1.1. The absorbed optical energy thermalises into an initial pressure rise, which relaxes into acoustic waves that propagate to the surface of the tissue, and are detected by the FP scanner. From these detected signals an image of the initial pressure rise can be reconstructed, which is equivalent to an image of the absorbed optical energy. The planar FP scanner is well suited to PA imaging since it simultaneously provides high sensitivity, a high density of small (sub-100 μm) acoustic elements over a centimetre-scale area, and a broad bandwidth extending to several tens of MHz. These features enable the FP scanner to provide high-resolution 3D *in vivo* photoacoustic images of biological tissues up to depths of approximately 10 mm beneath the skin surface [3, 4].

The contrast in a PA image is based on optical absorption, which allows optically absorbing molecules such as haemoglobin, melanin or lipids to be highlighted with good contrast. However, non-absorbing tissue structures cannot be visualised in PA images. An ultrasound (US) image, on the other hand, is formed from the scattering of acoustic waves at acoustic impedance changes. The contrast in ultrasound images is based on mechanical tissue properties and is not dependent on optical absorption. Ultrasound is therefore capable of providing contrast in non-absorbing tissues that are invisible to PA imaging. We therefore want to develop a dual-mode system that can acquire photoacoustic images and ultrasound images. Ideally, both modalities would be combined in the same system to allow for easy co-registration. Such a system would add complementary morphological ultrasound contrast to photoacoustic vascular images and thus have an extended clinical applicability.

Previously developed dual-mode photoacoustic and ultrasound imaging systems commonly employ piezoelectric ultrasound transducers for detection [5–10]. The majority of these systems are limited in their resolution performance due to the low detection bandwidth. Recently, capacitive micromachined ultrasound transduc-

ers (CMUTs) have increasingly found use in medical ultrasound imaging as they provide a broad bandwidth and high sensitivity [11]. However, due to the difficulty of making the transducer material transparent to the photoacoustic excitation light [12], most CMUT-based dual-mode systems deliver the excitation light from the side [13]. Although a number of CMUT arrays have been demonstrated for photoacoustic imaging with the excitation light delivered through the transducer [14, 15], this has not been extended to dual-mode imaging. The planar FP scanner, on the other hand, provides a sensor with an extended transparent window from 600-1200 nm, and a broad detection bandwidth combined with high sensitivity and a high density of small acoustic elements. These attributes make it a highly suitable ultrasound detection system not only for high-resolution PA imaging, but also for high-resolution 3D ultrasound imaging of biological tissues. If the planar FP scanner is modified to enable an ultrasound imaging modality, then it can be developed into a dual-mode imaging system.

To perform ultrasound imaging with the planar FP scanner as the detector, an ultrasound transmission mechanism needs to be added. For high-resolution tissue imaging applications, a broadband transmission is desirable which could be provided by the optical generation of ultrasound. Using short laser pulses, broadband high-frequency ultrasound waves can be generated in a range of absorbing materials [16]. Polydimethylsiloxane (PDMS) composite absorbers have been shown to exhibit a high thermoelastic conversion efficiency and provide acoustic generation with bandwidths in the tens of MHz range [17, 18]. Examples include the carbon-nanotube(CNT)-PDMS composite film, which provides MPa-range peak pressures [19], and the gold-nanoparticle(AuNP)-PDMS composite film, which has a wavelength-selective absorption spectrum [17].

There are a number of ultrasound image acquisition schemes which can broadly be split into three types based on the geometry of the transmitted wave: focused, diverging or planar waves. In this thesis, we only consider the use of planar ultrasound waves since their optical generation is most easily implemented with the FP

scanner set up. By placing a planar absorbing layer between the FP sensor and the medium and exciting it with a wide-field laser beam, planar ultrasound waves can be generated with the same FP scanner set up as for PA imaging (Fig. 1.1). This thesis will therefore be a first investigation into a pulse-echo plane-wave ultrasound imaging system using an optical ultrasound generation and the FP scanner for detection with the ultimate aim to develop a dual-mode photoacoustic and ultrasound imaging system based on the FP scanner system.

1.2 Aims

The aim of the work described in this thesis is to develop a dual-mode photoacoustic and ultrasound imaging system based on the planar FP scanner for detection and the optical generation of broadband planar ultrasound waves. Since the photoacoustic imaging modality of the FP scanner is well-characterised, we will initially focus on modifying the FP scanner for ultrasound imaging and then demonstrate the dual-mode imaging capability.

To achieve these aims the following goals were identified:

1. Development of an optical ultrasound imaging system based on the planar FP scanner and the optical generation of ultrasound in an absorbing layer.
2. Simulation of broadband plane-wave ultrasound imaging to understand the limitations in image quality.
3. Design and evaluation of compounding methods to improve the image quality of broadband plane-wave ultrasound imaging.
4. Demonstration of a dual-mode photoacoustic and ultrasound imaging system based on the planar FP scanner and the optical generation of ultrasound in a wavelength-selective absorbing layer.

1.3 Structure

An overview of the pertinent literature is provided in Chapter 2. This includes a background of the FP scanner and its use for PA imaging. Ultrasound imaging methods including the optical generation of ultrasound and plane-wave ultrasound imaging are reviewed. Finally, an overview of existing dual-mode photoacoustic and ultrasound imaging systems is given.

The thesis is structured according to the four goals stated above:

Goal 1, Chapter 3

The optical ultrasound imaging system based on the planar FP scanner is described in Chapter 3. This includes the characterisation of the optically generated planar ultrasound waves from a CNT-PDMS composite absorber, the heating effects during ultrasound generation and the spatial resolution the system can provide. The system's imaging performance is tested with arbitrarily shaped scatterers, tissue mimicking phantoms and *ex vivo* tissue samples.

Goal 2, Chapter 4

A simulation platform to study the limitations of broadband plane-wave ultrasound imaging is presented in Chapter 4. The aim is to understand the extent to which the broadband nature of the system impacted on the image quality of plane-wave ultrasound images. The frequency dependence of the image quality and the effect of spatial aliasing are studied, along with the spatial dependence of these effects.

Goal 3, Chapter 5

Compounding methods to improve the image quality in broadband plane-wave ultrasound imaging are explored in Chapter 5. Frequency compounding is demonstrated on simulated data and experimental data. The effect of angle compounding on broadband plane-wave images is explored via simulations. A system design for the optical generation of angled plane waves is described and key aspects are tested to assess the feasibility of the design. Imaging with an angled plane wave is demonstrated with a mechanically angled CNT-PDMS composite absorber and the

FP scanner for detection.

Goal 4, Chapter 6

The dual-mode photoacoustic and ultrasound imaging system based on the planar FP scanner for detection is described in Chapter 6. A dichroic coating made from a AuNP-PDMS composite is used for wavelength-selective absorption and transmission to facilitate both optical ultrasound generation and photoacoustic excitation. The complementary contrast of the two modalities of the dual-mode system is demonstrated by imaging phantoms that are acoustically scattering and optically absorbing.

The thesis is concluded in Chapter 7.

Chapter 2

Background

2.1 Photoacoustic imaging

2.1.1 The photoacoustic effect

The photoacoustic (PA) effect describes the generation of sound following the absorption of time-varying light. It was first discovered by Alexander Graham Bell in 1880 through his invention of the “photophone” [20]. The PA effect can be described in three steps [21]: (1) the absorption of light, (2) the thermalisation of the absorbed optical energy to an initial pressure increase p_0 , and (3) the propagation of the pressure as acoustic waves, see Fig. 2.1. For the PA effect to be useful for biomedical imaging, two conditions must be satisfied. The first one is thermal confinement, where the duration of the optical heating is required to be much less than the time for the heat to diffuse across a characteristic length, e.g. a blood vessel.

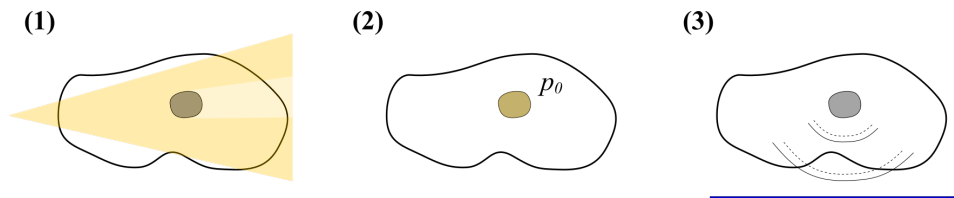


Figure 2.1: Photoacoustic effect: (1) Excitation and absorption of light. (2) Thermalisation of absorbed energy to localised initial pressure increase p_0 . (3) Propagation of initial pressure perturbation as acoustic waves, here detected by a planar ultrasound sensor (blue).

If this is satisfied, all the optical energy is deposited before any heat diffuses away from the absorbing region. The temperature rise can then be assumed to arise solely from optical heating. The second condition to be met is stress confinement, which requires the length of the optical pulse to be much less than the time for an acoustic wave to propagate across the absorbing volume. Satisfying this implies that all the optical energy is deposited before any energy propagates away from the absorbing region as an acoustic wave. If both the thermal and stress confinement conditions are satisfied, the initial pressure distribution p_0 is given by

$$p_0(\mathbf{r}) = \Gamma(\mathbf{r})H(\mathbf{r}) = \Gamma(\mathbf{r})\mu_a(\mathbf{r})\phi(\mathbf{r}) \quad (2.1)$$

where $H(\mathbf{r})$ is the absorbed optical energy at a point \mathbf{r} , Γ is the Grüneisen parameter, μ_a is the optical absorption coefficient, and ϕ is the optical fluence, i.e. the incident optical energy per unit area. The Grüneisen parameter Γ is given by

$$\Gamma = \frac{\beta c^2}{C_p} \quad (2.2)$$

where β is the volume thermal expansivity, c is the sound speed, and C_p is the specific heat capacity at constant pressure.

It can be seen from Eq. (2.1) that the initial pressure distribution $p_0(\mathbf{r})$ is proportional to the absorbed optical energy distribution $H(\mathbf{r})$. The contrast in PA images is therefore determined by optical absorption. Since the optical absorption is wavelength-dependent, images of different absorbing tissue components can be obtained. Typically, near-infrared (NIR) light (600-900 nm) is used for excitation due to the relatively low optical attenuation in tissue which enables high penetration depths [2]. At these wavelengths, the haemoglobin in the blood is more strongly absorbing than other major chromophores in tissue, such as water, lipids, collagen or elastin [22]. This strong preferential absorption of haemoglobin enables the vasculature to be visualised with high contrast in PA images [3]. By choosing a different wavelength, tissue types other than blood can be imaged, e.g. fat at 1210 nm [23].

The acoustic waves that propagate outwards from the initial pressure distribution $p_0(\mathbf{r})$ can be detected by an ultrasound sensor. From the detected signals an image of the initial pressure distribution $p_0(\mathbf{r})$ can be obtained with a resolution similar to ultrasound imaging. PA imaging thus benefits from the high specificity of optical absorption and the high spatial resolution of ultrasound.

There are different PA imaging strategies, including PA microscopy which involves the localised excitation of PA signals, and PA tomography where the whole region of interest in the medium is illuminated by the excitation light. In this work we only consider PA tomography, and will often refer to it as PA imaging.

2.1.2 Optical ultrasound detectors

A variety of optical ultrasound detectors have been previously demonstrated for photoacoustic imaging applications [24, 25]. These can broadly be split into refractometric and interferometric methods [25]. Since the former were shown to have poor sensitivity for low acoustic pressures on the order of 100 Pa which is necessary for PA imaging [25], we focus our review on interferometric methods in this section.

The Mach-Zehnder interferometer (MZI) is a two-beam interferometer where a laser beam is split into two optical paths, one of which is perturbed by the ultrasound wave and the other serves as a reference [25]. Fibre-based MZIs have shown a promising acoustic sensitivity of 180 Pa, but only have a low detection bandwidth of 5 MHz which is insufficient for PA imaging [26]. A free-space MZI with a higher bandwidth of 17 MHz was demonstrated for photoacoustic imaging [27]. However, since this type of interferometer relies on precise alignment and path length of the beams, this approach is not robust with regards to vibrations and electromagnetic noise, and is yet to be demonstrated outside of a lab setting [25].

Micro-ring resonators (MRR) have achieved a high sensitivity with an estimated NEP of 6.8 Pa (no measurement bandwidth stated) and a very broadband frequency response with a 3-dB bandwidth of 140 MHz [28]. These detectors were fabricated

on glass microscope slides and therefore are fully transparent and suitable for reflection mode imaging. However, the MRRs had a directional response at higher frequencies in the 10s of MHz and have not yet been fabricated in a dense array of detectors. They are thus not suitable for PA tomography in the current form, and have only been used for PA microscopy. More recently, an optomechanical ultrasound sensor based on a ring resonator on silicone was demonstrated in a 1D array of 10 sensors which were able to acquire a PA tomography image of polyamide sutures [29]. Further scaling to achieve denser arrays which could be applied to biomedical imaging is yet to be demonstrated.

A fibre Bragg grating (FBG) is a spectrally reflective element fabricated into the core of an optical fibre where reflections from the reflective index perturbations interfere constructively when the Bragg condition is satisfied [30]. FBGs have been shown to provide sensitivities of 100 Pa and bandwidths up to 77 MHz [31]. However, FBGs have a typical size of $10 \times 300 \mu\text{m}$ and should thus be treated as line detectors rather than point detectors [32]. This makes them suitable for PA microscopy or endoscopic applications, but not PA tomography. A miniaturised version of an FBG with a size of $0.5 \times 30 \mu\text{m}$ [33] has been demonstrated but not yet scaled up into a dense array of sensors which would be necessary for PA tomography.

FP interferometers are optically transparent and simultaneously provide a wide detection bandwidth, and small acoustic detectors with high sensitivity which make them suitable for high-resolution photoacoustic imaging. Various FP interferometer-based sensing arrangements have been demonstrated, including a fibre-optic plano-concave microresonator [34], a FP-based endoscopic probe [35], and the planar FP scanner for 3D PA tomography [1]. For photoacoustic tomography the planar FP scanner is best suited as it enables the detection across a dense array of points along the sensor. While the planar FP sensor does not allow for total light confinement within the interferometer and thus limiting its sensitivity for PA microscopy applications, it provides sufficient sensitivity for PA tomography. The next section describes the planar FP scanner in more detail.

2.1.3 The planar FP scanner

The planar FP scanner is highly suited for high-resolution imaging since it simultaneously provides (i) high sensitivity, with a noise-equivalent pressure (NEP) of 0.2 kPa over 20 MHz, (ii) a high density of small acoustic elements with a size of approximately 64 μm , and (iii) a very broadband frequency response in the tens of MHz range. As a result, the FP scanner system provides a resolution performance of the order of tens of μm [1]. The system has been shown to provide 3D high-resolution PA images of biological tissues up to depths of 10 mm [3, 4].

With the planar FP scanner, acoustic pressures are detected by interrogating the FP sensor head with a laser beam and measuring the reflected intensity, which changes in response to pressure-induced thickness changes of the interferometer spacer. The interrogation beam can be scanned across the sensor point-by-point to build up a 3D data set of acoustic pressure-time series. For a typical image the interrogation beam is scanned across a 15 mm \times 15 mm area with a step size of 100 μm to record acoustic pressure-time series at 22500 spatial points. This can lead to relatively long acquisition times, e.g. 20 min for an excitation laser with a pulse repetition frequency of 20 Hz. From the detected acoustic pressure-time series an image of the initial pressure distribution, which is proportional to the absorbed optical energy distribution (see Eq. (2.1)), can be recovered using a k -space reconstruction algorithm [36]. The working principle of the FP scanner is described in more detail in Section 3.2.2.

The mirrors of the FP interferometer are highly reflective around 1550 nm, which enables the relatively inexpensive and widely tunable C-L band (1516-1610 nm) lasers, originally developed for optical telecommunications applications, to be used as the sensor interrogation laser source [1]. At the same time, the sensor head of the FP scanner system has a large optical transparency window from the visible to the NIR (600-1200 nm). This not only allows for PA excitation light to be delivered through the sensor, but also for the delivery of an excitation laser pulse for the optical generation of ultrasound waves in an absorbing coating placed between

the sensor and the medium. The FP scanner can therefore be modified to be suitable for all-optical ultrasound imaging and dual-mode photoacoustic and ultrasound imaging.

2.2 Ultrasound imaging

Ultrasound imaging is based on acoustic waves and their propagation and interaction in inhomogeneous media. An important quantity is the acoustic impedance Z , defined as

$$Z(\mathbf{r}) = c(\mathbf{r})\rho(\mathbf{r}) \quad (2.3)$$

where c is the speed of sound and ρ is the density of the medium. An acoustic wave scatters off changes in the acoustic impedance within the medium. For example, at a surface with impedance mismatch (Z_1 to Z_2) a normally incident acoustic wave is partly reflected with the relative amplitude given by the reflection coefficient:

$$R = \frac{Z_2 - Z_1}{Z_2 + Z_1} \quad (2.4)$$

In biomedical ultrasound imaging acoustic impedance mismatches occur on a wide range of scales, from small clusters of living cells, blood cells or the extra-cellular matrix acting as point scatterers to large cysts, vessels or organ boundaries acting as specular scatterers. When an acoustic wave is transmitted into a tissue it gets reflected or scattered off these acoustic impedance changes. The scattered waves propagate to the tissue surface and are detected by an ultrasound sensor. From the detected signals an image of the scattering distribution can be reconstructed.

One of the project aims is to modify the FP scanner system with an added ultrasound transmission mechanism based on the optical generation of ultrasound. In the next two sections, previous work on optical ultrasound generation methods (Section 2.2.1) and imaging systems using optical ultrasound for transmission (Section 2.2.2) are reviewed.

2.2.1 Optical generation of ultrasound

In recent years there has been an increased interest in using the PA effect to generate ultrasound waves for biomedical ultrasound imaging [16, 37]. Typically, a thin absorbing layer is deposited on an optically transparent slab of backing material, which is often polymethylmethacrylate (PMMA). A pulse from a high-energy excitation laser is delivered to the absorbing layer through the backing which generates an acoustic pulse that propagates into the medium. We will therefore refer to the absorbing layer as the ultrasound transmitter coating. The advantage over piezoelectric transducers is the potential to generate wide bandwidth acoustic pulses using thin or highly absorbing transmitter coatings and short optical pulses. According to Eqs. (2.1) and (2.2) the magnitude of the optically generated pressure depends on the fluence, the optical absorption, and the Grüneisen parameter, which itself depends on the thermal expansivity, the sound speed and the heat capacity.

Metals were first proposed for optical generation of ultrasound by White in 1963 [38], as they have a very high optical absorption coefficient and a high Grüneisen parameter [39]. However, due to the very short optical absorption depth and the high thermal diffusivity, thermal confinement is difficult to satisfy in metals. The large acoustic impedance of metals makes transmission of optically generated ultrasound into biological tissues difficult. As a result, optical ultrasound generation in metals has primarily been used in non-destructive testing applications, while only few attempts have been made for biomedical imaging applications. The latter involved thin metal films coated with or sandwiched in between substrates, such as glass or PDMS, where the optical energy deposited in the metal film thermalised into a pressure rise [40, 41].

Nanocomposites have emerged as optical ultrasound transmitters for biomedical imaging applications in recent years, as research has improved their conversion efficiency from fluence to pressure. These materials generally consist of optically absorbing nanoparticles within a bulk substrate that thermalises the absorbed optical energy into a pressure rise. The absorbing nanoparticles are most commonly

carbon-based or metallic-based [16], and are typically embedded or over-coated with a polymer such as PDMS, polyurethane or epoxy [18].

PDMS is most often used as the bulk substrate due to its high thermal expansivity enabling high peak pressures in the MPa-range to be generated from the absorption [16, 17]. PDMS has a number of other advantages which make it suitable for biomedical imaging application: (i) It has a similar refractive index to commonly used backing materials, such as glass or PMMA, and thus allows for light to be coupled into the coating and delivered to the absorbing molecules [42]. (ii) The acoustic impedance of PDMS is similar to that of biological tissue which enables efficient coupling of ultrasound into the tissue [43]. (iii) PDMS is bio-compatible which allows for medical translation. However, like most other polymer substrates, PDMS is optically transparent and thus requires optically absorbing molecules to be integrated to fabricate nanocomposites for use as optical ultrasound transmitters.

Carbon-based absorbers use a variety of carbon allotropes for absorption, including carbon-black [44, 45], multi-walled carbon nanotubes (CNT) [19], carbon nanofibres [46], candle-soot carbon nanoparticles [47] and graphite powder [48]. The advantage of carbon-based absorbers is their high optical absorption and high damage threshold compared to other absorbers, which allow for high peak pressures to be generated [16]. Noimark *et al* used a multi-walled CNT-PDMS composite to generate acoustic pulses with MPa-range peak pressures and a broad bandwidth of tens of MHz [19].

Metallic absorbers most commonly use gold nanoparticles (AuNP) for absorption of the excitation light. The gold can be arranged into arrays over-coated by PDMS [49], or dispersed into PDMS [17]. The generated peak pressures using AuNP absorbers are typically lower than those using carbon allotropes due to the lower absorption and damage threshold. The advantage of AuNP absorbers is the wavelength-dependent absorption spectrum, which depends on the nanoparticle size, shape and composition [50]. This property allows the use of AuNPs for combined photoacoustic and ultrasound imaging systems, since photoacoustic ex-

citation light can be transmitted through the AuNP composite. More recently, a CuInS₂ quantum dot PDMS composite was demonstrated to have a tunable absorption spectrum by altering the size and composition of the quantum dots [51]. This property makes them a promising absorber for multi-modal imaging applications.

Organic dyes have been explored as alternative absorbers for optical US generation, such as crystal violet which has a wavelength-selective absorption spectrum suitable for multi-modal imaging. However, crystal violet-PDMS composites displayed poor photostability resulting in a reduction in the generated ultrasound pressures over time. More recently, a photostable NIR dye (Epolin, Epolight 9837) was demonstrated for multi-modal ultrasound imaging [52].

Absorption of light in biological tissues was demonstrated as an alternative ultrasound generation scheme for imaging without the need of an external absorber. Fincke *et al* demonstrated this using NIR light from 800 to 2000 nm for ultrasound imaging in bovine tissue [53]. The advantage of this scheme is the non-contact generation of ultrasound in superficial layers of the tissue. However, due to the low optical absorption in tissue at these wavelengths, the light is absorbed across a large volume leading to a small bandwidth (< 2 MHz) and thus very low resolution images.

2.2.2 Optical ultrasound imaging systems

Imaging with optically generated broadband ultrasound has been demonstrated using a black polyethylene film [37], and more recently using a carbon-black doped PDMS film [45]. Both systems, however, relied on narrowband piezoelectric transducers for detection and thus were not able to take full advantage of the high frequencies generated. The use of a linear array also meant these systems were only capable of 2D imaging.

Broadband optical generation of ultrasound has been combined with broadband detection using FP etalon-based ultrasound detectors [49, 54]. The sensors used, however, provided relatively low acoustic sensitivity, with a NEP of more than 9 kPa

over a 50 MHz bandwidth. As a result, these systems were only able to produce images of strongly scattering wire targets with significant signal averaging.

A system that is broadband in both ultrasound generation and detection with high acoustic sensitivity was demonstrated by Colchester *et al* in 2015 by placing a CNT-PDMS composite film and a FP sensor on the end of adjacent optical fibres [55]. By mechanically translating the probe, a virtual array of ultrasound transmit-receive elements was created, with which high-resolution and high-fidelity images of biological tissue were obtained. Using the same single-element FP sensor-based fibre optic ultrasound receiver this system has since been modified for a number of optical ultrasound applications: (i) Rotational all-optical ultrasound imaging was demonstrated with a side-viewing optical ultrasound transducer [56]. (ii) An endoscopic all-optical ultrasound imaging probe was developed by delivering the excitation light through a fibre bundle to a carbon black coating at its distal end [57]. (iii) Freehand video-rate all-optical ultrasound imaging was demonstrated with a hand-held probe consisting of 64 optical fibres guiding the excitation light to a planar CNT-PDMS film to generate individual fibre optic ultrasound transducers [58].

In this work we aim to use the planar FP scanner for detection and optically generated ultrasound waves for transmission. In the next session we discuss the possible ultrasound image acquisition schemes to implement with the FP scanner system.

2.2.3 Ultrasound image acquisition schemes

There are a number of ultrasound image acquisition schemes which can broadly be split into three types based on the geometry of the transmitted wave: focused, diverging or planar waves. In this section, we discuss the different schemes and explain why only planar waves are considered in this work.

Conventional B-mode ultrasound imaging systems transmit a series of focused ultrasound waves into the medium to obtain an image of the object line-by-line. The generation of focused waves is easily achieved with piezoelectric transducers by introducing electronic delays between individual elements. Optically generating

focused ultrasound waves is, in principle, possible by exciting an absorbing layer deposited on a curved surface [59]. However, this would be more difficult to achieve with the flat sensor surface of the planar FP scanner. Imaging with focused ultrasound waves would require multiple insonifications to obtain an image, and thus lead to long acquisition times.

Divergent ultrasound waves can be generated optically by focusing the excitation light onto a point on an absorbing layer. This point-like source generates a spherical wave whose pressure decreases with propagation due to geometric spreading. For this reason, diverging or point-like sources are typically used with a synthetic aperture approach [60]. This approach involves generating a large number of divergent sources, and for each source detecting the scattered field along an array of detection points to obtain a low-resolution image [61]. Combining the low-resolution images for each divergent source, a higher resolution image is obtained, since focusing is performed for each pixel in transmit (indirectly through combining individual images) and receive [62]. A synthetic aperture approach using optically generated ultrasound and the FP sensor would involve scanning a focused excitation beam across an absorbing layer to generate point sources, and for each point source detecting the field at a number of detection points along the sensor array. The advantage of this approach would be that lower powered lasers with higher pulse repetition frequencies can be used which can potentially reduce the imaging time. However, to be able to benefit from faster imaging time, this puts a limit on the number of detection points which means that this approach cannot make full use of the whole planar FP sensor array, thus limiting the image quality. Another advantage of this approach is that excitation and detection points could be spatially offset to avoid the heat of the excitation light potentially affecting the detection sensitivity. However, in practice, this would require the system to be more complicated as the excitation light needs to be scanned as well as the interrogation light. Such a system would therefore, compared to the FP scanner system, require an additional scanning system for the excitation light.

Planar ultrasound waves can be optically generated with the absorption of an excitation laser beam in a planar absorbing coating. The generation of planar ultrasound waves can thus be easily implemented into the FP scanner system by placing an absorbing layer between the sensor and the medium, while the rest of the set up can remain the same as for PA imaging (see Fig. 1.1). Since this thesis is a first exploration into ultrasound imaging with the FP scanner, we decided on the use of planar ultrasound waves for imaging as the practically simplest option. For each transmitted plane wave the detection point is moved across the FP sensor to scan the scattered ultrasound field along the sensor plane. Since each plane-wave ultrasound pulse would insonify the whole medium, plane-wave ultrasound imaging using the FP scanner would achieve similar acquisition rates to photoacoustic imaging with the FP scanner. The relatively long acquisition times were less of a concern for this work, since the priority of this thesis is to achieve the highest possible image quality. If in future, faster imaging times are required, e.g. for clinical translation, other acquisition schemes such as diverging sources with a reduced number of detection points should be considered. Other ways to speed up the acquisition time are discussed in the conclusion of the next chapter (Section 3.5).

The modified FP scanner system we aim to develop thus constitutes a pulse-echo plane-wave ultrasound imaging system. We therefore review the literature on plane-wave ultrasound imaging in the next section.

2.2.4 Plane-wave ultrasound imaging

During plane-wave ultrasound imaging, planar, or unfocused, waves are transmitted into the medium. The planar waves insonify the whole region of interest, as opposed to scanning it line-by-line with focused waves as in conventional B-mode ultrasound imaging. The back-scattered waves are detected across a planar detection array.

The most commonly used approach to image formation in plane wave imaging is the delay-and-sum algorithm. This involves the calculation of the time of flight for each pixel/detector pair for a given incident wave, and summing the corresponding signals from all the detector elements to fill up the pixels of the image [61, 63]. An

alternative approach are Fourier-based reconstruction methods which are based on a more accurate solution of the wave equation, and can be computationally less intensive due to the use of fast Fourier-transforms [64, 65]. More advanced alternative methods include nonlinear delay-and-sum alternatives such as delay-multiply-and-sum [66], model based inversions [67, 68], and more recently deep learning methods [69–71]. In this work, we opted for a Fourier-based reconstruction approach, as it provides the most simple algorithm, a fast computation time given the large number of detection points for 3D imaging.

The reconstruction algorithm used in this work is based on work by Norton and Linzer, who first solved the inverse problem for plane-wave imaging in 1981 [72], and Cheng and Lu, who provided a fast k -space reconstruction algorithm for a general so-called limited-diffraction beam, of which a plane wave is a special case [65]. The reconstruction algorithm for imaging with normal plane waves is described in Section 3.2.3, and the more generalised algorithm for imaging with angled plane waves is derived in Section 5.3.1.

For conventional ultrasound imaging with piezoelectric transducers, plane-wave imaging has the advantage of a very fast frame rate, typically more than a 100-fold higher than B-mode imaging [73]. However, the increase in the frame rate comes at the cost of degradation in the image quality, since the image is no longer focused in transmission as B-mode images are, but only focused in detection, see Fig. 2.2. The limitation in image quality from imaging with a single plane wave can be addressed by compounding several image frames taken with plane waves at different angles. This so-called angle compounding can be done coherently to improve resolution or incoherently to reduce speckle [73]. Montaldo *et al* showed that coherent angle compounding performs as well as multi-focus B-mode imaging but with a significantly higher frame rate [63]. A more detailed background on plane-wave ultrasound compounding is provided in Chapter 5.

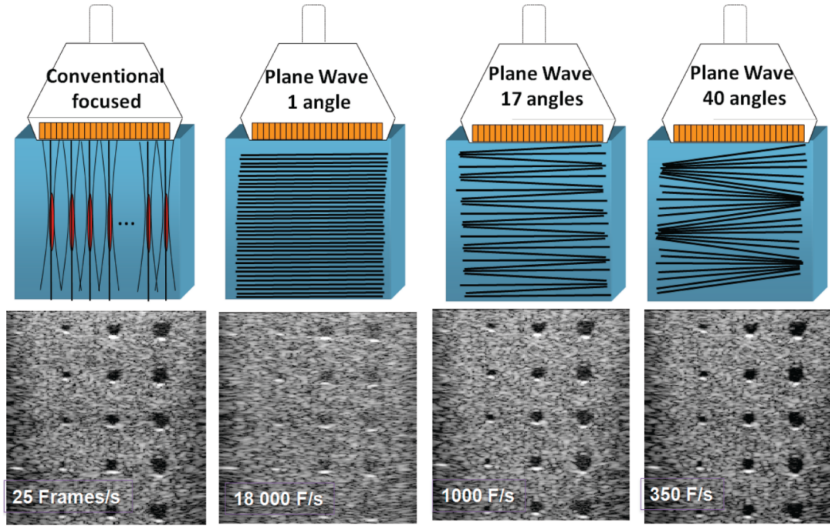


Figure 2.2: Conventional focused ultrasound vs ultrafast angle compounded imaging. Figure reprinted from [73] © 2014 IEEE.

2.3 Dual-mode imaging systems

Since both PA and US imaging require the detection of ultrasound, several attempts have been made to combine the two modalities in one system to benefit from the complementary contrast they provide. The different dual-mode systems can be broadly divided into three categories: (i) systems where both ultrasound generation and detection are based on piezoelectric transducers, (ii) hybrid systems that employ optical generation of ultrasound and piezoelectric detection, and (iii) all-optical dual mode systems where both ultrasound generation and detection are based on optical methods.

Piezoelectric dual-mode systems. The majority of dual-mode systems that have been developed are based on piezoelectric transducer arrays for the generation of US and the detection of PA and US signals, and incorporate a PA excitation source around the transducer array [5–10]. Since piezoelectric transducers operate over a low narrowband frequency range and have large detection elements, these systems were limited in the image resolution and fidelity they could provide.

Dual-mode systems with optical US generation & piezoelectric detection. In an attempt to address the bandwidth limitation of the US generation the PA effect was

used to optically generate US. This has been achieved by using a single excitation laser pulse to simultaneously excite PA waves and an US wave for reflection US imaging [74, 75]. Part of the excitation light was incident on the transducer surface of the piezoelectric transducer that was used for detection, which optically generated an US wave in the transducer surface. The remaining part of the excitation light was transmitted into the tissue to excite PA waves. This has been demonstrated with a linear array [74], and a full-ring array for PA and US computed tomography [75]. An alternative approach for the simultaneous excitation of PA waves and optical US waves was demonstrated with a wavelength-selective gold-PDMS absorber which partially transmitted and partially absorbed the excitation light [76]. The transmitted light excited PA waves, while the absorbed light optically generated an US wave. However, since all these systems still relied on piezoelectric detection methods they were not able to benefit from the high frequencies of the optically generated US transmission.

All-optical dual-mode systems. To make full use of the high bandwidth of optically generated US, various optical US detection schemes have been demonstrated in dual-mode imaging systems. A Mach-Zehnder interferometer was used as an optical ultrasound detector for dual-mode PA and US microscopy [77], 2D *ex vivo* tissue dual-mode imaging [78], and 3D *ex vivo* tissue dual-mode tomography [79]. Hsieh *et al* used a microring resonator for optical ultrasound detection, and the same excitation light to generate both PA and US signals [80] or a dichroic filter to switch between PA and US imaging modes [81]. A similar all-optical probe and synthetic aperture approach to Colchester *et al* [55] was adapted by Li *et al* for dual-mode imaging [82]. Li *et al* used one fibre coated with a carbon black-PDMS composite at its distal end for optical US generation, a fibre-tip FP sensor for detection, and, compared to Colchester *et al*, an additional optical fibre for wide-angle delivery of the PA excitation laser light.

2.4 Image property and image quality terms

In this section we define terms used for describing properties of photoacoustic and ultrasound images and their image quality.

Resolution. The spatial resolution of an image refers to the ability to distinguish between two image features that are positioned close together. Axial resolution corresponds to the ability to distinguish between two objects at different depths in the image, while the lateral resolution corresponds to the ability to distinguish between two objects at the same depth but different lateral positions within the imaging plane.

Point-spread function. One way to measure the spatial resolution is to determine the point(or line)-spread function (PSF/LSF) of the system. The PSF describes the response of an imaging system to a point source. This typically involves imaging a point-like object and measuring the size of the extended blob in the image that represents the point object. An object can be considered a point if its size is much smaller than the wavelength of the system. The term is typically used in optics, but can equally be used for ultrasound images.

Signal-to-Noise Ratio. The signal-to-noise ratio (SNR) is a measure that compares the level of a desired signal to the level of background noise. In the context of ultrasound imaging, this can be applied to the detected signal or the reconstructed image.

Contrast. The contrast is defined as the difference in image intensity between two image regions.

Contrast-to-Noise Ratio. The contrast-to-noise ratio (CNR) is a measure of how distinguishable two image regions are. It equal to the contrast between the two image regions divided by the noise, which can be taken as the standard deviation of the image intensities within each region.

Penetration depth. The penetration depth is a measure of how deep light or ultra-

sound can penetrate into a medium. It can also be used to refer to the maximum depth (distance to the sensor) at which a reasonable image of an object can still be formed.

Field of view. The field of view refers to the area or volume that an imaging system can take an image of.

Region of interest. The region of interest refers to an area within the image of particular interest.

Image fidelity. The image fidelity refers to how closely the image represents the object being imaged without any visible distortion or information loss.

Limited view problem. The limited view problem refers to the fact that a sensor array, due to its finite size, is only able to detect a fraction of the acoustic wave. This means that only a part of the waves emitted or scattered from an imaging object are detected by the sensor, which can result in an incomplete reconstruction of the object.

Limited view artefacts. The limited view of the sensor also results in the formation of limited view artefacts surrounding the image of an object. For example, in case of a point object, these limited view artefacts often take a wing-shape. In ultrasound literature, these artefacts are typically referred to as edge wave artefacts (and sometimes also side lobes, see below), but we will use the term limited view artefact as used by the photoacoustics community. In this work, we make the distinction between the incomplete reconstruction of an object due to limited view (see above) and the limited view artefacts described here, albeit both have the same root cause in the limited size of the sensor array.

Grating lobes. A consequence of having discrete transducer (or detector) elements rather than a continuous emitting (or detecting) surface is that grating lobes can occur. These are regions of constructive interference within the field. For a periodic placement of elements, grating lobes appear when the pathlength difference be-

tween adjacent elements is equal to the wavelength. In transmission, grating lobes have the effect of transmitting energy in unintended directions outside of the main lobe, which can lead to spurious images within the field of view of the image stemming from reflection of the grating lobes. Since we use continuously (optically) generated plane waves for transmission there should be no grating lobes transmitted in our case. In detection, the effect of grating lobes is that a signal originating (e.g. scattered) from one point in the medium will be reconstructed partly into other locations away from the main image of that point. These artefacts will be referred to as grating lobe artefacts and are discussed at length in Section 4.5.3.

Directional response. The directional response, or directivity, of a sensor describes its sensitivity to waves incident at different angles. Typically a sensor's response is dependent on both the direction of incidence as well as the frequency of the signal.

Side lobes. For a single transducer element, side lobes describe the areas or directions in which acoustic energy is transmitted into outside of the main lobe. This can lead to artefacts and noise in the image stemming from reflections of side lobes. Note, that these are not the same as grating lobes, which are due to *multiple* discrete transducers interfering with each other, while side lobes can appear for a *single* element. In the case of the optically generated plane wave, side lobes in transmission would correspond to the spherical edge waves generated at the edge of the excitation beam. However, this was not found to interfere with the system as the beam diameter was much larger than the detection area (see Section 3.2). In detection, the term side lobe would correspond to the directivity of a single sensor element. The directivity of the sensor can affect both grating lobes and limited view artefacts (which is why the latter may sometimes also be referred to as side lobes, although we will not use the term in that way here).

Dynamic range. The dynamic range is the ratio between the largest and smallest pixel intensity values that are contained in an image. This is usually expressed as a base-10 logarithmic value of the ratio between the smallest and largest values.

Single vs multiple scattering In order to reconstruct an image of the scatterer distribution some reconstruction algorithms, including the one we use (see Section 3.2.3), make the assumption of single scattering. This assumes that any back-scattered waves from reflections of the transmitted plane wave at scatterers in the object propagate without being scattered again, i.e. there is only one single scattering event for each back-scattered wave. This assumption is justified if the medium only contains weak scatterers or small acoustic impedance changes, which is typically the case in soft tissues. Then, any waves that are multiply scattered would be very weak in amplitude and negligible compared to the singly scattered waves. If there are strong scatterers in the medium, multiple scattering could be significant and result in the formation of image artefacts if a single scattering approximation was made. The single scattering approximation is also referred to as the Born approximation.

Chapter 3

Plane-wave ultrasound imaging with the FP scanner

3.1 Introduction

The overall aim is to design a dual-mode imaging system based on the planar FP scanner [1]. The planar FP scanner comprises an acoustic sensor based on a FP polymer film etalon that is interrogated by a focused laser beam which enables acoustically-induced changes in the etalon thickness to be detected. The FP scanner has previously been developed for PA imaging. Thus to achieve a dual-mode imaging system, an US generation capability needs to be added to the FP scanner system.

The basic design idea is to use optically generated, or laser-generated, ultrasound. For this purpose, the FP sensor was coated with an optically absorbing film that acted as an ultrasound transmitter coating, see Fig. 3.1. The coating was excited with nanosecond laser pulses delivered through the back of the FP sensor head. This generated plane-wave ultrasound pulses which propagated into the imaging target. The acoustic field scattered from the target was then mapped in 2D by the FP scanner, from which a 3D image of the scatterer distribution was recovered using a k -space reconstruction algorithm. The FP scanner system was thus modified to

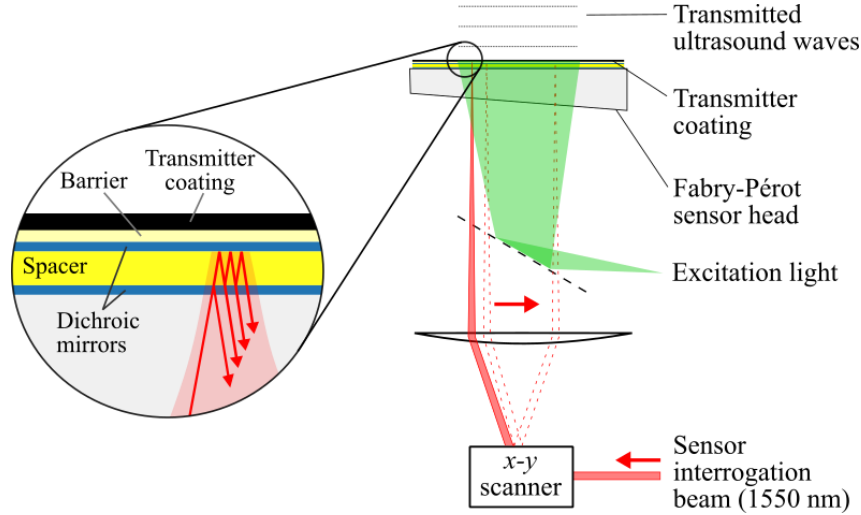


Figure 3.1: Schematic of the all-optical ultrasound imaging system, based on optically generated plane-wave ultrasound produced by the absorption of laser pulses in an ultrasound transmitter coating, and the detection of scattered waves with the planar FP scanner. Figure reprinted from [83] © 2021 IEEE.

provide a pulse-echo plane-wave US imaging modality, which operates all-optically on both transmit and receive. This system will thereafter be referred to as the optical US system.

In this chapter, we used US transmitter coatings that were strongly absorbing at all visible and NIR wavelengths. This was done to provide the best possible optical US generation for the initial development of the optical US system. To make the system dual-mode, the US transmitter coating would need to be transparent to the PA excitation light. Such a wavelength-selective, or dichroic, transmitter coating will be described in Chapter 6 to demonstrate a dual-mode system based on the FP scanner. The dual-mode system can then be used for PA imaging using the light transmitted through the coating to excite PA signals, and for US imaging using the light absorbed in the coating to generate an US wave. The US mode of the dual-mode system has the same working principle as the optical US system described in this chapter. The work in this chapter is, therefore, directly translatable to the US mode of the dual-mode system.

Outline. In this chapter, a description of the optical US system and its evaluation is provided. Section 3.2 describes the ultrasound generation and detection mecha-

nisms, as well as the image reconstruction method. In Section 3.3, we characterise the system's ultrasound generation and detection performance, and the spatial resolution it can provide. Finally, ultrasound images obtained by the system of scattering phantoms, tissue mimicking phantoms and *ex vivo* tissues are presented in Section 3.4.

3.2 System working principle

Details of the optical generation of US, and the fabrication and excitation of the US transmitter coatings are given in Section 3.2.1. The working principle and hardware details of the FP scanner used for US detection are described in Section 3.2.2. Finally, Section 3.2.3 describes the *k*-space reconstruction algorithm, how the data is handled before reconstruction and how images are processed after reconstruction.

3.2.1 Optical ultrasound generation

To optically generate US, laser pulses are absorbed in planar absorbing coatings, here referred to as US transmitter coatings. Due to the photoacoustic effect this will create planar US waves. In this section, we introduce the different coatings used in the optical US system, and describe methods for fabrication and excitation of the transmitter coatings.

Spray paint (SP) coating. For a first test of the system's feasibility, FP sensors were coated in a thin layer of black SP (*PlastiKote* Super Gloss Spray Paint). This resulted in a smooth coating with a strong optical absorption in the visible and NIR wavelength range.

CNT-PDMS coating. CNT-loaded PDMS films were prepared by Sacha Noimark using the method described by Noimark *et al* [19]. Multi-walled CNTs were functionalised for uniform dispersion in xylene (1.8 mL), and manually mixed with PDMS (1 g, MED-1000, Polymer Systems Technology, U.K.). Using doctor-blading methods, the solution was applied onto a polyimide film and cured at room temperature for 24 hours, before removing a thin CNT-PDMS film from the polyimide film. The CNT-PDMS film had an approximate thickness of 60-100 μm . In

order to coat the FP sensor head, the CNT-PDMS film was soaked in ethanol, which made it slightly swell up. After the film was placed on top of the FP sensor head, the ethanol evaporated and caused the film to shrink tightly to the FP sensor surface.

Excitation. Plane-wave ultrasound pulses were generated by illuminating the CNT-PDMS coating with 7-ns laser pulses from a fibre-coupled 1064-nm Q-switched Nd:YAG excitation laser (Quantel Laser, Ultra 50) with a pulse energy of 50 mJ, a Gaussian beam profile with diameter of approximately 20 mm, and a pulse repetition frequency (PRF) of 20 Hz.

The excitation laser has a pulse energy variation of less than 2% (RMS deviation from the mean for 99% of shots) as quoted by the manufacturer. The long-term (over 8 hours) pulse energy drift is reported to be less than 10%. These laser fluctuations were not accounted for as they did not significantly impact the imaging performance. The image quality is relatively insensitive to variations in the laser pulse energy due to the averaging effect of the reconstruction process.

As a multi-mode fibre was used to deliver the excitation light, there is the potential for the beam profile to be non-Gaussian. This would generate a plane wave with a non-uniform amplitude across the wave front, which would not impact the image fidelity but would have the effect of some areas of the image appearing darker than others. Since this was not observed in practice, we can assume that the excitation beam was sufficiently homogeneous across the imaging aperture.

Acoustic Attenuation. The CNT-PDMS film exhibits low frequency dependent acoustic attenuation over the majority of the frequency range relevant to the current study; e.g. a 100 μm film attenuates frequencies up to 22 MHz by less than 1.7dB [43]. The attenuation of the photoacoustic wave as it propagates through the CNT-PDMS film is thus negligible.

3.2.2 Optical ultrasound detection

Sensor. The FP sensor consists of two highly reflecting dichroic mirrors separated by a 20 μm spacer made of Parylene-C [84] thus forming a polymer etalon, see Fig. 3.1. A barrier layer of 2.5- μm -thick Parylene-C separated the etalon from the

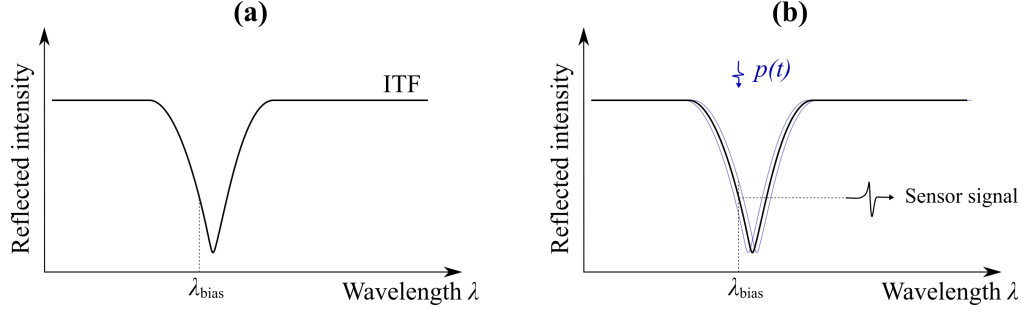


Figure 3.2: Concept of acoustic sensitivity of the FP scanner. **(a)** Choice of bias wavelength λ_{bias} at the maximum slope of the interferometer transfer function (ITF). **(b)** Acoustic waves incident on the FP sensor lead to a thickness change of the interferometer spacer which changes the reflected intensity at λ_{bias} .

transmitter coating. Incident acoustic waves modulate the etalon thickness resulting in a corresponding modulation of its reflectivity.

Interrogation. The reflectivity is read-out using a continuous wave interrogation laser beam (*Yenista Optics*, Tunics T100s-HP) focused on a point in the plane of the sensor. The spot size of the interrogation laser was 64 μm , which defines the element size of the acoustic detector to a first approximation [85].

Bias wavelength. To achieve optimum sensitivity, the interrogation laser was tuned to the wavelength corresponding to the maximum slope of the interferometer transfer function (ITF), hereafter referred to as the optimum bias wavelength [1], see Fig. 3.2a. When interrogated at the bias wavelength, acoustically-induced thickness changes of the interferometer spacer lead to a change in the reflected intensity, see Fig. 3.2b. The process of determining the bias wavelength for all interrogation points will be referred to as pre-tuning. The bias wavelength was selected after the CNT-PDMS coating had been irradiated by the pulsed laser excitation for approximately 3 minutes. This ensured the sensor attained the same thermal steady state that exists during image acquisition which is necessary for an accurate bias wavelength estimation.

Detection. The reflected light from the FP sensor is directed via a single-mode fibre-optic circulator (Thorlabs, 6015-3-APC) on to an InGaAs photodiode-amplifier unit (Hamamatsu, G9801-22, -3dB bandwidth 200 MHz) connected to a

250 MS/s digitizer (National Instruments, PCI-5114) with a 125 MHz analogue bandwidth, and a 50 kHz high-pass filter. Acoustic pressure time series were recorded sequentially at 22500 spatial points across the sensor by using a precision x - y galvanometer-based scanner (Cambridge Technology, 623XH) to scan the interrogation beam over a $15 \text{ mm} \times 15 \text{ mm}$ area with a step size of $100 \text{ }\mu\text{m}$. The acquisition time for one scan was approximately 20 min for an excitation laser with a PRF of 20 Hz.

Acoustic stability. The acoustic sensitivity of the sensor could be affected by a change in the temperature of the sensor. Since the pre-tuning and imaging were performed with the sensor in the thermal steady state from the pulsed laser excitation and ambient temperatures were stable, there was no change in temperature during the whole process. No long-term drifts in the acoustic sensitivity were observed.

3.2.3 Image reconstruction and processing

Inverse problem. The inverse problem for pulse-echo plane-wave ultrasound imaging has previously been solved by Norton and Linzer [72]. The reconstruction algorithm used in this chapter follows the work of Cheng and Lu [65], and is based on three main principles: 1) the imaging object is assumed to be a distribution of weak scatterers $f(x, y, z)$, i.e. multiple scattering is neglected; 2) any acoustic field can be written as a sum of propagating plane waves; and 3) any propagating plane wave can be described uniquely in terms of any three of (ω, k_x, k_y, k_z) , where ω is frequency, and k_x, k_y, k_z are the wavenumbers in the x, y, z directions, since they are linked by the dispersion relation $(\omega/c)^2 = k_x^2 + k_y^2 + k_z^2$, where c is the speed of sound. Here, x and y refer to the axes along the sensor plane, and z refers to the depth axis. Exploiting these principles, the acoustic pressure measured on a plane, $p(x, y, t)$, can be Fourier-transformed to provide $P(k_x, k_y, \omega)$, and then mapped to $F(k_x, k_y, k'_z)$ via the dispersion relation $k'_z = \omega/c + \sqrt{(\omega/c)^2 - k_x^2 - k_y^2}$, where ω/c is the additional phase due to the time (z/c) it takes the transmitted plane wave to arrive at scatterers at depth z . Finally, by computing the inverse Fourier-transform of $F(k_x, k_y, k'_z)$ the

3D scattering distribution $f(x, y, z)$ is obtained. The MATLAB code used to perform the inverse problem for 3D normal plane-wave imaging is shown in Appendix A.

Data processing. A backwards propagating plane wave emitted from the transmitter coating was detected by the sensor. Its contribution to the sensor signal was large in amplitude compared to the scattered wave signals, and therefore needed to be removed from the signal before reconstruction to avoid strong artefacts which would dominate actual features in the reconstructed image. Before reconstruction, the signal from the backwards propagating plane wave was thus removed from the sensor signal by replacing the first 1 μ s of the data with zeros.

The time point of $t = 0$ was set to the time of arrival of the backwards propagating plane wave at the sensor. The wave will have already travelled through the barrier layer at this point, but so will all other acoustic signals reflected from the imaging target. Thus choosing $t = 0$ as the time of arrival of the backwards propagating plane wave is approximately equivalent to setting $z = 0$ at the top of the barrier layer, i.e. the bottom of the US transmitter coating where the plane wave is generated. However, since the start of the acquisition, i.e. $t = 0$, was triggered on the excitation laser pulse, it did not coincide with the arrival of the backwards propagating plane wave. The sensor data thus needed to be corrected to account for this by removing the time samples until the arrival of the backwards propagating plane wave. This $t = 0$ correction was typically of the order of 10 ns.

Due to the periodic nature of the k -space algorithm, image features near the edge of the scanning area can wrap to the opposite side of the image. To avoid this, the sensor data was expanded in the x and y directions by zero-padding 10 additional points at either side of the scanning data.

The sensor data was up-sampled in x and y by a factor of 2 to give a spatial sampling step of 50 μ m. This up-sampling in space exploits the oversampling in time (temporal sampling interval of 4 ns) and thus z (sampling step of ~ 6 - μ m), and results in higher lateral resolution images.

The measured pressure time series were filtered with a low-pass Butterworth filter with a -3dB cut-off frequency of 30 MHz. This was done to remove high-frequency

noise beyond the acoustic detection bandwidth.

Reconstruction. The image was reconstructed onto a $17 \text{ mm} \times 17 \text{ mm}$ grid with $50 \text{ }\mu\text{m}$ spacing in x - y . The voxel size in depth z is given by the temporal sampling interval used multiplied by a factor of $c/2$.

Image processing. Envelope detection based on a Hilbert transform was performed on the reconstructed image, and time gain compensation was applied if necessary. The images were interpolated to a $25 \text{ }\mu\text{m} \times 25 \text{ }\mu\text{m} \times 10 \text{ }\mu\text{m}$ spacing in x - y - z using Fourier interpolation. Images are presented as maximum intensity projections (MaxIP) or mean intensity projections (MeanIP) through the whole 3D image volume or through slices of the volume. All optical ultrasound images are shown on a linear scale, as their dynamic range was not as large as for conventional ultrasound images which are typically displayed on a log compressed scale. All the features that can be highlighted in the respective optical ultrasound images are visible on a linear scale, and their visibility is not improved on a log compressed scale (see Section 3.4.4).

The time for reconstruction and processing using an Intel Core i7-7700K CPU @ 4.20 GHz and 32 GB RAM was approximately 30 s.

3.3 System characterisation

Before the optical US system can be used for imaging, its generation (Section 3.3.1) and detection (Section 3.3.2) capabilities need to be characterised. Since the optical generation of US also generates heat we studied the effect of heat on the acoustic sensitivity of the FP sensor (Section 3.3.3). Finally, the system's resolution performance was characterised (Section 3.3.4).

3.3.1 Mapping of optically generated ultrasound

3.3.1.1 Characterisation method

Set up. The optical ultrasound generation from photoacoustically excited CNT-PDMS films and SP films were characterized in terms of their peak pressure, wave

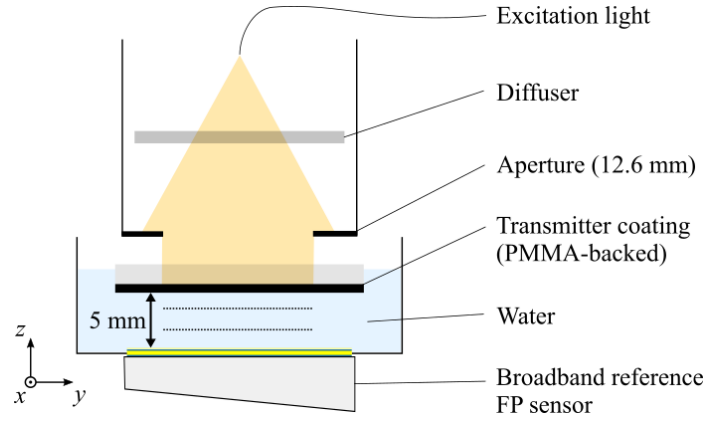


Figure 3.3: Set-up for characterising ultrasound pulses generated by the absorption of laser pulses in a transmitter coating and propagated through 5 mm of water, and mapped using a broadband all-hard-dielectric reference FP sensor. Figure adapted from [83] © 2021 IEEE.

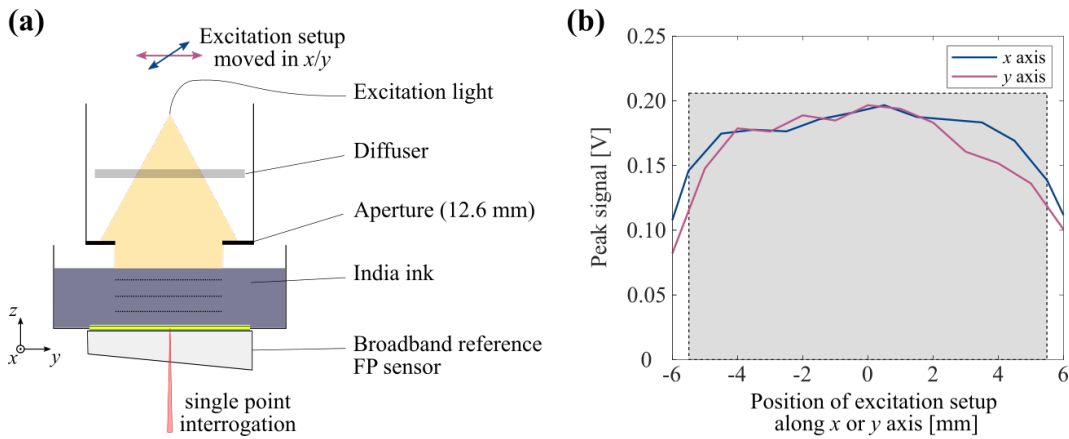


Figure 3.4: Profiling of the excitation beam used in the characterisation measurements. **(a)** Set-up, with excitation beam delivered through a diffuser tube and India ink as an absorber for the generation of photoacoustic waves. **(b)** Beam profiles obtained by moving the excitation setup along the x- and y-axes and taking the peak photoacoustic signal at each point as a measure for the beam intensity profile. Uniform part (to within 20%) marked with grey box.

front planarity and bandwidth using the set-up shown in Fig. 3.3.

Excitation. The output of the excitation laser fibre was passed through a diffuser and an aperture of 12.6 mm diameter to homogenise its fluence across a known area. Note, that the diffuser and aperture were only used in this experimental arrangement, not the set-up used for imaging experiments, which is shown in Fig. 3.1. The excitation beam was characterised for its uniformity by using India ink as a uniform absorber to generate a photoacoustic plane wave, see Fig. 3.4a. The amplitude of

the planar wavefront generated in the India ink is proportional to the intensity profile of the excitation beam. The excitation beam setup was translated along the x and y axes, and the generated wave measured at a stationary point on a broadband reference FP sensor, that is described in more detail below. Hence the peak amplitude of the pressure time series at each position of the excitation beam can be taken as a measure of the beam profile. The beam profile was shown to be uniform to within 20% over an area with diameter 11.0 ± 0.5 mm, i.e. slightly smaller than the aperture of the tube, see Fig. 3.4b. The energy of each laser pulse was assumed to be uniformly spread across this area to give an estimate for the fluence of the excitation beam (22 ± 2 mJ/cm²). This excitation beam was delivered to US transmitter films made of SP or CNT-PDMS deposited on a 5-mm thick polymethylmethacrylate (PMMA) slab to photoacoustically generate ultrasound. The end of the excitation beam tube was moved as close as possible to the absorbing coating to ensure an energy fluence similar to the one determined above.

Detection. The reference FP sensor used to map the field had an all-hard-dielectric spacer layer and provided a theoretical thickness-mode limited bandwidth in excess of 1 GHz, and a constant frequency response to within 1 dB in the range 1-40 MHz [86]. The reference FP sensor was positioned parallel to the transmitter films and separated in water by a distance of $d = 8.5$ mm for CNT-PDMS and SP. The incident ultrasound waves generated from the SP and CNT-PDMS transmitter films were mapped over a $14 \text{ mm} \times 14 \text{ mm}$ area, with a step size of $100 \text{ }\mu\text{m}$, element size of $64 \text{ }\mu\text{m}$ and temporal sampling interval of 4 ns.

3.3.1.2 Comparison of SP and CNT-PDMS coatings

In this section, we present results from the mappings of the optical US fields generated from SP and CNT-PDMS films, and compare the performance of the two transmitter coating materials. A map of the peak pressure distribution in the xy -plane, profiles through the wavefront in x and y , and a pressure time series are shown in Fig. 3.5 for the CNT-PDMS coating and in Fig. 3.6 for the SP coating. All numerical values and figures comparing SP and CNT-PDMS performance were

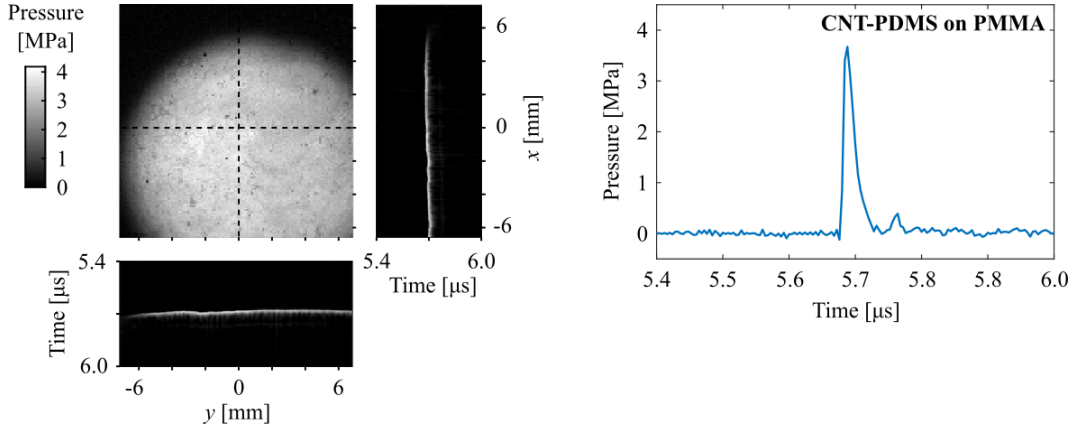


Figure 3.5: Map of peak pressure distribution in xy plane, profiles through the wavefront in x and y , and pressure time series at the centre of the sensor produced by a CNT-PDMS composite transmitter coating on a PMMA slab.

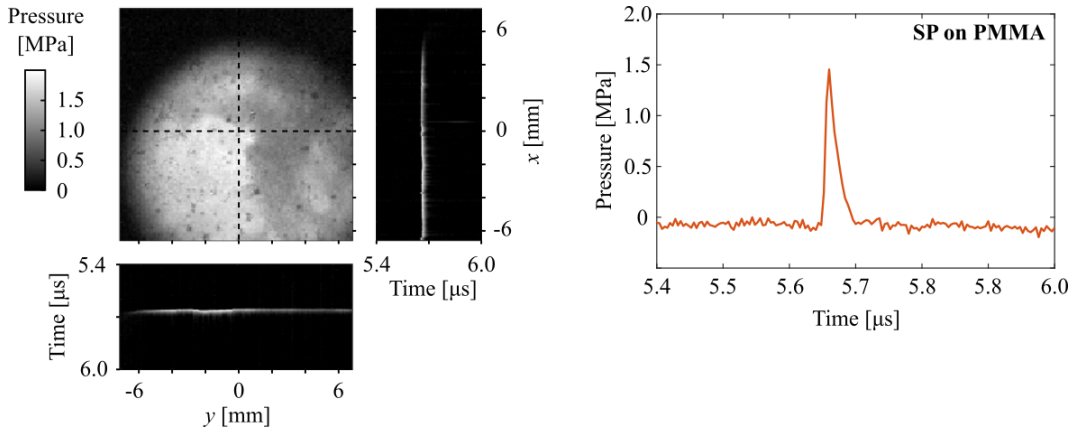


Figure 3.6: Map of peak pressure distribution in xy plane, profiles through the wavefront in x and y , and pressure time series at the centre of the sensor produced by a SP transmitter coating on a PMMA slab.

obtained from back-to-back measurements in a single experiment to ensure that experimental parameters, particularly the excitation set-up, were the same across measurements. The measurement mapping the ultrasound output of the CNT-PDMS coating to characterise its performance was repeated for a journal paper [83]. The results of this repeat measurement are shown in Appendix B to avoid confusion and allow for a fair comparison of CNT-PDMS and SP performance in this section.

Generation efficiency. The generation efficiency of a coating is defined as the peak pressure generated in the coating per unit of absorbed fluence. Since the pressure generated in the coating cannot be directly measured, a large circular excitation

beam was used to generate a plane wave that propagates without significant attenuation due to geometrical spreading of the wavefront. A region of interest (ROI) was defined in the xy -plane, to include the majority of the circular wavefront but exclude the edges of the wave since those parts may contain edge waves with lower peak pressures and later times of arrival than the plane wave. For each sensor interrogation point the peak pressure was determined in the detected pressure time series. To obtain an estimate of the average peak pressure across the wavefront the mean and standard deviation of the peak pressure values at all interrogation points in the ROI were determined.

The optical US pulses produced by the CNT-PDMS coating had an average peak pressure of 3.0 ± 0.3 MPa, giving a generation efficiency of 0.14 ± 0.03 MPa cm² / mJ. The average peak pressure generated by the SP coating was 1.2 ± 0.3 MPa, giving a generation efficiency of 0.056 ± 0.019 MPa cm² / mJ. Thus CNT-PDMS films generate approximately 2.5 times as much peak pressure as SP coatings. Note, that these generation efficiencies are stated for a propagation distance of $d = 8.5$ mm in water.

Uniformity of amplitude. To assess the uniformity of the peak pressure amplitude across the generated wavefront, the peak pressures of the time series for each interrogation point were extracted. The plane wave generated by the CNT-PDMS film is uniform to within 10% in amplitude, while the wave generated by the SP film is much less uniform. The non-uniformity of the measured peak pressure can have a number of potential causes: a non-uniformity in the excitation source fluence distribution, a non-uniformity in the absorbing coating, or a non-uniformity in acoustic sensitivity at different interrogation points across the detecting reference FP sensor head. Comparing the x - y peak pressure maps in Fig. 3.5 for CNT-PDMS and Fig. 3.6 for SP (and Fig. 3.7 for a CNT-PDMS coating on an FP sensor), a spatial correlation between the patterns can be observed. Since the pattern is the same across different absorbing coatings, a non-uniformity in the absorbing coating can be ruled out. The excitation source fluence was characterised for its uniformity

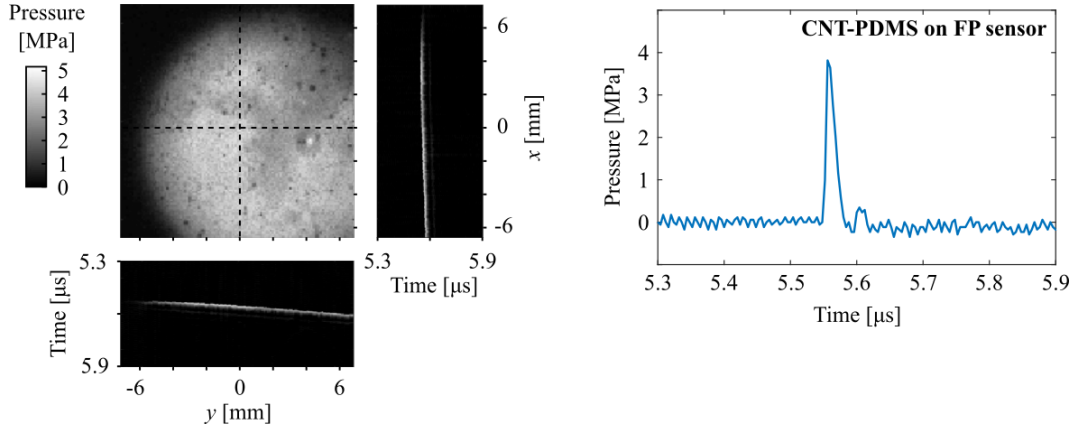


Figure 3.7: Map of peak pressure distribution in xy plane, profiles through the wavefront in x and y , and pressure time series at the centre of the sensor produced by a CNT-PDMS composite transmitter coating on a FP sensor.

in Fig. 3.4, and did not exhibit a pattern similar to the one observed in the measured peak pressure maps in Figs. 3.5 to 3.7. The non-uniformity in the measured peak pressure can therefore be attributed to a non-uniformity in acoustic sensitivity at different interrogation points across the detecting reference FP sensor head. The repeat measurement of the output from the CNT-PDMS coating, see Fig. B.1 in Appendix B, was carried out with a different reference FP sensor with the same properties as the one used in this section, and was able to measure a more uniform wavefront amplitude.

Planarity of wave. To assess the planarity of the generated waves the time of arrival (TOA) of the peak pressure at each interrogation point was extracted. The TOA for all interrogation points within the ROI is fitted to a plane. For both SP and CNT-PDMS films the maximum deviation within the ROI is of the order of 8-12 ns. The waves are thus planar to within $\lambda/10$ at 10 MHz.

CNT-PDMS coating on FP sensors. Finally, a CNT-PDMS film was used to coat a FP sensor used for imaging to map the field that would be generated during an imaging experiment, see Fig. 3.7. The only difference compared to the PMMA-backed CNT-PDMS coating was a slightly elevated ‘noise’ level of weak acoustic signals arriving within a few μs of the plane wave wavefront. These can be attributed to imperfections in the transmitter coating, such as tiny trapped air bubbles between

the transmitter coating and the FP sensor, or roughness of the barrier layer of the FP sensor (not the FP interferometer spacer layer). These imperfections act like acoustic point sources which cause the formation of weak spherical waves. The amplitude of these parasitic spherical waves is much smaller than the main plane wave and is attenuated with propagation due to geometric spreading. Any back-scattered waves from reflections of these parasitic spherical waves will thus be weak and do not impact the performance of the system.

For both CNT-PDMS coatings on the PMMA slab and the FP sensor (Figs. 3.5 and 3.7) a weak second peak was measured approximately 100 ns after the back-propagating plane wave was detected. This peak corresponds to a weak partial reflection of the forward-propagating plane wave at the PDMS-water boundary which generated a weak back-propagating plane wave. Since this part of the signal is usually replaced with zeros it does not affect the performance of the system.

3.3.1.3 Non-linear propagation

Ultrasound waves can only be detected after propagating some distance through a medium (e.g. water). The propagation may be non-linear for waves generated with high peak pressures. During non-linear propagation, parts of the wave with higher pressure travel at higher sound speeds than those with lower pressure. This leads to a change in the acoustic pulse shape, which in turn results in a change in the frequency content of the pulse. In order to determine the bandwidth of the optical ultrasound generation we therefore need to study non-linear propagation for different amplitudes of optical ultrasound pulses first.

Method. Different amplitude pulses were generated by varying the fluence of the excitation beam incident on the PMMA-backed CNT-PDMS coating. This was done by inserting neutral density (ND) filters with a range of optical densities (0.3, 0.5, 1) between the excitation light source and the absorbing CNT-PDMS films in the set-up shown in Fig. 3.3. This method of varying the incident fluence ensured that the optical pulse duration remained the same for all measurements. Assuming linear conversion of optical energy to pressure, this means that any acoustic pulse

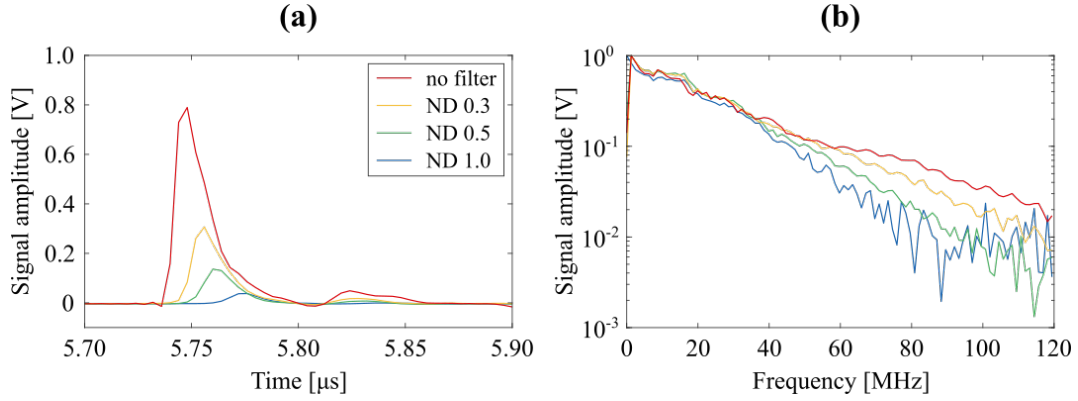


Figure 3.8: Non-linear propagation of optical ultrasound produced by a CNT-PDMS transmitter coating for a range of ND filters to vary the fluence. The ultrasound waves propagated 8.5 mm in water before being detected with a broadband reference FP sensor. **(a)** Pressure time series in the centre of the excitation beam with a temporal sampling step of 4 ns and 1000 averages, and **(b)** corresponding normalised frequency spectra.

shape variations observed can be attributed to non-linear acoustic propagation. An alternative method to vary the incident fluence by changing the Q-switch delay on the excitation laser was shown to be unsuitable to study non-linear propagation as the optical pulse duration was changed as well (Appendix C). The generated ultrasound waves were detected after a propagation distance of 8.5 mm at a single interrogation point on the reference FP sensor with a temporal sampling interval of 4 ns. The pressure time series were Fourier transformed to obtain frequency spectra.

Results. Ultrasound waves with a range of peak pressures from 120 kPa to 2.5 MPa were generated, which should exhibit varying degrees of non-linear propagation. ND filters with lower optical density, giving rise to larger fluences and thus generating higher peak pressures, yielded acoustic pulses that were narrower and sharper towards the front edge, see Fig. 3.8. The acoustic pulses have similar frequency spectra up to 40 MHz, and higher peak pressures resulted in broader frequency spectra with more energy at frequencies above 40 MHz. This trend is expected to be observed for varying degrees of non-linear propagation.

Conclusion. We can thus conclude that non-linear propagation was observed for optical ultrasound pulses with peak pressures in the MPa-range (e.g. measurement

without ND filter, red line in Fig. 3.8), while low peak pressure pulses in the 100s of kPa-range propagated linearly (e.g. measurement with ND filter with optical density 1, blue line in Fig. 3.8). This knowledge will be used in the next section to estimate the bandwidth of a linearly and a non-linearly propagated pulse.

3.3.1.4 Bandwidth

Method. In order to determine the bandwidth of the acoustic plane wave emitted by the CNT-PDMS transmitter film, measurements of the pressure time series were made at a single interrogation point in the centre of the reference FP sensor with a temporal sampling interval of 0.8 ns using a 350 MHz digitizing oscilloscope (Tektronix, 5034D). A measurement was first obtained with a ND filter with an optical density of 1 at 1064 nm (90% attenuation) placed between the aperture and the PMMA backing, in order to reduce the laser pulse energy and consequently the peak pressure to ensure linear acoustic propagation through the water, as shown in Section 3.3.1.3. The measurement was then repeated but without the ND filter in place resulting in non-linear propagation. Note, that these two measurements are equivalent to the measurements in Section 3.3.1.3 with ND filter of optical density 1 and without ND filter, shown in Fig. 3.8. The difference of the measurements in this section compared to those in the previous section is the increased bandwidth of the oscilloscope used for detection to provide a more accurate estimate of the bandwidth of the optical US generation. To ensure similar SNR in both cases, 1024 averages were used in the linear case and 12 averages in the non-linear case. Since the former measurement is acquired in the absence of non-linear propagation it provides a measure of the inherent acoustic bandwidth that the CNT-PDMS coating provides. For each measurement, the time series was filtered to remove any DC offset, windowed with a 0.4 μ s Tukey window centred around the peak, before taking the Fourier transform to obtain the frequency spectrum.

Results. Monopolar ultrasound pulses with full-width-half-maximum (FWHM) pulse width of 16 ns were recorded in both cases, see Fig. 3.9a. The linearly propagating pulse had a broadband frequency spectrum with a -6dB bandwidth of 22

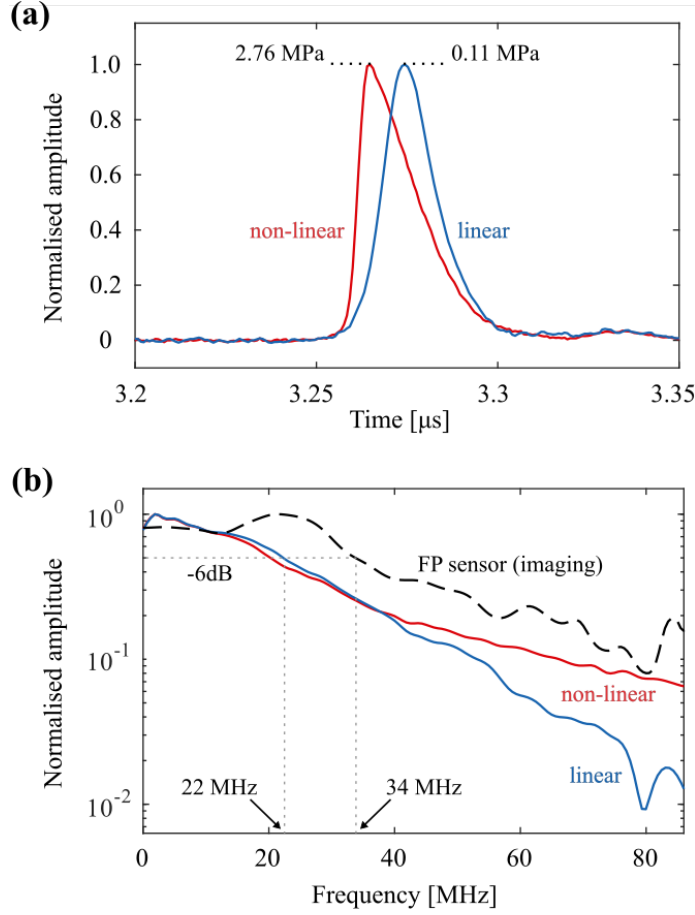


Figure 3.9: Characteristics of optically generated ultrasound pulses. **(a)** Normalised time-domain signals of linearly and non-linearly propagated pulses. **(b)** Normalised frequency spectra of linearly and non-linearly propagated pulses, and frequency response of FP sensor used for imaging. Figure reprinted from [83] © 2021 IEEE.

MHz, Fig. 3.9b. The non-linearly propagating pulse had a similar -6dB bandwidth, but contained more energy at frequencies above 40 MHz.

Conclusion. In this section, the bandwidth of the US pulses generated from the optical absorption of nanosecond laser pulses in a CNT-PDMS transmitter film were measured. The measurements show that the optical US system transmits monopolar US pulses with bandwidths in the tens of MHz range. Such high transmit bandwidths should allow for high-resolution imaging of tissue structures, assuming a sufficiently broadband detection system. The bandwidth of the planar FP scanner used as the detection system in the optical US system is measured in the next section.

3.3.2 Fabry-Pérot scanner bandwidth

The acoustic bandwidth of the FP sensor used for imaging was measured using a broadband (1-70 MHz) laser-generated ultrasound source [34] and the broadband reference FP sensor described in Section 3.3.1.1. The output of the source was measured at 4 different points on both sensors with a temporal sampling interval of 4 ns and averaged 100 times for the imaging sensor and 1000 times for the reference sensor. Each measurement was filtered to remove any DC offset and windowed with a 0.4 μ s Tukey window centred around the peak, before taking the Fourier transform to obtain the frequency spectrum. Dividing the frequency spectrum of the signal detected by the imaging sensor by that detected by the reference sensor, and averaging over the resulting 16 spectra gave the imaging FP sensor's frequency response, shown in Fig. 3.9b (black dashed line). From this data, the -3dB and -6dB bandwidths of the FP sensor were estimated to be 30 MHz and 34 MHz, respectively. Based on the sensitivity of the sensor described by Zhang *et al* [1], which was of a similar design, the peak NEP was estimated to be approximately 0.3 kPa over a 20 MHz measurement bandwidth.

3.3.3 Heating effects

With each laser pulse used to generate an ultrasound wave, heat was deposited in the transmitter coating. This generated a thermal wave that diffused through the sensor layers, causing thermal expansion of the spacer, and thus a shift in the ITF. The shift in the ITF due to the thermal wave did not appear in the sensor signal, since it had a much longer (ms) time scale compared to acoustic signals (μ s) and could thus be filtered out by the 50-kHz high-pass filter on the photodiode-amplifier unit. The shift in the ITF could, however, result in the bias wavelength no longer corresponding to the point of maximum slope on the ITF which could potentially reduce the acoustic sensitivity of the FP sensor, see Fig. 3.10. In this section, we assess the effect of the thermal wave on the acoustic sensitivity of the sensor.

Method. The set up for the measurement was the same as for imaging (Fig. 3.1), with the sensor immersed in a water bath. The distance between the sensor and the

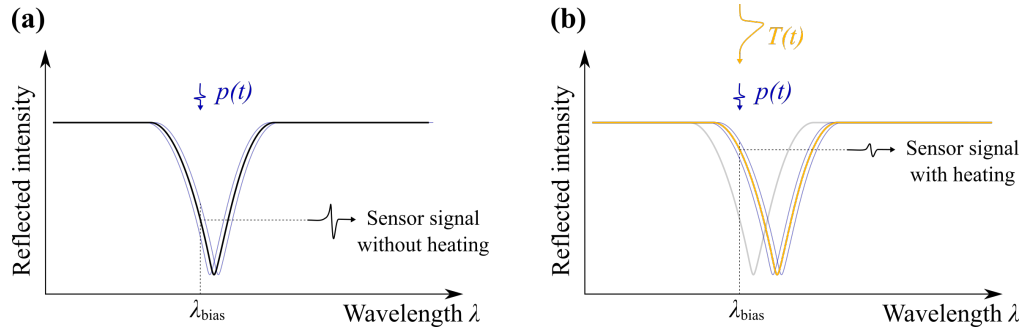


Figure 3.10: Heating effects on the sensitivity of the sensor. **(a)** Acoustic sensitivity in the absence of external heating. **(b)** Heat-induced shift in the ITF results in bias wavelength no longer corresponding to the point of maximum slope leading to a reduced sensitivity to acoustic signals.

water surface was approximately 15 mm. The sensor was interrogated at a single point, and the 50 kHz high-pass filter on the photodiode-amplifier unit was disabled. This way both thermal and acoustic signals could be monitored simultaneously.

Overview. Every excitation laser pulse deposited the same amount of thermal energy in the FP sensor. Hence the sensor heats up until it reaches a thermal steady state where the rate of dissipation of heat matches the laser pulse heating rate. Only when the sensor is in the steady state can it be pre-tuned and data acquired, as then there should be no long term thermal drifts in the ITF which could lead to a change in acoustic signal sensitivity. In Section 3.3.3.1, we investigate how long after exposing the transmitter coating to repeated pulsed excitation the sensor reaches the steady state. In Section 3.3.3.2, pulse-to-pulse thermal processes are studied to see if the arrival time of the thermal wave can be separated from the arrival times of acoustic signals. Potential problems of heating during pre-tuning are discussed in Section 3.3.3.3.

3.3.3.1 Long-term heating effects

Setup. The interrogation laser was tuned to the bias wavelength at room temperature. The sensor signal was measured with a temporal sampling interval of 5.8 ms over a duration of several minutes, see Fig. 3.11. The sampling rate had to be relatively low so as to not exceed the memory limits of the digitiser over the long acquisition time. A few seconds after the start of the acquisition the excitation laser

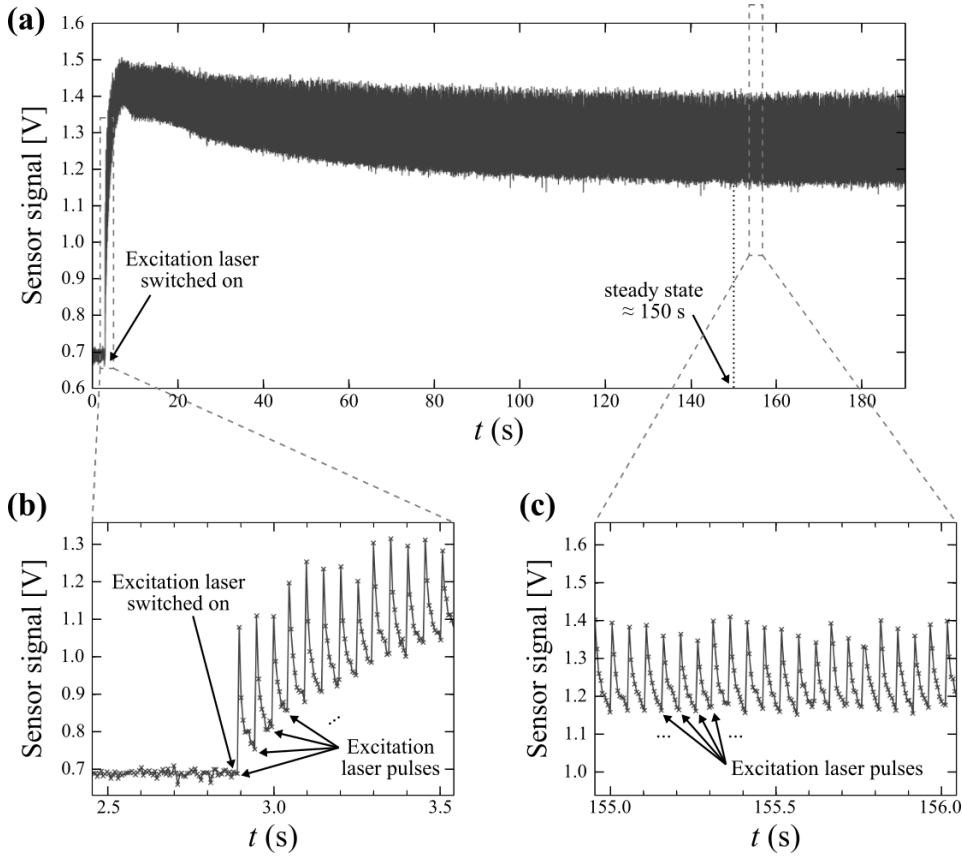


Figure 3.11: Timescale of long-term heating effects. The sensor bias wavelength was chosen at room temperature. The excitation laser was switched on a few seconds after the start of the acquisition. (a) Sensor signal shown over 190 s, reaching a steady state after 150 s, and zoomed in on (b) the start of excitation laser pulsing and (c) the steady state to demonstrate pulse-to-pulse heating.

was switched on, exposing the transmitter coating to repeated excitation laser pulses at a PRF of 20 Hz.

Results. The sensor was observed to heat up and reach its maximum temperature within a few seconds, see Fig. 3.11a. In the following minutes, the heat dissipation rate increased and eventually matched the heating rate, reaching a thermal steady state, after roughly 2.5 minutes. On the smaller time scales in Fig. 3.11b and c we observe peaks in the thermal wave signal spaced by roughly 50 ms. These peaks approximately coincide with the excitation laser pulses which were incident with a PRF of 20 Hz. After each excitation pulse, the sensor signal increases sharply, indicating a sudden shift in the ITF due to the heat from the pulse. The sensor signal then decays approximately exponentially until the next excitation pulse is incident.

At the start of the heating process, when the sensor is still at room temperature, the heat deposited by each excitation pulse does not completely dissipate in the time until the next excitation pulse, leading to an increase in the sensor's temperature on a timescale of a second, Fig. 3.11b. In the steady state, the energy deposited by each excitation pulse dissipates in the time until the next pulse, such that there is no drift in the sensor's temperature on the timescale of a second, Fig. 3.11c. However, despite being in the thermal steady state, the sensor signal fluctuates sharply on the time scale of 50 ms, coinciding with the PRF of the excitation laser pulses. This indicates that the ITF is oscillating along the wavelength axis as a result of the repeated heat deposition from the excitation laser pulses.

Conclusion. We conclude that the steady state is reached 2.5 minutes after the first exposure of the transmitter coating to the pulsed excitation laser. Therefore, it is necessary to wait for this period before beginning the imaging procedure. There are however pulse-to-pulse fluctuations in the sensor signal, and thus in the ITF position, that could affect acoustic signal sensitivity. These fluctuations could not be fully resolved with the low sampling rate of this measurement (temporal sampling interval of 5.8 ms), and will be measured in the next section.

3.3.3.2 Pulse-to-pulse heating effects

Setup. In this measurement, the transmitter coating was exposed to the pulsed excitation laser for an extended period of several minutes to allow a thermal steady state to be established. When the thermal steady state was reached, the bias wavelength was chosen. The acquisition of the sensor signal was triggered off of the excitation laser pulse using a fast photodiode, and measured with a temporal sampling interval of 100 ns over a time period of 70 ms.

Results. Figure 3.12a shows the sensor signal over a timescale of two excitation pulses. The sensor was observed to heat up quickly after each excitation pulse, with the deposited heat dissipating between the two excitation pulses. Figure 3.12b shows the sensor signal over a time scale of 200 μ s around the first excitation pulse, and includes several acoustic signals and the onset of the thermal signal. The arrival

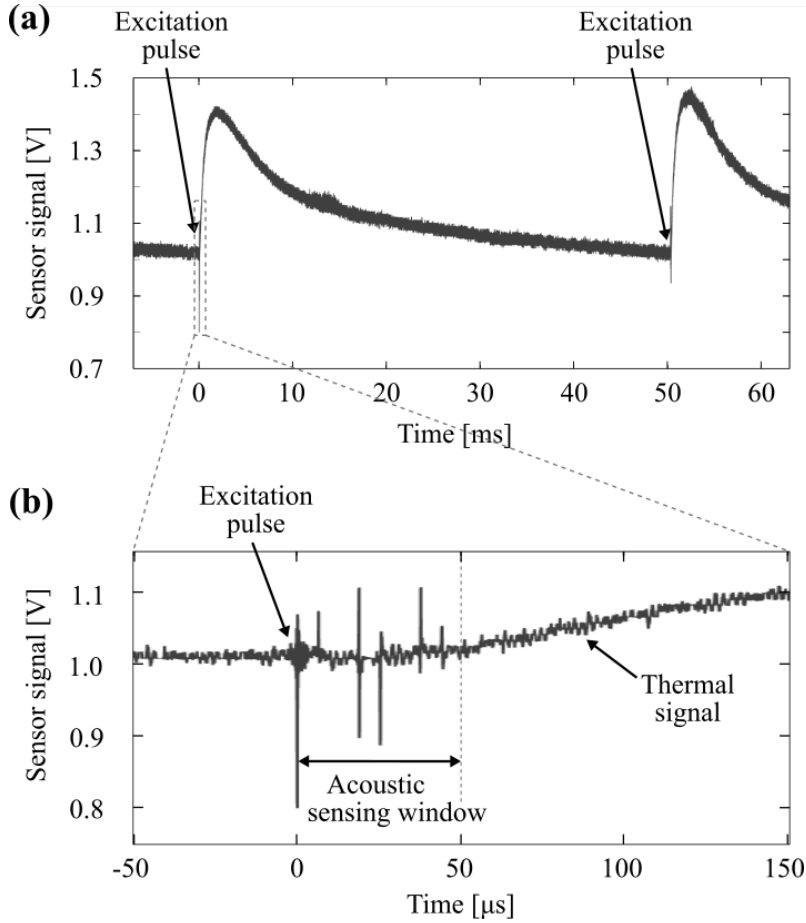


Figure 3.12: Timescale of pulse-to-pulse heating effects. The sensor bias wavelength was chosen in the thermal steady state. Sensor signal shown over a timescale of (a) two excitation laser pulses and (b) zoomed in on the acoustic sensing window. Figure reprinted from [83] © 2021 IEEE.

of the thermal wave is delayed by about 50 μ s after each excitation laser pulse. This is due to the time it takes for the thermal wave to diffuse through the 2.5 μ m thick Parylene-C barrier layer, which separates the transmitter coating from the sensor layers (Fig. 3.1). In this 50 μ s time window between the excitation pulse and the arrival of the thermal wave, acoustic signals can be detected without the loss of sensitivity caused by thermally induced bias wavelength changes. Indeed, some acoustic signals were detected in the 50 μ s acoustic sensing window, see Fig. 3.12b. These signals arise from time-delayed reflections of the plane wave emitted by the coating from the interface between the air and the surface of the water layer above the sensor and reflections of the backwards propagating plane wave at the sensor head backing-air interface. It is worth noting that during the 50 μ s acoustic sensing

window the signal associated with the thermal wave from the previous excitation pulse is still decaying slightly. The slope of that decay is, however, very small and can be neglected on the timescale of acoustic signals.

Conclusion. We conclude that the acquisition of acoustic signals with the FP scanner is not affected by the heat generated during optical ultrasound generation for the first 50 μs of the acquisition. The equivalent pulse-echo imaging depth of a 50 μs delay is approximately 37.5 mm. This is more than sufficient for superficial tissue structures, e.g. lymph nodes, as well as to match PA imaging depths. If greater imaging depths are required, the arrival of the thermal wave could be further delayed by increasing the thickness of the barrier coating.

3.3.3.3 Effect of heating during pre-tuning

In the previous sections, measurements taken during the thermal steady state (Fig. 3.11c and Fig. 3.12) indicate that the ITF is oscillating along the wavelength axis at a frequency equalling the PRF of the excitation laser as a result of the heat from repeated excitation pulses. However, we also concluded that pre-tuning of the sensor, i.e. sampling its ITF to find the optimum bias wavelength, should take place within the thermal steady state. This means that during the pre-tuning procedure the sensor's ITF, that is being sampled, is not stationary but oscillating at the laser's PRF. The ITF position that we wish to sample is the one just after an excitation pulse is incident and before the resulting thermal wave arrives, as this is the acoustic sensing window. The thermally induced oscillations of the ITF could potentially corrupt some samples on the ITF fringe, and lead to a sub-optimal choice of the bias wavelength and thus a reduced acoustic sensitivity, see Fig. 3.13. In this section, we investigate the effect of the thermally induced ITF oscillations during the pre-tuning procedure on the acoustic sensitivity of the sensor.

Pre-tuning at a single point. When interrogating the sensor at a single point, as was done in Section 3.3.3.2, the sensor is pre-tuned by sampling the ITF quickly along the wavelength axis. This takes place over a few hundreds of ms during which time only few excitation pulses are incident, resulting in only few periods of thermally

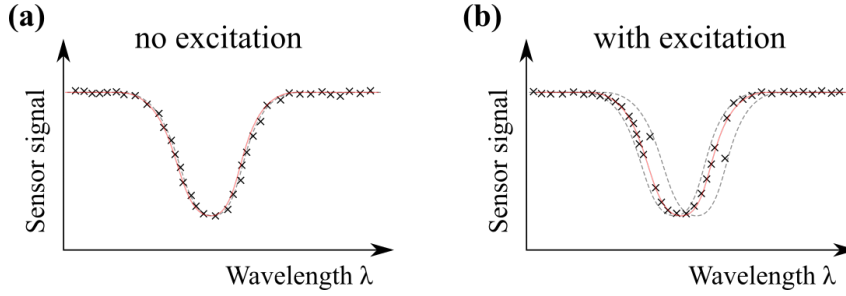


Figure 3.13: Schematic to demonstrate heating effects on pre-tuning. (a) without excitation laser and (b) with excitation laser incident on the transmitter coating to demonstrate that the excitation heating does not affect pre-tuning. Grey dotted line in (a) shows position of ITF at room temperature, while the grey dotted lines in (b) show the position of the ITF just before the arrival of the thermal wave from an incident excitation pulse and the position of the maximally heat-shifted ITF. Measured reflectivity values during pre-tuning (black crosses) and fitted ITF (red) to determine bias wavelength.

induced oscillation of the ITF. While sampling the relatively thin ITF fringe, which determines the bias wavelength, it is therefore unlikely that the ITF is significantly shifted due to thermally induced oscillations. The ITF fringe can thus be sampled without significant corruption from ITF oscillations. In the unlikely event that the sampling of the ITF fringe coincides with a significant ITF shift during a thermally induced oscillation, the shape of the fringe is very obviously distorted. In that case, the pre-tuning procedure can simply be repeated to obtain an uncorrupted sampling of the ITF. For single-point interrogation the sampling of the ITF is thus not affected by the thermally induced ITF oscillations, resulting in the choice of the optimum bias wavelength and no loss in the acoustic sensitivity.

Pre-tuning the whole sensor. For multi-point interrogation, as is necessary for imaging, the pre-tuning procedure is slightly different. The system does a spatial interrogation scan at one wavelength, then increments the wavelength, and repeats the spatial scan, such that the ITF at every point on the sensor is built up wavelength-by-wavelength. For each wavelength, the spatial scan can take from hundreds of ms to the order of 1 s, with the whole pre-tuning procedure taking up to 1 min. During this time thermally induced oscillations of the ITF occur at a rate equal to the laser's PRF, in this case 20 Hz. This means that some samples of the ITF at

every interrogation point will be significantly corrupted by the thermally induced ITF oscillation. This could potentially result in a sub-optimal choice of the bias wavelength and thus a reduced acoustic sensitivity.

Another issue related to heating is the local heating of the sensor at the current interrogation point due to the thermal energy deposited by the interrogation laser. This heat can significantly reduce the acoustic sensitivity of the sensor, and depends on the time the interrogation laser is incident at any given point, which in turn depends on the sampling rate of interrogation points during the imaging procedure.

Method. To verify that the sensor was correctly biased in the thermal steady state without loss of sensitivity, we designed a simple experiment. A planar piezoelectric transducer (Olympus Panametrics V381-SU, 3.5 MHz centre frequency) provided a planar US pulse which served as a constant signal to be measured by the scanner. The sensor would either be pre-tuned without being exposed to excitation laser pulses ('cold PT'), or with excitation laser pulses incident on the transmitter coating such that the sensor is within its thermal steady state ('hot PT'). For signal acquisition the scanner was operated in three different modes:

- 'cold 1 kHz': No excitation laser incident on the transmitter coating, with the signal acquisition triggered off of an electronic pulser at 1 kHz.
- 'cold 20 Hz': No excitation laser incident on the transmitter coating, with the signal acquisition triggered off of the excitation laser at 20 Hz.
- 'hot 20 Hz': Excitation laser incident on the transmitter coating, with the signal acquisition triggered off of the excitation laser at 20 Hz.

The first acquisition mode ('cold 1 kHz') was included to provide an acquisition with a fast sampling rate of interrogation points, to compare to the second acquisition mode ('cold 20 Hz') where the sampling rate of interrogation points is the same as for imaging experiments with the 20 Hz excitation laser. This comparison will demonstrate the effect of interrogation heating. The comparison between the last two acquisition modes ('cold 20 Hz' and 'hot 20 Hz') will demonstrate the effect of

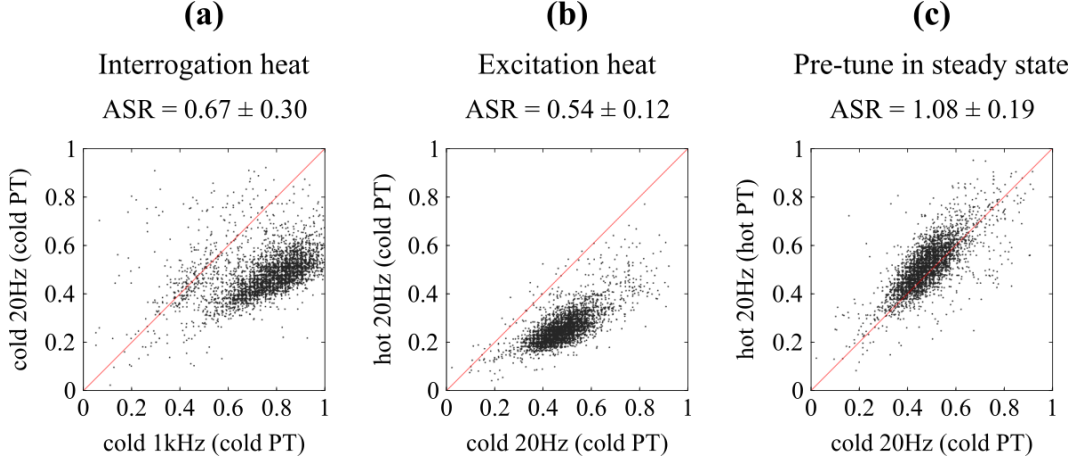


Figure 3.14: Heating effects on pre-tuning. Comparison of sensitivity of different acquisition modes with average sensitivity ratio (ASR) given. **(a)** Sensitivity loss from interrogation heat when the interrogation points are sampled at 20 Hz compared to 1 kHz. **(b)** Sensitivity loss from excitation heat when pre-tuning without exposure to excitation light. **(c)** No sensitivity loss when pre-tuning in thermal steady state. All axes are on the same scale in arbitrary units of the sensor signal amplitude.

excitation heating.

All acquisition modes were set up such that the transducer would emit an US pulse upon each trigger event. From the detected US pulses the peak signal was extracted for each interrogation point. To compare two acquisition modes X and Y, the peak signal at each interrogation point from mode X is compared to the peak signal at the same interrogation point from mode Y. This data will be presented in a scatter plot with the x and y axes representing the peak signal amplitude from mode X and Y, respectively, and each data point representing the peak signal from the two modes at the same interrogation point, see Fig. 3.14. We define the average sensitivity ratio (ASR) as the ratio of the peak signals of mode Y divided by those from mode X, averaged over all interrogation points. The average sensitivity ratio thus gives a measure of how much more or less sensitive acquisition mode Y is compared to acquisition mode X.

Effect of the interrogation heat. First, we compare the two acquisition modes without the excitation laser incident on the transmitter coating ('cold 20 Hz' and 'cold 1kHz'), using the pre-tuning map obtained in the cold state of the sensor

(‘cold PT’). The only difference between the two acquisition modes is the sampling rate of interrogation points, i.e. the amount of time the interrogation laser is incident on each sensor interrogation point (50 ms for ‘cold 20 Hz’ compared to 1 ms for ‘cold 1 kHz’). Since the acquisition and pre-tuning modes in this comparison did not involve the exposure to excitation heat, any difference in acoustic sensitivity can be attributed to the interrogation heat. The sensitivity loss due to interrogation heat was found to be significant, see Fig. 3.14a, with an average sensitivity ratio of 0.67 ± 0.30 . This difference in sensitivity is due to the difference in time that the interrogation laser was incident on the sensor at each given interrogation point, leading to a different amount of heat-shifting of the ITF during acquisition.

Effect of the excitation heat. Second, we compare the sensitivity of the acquisition mode with the excitation light pulses incident on the transmitter coating (‘hot 20 Hz’) with an acquisition mode without exposure to excitation light pulses (‘cold 20 Hz’), using the pre-tuning map obtained without exposure to excitation (‘cold PT’) for both acquisition modes. This comparison demonstrates the sensitivity loss due to the heat from excitation laser pulses, when the sensor is not pre-tuned within the thermal steady state. Note, that for both acquisition modes compared here the sampling rate of interrogation points was the same (20 Hz) to ensure that the effect of interrogation heating is the same for both measurements, such that any loss in sensitivity can be purely attributed to excitation heat. The sensitivity loss due to excitation heat was found to be significant, see Fig. 3.14b, with an average sensitivity ratio of 0.54 ± 0.12 . The scatter plot in Fig. 3.14a shows a spread-out point cloud, indicating that the sensitivity loss due to deposition of heat from excitation laser pulses was not uniform across all interrogation points. This was indeed the case as the excitation laser beam had a Gaussian beam profile.

Compensation by pre-tuning in steady state. Finally, we compare the sensitivity of the acquisition mode with the excitation light pulses incident on the transmitter coating (‘hot 20 Hz’), i.e. within the thermal steady state, using a pre-tuning map obtained within the thermal steady state (‘hot PT’) with an acquisition mode

without exposure to excitation light pulses ('cold 20 Hz'), using the pre-tuning map obtained without exposure to excitation ('cold PT'). This comparison thus demonstrates the recovery of the acoustic sensitivity loss observed in the previous paragraph, when the sensor is pre-tuned within the thermal steady state instead of in a cold state without exposure to excitation light. In this case, no loss in sensitivity was observed, see Fig. 3.14c, with an average sensitivity ratio of 1.08 ± 0.19 . This shows that pre-tuning within the thermal steady state is sufficient to negate the effect of a thermal shift of the ITF due to the increase of the sensor's temperature observed in Fig. 3.11a and b. It also shows that there is no loss in sensitivity due to the thermally induced oscillations of the ITF (Fig. 3.11c and Fig. 3.12) that occur during pre-tuning in the thermal steady state. The sensitivity was even slightly improved in the hot acquisition mode compared to the cold acquisition mode, with the average sensitivity ratio being slightly above 1. This is likely due to the thermally induced ITF oscillations causing the fit to the measured ITF to be slightly shifted up along the wavelength axis compared to the ITF position just before the arrival of the thermal wave from an incident excitation pulse, see Fig. 3.13b. This would lead to a slight overestimation in the bias wavelength at each interrogation point, which could partially compensate for the sensitivity loss due to interrogation heating described above.

Conclusion. We conclude that there is no loss in acoustic sensitivity due to the excitation heat, when the system is pre-tuned within the thermal steady state. Pre-tuning within the thermal steady state may also reduce the effect of sensitivity loss due to interrogation heat.

3.3.4 Spatial resolution

Setup. To determine the spatial resolution the system can provide, measurements of the instrument line-spread function (LSF) were made. This was achieved by imaging a target comprising a row of strongly scattering tungsten wires (Fisher Scientific, 7440-33-7) immersed in water, see Fig. 3.15. The wires were 27 μm in diameter, spaced by 1 mm and arranged parallel to each other and to the FP sensor.

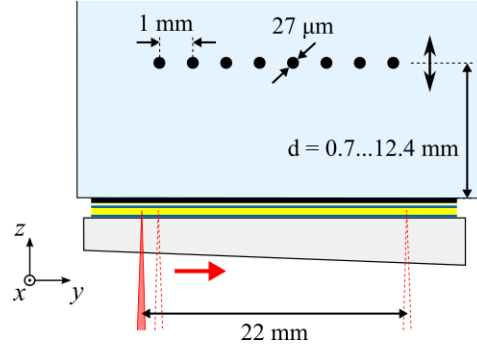


Figure 3.15: Set-up used to estimate the line spread function of the system. The phantom comprised a row of $27\ \mu\text{m}$ diameter tungsten wires immersed in water, and was positioned at different depths from the sensor ranging from 0.7 to 12.4 mm. At each depth a 2D image was acquired by scanning the interrogation beam across a 22 mm long line in steps of $20\ \mu\text{m}$. Figure reprinted from [83] © 2021 IEEE.

The target was imaged at varying depths from 0.7 to 12.4 mm in approximately 1 mm steps. To acquire each image, the sensor interrogation beam was scanned across a 22 mm long line, in steps of $20\ \mu\text{m}$ in the direction perpendicular to the wires. The acoustic pressure time series were recorded at each point with a temporal sampling interval of $dt = 4\ \text{ns}$ and without any signal averaging.

Temperature gradient. The absorption of the excitation laser pulses in the coating produced heat that diffused away into the surrounding water. This established a temperature gradient in the water bath leading to a slightly varying sound speed as a function of depth. The reconstruction algorithm however requires a single value for the sound speed. Thus, in order to reconstruct the images, a uniform sound speed needs to be assumed for all images of the wires at different depths.

Sound speed and t_0 search. Also unknown, besides the sound speed, is the exact time at which the optical US wave was generated (t_0) since this does not typically coincide with the start time of the acquisition, as described in Section 3.2.3. Knowledge of t_0 is important for the reconstruction since the time point of $t = 0$ needs to be set to t_0 for an accurate reconstruction of the object. To find a suitable sound speed and t_0 value, an exhaustive search over a range of values for both was performed. The sound speed and t_0 value pair that gave the highest average resolution

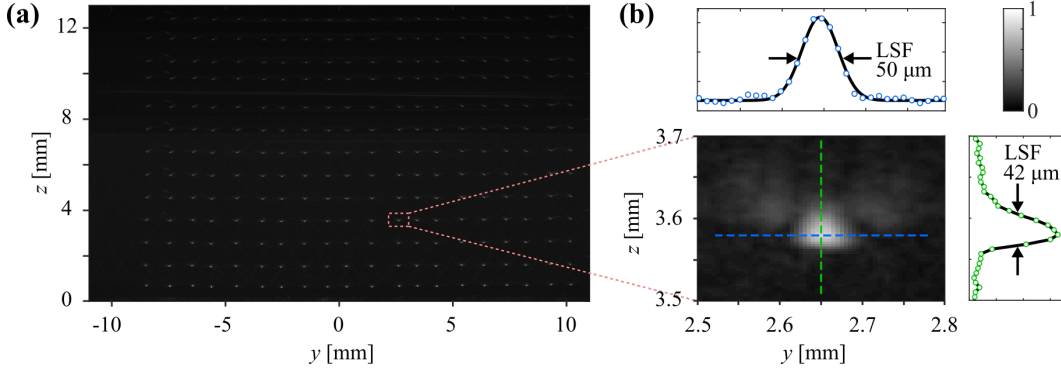


Figure 3.16: Estimation of system line spread function. **(a)** Compound ultrasound image of wires at all depths. **(b)** Expanded view of single wire. The lateral LSF was determined by fitting a Gaussian function to the profile of the wire image intensity and measuring the FWHM. The axial LSF was determined by linearly interpolating the profile before measuring the FWHM. Figure adapted from [83] © 2021 IEEE.

for targets within a central $6 \text{ mm} \times 12 \text{ mm}$ window in the yz plane was selected for reconstruction. This search resulted in a sound speed value of 1489 m/s and a t_0 value of $14 \times dt$.

Reconstruction. The data was upsampled along the y axis by a factor of 2 to give a spacing of $10 \mu\text{m}$. Each image was reconstructed on a $22 \text{ mm} \times 13 \text{ mm}$ y - z grid with $10 \mu\text{m} \times 6 \mu\text{m}$ spacing, envelope detected, and interpolated to $5 \mu\text{m}$ in the lateral y direction using Fourier interpolation. Fig. 3.16a shows the compound image obtained by summing the images of the target acquired at each depth.

LSF. The lateral and axial LSF were obtained by taking horizontal and vertical profiles through the maximum intensity point of the wire image, and measuring the FWHM, see Fig. 3.16b. In the lateral direction a Gaussian function was fitted to the profile, while in the axial direction linear interpolation was applied, to determine the FWHM. For the Gaussian fit a constant intensity offset was included as a variable, which was important to allow for an accurate fit and estimation of the lateral FWHM.

Contour plot. To illustrate the spatial dependence of the lateral resolution, the data for the lateral resolution of all the wire targets was interpolated in the yz plane, and

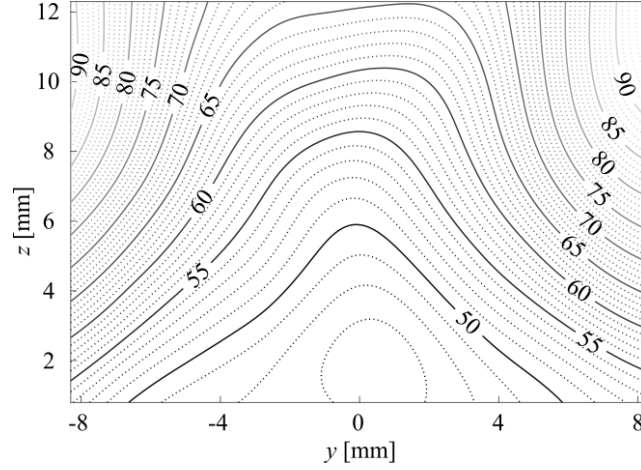


Figure 3.17: Contour plot of lateral resolution in yz plane, in units of μm . Figure reprinted from [83] © 2021 IEEE.

smoothed with a Gaussian filter with 1.5 mm blurring radius (1σ) before contours were applied. The resulting contour plot shows the spatial dependence of the lateral resolution over a 16×12 mm area in the yz plane, see Fig. 3.17. The lateral resolution can be observed to decrease with increasing depth from the sensor, and decrease at lateral positions further away from the centre of the sensor. Both of these trends are due to limited view, i.e. the finitely sized sensor detecting only a fraction of the wave scattered off the wire. The lateral resolution appears to be symmetric in the y axis, i.e. along the sensor, as one would expect from a symmetric system. The spatial dependence of the lateral resolution of the optical US system based on the FP scanner is comparable to the one obtained for photoacoustic imaging with the FP scanner [1].

Uncertainty. Given a sound speed uncertainty of 1 m/s due to the temperature gradient in the water, the average error in the lateral resolution was estimated to range from $0.5 \mu\text{m}$ at 1 mm depth to $6 \mu\text{m}$ at 12 mm depth.

Axial resolution. The axial resolution was found to be $44 \pm 3 \mu\text{m}$ across the whole field of view. As expected, the axial resolution showed no significant spatial variation, as it is largely defined by the bandwidth of the generated pulses and the sensor.

3.3.5 Safety

In this section, the safety of imaging with optically generated ultrasound is discussed. For diagnostic ultrasound the two main considerations are the thermal and cavitation effects on the tissue [87].

The thermal hazard arises from energy deposited in the tissue as an acoustic wave propagates through it due to the acoustic attenuation it experiences. For example, in soft tissues the acoustic attenuation coefficient is approximately $0.3 \text{ dB cm}^{-1} \text{ MHz}^{-1}$. Most of the deposited energy is converted into heat, which causes a temperature rise in the tissue. If the temperature rises above 43°C , thermally sensitive proteins start to denature which after long exposure times can cause cell death. During conventional piezoelectric B-mode imaging, which is generally considered safe, tissues are insonified by focused acoustic pulses with peak pressures in the 0.5-5.5 MPa range at the focus, and repetition frequency of up to several kHz. In comparison, the ultrasound waves generated by the system described in this chapter were planar acoustic pulses with similar peak pressures of 3-5 MPa, but with a much lower repetition frequency of 20 Hz. The deposition of thermal energy in the tissue is thus several orders of magnitude lower for the optical ultrasound system than for conventional focused B-mode imaging, and therefore unlikely to be an issue. If the optical ultrasound system were to be used with excitation lasers with higher pulse repetition rates, the energy deposition per unit time would be higher but the exposure time would be reduced, minimising the risk from overheating.

Another thermal issue is the heating of the transducer itself, which leads to the diffusion of thermal energy into the tissue in contact with the transducer. For conventional B-mode imaging this is not an issue over short scan times. For the optical ultrasound system, however, optical energy is deposited in the transmitter coating during optical ultrasound generation, leading to an increase in its temperature. This has not been found to be an issue in the *ex vivo* tissue imaging experiments (Section 3.4.3) and preliminary *in vivo* imaging tests on human tissue. Typically, a layer of ultrasound coupling gel would separate the transmitter coating from the tissue surface, reducing the effect of thermal diffusion. However, to translate this system

for use in a clinical setting the potential safety issue from the transmitter coating heating would need to be reviewed. This could be done by imaging an acoustically absorbing tissue mimicking phantom with a thermocouple embedded near the surface of contact with the transmitter coating.

The cavitation hazard arises from the potential of bubble formation, or cavitation, due to periods of high negative acoustic pressure. Bubbles expand and contract along with the variations in pressure. At high peak acoustic pressures the contractions can become unstable, leading to the collapse of bubbles under the inertia of the surrounding liquid. This so-called “inertial” cavitation presents a mechanical hazard in form of strong mechanical forces exerted on the surrounding tissue, and a chemical hazard due to the high instantaneous temperatures generated during rapid bubble compression, which create highly reactive conditions. The risk of inertial cavitation scales with the maximum negative acoustic pressure within the tissue. For conventional B-mode imaging, which is considered safe, the acoustic pulses have positive and negative peak pressures of up to 5 MPa at the focus. The optical ultrasound system, on the other hand, transmits monopolar pulses with a positive peak pressure of a similar or lower amplitude. Coupled with the fact that the optical ultrasound pulses are planar, i.e. unfocused, it is unlikely that large negative acoustic pressures would occur in the scattered acoustic field within the tissue. Another factor increasing the likelihood of cavitation is the duration over which the high negative peak pressure occurs. The optical ultrasound pulses had a FWHM pulse width of 16 ns, which is equivalent to the half period of a 31 MHz acoustic wave and can thus be considered short. At this frequency, cavitation does not occur at the acoustic pressures generated by the optical ultrasound system. The optical ultrasound system can therefore be considered safe in relation to the cavitation hazard.

3.4 Imaging experiments

In this section, the performance of the optical ultrasound system was tested with arbitrarily shaped scatterers (Section 3.4.1), tissue mimicking phantoms (Section 3.4.2) and *ex vivo* tissue samples (Section 3.4.3). The latter two were also

imaged with a clinical ultrasound scanner (Ultrasonix, SonixMDP) for comparison.

The goal of this section is to demonstrate the imaging capability of the optical ultrasound system by showing the best possible images it can provide. The clinical scanner images are shown as a reference to validate the optical ultrasound images against. The comparison of the optical ultrasound system with a standard ultrasound scanner serves as an indication of its performance, rather than a rigorous or exhaustive comparison of ultrasound imaging systems. When comparisons are made between the images, these are only to point out differences in the image features which are due to varying bandwidths and slice thicknesses.

The optical ultrasound images are displayed without log compression on a linear scale, while the clinical ultrasound images are displayed on a log compressed scale. Section 3.4.4 demonstrates why a linear scale was sufficient to display all image features in the optical ultrasound images. Section 3.4.5 shows the frequency content of the detected signals for some of the imaging experiments, and compares them to the frequency content of the acoustic source and the sensor response. Section 3.4.6 explores the effect of slice thickness on the optical ultrasound images and compares them to the clinical ultrasound images.

The clinical ultrasound images shown in this section are cropped from screenshots of the clinical scanner. The uncropped screenshots from the clinical scanner are included in Appendix D.

Sound speed. For the reconstruction of the optical ultrasound images an approximate sound speed value was chosen based on the composition of the medium and is stated in the figure caption for each imaging object. The sound speed values were not optimised, as was done for the resolution measurement in Section 3.3.4. Thus there remains room for the images to be further improved in image quality by optimising the sound speed value, e.g. by exhaustively testing a range of values and maximising a pre-defined image quality metric. For the clinical ultrasound scanner the sound speed value was not changed for each imaging object, but kept as the

scanner's default value of 1540 m/s. An empirical test (imaging a needle target) showed that a change in the sound speed almost only results in a linear stretching of the image along the depth axis proportional to the sound speed value. However, we recognise that the sharpness of the clinical ultrasound images could potentially be improved by choosing more accurate sound speed values. Therefore, for both the optical and clinical ultrasound images shown in this section there is potential for improvement through sound speed optimisation.

Focusing. Multi-focusing was used for one clinical ultrasound image in this section (Fig. 3.20). However, since only one of the foci was within the cropped image area, the locations of the foci are not shown here, but only in the full screenshot of the clinical image in Fig. D.2. For all other clinical images no information or option to change the focus was provided by the clinical scanner.

Colour bars. The colour bars displayed next to the optical ultrasound images are grey colour bars, where the minimum and maximum pixel values are normalised to 0 and 1. In most cases the colour bar is a standard linear grey scale. In some cases the colour bar has been brightened with the *brighten()* function in MATLAB, which is specified in the appropriate figure captions. The colour bars displayed by the clinical ultrasound scanner were not clearly presented (see Appendix D). These were assumed to be linear grey scale and reproduced in MATLAB.

3.4.1 3D imaging of arbitrarily shaped scatterers

To demonstrate the ability of the system to provide 3D ultrasound images, phantoms with well-defined scattering structures of arbitrary geometry were imaged.

Optical fibre knot. The first phantom was an optical fibre of 200 μm diameter, tied into a knot, positioned approximately 5 mm away from the sensor and immersed in water, see Fig. 3.18a. The 3D image was reconstructed with a sound speed $c = 1484$ m/s and is presented as MaxIPs in the xy , xz and zy planes, see Fig. 3.18b. The z - y MaxIP in Fig. 3.18b demonstrates acoustic shadowing that occurs behind the strongly scattering fibre, where the ultrasound wave was unable to propagate.

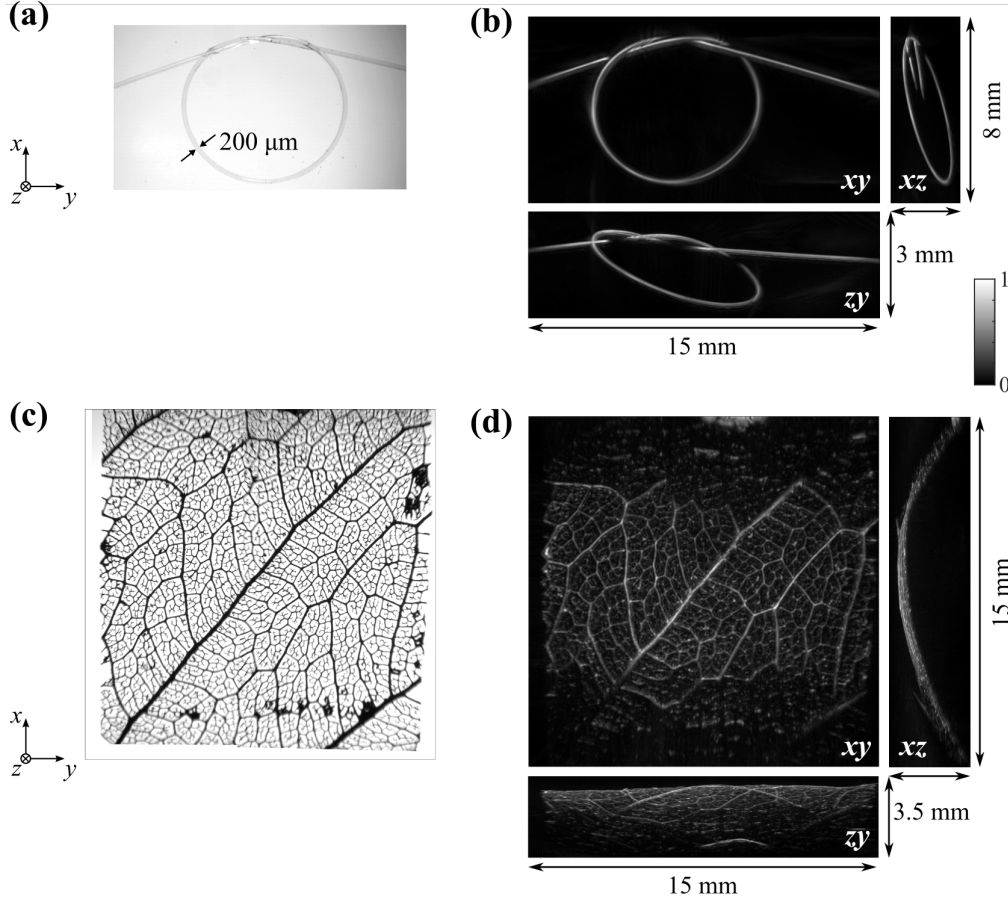


Figure 3.18: Ultrasound imaging of arbitrarily shaped scattering structures: (a) Photograph and (b) maximum intensity projections of 3D ultrasound image of an optical fibre knot (dynamic range 28 dB). (c) Photograph and (d) maximum intensity projections of 3D ultrasound image of a polymer leaf skeleton (dynamic range 21 dB). Figure adapted from [83] © 2021 IEEE.

Polymer leaf skeleton. The second phantom was a polymer skeleton that resembles a leaf with structures of dimensions in the range of tens to hundreds of μm (Fig. 3.18c). The average frequency spectrum of the received pressure time series data acquired when imaging the polymer leaf is discussed in Section 3.4.5. The polymer leaf image was reconstructed with a sound speed $c = 1484 \text{ m/s}$ and presented in the same way as the knot, see Fig. 3.18d.

For both phantoms, comparison with the photographs shows that the reconstructed image provides an accurate representation of the scattering structures. As expected, the system was able to resolve structures down to approximately $50 \mu\text{m}$.

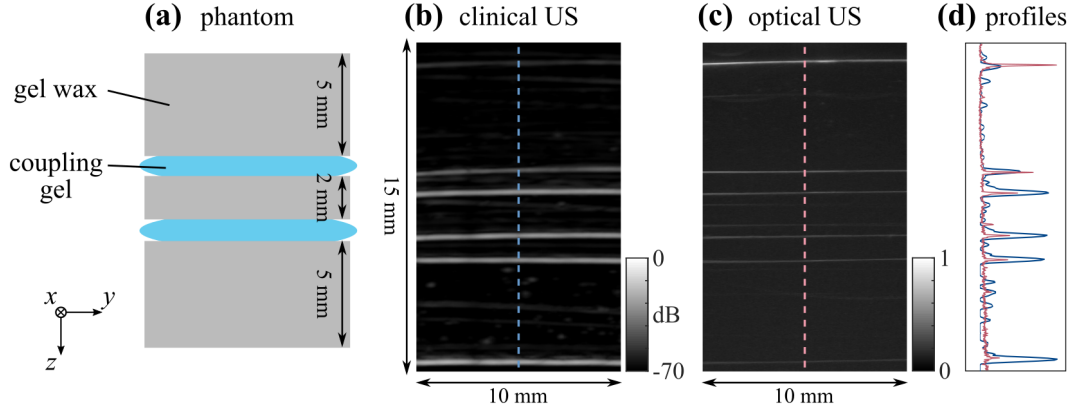


Figure 3.19: Ultrasound imaging of layered gel wax-based tissue-mimicking phantom: **(a)** Schematic of the phantom. **(b)** Clinical ultrasound scanner image at 20 MHz centre frequency (full screenshot in Fig. D.1). **(c)** Mean intensity projection through a 2 mm slice of the 3D all-optical ultrasound image (dynamic range 15 dB). **(d)** Comparison of depth profiles acquired with the clinical scanner (blue) and the FP scanner (red). Figure adapted from [83] © 2021 IEEE.

3.4.2 Imaging of tissue mimicking phantoms

To demonstrate the feasibility of the system for visualising biological tissues, two tissue-mimicking phantoms (TMM) were imaged with the FP scanner, as well as a clinical ultrasound scanner (Ultrasonix, SonixMDP) for comparison.

Layered gel-wax phantom. The first phantom was designed to have interfaces with acoustic impedance mismatches (all values stated in units of $10^6 \text{ kg m}^{-2} \text{ s}^{-1}$) similar to those present in tissue. It comprised three layers of gel wax [88] (impedance 1.22) placed parallel to the sensor surface, see Fig. 3.19a. The layers were acoustically coupled by ultrasound coupling gel (OptiLube Lubricating Jelly, impedance 1.55). This made for an impedance mismatch of 0.33 at all boundaries, equivalent to a blood-fat interface (1.66 – 1.33). The clinical scanner and the FP scanner acquired images from opposite sides of the phantom; the clinical scanner from above and the FP scanner from below. This allowed the phantom to remain stationary and avoid deformation while imaging with both systems. Using the clinical scanner with a high frequency probe (L40-8/12, resolution mode, 20 MHz centre frequency), a B-mode image of a slice through the phantom was obtained, Fig. 3.19b. The optical ultrasound image was reconstructed with a sound speed $c = 1470 \text{ m/s}$ and is presented in Fig. 3.19c as a MeanIP over a slice of thickness 2 mm through the

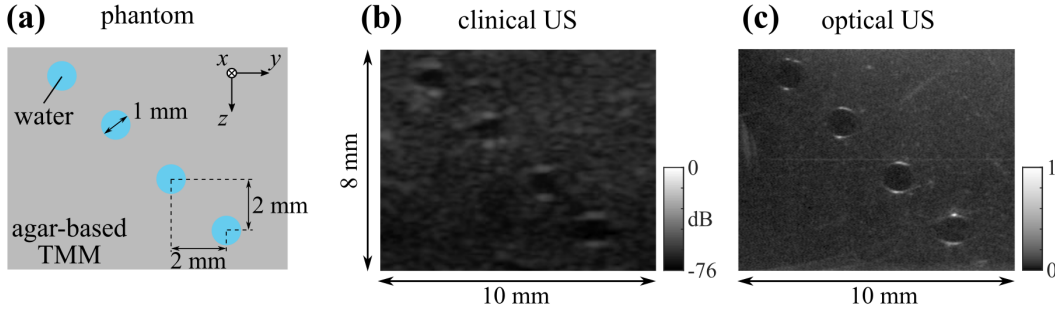


Figure 3.20: Ultrasound imaging of agar-based tissue-mimicking phantom. **(a)** Schematic of the phantom. **(b)** Clinical ultrasound scanner image at 14 MHz centre frequency (full screenshot in Fig. D.2). **(c)** Mean intensity projection through a 2 mm slice of the 3D all-optical ultrasound image (dynamic range 14 dB). Figure adapted from [83] © 2021 IEEE.

3D image volume. The profiles through the centre of both images show that the FP scanner image provides higher axial resolution than the clinical scanner image, see Fig. 3.19d. This is expected due to the broader bandwidth of the FP scanner-based system. Another effect that could contribute to the difference in resolution is the difference in slice thickness, which is explored in Section 3.4.6. The relative magnitudes of the peaks in both depth profiles decay in opposite directions along the z axis, since the phantom was imaged from opposite sides by the two scanners. From the depth profile of the FP scanner image (red) the SNR is measured to be 30 at 1 mm depth, 5 at 10 mm depth, and 3 at 15 mm depth.

Agar-based scattering phantom. The second phantom was designed to have sound speeds and scattering coefficients similar to those present in tissue. An agar-based TMM, utilising glycerol for sound speed modification, and orgasol for scattering was made (0.6 g agar, 2.2 g glycerol, 0.36 g orgasol, 16.84 g water). The mixture was poured into a custom 3D-printed mould to make a block of TMM with cylindrical cavities of approximately 1 mm diameter that were filled with water, see Fig. 3.20a. Using the clinical scanner with the standard probe (L14-5/38, resolution mode, 14 MHz centre frequency) a B-mode image of a slice through the phantom was obtained, see Fig. 3.20b. The optical ultrasound image was obtained by incoherent frequency compounding to improve image contrast [89]. To implement this, the detected pressure time-series data was band-pass filtered with centre frequencies

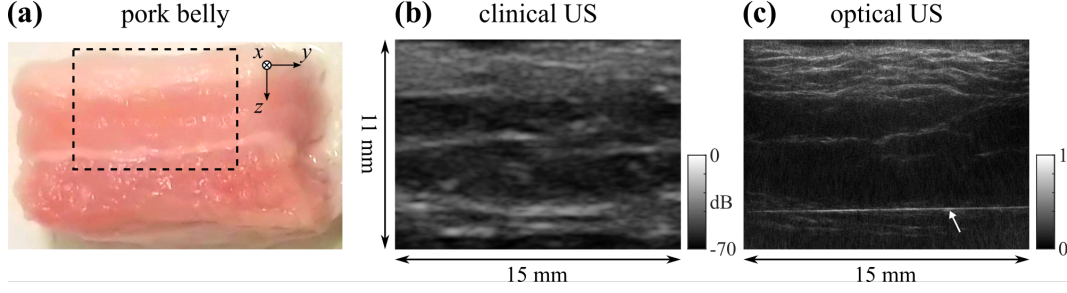


Figure 3.21: Ultrasound imaging of *ex vivo* pork belly. (a) Photograph of pork belly sample showing layers of fat and muscle tissue, and imaging ROI. (b) Clinical ultrasound scanner image at 14 MHz centre frequency (full screenshot in Fig. D.3). (c) Mean intensity projection through a 2 mm slice of the 3D all-optical ultrasound image (dynamic range 8.8 dB). Line feature marked with an arrow is an image artefact corresponding to the reflection of the back-propagating plane-wave from the back of the sensor head. Figure adapted from [83] © 2021 IEEE.

of 2, 3, 4, ..., 15 MHz and a bandwidth of 10 MHz to produce 14 filtered versions of the pressure time-series data. These were then used to reconstruct 14 images, which were envelope detected before they were summed to obtain the compound image. The sound speed used for reconstruction was $c = 1544$ m/s. The compounded optical ultrasound image is presented in Fig. 3.20c as a MeanIP over a slice of thickness 2 mm through the 3D image volume. Comparing the two images in Fig. 3.20b and Fig. 3.20c, the FP scanner image is observed to show the boundaries of the holes with higher resolution and exhibit a finer grain of speckle, both due to the broader generation and detection bandwidth of the FP scanner system.

3.4.3 *Ex vivo* tissue imaging

The suitability of the system for imaging soft tissues was evaluated by imaging several tissue samples.

Pork belly. The first tissue sample was a piece of pork belly immersed in water, see Fig. 3.21a. Using the clinical scanner with the standard probe (L14-5/38, resolution mode, 14 MHz centre frequency) a B-mode image of a slice through the tissue was obtained, Fig. 3.21b. The optical ultrasound image of approximately the same tissue region was reconstructed with a sound speed $c = 1460$ m/s and is presented in Fig. 3.21c as a MeanIP over a slice of thickness 2 mm through the 3D image volume.

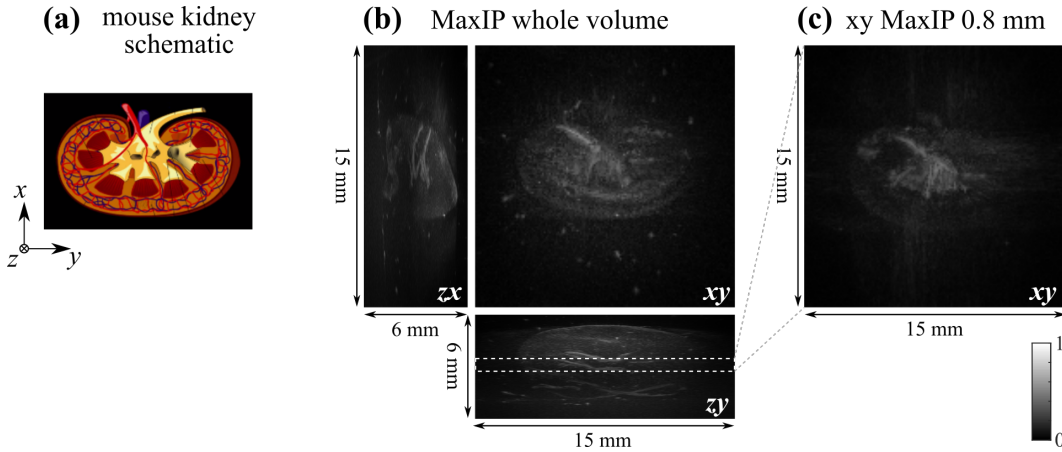


Figure 3.22: Ultrasound imaging of an *ex vivo* mouse kidney. (a) Schematic of a mouse kidney, showing the fat-based calyces (yellow), renal artery (red) and vein (blue) and remaining kidney tissue (purple). (b) Maximum intensity projections through the whole volume of the 3D all-optical ultrasound image. (c) Maximum intensity projection through 0.8 mm slice of the all-optical ultrasound image in *xy*-plane.

The images show some structural resemblance, as both exhibit stronger scattering in the superficial fat layer, and a lateral structure within the muscle tissue below. The high resolution of the FP scanner image is illustrated by the representation of the fat layer, which shows striations that are not clearly resolved in the clinical scanner image. These striations are likely to represent the morphology of the fat layer, e.g. the extracellular matrix. The line feature marked with an arrow in the optical ultrasound image is an image artefact corresponding to the reflection of the plane-wave from the back face of the sensor head and could be avoided by increasing the thickness of the sensor backing. The average frequency spectrum of the received pressure time series data is discussed in Section 3.4.5. The effect of the difference in slice thickness is discussed in Section 3.4.6.

Mouse kidney. An *ex vivo* mouse kidney was embedded in a block of agar gel (2% agar) to fix it in place and immersed in water for acoustic coupling for US imaging. The optical US image was reconstructed with a sound speed $c = 1520$ m/s and is presented as MaxIPs through the whole 3D image volume, and a *xy* MaxIP through a 0.8 mm slice of the volume, see Fig. 3.22. In all of the projections one can clearly see the boundary between the fat-based calyces and the remaining kidney tissue,

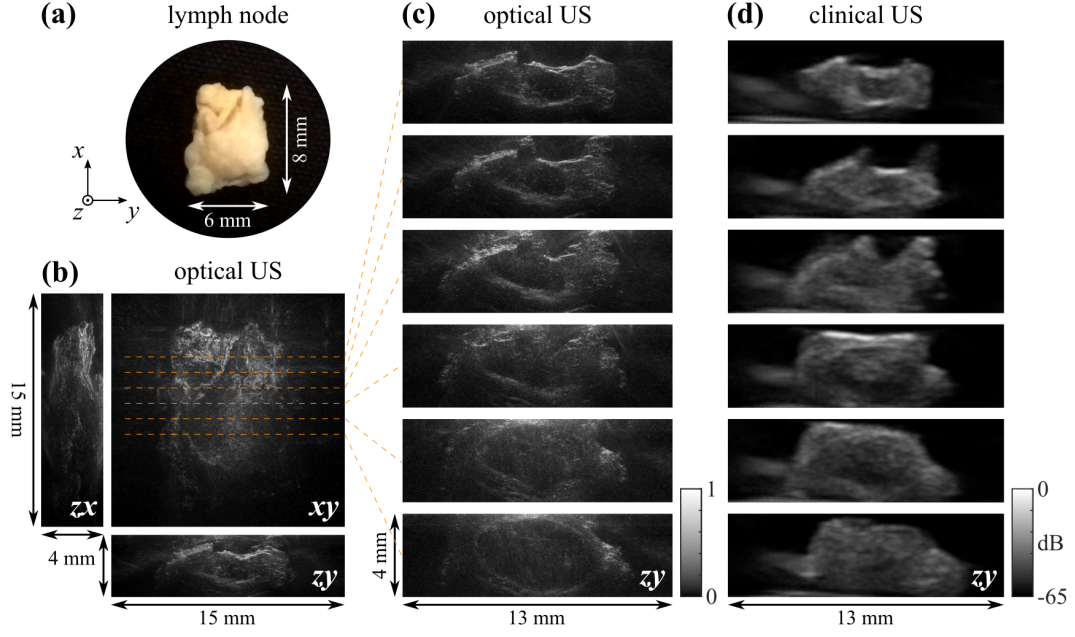


Figure 3.23: Ultrasound imaging of *ex vivo* human lymph node. (a) Photograph of the lymph node. (b) Maximum intensity projections through the whole volume of the 3D all-optical ultrasound image (dynamic range 22 dB). (c) Maximum intensity projections through 2 mm slices of the all-optical ultrasound image in zy -plane, and (d) corresponding clinical ultrasound images at 14 MHz centre frequency (full screenshots in Fig. D.4). The colour bar for the optical ultrasound images in (b) and (c) was brightened with *brighten(0.3)* in MATLAB. Figure adapted from [83] © 2021 IEEE.

together with the strong reflections from the renal artery and vein. In the slice MaxIP in Fig. 3.22c, the cortex of the kidney which contains numerous small vessel structures becomes apparent.

Human lymph node. An *ex vivo* human lymph node (Fig. 3.23a) immersed in water was also imaged with the FP scanner and the clinical scanner. The optical ultrasound image was reconstructed with a sound speed $c = 1520$ m/s and is presented in Fig. 3.23b as MaxIPs through the entire 3D image volume. Figure 3.23c represents a series of MaxIPs through different z - y slices of 2 mm thickness. The clinical scanner images of the equivalent z - y slices obtained with the standard probe (L14-5/38, resolution mode, 14 MHz centre frequency) are shown in Fig. 3.23d. In the x - y MaxIP of the whole 3D image volume (Fig. 3.23b), the sharp fold in the top surface of the lymph node is clearly visible. In the z - y slice MaxIPs (Fig. 3.23c) the boundary between the fat surrounding the lymph node and the water can be seen.

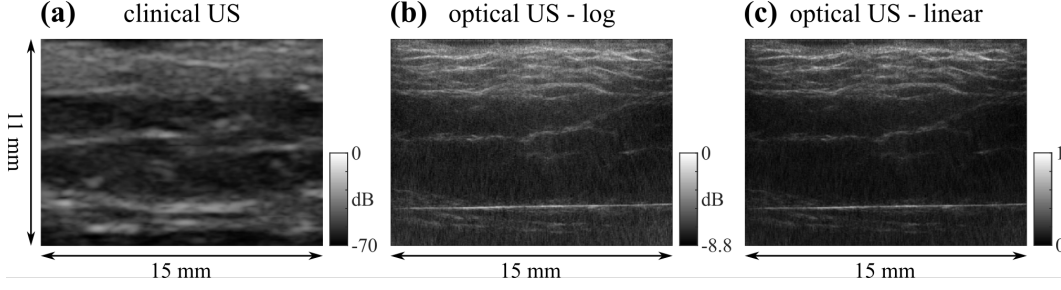


Figure 3.24: Comparison of *ex vivo* pork belly image on log and linear scales (same data as Fig. 3.21). (a) Clinical ultrasound scanner image at 14 MHz centre frequency (full screenshot in Fig. D.3). Mean intensity projection through a 2 mm slice of the 3D all-optical ultrasound image displayed on (b) a logarithmic scale and (c) a linear scale.

Typical for ultrasound images of lymph nodes, a weakly echogenic ‘dark void’ in the centre of the node is observed in the slice images in Fig. 3.23c and Fig. 3.23d.

Fly-through videos of the 3D image volumes from the pork belly (Fig. 3.21) and the human lymph node (Fig. 3.23) were published and can be viewed online [83].

3.4.4 Dynamic range and logarithmic compression

Conventional ultrasound images are typically displayed on a logarithmic scale since their dynamic range is large. In this section, we demonstrate why it was not optimal to display the optical ultrasound images on a logarithmic scale. This will be demonstrated on the reconstructed image data from imaging the *ex vivo* pork belly (Fig. 3.21). A logarithmic compression was performed by first normalising the image data to values between 0 and 1:

$$\text{normalised image} = \frac{\text{image} - \min(\text{image})}{\max(\text{image}) - \min(\text{image})} \quad (3.1)$$

before computing a log compression with a factor of 20:

$$\text{log compressed image} = 20 \cdot \log_{10}(\text{normalised image}). \quad (3.2)$$

The log compressed image was then displayed on a standard grey scale, see Fig. 3.24b, to compare to the linearly displayed image in Fig. 3.24c.

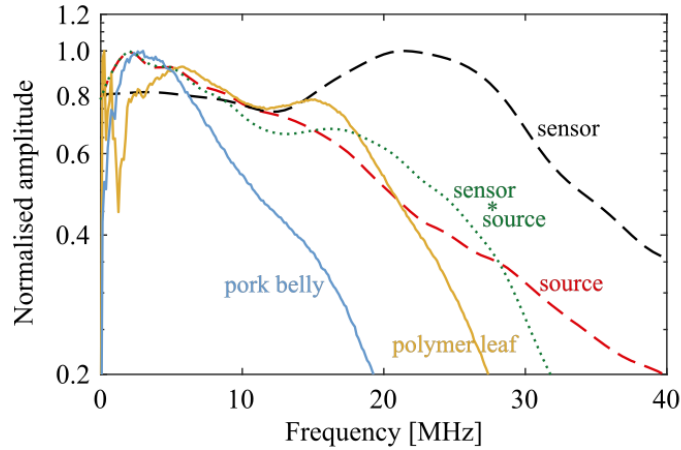


Figure 3.25: Average frequency spectra of received data from imaging the polymer leaf skeleton phantom (yellow) and the pork belly tissue sample (blue); also shown are frequency spectra of the FP sensor (dashed black), the optical ultrasound source (dashed red), and the product of sensor and source (dotted green). Figure adapted from [83] © 2021 IEEE.

The comparison reveals that the majority of the features that can be highlighted in the ultrasound image are visible on both logarithmic and linear scale. The log compression did not improve the visibility of the features, nor did it reveal any additional features. The reason for this is the relatively low dynamic range of 8.8 dB contained in the optical ultrasound image, which is not as large as for the clinical ultrasound image (Fig. 3.24a) with a dynamic range of approximately 40 dB. Note, that the dynamic range of the clinical ultrasound image displayed in Fig. 3.24a is not equal to the whole dynamic range (70 dB) displayed in the colour bar next to it, as this is a cropped version of the complete clinical ultrasound image which had a larger dynamic range (see Fig. D.3).

3.4.5 Frequency content of detected signal

The average frequency spectra of the received pressure time series data acquired when imaging the polymer leaf skeleton phantom and the pork belly tissue sample with the FP scanner are shown in Fig. 3.25. At frequencies from 5 to 20 MHz, the polymer leaf skeleton spectrum approximately resembles the product of the sensor and source spectra, since the leaf was immersed in water which exhibits low acoustic attenuation. The pork belly spectrum appears to be less broadband due to the frequency dependent attenuation from propagation through the tissue. This

begs the question, as to whether the optical ultrasound scanner's improved spatial resolution compared to the clinical ultrasound scanner is solely due to its broader bandwidth, or whether other factors contribute to this. The slice thickness of the images could account for some of the difference in resolution and will be explored in the next section.

3.4.6 Slice thickness

In this section, we explore the effect of slice thickness on the optical ultrasound images. This is done for two reasons: Firstly, we justify why many images in this chapter were displayed as mean or maximum intensity projections through 2 mm slices of the 3D image volume, rather than displaying a single non-averaged slice or a slice with a different thickness. Secondly, we compare optical ultrasound images of different slice thicknesses to the clinical ultrasound image to evaluate how much the improved resolution of the optical ultrasound images is due to reduced slice thickness or increased bandwidth. This will be demonstrated on the reconstructed image data from imaging the *ex vivo* pork belly (Fig. 3.21).

A single slice of the optical ultrasound image of the pork belly of thickness 50 μm , see Fig. 3.26a, shows the striations in the fat layer at the top of the pork belly with high resolution. However, due to the small slice thickness the striation features are not connected, but appear broken up. This is because the anatomy behind the striations has some out-of-plane dimension to it, and cannot be displayed fully in one single slice. Note, that the 50 μm slice used here corresponds to the slice thickness after reconstruction and before interpolation.

Averaging over a small slice thickness, e.g. from 1-4 mm, see Fig. 3.26b-d, improves the visibility of the striation features compared to the single slice image (Fig. 3.26a) as they now appear connected throughout the slice. Averaging over an increasingly larger slice thickness, e.g. from 6-10 mm, see Fig. 3.26e-g, results in more features of the tissue from previously out-of-plane depths being displayed in the image, and also increases the blurriness of all the features since they are being averaged with more slices from other out-of-plane depths. A slice thickness of

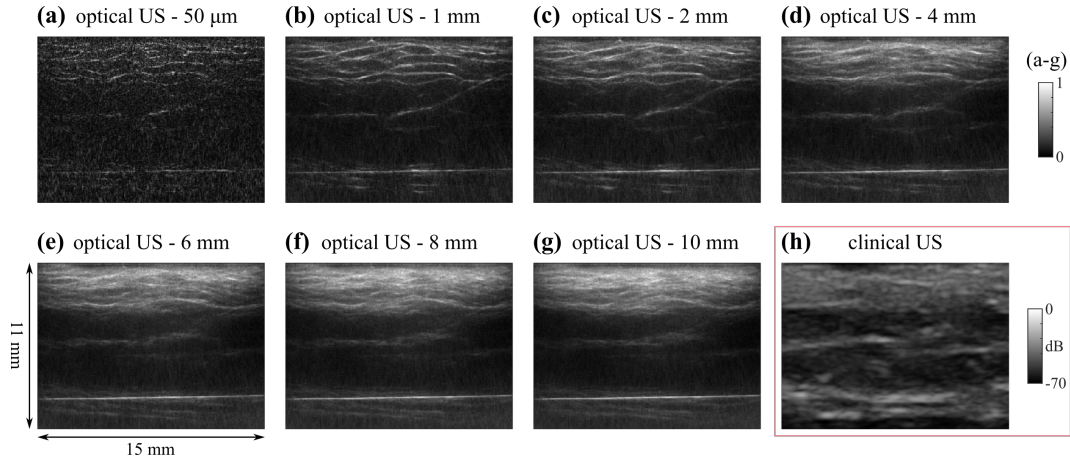


Figure 3.26: Effect of slice thickness on *ex vivo* pork belly image. Mean intensity projection through a slice of the 3D all-optical ultrasound image with slice thickness (a) 50 μm , (b) 1 mm, (c) 2 mm, (d) 4 mm, (e) 6 mm, (f) 8 mm, (g) 10 mm (all images were individually normalised). (h) Clinical ultrasound scanner image at 14 MHz centre frequency (full screenshot in Fig. D.3).

2 mm proved to be a reasonable thickness to compromise between increasing the visibility of the features, while still displaying them with high resolution and not including too many features to clutter the image.

The slice thickness of the clinical scanner image varies along the depth axis due to the length of the piezoelectric elements which result in elevational (out-of-plane) focusing. The piezoelectric elements of the clinical scanner had a length of approximately 10 mm. The depth-dependent slice thickness of the clinical scanner image, Fig. 3.26h, should therefore be comparable to a range of slice thicknesses between 1 and 10 mm, i.e. those shown for the optical ultrasound image in Fig. 3.26a-g. Since the clinical ultrasound image (Fig. 3.26h) shows the striation features more blurry than the thickest 10 mm slice through the optical ultrasound image (Fig. 3.26g), not all of the blurring in the clinical image is due to the increased slice thickness of the clinical scanner. Part of the blurring must therefore be due to the lower bandwidth of the clinical scanner resulting in higher frequencies not being detected. The optical ultrasound scanner must therefore have detected higher frequencies, despite the attenuation that those higher frequencies experience during propagation through tissue as observed in Fig. 3.25. We can thus conclude that the improved resolution of the optical ultrasound scanner, is due to a combination of the broader bandwidth

and the smaller slice thickness compared to the clinical ultrasound scanner.

3.5 Conclusion

3.5.1 Summary

A broadband all-optical plane-wave ultrasound imaging system for high-resolution 3D imaging of biological tissues was developed. The system is based on the planar FP scanner for ultrasound detection and the optical generation of ultrasound in absorbing films. The FP sensor head was coated with an absorbing film which acts as an US transmitting layer. The US transmitter film was excited with nanosecond laser pulses to generate plane-wave ultrasound pulses, which were transmitted into the target for pulse-echo imaging. US transmitter films made from a SP coating and a CNT-PDMS composite were characterised and their performance compared. The generation efficiency of the CNT-PDMS composite was found to be $2.5\times$ higher than that of the SP coating. The CNT-PDMS transmitter film generated monopolar ultrasound pulses with MPa-range peak pressures, a -6dB bandwidth of 22 MHz and were planar to within $\lambda/10$ at 10 MHz. The heat generated during optical US generation was shown to not negatively impact the acoustic sensitivity of the FP sensor. The scattered acoustic field was detected across a $15\text{ mm} \times 15\text{ mm}$ scan area with a step size of $100\text{ }\mu\text{m}$ and an optically defined element size of $64\text{ }\mu\text{m}$. The -3 dB bandwidth of the sensor was 30 MHz. A 3D image of the scatterer distribution was recovered using a k -space reconstruction algorithm. To obtain a measure of spatial resolution, the instrument line-spread function (LSF) was measured as a function of position. At the centre of the scan area, the depth-dependent lateral LSF ranged from 46 to $65\text{ }\mu\text{m}$ for depths between 1 and 12 mm. The axial LSF was independent of position and measured to be $44\text{ }\mu\text{m}$ over the entire field of view. To demonstrate the ability of the system to provide high-resolution 3D images, phantoms with well-defined scattering structures of arbitrary geometry were imaged. To demonstrate its suitability for imaging biological tissues, phantoms with similar impedance mismatches, sound speed and scattering properties to those present in the tissue, and *ex vivo* tissue samples were imaged. Compared to conventional

ultrasound scanners, the system offers the prospect of improved image quality for superficial tissue imaging. High-resolution imaging is enabled due to the high frequencies the system operates at and the fine spatial sampling of the sensor, while the broadband generation and detection provide spatial fidelity. Another advantage is the 3D imaging capability of the system, as most conventional high-frequency ultrasound scanners can only form 2D images. In its current state the system is able to provide a penetration depth of up to 10 mm for *in vivo* tissue imaging.

3.5.2 Outlook

The main limitation of the system is the poor SNR and contrast at depths beyond 5-7 mm, as is evident in the images of the pork belly and the agar-based tissue mimicking phantom. To better understand the underlying cause of this limitation and identify ways to overcome it, broadband plane-wave pulse-echo US imaging simulations are studied and presented in Chapter 4.

There remains scope to improve the system's performance with respect to SNR, contrast and penetration depth. By modifying the temporal characteristics of the excitation laser (e.g. the pulse width), for example by using a fibre laser [90], the frequency content of the generated ultrasound can be tuned to increase the energy at lower frequencies which are attenuated less and thus penetrate more deeply in tissue. The concept of temporal modulation of the excitation light and the resulting trade-off between resolution and penetration depth was demonstrated for a single-element all-optical ultrasound probe [91].

Spatial or angle compounding also has the potential to improve SNR and thus penetration depth and image contrast [63, 73]. Photoacoustic generation of angled plane waves can be achieved by scanning a focused excitation beam across the transmitter coating [92]. A study into the effect of angle compounding on broadband plane-wave pulse-echo US imaging, and a demonstration of how angle compounding could be realised in practice with the planar FP scanner are presented in Chapter 5.

Another limitation of the system is the long acquisition time due to the low pulse repetition frequency of the excitation laser used, the large number of detection points required for each scan and the sequential nature of the sensor read-out. This can be addressed by using a higher pulse repetition frequency laser and parallelising the sensor read-out by the use of multiple interrogation beams [93] or wide-field illumination and a camera-based sensor array [94], with the potential to achieve sub-second acquisition times.

The bandwidth of the system is currently limited by the laser pulse duration and thicknesses of the FP sensor spacer and the CNT-PDMS film. By reducing all three, there is the potential to increase the bandwidth to 100 MHz or higher, albeit at the cost of sensitivity and thus image SNR.

In this chapter, the planar FP scanner, originally developed for photoacoustic imaging, was modified into an optical ultrasound imaging system by including a transmitter coating for optical ultrasound generation. Ultimately, the goal is to develop a dual-mode system that can obtain co-registered photoacoustic and ultrasound images. One way to realise such a dual-mode system would be to incorporate a dichroic transmitter coating that is transparent to wavelengths used for photoacoustic imaging but provides strong absorption at a wavelength used for generating ultrasound [17]. A dual-mode imaging system based on the FP scanner is presented in Chapter 6.

Chapter 4

Simulation of plane-wave ultrasound imaging

4.1 Introduction

In Chapter 3, an all-optical plane-wave ultrasound imaging system based on the FP scanner was presented. Compared to previous ultrasound imaging systems, the main novelty of this system is the broad bandwidth of the ultrasound generation and detection. In this chapter, we examine the impact of a broadband system on the ultrasound image quality.

In photoacoustic imaging contrast is created by optical absorption. Biological tissues contain volume absorbers, e.g. blood vessels, typically with dimensions from tens of μm to 1 mm. To accurately depict these absorbers, the detection system needs to be responsive to frequencies in the single to tens of MHz range. This is why the FP scanner (with a bandwidth of 30 MHz) coupled with optically generated ultrasound (with a broad bandwidth in the tens of MHz range) are well suited for photoacoustic imaging of blood vessels. It is important to note that low frequencies in the single MHz range are necessary to display larger, mm-scale objects as “filled-in” volumes rather than just boundaries. An ultrasound image is created by the scattering of acoustic waves at interfaces arising from acoustic impedance

changes within a medium. One source of contrast in ultrasound images are boundaries and small scatterers. This begs the question, if low frequencies are necessary to image boundaries and small scatterers with high resolution. What do the low frequencies of a broadband signal contribute in terms of image quality? Is it enough, or why is it not enough, to only use high frequencies to obtain a high-resolution ultrasound image? This research question will be referred to as **Question 1** in this chapter.

Another source of contrast in ultrasound images is speckle, which arises from a high density of diffusive scatterers, i.e. objects that are much smaller than the acoustic wavelength, with sizes in the tens of μm . Tissue regions with different scatterer densities will have a different speckle pattern in the image, which can be used to distinguish the regions. The images obtained by the broadband optical ultrasound system developed in Chapter 3 contain speckle with a very fine grain size at a spatial scale comparable to its resolution and pixel size. A scattering contrast can still be defined for regions with different scatterer densities, as the difference in the intensity distributions of the pixels in different regions of the image. Scattering contrast was of relevance when imaging the agar-based tissue mimicking phantom in Section 3.4.2, which contained a scattering medium with non-scattering cylindrical inclusions filled with water. In the broadband image of this phantom, the contrast between the scattering and non-scattering region was low. To improve the scattering contrast frequency compounding was applied. This involved frequency filtering the sensor data with a series of frequency filters before reconstructing to obtain band-pass filtered images. Images filtered with a higher frequency band-pass filter exhibited lower contrast, see Fig. 4.1. Therefore, band-pass filters with centre frequencies from 2 to 15 MHz were selected for frequency compounding in Section 3.4.2. A question, however, remains: Why does filtering the data to higher frequencies result in lower contrast images? This research question will be referred to as **Question 2** in this chapter.

To answer these questions a simulation platform that models broadband plane-wave

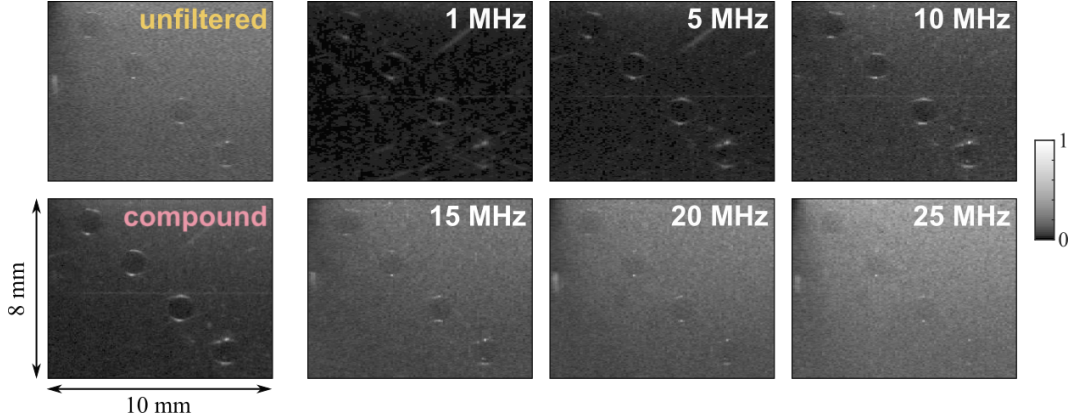


Figure 4.1: Unfiltered broadband image, frequency compounded image, and band-pass frequency filtered images of agar-based tissue-mimicking phantom from data acquired in Section 3.4.2. The frequency filters used were Gaussian filters with centre frequencies ranging from 1 to 25 MHz and a bandwidth of 10 MHz. Images were individually normalised and displayed with the same colour bar (grey scale brightened with *brighten(0.5)* in MATLAB).

ultrasound imaging was created. Using the simulation platform the impact of frequency on image quality was studied.

Outline. In Section 4.2 the literature on simulating ultrasound imaging is reviewed. Section 4.3 gives details about the simulation platform used, and compares the simulated images to experimental images. The dependence of the image quality, specifically contrast, on frequency is studied in Section 4.4. In Section 4.5, the effect of spatial aliasing on frequency and image quality is explored. The spatial dependence of image quality is simulated in Section 4.6. An outlook of what can be done to further this work is provided in Section 4.8, before the findings of the chapter are summarised in Section 4.9.

4.2 Literature review

Previous simulations of ultrasound imaging were not designed for systems that are as broadband as the optical ultrasound system based on the FP scanner. The acoustic pulses have been modelled as either single frequency pulses [95] or narrowband low frequency pulses [96–99]. This is because conventional ultrasound systems are much more narrowband with bandwidths in the single MHz-range due to the limitation of piezoelectric transducers. There has, therefore, been no need to simulate

broadband ultrasound imaging previously.

The aim of this section is to inform the design of the simulation platform for broadband plane-wave ultrasound imaging. It includes considerations on how to represent an acoustically scattering medium, and how to generate sensor data by running a forward model. To reconstruct an image of the scattering distribution from the detected pressure-time series data, the algorithm described in Section 3.2.3 was used.

4.2.1 Representation of acoustically scattering medium

Particle/discrete model. In this approach, particles that act as point scatterers are placed into otherwise non-scattering, “empty” space [95, 96]. Assuming weak scattering, multiple scattering can be ignored and each particle can be treated individually. The detected pressure wave can be obtained by adding up the scattered waves from all the particles and with appropriate phase delays. This approach is suitable if the medium is modelled using few particles as then the computational effort is low.

Continuum model. In this approach, the medium is continuous with local fluctuations in acoustic properties that represent statistical variations in the scatterer density [97]. This approach is suitable for modelling tissues with a high scatterer density. The medium needs to be split into a grid of voxels, and each voxel assigned individual acoustic properties. The simulation grid size needs to be chosen much smaller than the wavelength of the ultrasound source, e.g. $< \lambda/10$, so that the whole volume of any given voxel interacts with approximately the same phase of the incident wave. In the case of a broadband ultrasound source, a cut-off frequency such as the -3dB bandwidth can be used to calculate an equivalent wavelength. For a broadband source with -3dB bandwidth of 22 MHz, as measured in Section 3.3.1.4, the equivalent wavelength would be 68 μm .

Hybrid model. This is a hybrid of the two models described above [98, 99]. At the start particles are placed in space, similar to the particle model. Then, the medium is dissected into a grid of voxels. Similar to the continuum model, the size of the voxels is chosen to be much smaller than the acoustic wavelength, e.g. $< \lambda/10$.

Since the voxels are small, all particles within any given voxel can be assumed to interact with the same part of the incident wave. Each voxel can thus be accurately represented as a single equivalent scatterer at the centre of the voxel with a volume equal to the sum of the individual scatterer volumes. An even more accurate representation places the equivalent scatterer at the centre of mass of the group of individual particles [99, 100]. This model combines the strengths of both the particle and continuum methods, as a large number of point scatterer particles can be modelled efficiently by grouping them into voxels.

4.2.2 Forward model

In a simulation the forward model describes how sensor data is generated from a given source, medium and detector. As described in the previous section there are a number of different forward models that are suitable for different kinds of simulated media.

Spatial impulse response. If the medium is represented as a collection of discrete scatterers the detected signal can be obtained by adding the contributions from each scatterer. Weak scattering is assumed in this case so that multiple scattering can be ignored and the scatterers can be treated independently. The individual contributions from each scatterer can be derived from the so-called spatial impulse response, which is the ultrasound field scattered from the scatterer and measured at a specific point in space as a function of time when the source is considered a Dirac delta function [101]. For a general source the response can be found by convolving the source function with the spatial impulse response. The responses for each of the scatterers can then be summed with the appropriate phase delays to generate the field at specified sensor positions. This method has the advantage of being computationally efficient if the number of scatterers is low. It is, however, not suitable for a medium composed of a large number of scatterers such as a highly scattering soft tissue. Another disadvantage is that the pressure field cannot be observed over the whole space, but only at the defined sensor points. Simulation platforms based on spatial impulse responses include Field II [102] and FOCUS [103].

Full-wave model. In a full-wave forward model, no assumptions of independent weak scatterers are made when modelling the ultrasound wave propagation. Instead, the ultrasound wave is transmitted through the whole medium and the pressure field is calculated at all times and in all of space, rather than only at specified sensor locations. This is typically more computationally intensive than the spatial impulse response method, unless there is a high number of scatterers or the medium cannot be described as a collection of discrete scatterers, in which case the spatial impulse response method cannot be applied. The most commonly used numerical methods for solving partial differential equations in acoustics are the finite-difference, finite-element, and boundary-element methods. To study broadband, rather than single-frequency, ultrasound imaging a time-domain forward model is required. The drawback with classical finite-difference and finite-element approaches is that, for time domain modelling of broadband or high-frequency waves, they can become cumbersome and slow [104]. This is due to the requirements for many grid points per wavelength and small time-steps to minimise unwanted numerical dispersion. These problems can be reduced with a pseudospectral method combined with a k -space approach. An example of a time-domain full-wave model based on k -space pseudospectral methods is the forward model provided by the ultrasound simulation tool *k-wave* [104]. *k-wave* has been shown to be more accurate than finite-difference forward simulation methods for the same size of spatial and temporal steps.

4.3 Simulation platform

In this chapter, we wish to model scattering tissue with a range of scattering strengths to study scattering contrast. In order to model highly scattering media, if using the particle model, these would likely have a high density of point scatterers. The continuum model is better suited than the particle model at modelling high scatterer density. Our first simulations using both models showed that the continuum model provides images that are visually more similar to experimental images of scattering tissues or tissue-mimicking phantoms. *k-wave* was therefore the full-wave forward model of choice for our simulations. *k-wave* also has the advantage

of having been developed by members of the research group. The reconstruction described in Section 3.2.3 is already based on k -wave. Since we are using a full-wave model there would be no computational benefit in using the hybrid model to represent the scattering medium. We thus decided to use a continuum approach to model the medium and a full-wave approach as the forward model. The simulation platform is based on the k -wave package in MATLAB [104]. The code can be found on GitHub [105] under the file name `simul_scatt.m`.

Assumptions. We assume the media are static throughout the duration of the simulation. We do not assume that scattering is weak (Born approximation), or that scattering is frequency independent, nor that we are operating in the far-field, as is commonly done. These assumptions were not necessary since we opted for a full-wave forward model. We are therefore allowing multiple scattering to occur when running the forward model. Note, that the reconstruction algorithm described in Section 3.2.3 ignores multiple scattering and hence assumes weak scattering. Our simulation approach will thus also test the accuracy of the Born assumption made by the reconstruction algorithm.

Simulation grid. The simulations were run on a 2D grid with 1536×1024 grid points of $10 \times 10 \mu\text{m}$ size. The grid size was chosen as $10 \mu\text{m}$ to ensure that it is much smaller than the wavelengths associated with the frequencies contained in the acoustic field (-3dB bandwidth of 22 MHz). The whole grid represents an approximately $15 \times 10 \text{ mm}$ area in the xy plane, where the x axis is parallel to the sensor and the y axis represents depth. This simulation grid thus gave a similar field of view as provided by the planar FP scanner in practice.

Medium. The acoustic properties of the medium were first assigned to resemble those of water, i.e. a sound speed of $c_0 = 1500 \text{ m/s}$, and a density of $\rho_0 = 1000 \text{ kg/m}^3$. Two types of phantoms were used in simulations: a point scatterer in an otherwise non-scattering medium, and a random scattering medium with a circular non-scattering inclusion. The phantoms are described in greater detail in Section 4.3.1. A perfectly matched layer (PML) with a thickness of 20 grid points (0.2

mm) was chosen to absorb the acoustic field at the boundary of the simulation grid.

Source & sensor. A time varying pressure source with a monopolar pulse shape and a FWHM pulse width of 16 ns was chosen to approximately model the optical ultrasound source generated in the experiments, and characterised in Section 3.3.1. The source was spatially apodised along the x axis with a Gaussian intensity profile, modelling the Gaussian excitation beam used during optical ultrasound generation and as described in Section 3.2.1. The sensor was made up of individual sensor points placed to form an array along the x axis and spaced by 10-200 μm . The source and the sensor were placed at the same depth of 0.21 mm, i.e. one grid point adjacent to the PML.

Sensor directivity. Apart from preliminary simulations in Section 4.7, the directivity of the sensor was not modelled. This was a deliberate choice since the FP sensor has a complicated directional response that varies depending on its composition and for which there is no analytical model [106]. We therefore studied the effects that limit the image quality separately from the directivity, i.e. for a general omnidirectional sensor. For all simulations, apart from those in Section 4.7, the sensor was modelled as an array of point-like detectors with an omnidirectional response. In Section 4.7, preliminary simulations on the effect of the sensor directivity on the formation of artefacts and the image quality are presented. The directional response was modelled by averaging the signal from a number of adjacent detection points.

Forward simulation & image reconstruction. The forward simulation was run in C++ using a first-order k -space model [104]. The time for a single forward simulation of a 1536×1024 grid using an Intel Core i7-7700K CPU @ 4.20 GHz and 32 GB RAM was approximately 20 minutes. There is the option to band-limit the sensor data either with the same frequency spectrum as the FP sensor used for imaging or a custom frequency filter. Gaussian noise can be added to the sensor data. Since the source and the sensor overlap spatially, the source pressure is detected in the sensor data. This source contribution is large in amplitude compared to the scattered signals, and therefore needs to be removed from the signal before

reconstruction so that it does not dominate the actual features in the reconstructed image. In some cases, the source contribution was removed from the sensor data by subtracting a set of sensor data obtained by transmitting the source through an entirely non-scattering medium, i.e. sensor data that only contains the source contribution. In some of the earlier simulations in this chapter, the source contribution was instead removed by applying a Tukey window on the time series to suppress the first 1 μs of detected signals which included the source contribution. This approach caused the image region near the sensor plane to fade, but this did not affect the analyses carried out thereafter. For the image reconstruction, there are the options to spatially upsample the sensor data by a factor of 2 along the x axis, to frequency filter the sensor data additionally, and to apply an envelope detection to the image.

4.3.1 Simulated phantoms

Point scatterer. The first simulated phantom was a single point scatterer made to resemble the situation of a wire in a water bath. The point scatterer was modelled by either a single pixel representing a point scatterer of 10 μm diameter or a 5-pixel cross representing a point scatterer of approximately 30 μm diameter. The point scatterer had a sound speed of $c_p = 1500$ m/s and density of either $\rho_p = 1200$ or 5000 kg/m^3 , and was placed in an otherwise non-scattering medium with acoustic properties of $c_0 = 1500$ m/s and $\rho_0 = 1000$ kg/m^3 , see Fig. 4.2a. Note, that this means the acoustic impedance between the point scatterer and the medium comes purely from a density change, rather than a sound speed change or a mixture of both. This phantom will be used to explore the frequency content of the scattered wave and the shape of artefacts surrounding the main reconstructed feature of a single point scatterer.

Random scattering medium. The second simulated phantom was a scattering medium with a non-scattering inclusion. This phantom was meant to be a representation of the agar-based tissue mimicking phantom with cylindrical water-filled inclusions imaged in Fig. 3.20 in Section 3.4.2. The scattering medium was achieved by assigning random variations of sound speed and density at each grid point, with

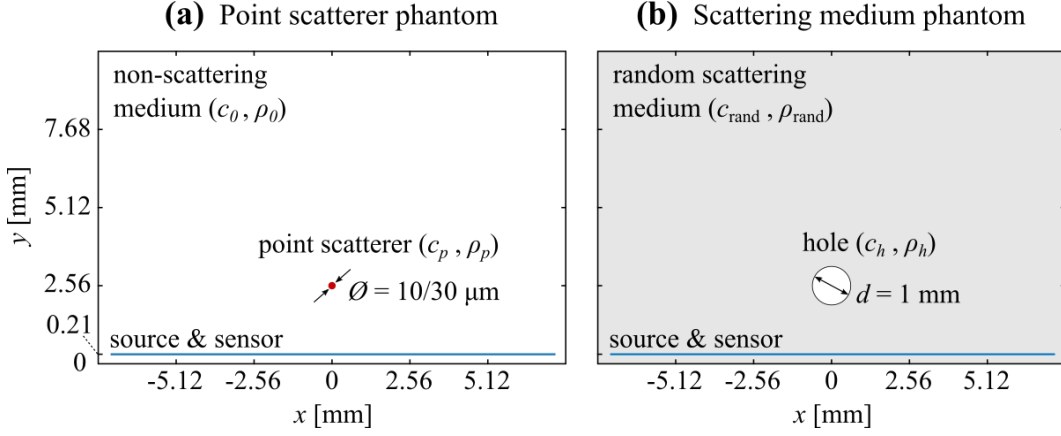


Figure 4.2: Phantoms used in simulations: (a) Point scatterer in non-scattering medium, and (b) random scattering medium with circular non-scattering inclusion, here referred to as ‘hole’.

the mean values of $c_0 = 1500$ m/s and $\rho_0 = 1000$ kg/m³. Since the grid size of $10\text{ }\mu\text{m}$ was chosen to be much smaller than the wavelengths associated with the frequencies contained in the acoustic field, the random medium will act as a continuum rather than individual point scatterers. Within the scattering medium of this phantom a circular non-scattering inclusion, also referred to as ‘hole’, was placed and given uniform acoustic properties (c_0, ρ_0) equivalent to the average properties of the surrounding scattering medium, see Fig. 4.2b. The hole phantom was used to study the effect of frequency and spatial aliasing on the scattering signal-to-noise ratio (SNR) and the scattering contrast-to-noise ratio (CNR) between the hole and the surrounding scattering medium.

Image quality definition. To determine scattering SNR and CNR in the reconstructed image, regions of interest (ROI) were defined for the hole and the scattering medium, see Fig. 4.3a. In each ROI the image pixel intensities form a distribution, see Fig. 4.3b, from which mean and standard deviation were calculated. The scattering SNR and CNR were then defined as follows:

$$\begin{aligned} \text{Scattering SNR} &= \frac{\mu_{\text{medium}}}{\mu_{\text{hole}}} \\ \text{Scattering CNR} &= \frac{\mu_{\text{medium}} - \mu_{\text{hole}}}{\sigma_{\text{medium}} + \sigma_{\text{hole}}} \end{aligned} \quad (4.1)$$

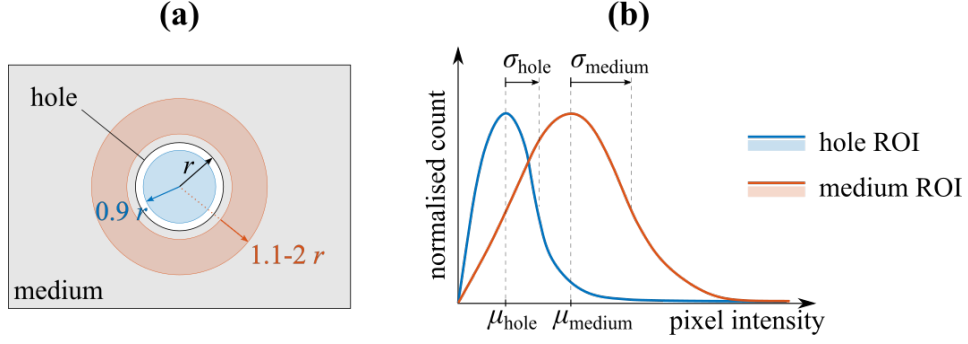


Figure 4.3: Definition of scattering SNR and CNR for a hole in a random scattering medium. **(a)** Schematic of the image of a random scattering medium phantom with ROIs defined for the hole and the surrounding scattering medium. **(b)** Intensity distributions for each ROI, used to calculate means and standard deviations. Scattering SNR and CNR are defined in Eq. (4.1).

where μ_{hole} , σ_{hole} , μ_{medium} and σ_{medium} are the mean and standard deviation of the intensity distributions in the hole and scattering medium ROIs, respectively. The scattering SNR thus indicates how different the hole and scattering medium ROIs are in their mean intensity. A high scattering SNR, however, does not necessarily indicate good image quality as the intensity distributions could be very wide and overlap, making the hole stand out less from the scattering medium. The scattering CNR was thus defined to take into account the width of the intensity distributions and is therefore a better measure for how distinguishable the hole and scattering medium are.

Fluctuation parameters. The grid point fluctuations of sound speed and density were achieved by defining a range for the sound speed variation Δc and the density variation $\Delta \rho$. For each grid point, or voxel, random values from the ranges

$$\begin{aligned} c_{\text{voxel}} &\in \left[c_0 - \frac{\Delta c}{2}, c_0 + \frac{\Delta c}{2} \right] \\ \rho_{\text{voxel}} &\in \left[\rho_0 - \frac{\Delta \rho}{2}, \rho_0 + \frac{\Delta \rho}{2} \right] \end{aligned} \quad (4.2)$$

were picked for the sound speed and the density. Appropriate values for the maximum sound speed and density fluctuations $(\Delta c, \Delta \rho)$ were selected using an exhaustive search and comparing the image quality to the experimental data from the

agar-based tissue mimicking phantom (Section 4.3.2).

Repeatability. The repeatability of the scattering medium simulations was tested by running the same simulation setup with a number of different instances of randomly generated scattering media with the same maximum sound speed and density fluctuations $(\Delta c, \Delta \rho)$. For this test, a maximum sound speed fluctuation of $\Delta c = 40$ m/s and a maximum density fluctuation of $\Delta \rho = 80$ kg/m³ were selected, as those were the values used in most simulations in this chapter. Using these values, 11 medium instances were generated. The scattering SNR of the resulting 11 images was within the range 1.88 ± 0.18 (2σ), and the scattering CNR was within 0.57 ± 0.08 (2σ). For random scattering media with maximum sound speed and density fluctuations of $\Delta c = 40$ m/s and $\Delta \rho = 80$ kg/m³, the SNR and CNR values stated in this Chapter thus have to be treated to have an uncertainty of 0.18 and 0.08, respectively.

4.3.2 Comparison of scattering media

In this section, the simulated random scattering medium phantom is compared to the image of the agar-based tissue mimicking phantom obtained in the experiment (Fig. 3.20 in Section 3.4.2). First, values for the maximum sound speed and density fluctuations $(\Delta c, \Delta \rho)$ needed to be selected for the random scattering medium. This was done to ensure the scattering SNR and CNR in the simulated images were of the same order of magnitude as those in the experimental images of the agar-based tissue mimicking phantom. The selection of the fluctuation parameters was done by undertaking an exhaustive search of both parameters and then comparing the scattering SNR and CNR to the agar phantom image. Note, that this is not a full validation of the scattering medium model, nor are we trying to get the SNR and CNR values to be identical to the experimental image. This section merely presents a comparison to show the model is a reasonable representation of the experiment.

Choice of fluctuation parameters. The maximum sound speed fluctuation Δc was varied from 0 to 150 m/s in steps of 10 m/s and the maximum density fluctuation $\Delta \rho$ from 0 to 100 kg/m³ in steps of 10 kg/m³, and for each pair of values a simulation was run. The scattering SNR and CNR were determined from the reconstructed

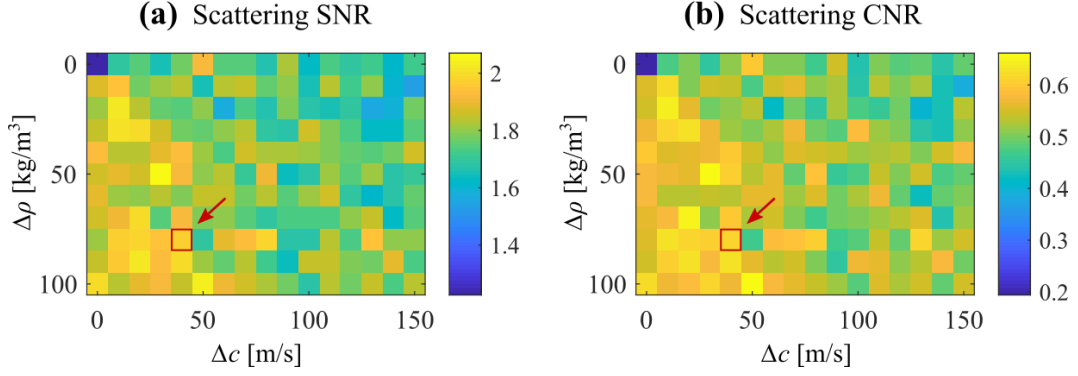


Figure 4.4: Scattering SNR and CNR for hole phantom with different values of sound speed fluctuation Δc and density fluctuation $\Delta \rho$.

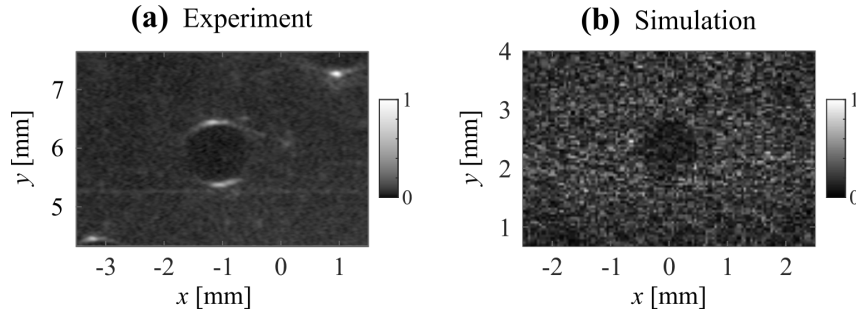


Figure 4.5: Comparison of images of scattering media obtained from experiments and simulations. **(a)** Experimentally obtained image of agar-based tissue mimicking phantom (Section 3.4.2). **(b)** Simulated image of random scattering medium.

images for each $(\Delta c, \Delta \rho)$ value pair, see Fig. 4.4, and compared with experimental values obtained from imaging the agar phantom. The simulated data was frequency filtered with a Gaussian filter of 1 MHz centre frequency and 20 MHz bandwidth to approximately limit the frequency content in the simulated data to the one detected in the experimental data. For the agar phantom the scattering SNR was 1.14, while the scattering CNR was 0.50. Figure 4.4 shows that for all $(\Delta c, \Delta \rho)$ value pairs the scattering SNR ranged from 1.5 to 2.1, while the CNR ranged from 0.38 to 0.66. For the simulations of the random scattering medium in this Chapter, maximum sound speed and density fluctuations of $\Delta c = 40$ m/s and $\Delta \rho = 80$ kg/m³ were chosen, resulting in a scattering SNR of 1.97 and CNR of 0.62.

Comparison of images. The CNR is comparable to that of the agar phantom image, while the SNR is significantly higher since the simulation was noiseless, see Fig. 4.5. The SNR in the simulated image can be lowered by introducing noise to

the sensor data, which would increase the mean intensity of the intensity distribution in both hole and medium ROIs. Another difference between the experimental and simulated image in Fig. 4.5 are the strongly scattering features at the top and bottom of each inclusion that are visible in the agar phantom image but not in the simulated image. This is due to a difference in the average acoustic properties of the agar medium and the water-filled inclusion which leads to a strong specular reflection at the agar-water boundary. Due to the limited view problem (the sensor, due to its finite size, only being able to detect a fraction of the acoustic wave) only the top and bottom edges of the inclusion boundary appear in the image. These features do not appear in the simulated image since there is no difference in the average acoustic properties of the medium and the hole inclusion in the random scattering medium. This choice was made intentionally to make sure that the visibility of the hole is judged purely on the basis of the scattering contrast rather than specular features at the boundary.

4.4 Frequency dependence of image quality

In this section, we aim to determine the frequencies in the sensor data which contribute to improved SNR and CNR, and work out which imaging parameters (namely the spatial sampling interval and the image voxel size) have an impact on the frequency dependence of the image quality.

The method to study the frequency dependence of the image quality is described in Section 4.4.1. The effect of simulation and imaging parameters on the frequency dependence of the image quality is studied in Section 4.4.2. Finally, the frequency dependence of the image quality of simulated images and experimental images is compared in Section 4.4.3.

4.4.1 Method and interpretation

Method. Sensor data from experimentally acquired images of the agar-based TMM (Section 3.4.2) and from the simulated images of the random scattering medium (Section 4.3) were used in this section. First, the sensor data was filtered with a

range of Gaussian frequency filters. The frequency filters had centre frequencies varying from 1 to 35 MHz and FWHM bandwidths ranging from 1 to 40 MHz. For each filter, the scattering SNR and CNR of the reconstructed image were determined and displayed on a 2D plot as a function of the centre frequency and the bandwidth.

Interpretation. For very narrowband filters with bandwidths from 1-2 MHz the images are very low in resolution, presenting a large grainy speckle pattern which results in noisy image quality data. For the purpose of interpreting the plots, this noise at the very low bandwidths shall be ignored. For slightly more broadband filters with bandwidths between 3-7 MHz, the speckle pattern has a smaller grain and the bandwidth is sufficiently broad to obtain a reasonable image of the hole in the random scattering medium. At the same time, these bandwidths are narrow enough, that each image is reconstructed from only a relatively small range of frequencies around a given centre frequency, allowing for conclusions to be made for that centre frequency in relation to the image quality it provides. Frequency filters with bandwidths from 3-7 MHz thus provide a good measure for which frequencies contribute to image quality. For filters that are more broadband, with bandwidths exceeding 10 MHz, a large range of frequencies around a given centre frequency is used to reconstruct the image. Since the image quality contribution for each frequency varies, using a large range of frequencies to reconstruct an image does not allow for conclusions to be drawn for specific frequencies within the range.

4.4.2 Effect of simulation and imaging parameters

In this section, we study the effect of imaging parameters, namely the spatial sampling interval and the image voxel size, on the frequency dependence of the image quality of simulated images. However, before doing so, we need to ensure that simulation parameters, namely the simulation grid size and the medium granularity, do not impact the simulated image quality. These parameters arise for simulated data, but not for experimental data. Thus, for the simulations to be representative of the experiment, the image quality should be independent of these simulation parameters. For this purpose, simulations were designed to vary either the simulation grid

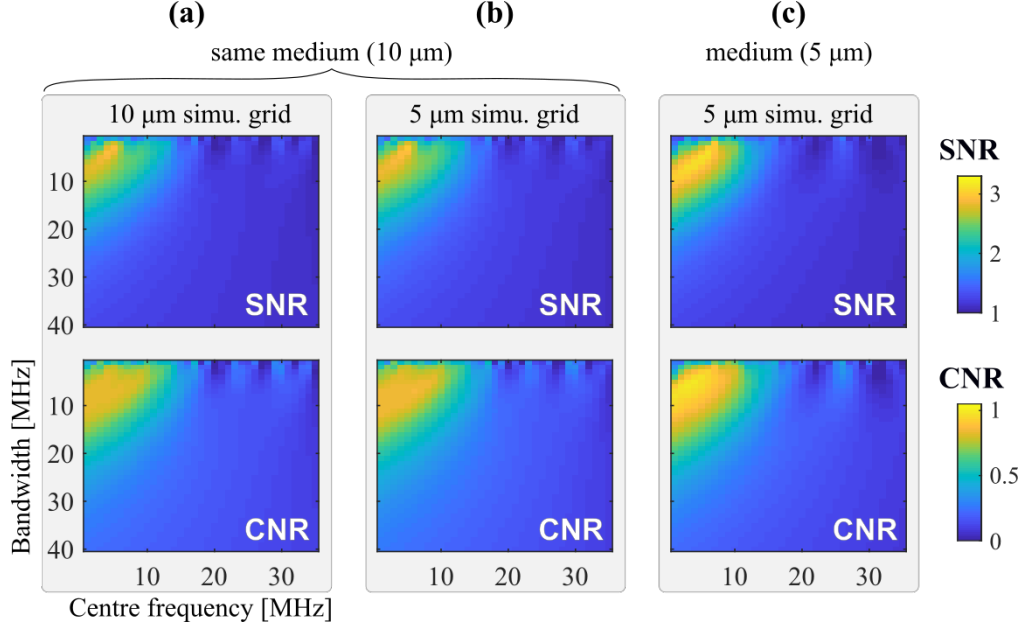


Figure 4.6: Effect of simulation grid size and medium granularity on frequency dependence of the image quality. Simulation of random scattering medium with a granularity of 10 μm run on simulation grid size of (a) 10 μm and (b) 5 μm . (c) Simulation of random scattering medium with a granularity of 5 μm run on simulation grid size of 5 μm . For all simulations the sensor step size was 100 μm and the image voxel size was 50 μm .

size, the medium granularity, the spatial sampling interval (also referred to as the sensor sampling step size), or the image voxel size.

Simulation grid size. For the first simulation, a random scattering medium with a granularity of 10 μm was generated. The simulation was then run with a 10 μm and a 5 μm grid size. In both cases, the sensor sampling step size was 100 μm , and the received data was upsampled along the sensor array by a factor of 2 before image reconstruction to yield a 50 μm image voxel size. The frequency dependence of the image quality for the 10 μm and the 5 μm simulation grid sizes, see Fig. 4.6a and b, shows almost no difference. This was expected since the simulation grid size determines the maximum frequency supported by the simulated grid, which was 75 MHz in the 10 μm case and 150 MHz in the 5 μm case. Since 75 MHz is much higher than the 22 MHz bandwidth of the source, the 10 μm grid was able to support all the frequencies contained within the simulated acoustic field. We thus conclude that a 10 μm simulation grid size is sufficiently small to accurately represent the

random scattering medium, but has no effect on the image quality or its frequency dependence.

Medium granularity. For the second simulation a random scattering medium with a granularity of 5 μm was generated on a 5 μm simulation grid size, Fig. 4.6c, and compared to the 10 μm granular medium simulated on the same simulation grid size, Fig. 4.6b. A different random scattering medium was generated to account for the medium granularity change. The two scattering media compared here are therefore not identical. Nonetheless their frequency-dependent image quality plots are quite similar, see Fig. 4.6b and c. This was expected since 10 μm is much smaller than the smallest wavelengths in the acoustic field (the -3dB bandwidth frequency of 22 MHz is equivalent to a wavelength of 68 μm). The medium granularity of 10 μm is thus sufficiently small for the medium to be perceived as an averaged random medium rather than a collection of point scatterers, and has no significant effect on the image quality and its frequency dependence.

Sensor sampling step size. The next set of simulations was run with the same instance of a random scattering medium with granularity 10 μm on a simulation grid of size 10 μm . The sensor was sampled with a step size of 100 μm or 50 μm . The 100 μm sampled data was upsampled by a factor of 2 along the sensor axis before image reconstruction, while the 50 μm sampled data was reconstructed without up-sampling. This ensured that both images had a voxel size of 50 μm . The frequency dependent image quality of the upsampled 100 μm data is shown in Fig. 4.7b, and that of the 50 μm data in Fig. 4.7c. In comparing these two plots, a distinct difference in the frequency dependence of the image quality as a result of increased spatial sampling can be observed. The upper cut-off frequency is increased from approximately 10 MHz to 20 MHz. This doubling in the cut-off frequency is to be expected, since the acoustic field is spatially sampled twice as finely.

Image voxel size. From the same set of simulations as in the previous paragraph, another comparison can be drawn between the images reconstructed from sensor data with and without upsampling. For the 100 μm sampled data, in comparing

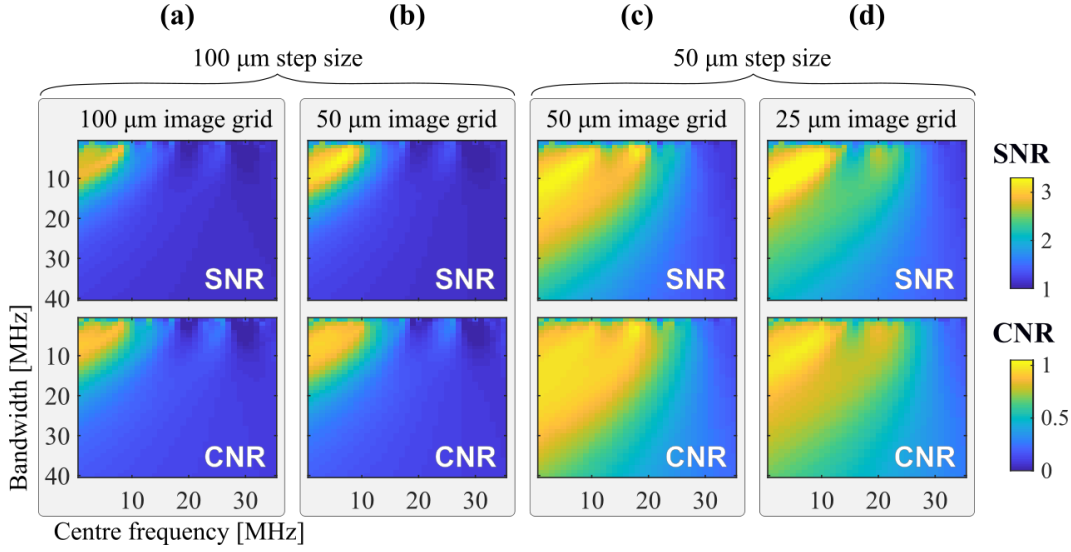


Figure 4.7: Effect of sensor sampling step size and image voxel size on frequency dependence of the image quality. All simulations are of the same random scattering medium with granularity $10\ \mu\text{m}$ and run on a simulation grid size of $10\ \mu\text{m}$. Sensor sampled at $100\ \mu\text{m}$ and image reconstructed onto grid sizes of (a) $100\ \mu\text{m}$, and (b) $50\ \mu\text{m}$. Sensor sampled at $50\ \mu\text{m}$ and image reconstructed onto grid sizes of (c) $50\ \mu\text{m}$, and (d) $25\ \mu\text{m}$.

Fig. 4.7a and b, we observe an improvement in the absolute values of the SNR and the CNR when upsampling. This is an expected outcome, since upsampling of the sensor data exploits the oversampling of the acoustic field in time to improve the undersampling in space. The upper cut-off frequency however remains unchanged. A similar effect can be observed in the comparison of the $50\ \mu\text{m}$ sampled data in Fig. 4.7c and d. The upper cut-off frequency in the upsampled $50\ \mu\text{m}$ data is less visible since the amplitude of the SNR and the CNR values is significantly improved for frequencies lower than that.

Upper cut-off frequency. The comparisons made so far indicate that only the spatial sampling step size affects the upper cut-off frequency. To confirm this conclusion, the simulation described in the paragraphs above was repeated with the same random scattering medium with a granularity of $10\ \mu\text{m}$ on a simulation grid size of $10\ \mu\text{m}$. The sensor was sampled with step sizes of 200, 100, 50 or $20\ \mu\text{m}$, and images were reconstructed without upsampling. The frequency dependence of the image quality shows an increase in the scattering SNR and CNR with increased

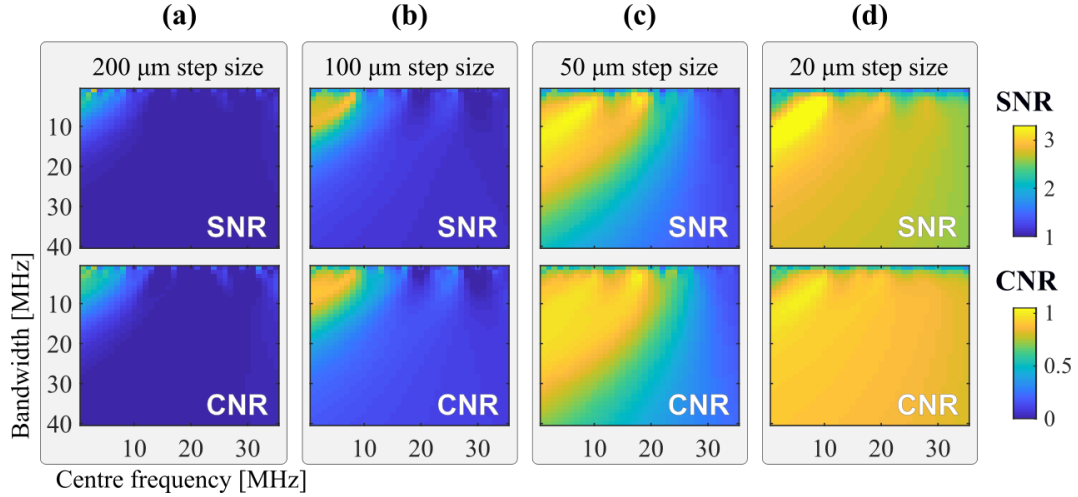


Figure 4.8: Effect of spatial aliasing on frequency dependence of the image quality. All simulations are of the same random scattering medium with granularity $10\ \mu\text{m}$ and run on a simulation grid size of $10\ \mu\text{m}$. The sensor was sampled at (a) $200\ \mu\text{m}$, (b) $100\ \mu\text{m}$, (c) $50\ \mu\text{m}$, (d) $25\ \mu\text{m}$. Images were reconstructed without upsampling the sensor data so the sensor sampling step size is equivalent to the image voxel size.

spatial sampling, see Fig. 4.8. The upper cut-off frequency increases with higher spatial sampling, i.e. higher temporal frequencies contribute to better image quality when the sensor is spatially sampled more finely. If frequencies above the upper cut-off frequency are included in the reconstruction there is a decline in the SNR and the CNR.

Summary. Out of the simulation and imaging parameters tested, only a change in the sensor sampling step size had a significant impact on the upper cut-off frequency in the frequency-dependent image quality plots. Decreasing the simulation grid size or the medium granularity had no effect. Decreasing the image voxel size improved the SNR and the CNR, but did not affect which frequencies contributed to them.

4.4.3 Experiment vs simulation

Parameters. Experimental and simulated data were acquired with the same imaging parameters. For both, the spatial sampling interval was $100\ \mu\text{m}$, and the sensor data was upsampled by a factor of 2 to obtain an image voxel size of $50\ \mu\text{m}$. The simulation was run on a grid size of $10\ \mu\text{m}$ and a random scattering medium with a granularity of $10\ \mu\text{m}$ was used.

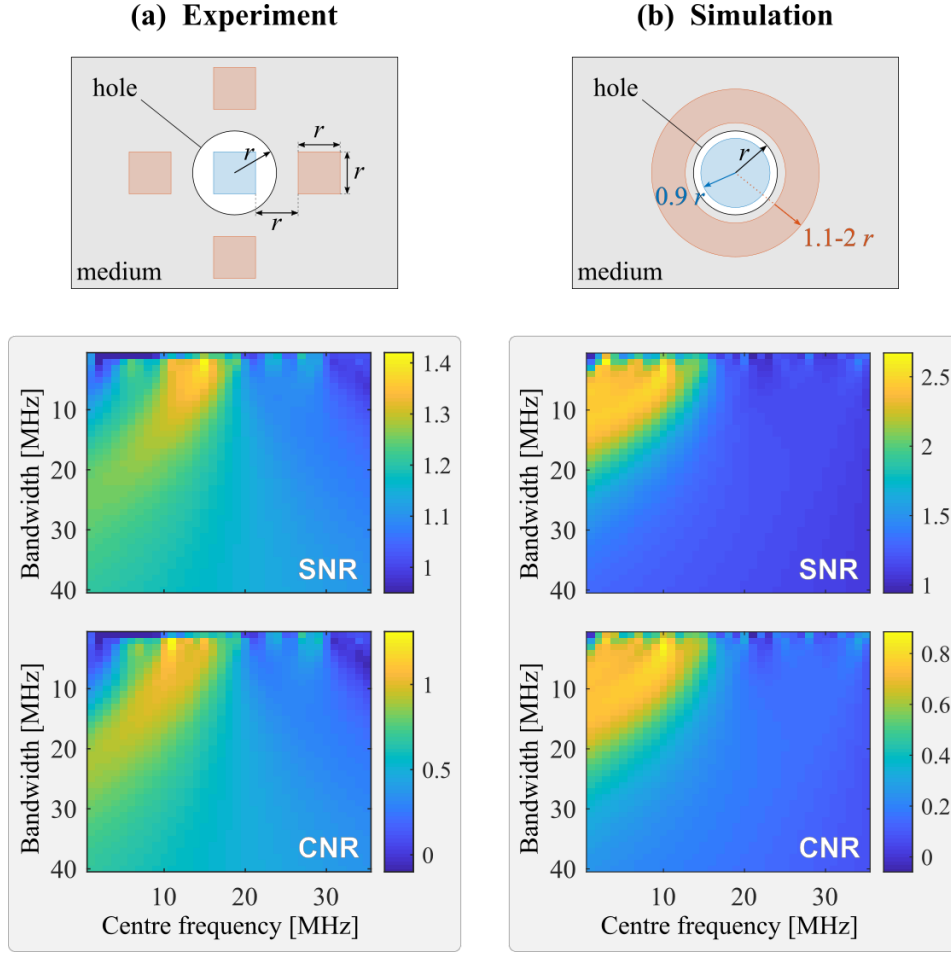


Figure 4.9: Frequency dependence of the image quality of scattering phantoms. SNR and CNR of (a) experimentally acquired images of agar-based tissue mimicking phantom and (b) simulated images of random scattering phantom, where the sensor data has been filtered by Gaussian frequency filters with centre frequencies ranging from 1 to 35 MHz and with bandwidths ranging from 1 to 40 MHz.

Comparison. Plots of the frequency dependence of the image quality for both the experimentally acquired image of the agar phantom and for the simulated image of the random scattering medium are shown in Fig. 4.9. For the agar phantom, frequencies from 10-17 MHz appear to contribute to the scattering SNR and CNR, see Fig. 4.9a. The upper cut-off frequency around 17 MHz is significantly below the -3dB bandwidth of the acoustic generation of 22 MHz, from which it can be concluded that frequencies higher than the upper cut-off frequency provide poor SNR and CNR. The simulated images of the scattering phantom show a similar behaviour with an upper cut-off frequency of approximately 12 MHz, Fig. 4.9b. The

experimental data shows a lower cut-off frequency which is not observed in the simulations. This is likely due to a difference in the size of scatterers. In the agar-based phantom, orgasol particles with a size of 10 μm were included to provide acoustic scattering, similar to the size of scatterers in the simulations. However, since orgasol is a hydrophobic molecule, some molecules may have clumped together into larger particles with sizes from several 10s to 100s μm . This is similar to the wavelength of the frequencies contained in the acoustic field. In this regime of scattering the frequency dependence of scattering is complicated which may explain the difference in the frequency dependence of image quality in the experimental data.

Conclusion. In this section, the trend discussed in Question 2 (‘Why do high frequencies contribute to lowering the image contrast’) was quantified. Experimental and simulated images were shown to have a similar frequency dependent behaviour with an upper cut-off frequency limiting which frequencies contribute to better SNR and CNR. The simulated image quality was also shown to be independent of the simulation parameters, including the grid size and the medium granularity. Going forward, the simulations can thus be treated as a reasonable representation of the experiment. Out of the imaging parameters tested, namely the spatial sampling interval and the image voxel size, only the spatial sampling interval had a significant effect on the frequency dependence of the image quality. Higher frequencies contributed to better SNR and CNR when the sensor was spatially sampled more finely. The effect of spatial aliasing will be further explored in the next section. The work in this section will also be used to inform which frequency filters should be chosen for frequency compounding, which is demonstrated in Section 5.2.

4.5 Spatial aliasing

In the previous section, we established that the spatial sampling of the sensor determines which temporal frequencies contribute to the image quality. In this section, we examine why this is the case and demonstrate the effect of spatial aliasing in frequency space as well as in the reconstructed image. We investigate the role of spatial aliasing in the contrast reduction at higher frequencies (Question 2), and why

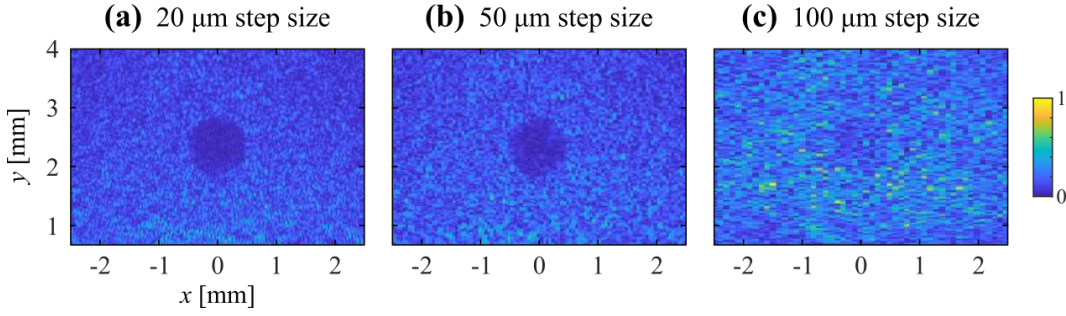


Figure 4.10: Effect of spatial aliasing on images of the random scattering medium, when the acoustic field was sampled with a step size of (a) 20 μm , (b) 50 μm , (c) 100 μm . Images were individually normalised, and cropped to the same field of view around the non-scattering hole.

lower frequencies are valuable for image fidelity and contrast (Question 1).

4.5.1 Aliasing with the random scattering medium

In this section, we study the effect of spatial aliasing on the frequency content of the sensor data and on the reconstructed image of a random scattering medium.

Aliasing in images. To illustrate the effect of spatial aliasing on the image contrast, images of a random scattering medium were reconstructed from sensor data obtained with a spatial sampling step size of 20, 50 and 100 μm , see Fig. 4.10. Each set of sensor data was frequency filtered with a Gaussian filter of 1 MHz centre frequency and 20 MHz bandwidth to approximately model the frequency content in experimental data. The hole in the random scattering medium appears with good contrast in the images sampled with a step size of 20 and 50 μm , and with poor contrast in the 100 μm sampled image. To understand the effect of spatial aliasing on the image contrast the sensor data must be studied in frequency space.

2D-FT plots. The spatial sampling of the sensor determines the highest spatial frequency k_x of the sensor data, where x is along the sensor plane. To fully understand the effect of spatial sampling on the image quality we must therefore look at temporal and spatial frequencies in the sensor data. For this purpose the sensor data $p(x, t)$ was Fourier transformed (FT) along both spatial and temporal axes to obtain the 2D-FT data $P(k_x, \omega)$. A 2D-FT plot displays the amplitude of signals that have a given spatial frequency k_x and temporal frequency ω . To illustrate the effect of spa-

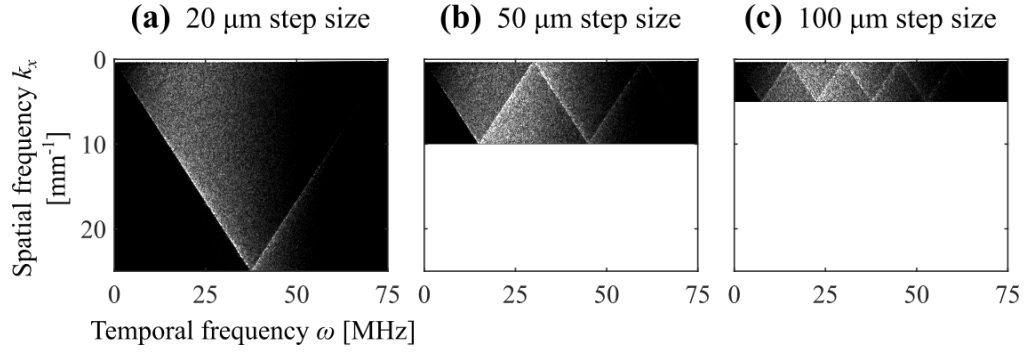


Figure 4.11: Effect of spatial aliasing on sensor data in frequency space. 2D-FT plots of the sensor data when sampled with a step size of (a) 20 μm , (b) 50 μm , (c) 100 μm . Axes in all three plots are the same to illustrate the limitation in spatial frequencies detectable at large sensor sampling step size.

tial aliasing on the spatial and temporal frequency content of the sensor data from a random scattering medium, 2D-FT plots for a sensor sampling step size of 20, 50 and 100 μm were generated, see Fig. 4.11. Note, that all 2D-FT plots in this and the following sections were normalised to their individual minimum and maximum values and plotted on a linear grey scale. The plots were enhanced by brightness and contrast filters in INKSCAPE. This was necessary to improve the visibility to highlight the location of the data within the plots, and acceptable since we are not interested in the absolute or relative intensity of the plots.

2D-FT comparison. By comparing the 2D-FT plots of Fig. 4.11 aliasing of the representation of the sensor data can be observed. Firstly, the highest measured spatial frequency is equal to $1/(2\Delta x)$, where Δx is the spatial sampling step, e.g. 25 mm^{-1} for 20 μm , or 10 mm^{-1} for 50 μm . This is the spatial Nyquist frequency given a sensor sampling step size of Δx . To acquire sensor data that has not been spatially aliased one would need to sample at the same spatial interval as the simulation grid size, in this case 10 μm . When undersampling, i.e. sampling with a step size larger than 10 μm , any signals that have a higher spatial frequency than the Nyquist frequency are aliased to lower spatial frequencies. This appears in the plot as a ‘folding’ of the data at the maximum (Nyquist) and minimum (zero) spatial frequencies, see Fig. 4.11. The higher the spatial frequency, the more severe is the spatial undersampling down to a lower spatial frequency.

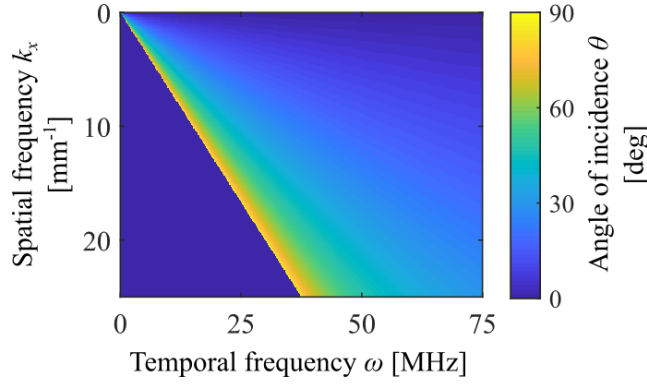


Figure 4.12: Map of angle of incidence associated with each spatial frequency k_x and temporal frequency ω value pair.

Angle of incidence (AOI). A common feature in all 2D-FT plots in Fig. 4.11 is a threshold line starting at the origin of the plot (0 mm^{-1} , 0 MHz) with a slope of $(1500 \text{ m/s})^{-1}$. All of the sensor data lies on one side of this line. To understand this feature we need to consider the AOI of a given acoustic wave. Defining the AOI as the angle θ between the wave vector of the acoustic wave and the normal of the sensor plane, the spatial frequency k_x and temporal frequency ω can be related via the equation

$$k_x = \frac{\omega}{c} \sin \theta. \quad (4.3)$$

Using Eq. (4.3) the AOI θ can be calculated for each point in the 2D-FT plot. The intensity of the plot at that point then signifies the intensity of signals that were detected with that particular spatial frequency k_x , temporal frequency ω and resulting AOI θ . The slope with gradient $(1500 \text{ m/s})^{-1}$, i.e. $1/c$, thus corresponds to signals with an AOI of 90° , i.e. that have travelled parallel along the sensor plane with a sound speed c of 1500 m/s . All of the sensor data lies on one side of the diagonal with slope $1/c$ since $\sin \theta$ is always smaller than 1. As a result of spatial aliasing the position of the sensor data points in the 2D-FT plots changes. This can be interpreted as a change in the apparent AOI of the detected acoustic wave.

AOI transformation. Using Eq. (4.3), a map for the AOI for every point in the 2D-FT plot can be obtained, see Fig. 4.12. This map can be used to transform 2D-FT plots into AOI plots, where the sensor data is displayed as a function of AOI

and temporal frequency. Having a better understanding of the AOI of the detected acoustic field is useful since the sampling of any wave that is not normally incident onto the sensor is partially determined by the spatial sampling. However, since the random scattering medium effectively contains lots of scatterers across the medium, the AOI data cannot be easily interpreted. We will, therefore, study the effect of spatial aliasing on single point scatterers in the following section, and look at how aliasing affects the data in 2D-FT and AOI plots.

4.5.2 Aliasing of a single point scatterer

In this section, we study the 2D-FT and AOI plots generated from imaging a single point scatterer in a non-scattering medium. For a single point scatterer the scattered acoustic signals come from a single location. The AOI plots are thus easier to interpret compared to those from imaging a random scattering medium.

Method. The point scatterer used here was assigned a sound speed of 1500 m/s and a density of 1200 kg/m^3 , had a diameter of $30 \text{ }\mu\text{m}$, was located 2.35 mm away from the sensor, and in a central position. The sensor was sampled with a spatial sampling interval of either 10 or $100 \text{ }\mu\text{m}$. The smaller sampling interval of $10 \text{ }\mu\text{m}$ was chosen so that the sensor data is acquired without any aliasing, since all frequencies that are supported by the simulation grid can also be detected by this sensor sampling. The larger sampling interval of $100 \text{ }\mu\text{m}$ was chosen to acquire sensor data with aliasing, and is also the typical spatial sampling interval used in experiments. For both sampling intervals the sensor data was Fourier transformed to obtain the 2D-FT plots. The 2D-FT plots were then transformed into AOI plots using the method described in Section 4.5.1. Each 2D-FT and AOI plot was normalised to its individual minimum and maximum value. This was done to aid visibility, and is acceptable since we are less interested in the intensity and relative intensity of the plots than we are in the location of the data within the plots. The 2D-FT and AOI plots for both sampling intervals are shown in Fig. 4.13.

Fully sampled data. In the 2D-FT plot of the $10 \text{ }\mu\text{m}$ sampled sensor data, Fig. 4.13a, all of the sensor data lies to one side of the line with a slope of $1/c$ (or-

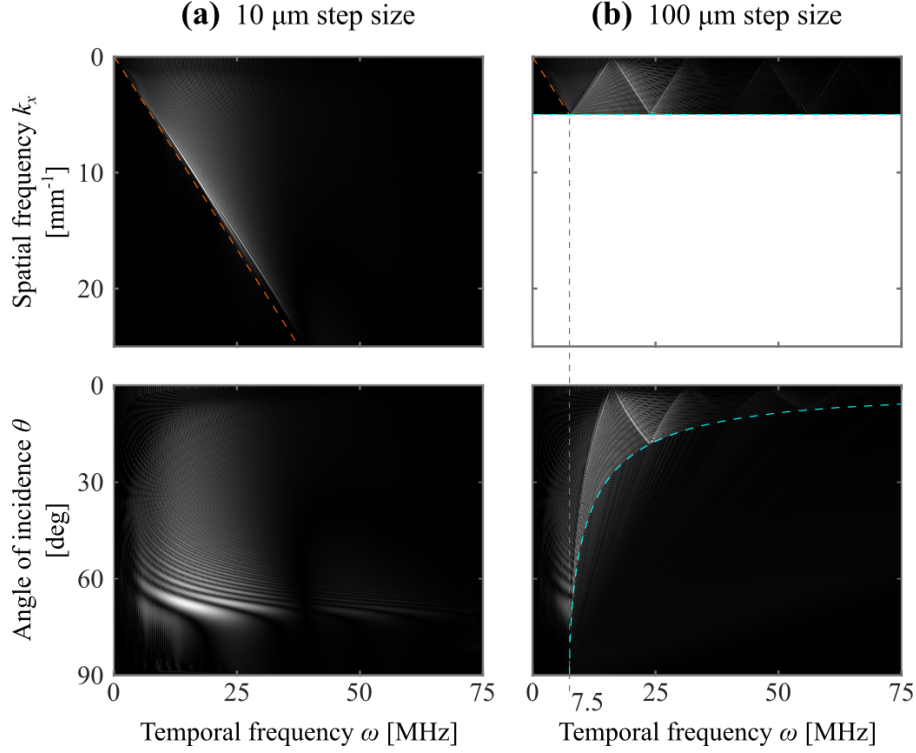


Figure 4.13: Effect of spatial aliasing on sensor data in frequency space (top row) and as a function of AOI and temporal frequency (bottom row) shown for: **(a)** Fully sampled sensor data with a 10 μ m step size, and **(b)** spatially aliased sensor data with a 100 μ m step size. Orange dashed lines indicate the threshold in 2D-FT plots with a slope of $1/c$ equivalent to an AOI of 90° . Blue dashed lines indicate the spatial Nyquist frequency threshold of 5 mm^{-1} associated with a step size of 100 μ m.

ange dashed line), similar to what was observed for the random scattering medium in the previous section. A majority of the sensor data is located near that line, suggesting that a large fraction of the scattered signals were detected at higher AOIs. This is visually confirmed in the AOI plot for the 10 μ m sampled data which shows acoustic waves were received at AOIs up to 75° . Note, that AOI plots are not a representative way to show how much energy was received at a given AOI, since the transformation from 2D-FT to AOI plots is non-linear.

Spatially aliased data. For the aliased data sampled at 100 μ m a “folding” of the sensor data in the 2D-FT plot from spatial frequencies above the spatial Nyquist frequency of 5 mm^{-1} to spatial frequencies below 5 mm^{-1} was observed, see Fig. 4.13b, as was observed for the random scattering medium in the previous sec-

tion. In the AOI plot this is manifested as a hyperbola-shaped threshold (blue dashed line). For temporal frequencies below 7.5 MHz, which is the temporal equivalent of the spatial Nyquist frequency, all signals regardless of the AOI can be measured without aliasing. The temporal equivalent of the spatial Nyquist frequency for a given spatial sampling interval of Δx will be referred to as the *temporospatial Nyquist frequency* and is given by $c/(2\Delta x)$. The temporospatial Nyquist frequency is not to be confused with the temporal Nyquist frequency which depends on the temporal sampling interval and is not relevant in this discussion due to sufficiently high temporal sampling. Temporal frequencies above the temporospatial Nyquist frequency will be referred to as *super-Nyquist frequencies*, while those below the temporospatial Nyquist frequency will be referred to as *sub-Nyquist frequencies*. For super-Nyquist frequencies, i.e. frequencies above 7.5 MHz, the signal may or may not be aliased depending on the AOI. Waves with an AOI lower than the threshold angle for a given temporal frequency (blue dashed line in Fig. 4.13b) are detected without aliasing. Waves with an AOI higher than the threshold angle for a given temporal frequency are aliased to lower AOIs, demonstrated in the comparison of AOI plots of Fig. 4.13a and b. However, the new aliased AOI is different for each temporal frequency. A broadband signal will, therefore, get aliased to a range of new AOIs depending on the frequency content of the signal. We will study how this manifests in the reconstructed images in the next section.

4.5.3 Grating lobe artefacts

In this section, we show how spatial aliasing affects images of point scatterers at different frequency ranges. For this purpose, we use a single point scatterer and look at the artefacts generated due to spatial aliasing, or grating lobe artefacts as they are typically referred to in conventional ultrasound literature. First, images were generated from narrowband frequency filtered data. Second, the effect of making the signal more broadband is explored. Finally, we discuss the effect of grating lobe artefacts on different types of images and how it can be reduced.

Method. A single point scatterer of diameter 10 μm located 2.35 mm away from

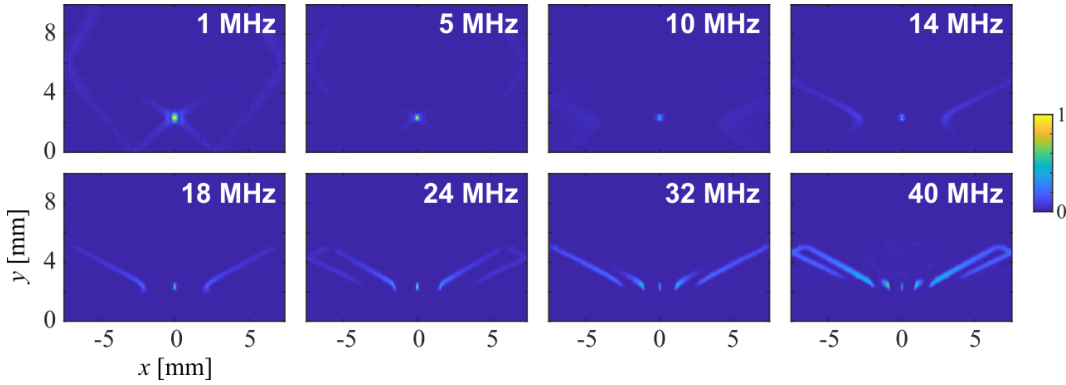


Figure 4.14: Images of a point scatterer for narrowband frequency filtered data with increasing centre frequencies from 1 to 40 MHz and a bandwidth of 2 MHz, showing grating lobe artefacts for centre frequencies above the temporospatial Nyquist frequency of 7.5 MHz. Images were individually normalised.

the sensor, and in a central position was simulated with a sound speed of 1500 m/s and a density of 5000 kg/m^3 . The sensor was sampled with a spatial sampling step of $100 \text{ }\mu\text{m}$ to ensure that spatial aliasing would occur for super-Nyquist frequencies, i.e. frequencies above 7.5 MHz. The simulated sensor data was filtered with different Gaussian temporal frequency filters, before reconstructing to obtain frequency filtered images. First, we used narrowband frequency filters with a bandwidth of 2 MHz and varied the centre frequency from 1 to 40 MHz. The filters were thus narrowband enough to consider the resulting data and images approximately single frequency. Then, for filters with super-Nyquist centre frequencies (above 7.5 MHz) the signals are aliased more or less equally strong, i.e. to approximately the same new AOI. Second, we picked a centre frequency above the temporospatial Nyquist frequency of 7.5 MHz, in this case 18 MHz was chosen, and the bandwidth was varied from 2 to 21 MHz. This way, spatially aliased images with increasing bandwidths can be compared, starting from a narrowband, almost single-frequency image to a broadband image where most of the frequency content is above the temporospatial Nyquist frequency of 7.5 MHz and thus still being aliased.

Narrowband grating lobe artefacts. Figure 4.14 shows images of the single point scatterer where the $100 \text{ }\mu\text{m}$ sampled sensor data has been filtered with narrowband frequency filters with centre frequencies from 1 to 40 MHz and with a bandwidth

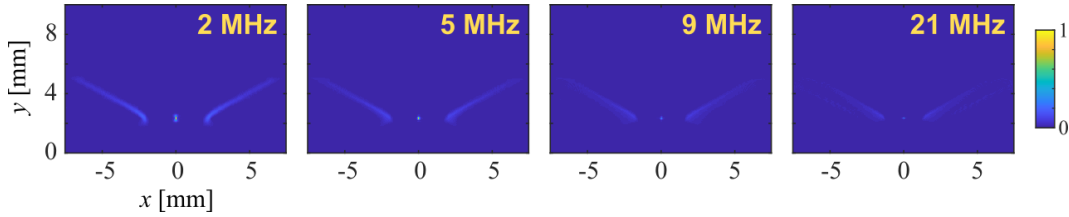


Figure 4.15: Images of a point scatterer for frequency filtered data with a centre frequency of 18 MHz and increasing bandwidths from 2 to 21 MHz, showing a decrease in grating lobe intensity with increasing bandwidths. Images were individually normalised.

of 2 MHz. For centre frequencies below the temporospatial Nyquist frequency of 7.5 MHz, i.e. when there is no aliasing, there are no grating lobes in the image. At these frequencies the image of the point scatterer has a lower resolution and limited view artefacts are more visible, due to the low and narrowband frequency content of the acoustic wave. Above the temporospatial Nyquist frequency of 7.5 MHz, grating lobe artefacts are visible on either side of the point scatterer in the horizontal x direction and at a similar depth. With increasing frequency, the grating lobe artefacts have an increasing amplitude relative to the peak amplitude of the reconstructed feature of the point scatterer and are closer to the main feature in the horizontal x direction. At frequencies from 24 MHz and above, multiple grating lobes are observed on both sides of the reconstructed image of the point scatterer.

Broadband grating lobe artefacts. Figure 4.15 shows images of the single point scatterer where the 100 μm sampled sensor data has been filtered with increasingly broadband frequency filters with a centre frequency of 18 MHz and bandwidths ranging from 2 to 21 MHz. The effect of an increasing bandwidth on the point scatterer image is an increase in resolution, as is expected due to higher temporal frequencies being included. With increased bandwidth the grating lobe artefact remains in the same position but decreases in amplitude relative to the reconstructed feature of the point scatterer. This is because different narrowband frequency filters have different grating lobe positions relative to the main reconstructed feature. Combining a range of narrowband frequency filters into a broadband filter then has an averaging effect on the position of the grating lobe. For a fixed centre frequency

the position will remain the same, however, with an increased bandwidth more narrowband grating lobes with a range of horizontal positions will be averaged. Note that “averaging” here actually refers to summing of the individual narrowband images before they are envelope detected, and then applying envelope detection to the final broadband compound image. Since summing narrowband grating lobe artefacts before envelope detection leads to some cancelling of the artefacts from the different bands, the final broadband grating lobe artefact is reduced in its amplitude relative to the main reconstructed feature. The effect of using a broadband signal is thus to broaden the grating lobe artefacts and reduce their intensity, which ultimately results in an improvement of contrast.

Discussion of the effects of grating lobe artefacts. We conclude that super-Nyquist frequencies are not sampled finely enough in space and thus cause the formation of grating lobes observed in the reconstructed images. For each scattering object the grating lobes contribute to image intensity elsewhere in the image, which can lead to a decrease in image quality, specifically image contrast. However, high temporal frequencies also enable high-resolution imaging of point scatterers, boundaries and any other specular scattering targets. Hence, it depends on the type of phantom or the desired image, which frequencies should be included in the image reconstruction.

For a point scatterer, broadband grating lobes are located away from the main reconstructed feature of the point scatterer in the background of the image, and thus have no detrimental effect on the image quality of the point scatterer itself. If only high frequencies are used, the grating lobes are more visible, as shown by the narrowband grating lobe artefacts in Section 4.5.3. However, for a broadband system that includes sub-Nyquist frequencies, grating lobes are barely visible and do not reduce the image quality significantly. The value of lower, sub-Nyquist frequencies therefore lies in the fact that they are sufficiently spatially sampled to portray point scatterers without grating lobes and thus only reconstruct the point scatterer at its actual location in the image. Lower, sub-Nyquist frequencies in a broadband sys-

tem therefore contribute to contrast improvement as well as image fidelity, which answers Question 1 of the motivation of this chapter.

The image of the hole in the random scattering medium is represented by a negative contrast, i.e. a lack of scattering in the hole. In this case, scatterers everywhere else in the medium are contributing to image intensity in the hole through grating lobe artefacts. Grating lobe artefacts thus have a detrimental effect on image quality, specifically on the scattering contrast of the hole. The more energy of the transmitted ultrasound wave that is contained in higher, super-Nyquist frequencies, the more severe is the contrast reduction, which is the trend we aimed to explain in Question 2 of the motivation of this chapter.

The contrast reduction due to grating lobes can be reduced by (i) filtering the received signals, or alternatively limiting the acoustic source, to only include sub-Nyquist frequencies, but this also limits the resolution performance (Fig. 4.14), or by (ii) using a broadband source, that includes sub- and super-Nyquist frequencies, as this reduces the relative intensity of grating lobe artefacts and thus reduces image contrast less compared to if only high, super-Nyquist frequencies are used. A broadband source also provides a high-resolution performance due to the high temporal frequencies. Another method to reduce the effect of grating lobe contrast reduction is frequency compounding, which will be explored in Section 5.2.

4.6 Spatial dependence

Previously, when studying spatial aliasing and grating lobes, we only considered a single point scatterer at one position in the imaging area. In this section, we study how spatial aliasing varies with depth and lateral position, and how this impacts the spatial dependence of the image quality. First, the spatial dependence of aliasing is studied by generating 2D-FT and AOI plots of point scatterers at different locations in the imaging area (Section 4.6.1). Then, we study how spatial aliasing affects the spatial dependence of image quality for the random scattering medium (Section 4.6.2).

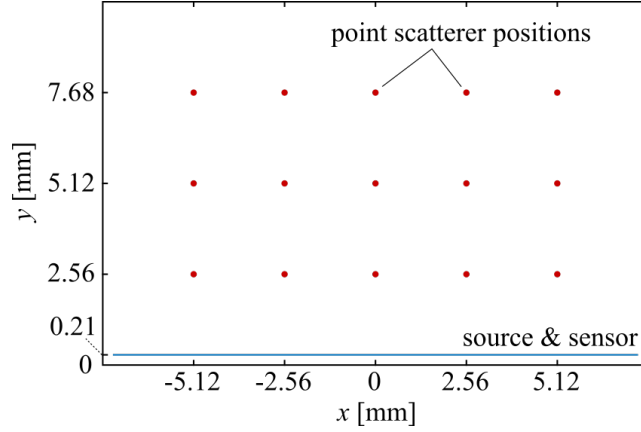


Figure 4.16: Positions of the point scatterers used to generate the 2D-FT and AOI plots in Figs. 4.17 and 4.18.

4.6.1 Spatial dependence of aliasing

Method. A single point scatterer with a diameter of $30\text{ }\mu\text{m}$, a sound speed of 1500 m/s and a density of 1200 kg/m^3 was simulated. The sensor was sampled with a step size of $10\text{ }\mu\text{m}$ to obtain a fully sampled data set without spatial aliasing. The point scatterer was placed at a number of positions in the simulation grid, see Fig. 4.16. For each position of the point scatterer 2D-FT and AOI plots were generated. Each individual 2D-FT and AOI plot was normalised to its individual minimum and maximum value to aid the visibility of the location of the data in each plot. Figure 4.17 shows the 2D-FT plots for the point scatterer at the different locations. In each 2D-FT plot, an orange dashed line indicates the threshold with a slope of $1/c$, which is equivalent to the maximum possible AOI of 90° .

Positional dependence of AOI. Two trends as a function of position can be observed. Firstly, for point scatterers closer to the sensor more of the received data is in the higher spatial frequencies than for point scatterers further away from the sensor. Secondly, using the orange dashed lines with a slope of $1/c$ as a reference, we can observe that the slope of the lower edge of the sensor data is higher the closer the point scatterer is to the sensor, and higher the further away it is from the centre of the sensor. The lower edge of the sensor data corresponds to the signals received with the largest AOI. Both trends can thus be explained using the transformation to the AOI plots. The AOIs of the received scattered waves are higher for point

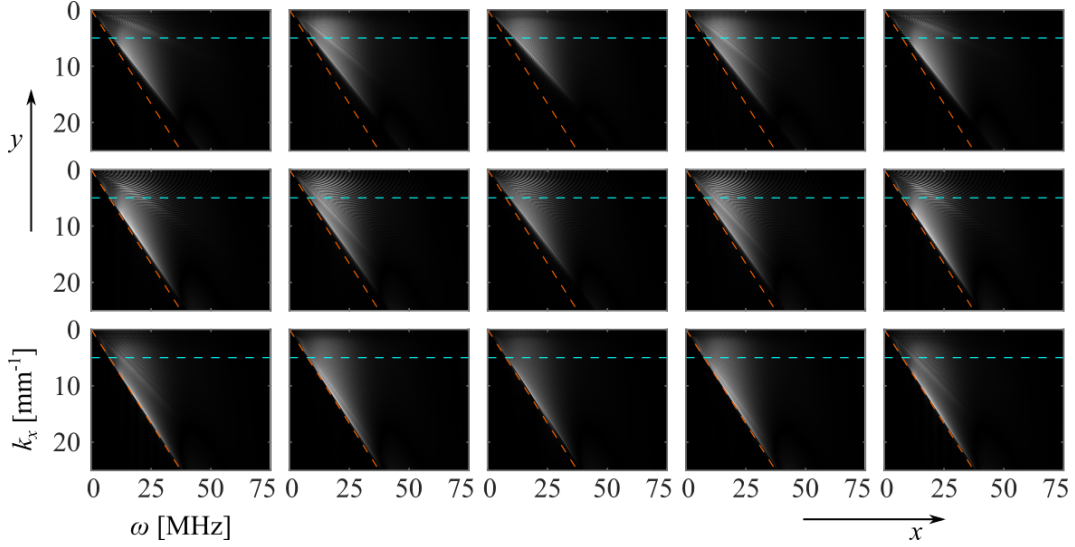


Figure 4.17: Spatial dependence of aliasing in frequency space. 2D-FT plots for differently-positioned point scatterers (positions shown in Fig. 4.16) when the sensor was sampled with a step size of $10\ \mu\text{m}$, i.e. without spatial aliasing. In each 2D-FT plot, a line indicating the threshold with a slope of $1/c$ equivalent to an AOI of 90° (orange dashed), and a line indicating the spatial Nyquist frequency threshold of $5\ \text{mm}^{-1}$ associated with a step size of $100\ \mu\text{m}$ (blue dashed) is marked.

scatterers closer to the sensor than for point scatterers further away from the sensor, see Fig. 4.18. The same but slightly weaker trend of higher AOIs can be observed for point scatterers that are laterally further away from the centre of the sensor compared to those that are closer to the centre. These differences in AOI for differently positioned point scatterers can be easily visualised by looking at the maximum AOI of signals from point scatterers at different depths and at different lateral positions, see Fig. 4.19.

Positional dependence of aliasing. The trends in the positional dependence of the spatial frequencies and the AOIs of the received data have important implications for the positional dependence of the effect of spatial aliasing. In Section 4.5.2 we found that signals with a spatial frequency above the spatial Nyquist frequency (or equivalently an AOI above the threshold AOI for a given super-Nyquist temporal frequency) are aliased to lower spatial frequencies and lower AOIs. The threshold of the spatial Nyquist frequency of $5\ \text{mm}^{-1}$ for a spatial sampling interval of $100\ \mu\text{m}$ is indicated in the 2D-FT plots in Fig. 4.17 as a blue dashed line, and the equivalent

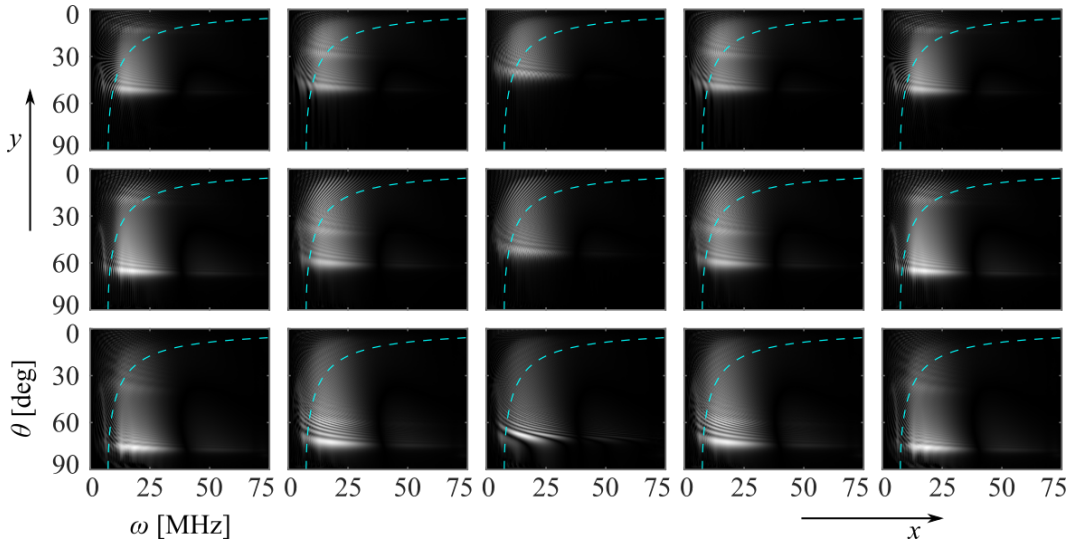


Figure 4.18: Spatial dependence of aliasing in angle-frequency space. AOI plots for differently-positioned point scatterers (positions shown in Fig. 4.16) when the sensor was sampled with a step size of $10\ \mu\text{m}$, i.e. without spatial aliasing. In each AOI plot, a line indicating the spatial Nyquist frequency threshold of $5\ \text{mm}^{-1}$ associated with a step size of $100\ \mu\text{m}$ (blue dashed) is marked.

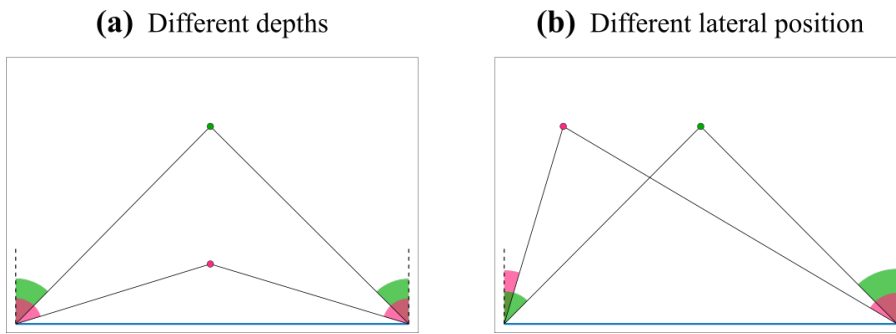


Figure 4.19: Schematic to show difference in maximum AOI for point scatterers at (a) different depths and (b) different lateral positions relative to the sensor (blue). In both cases the pink point scatterer has a larger maximum AOI than the green point scatterer.

AOI threshold for the same spatial sampling interval is shown in the AOI plots in Fig. 4.18. The threshold lines visualise the amount of sensor data that would be aliased at a spatial sampling interval of $100\text{ }\mu\text{m}$, and how this amount varies depending on the position of the scatterer. A larger fraction of the sensor data is aliased for point scatterers near the sensor compared to those further away from the sensor, and similarly for point scatterers further away from the centre of the sensor compared to those closer to the centre. The effect of spatial aliasing is therefore more severe closer to the sensor, and at lateral positions further away from the centre of the sensor.

Conclusion. Acoustic waves scattered from scatterers near the sensor, and from scatterers laterally further away from the centre of the sensor, are received at higher AOIs compared to those further away from the sensor, and laterally closer to the centre of the sensor. As a result, the image of scatterers near the sensor and laterally further away from the centre is more strongly affected by spatial aliasing. We would therefore expect a stronger contrast reduction due to grating lobe artefacts near the sensor and laterally further away from the centre. This hypothesis will be explored in the next section by simulating random scattering media with the hole located at different positions relative to the sensor to measure the spatial dependence of contrast and the effect of spatial aliasing on this.

4.6.2 Spatial dependence of image quality

In this section, we study how spatial aliasing affects the spatial dependence of image quality. As we learned in the previous section, scatterers are more strongly aliased when they are close to the sensor and laterally further away from the centre of the sensor. We would, therefore, expect spatial aliasing to decrease the image quality near the sensor, and laterally further away from the centre, more strongly than elsewhere. In practice, more effects besides spatial aliasing influence the spatial dependence of the image quality, such as acoustic attenuation and limited view artefacts. However, in this section we study the effect of spatial aliasing in the absence of attenuation. The effect of limited view artefacts on image quality was not

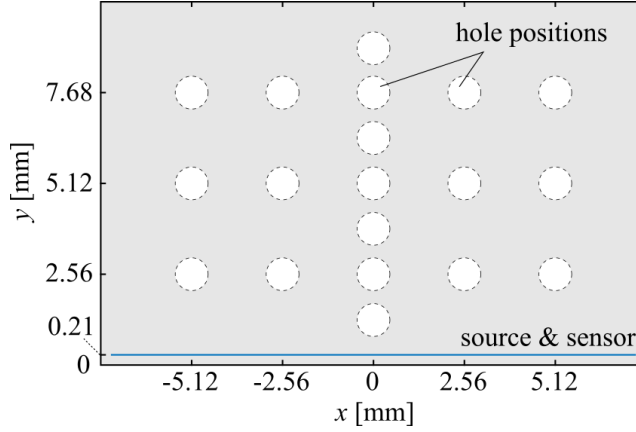


Figure 4.20: Positions of the hole in a random scattering medium used for measuring spatial dependency of the scattering SNR and CNR in Figs. 4.21 and 4.23.

separated from the effect of spatial aliasing, as limited view artefacts will always be present due to the limited size of the sensor.

Method. A random scattering medium was simulated with the same average acoustic properties ($c_0 = 1500$ m/s, $\rho_0 = 1000$ kg/m³) and the same maximum sound speed and density fluctuations ($\Delta c = 40$ m/s, $\Delta \rho = 80$ kg/m³) as previously. A single non-scattering inclusion, the “hole”, with the same acoustic properties ($c_0 = 1500$ m/s, $\rho_0 = 1000$ kg/m³) as previously, was placed at a number of positions in the random scattering medium, see Fig. 4.20. The sensor was sampled with either a step size of 10 μ m for a spatially fully sampled data set, or a step size of 100 μ m for a spatially aliased data set. For each hole position an image was reconstructed. This was first done without frequency filtering of the sensor data to obtain the unfiltered broadband image, and then with frequency filtered sensor data using a Gaussian filter with a centre frequency of 1 MHz and a bandwidth of 10 MHz to obtain a low-frequency image. The scattering SNR and CNR were extracted from each image using the method described in Section 4.3.1. The values for the scattering SNR and CNR for each hole position were interpolated in space to give an approximate map of the spatial dependence of the image quality for both the unfiltered broadband image and the low-frequency image. The hole positions were simulated separately to ensure that the image quality estimates at different positions were independent of each other. The interpolated maps can therefore be interpreted as scattering SNR

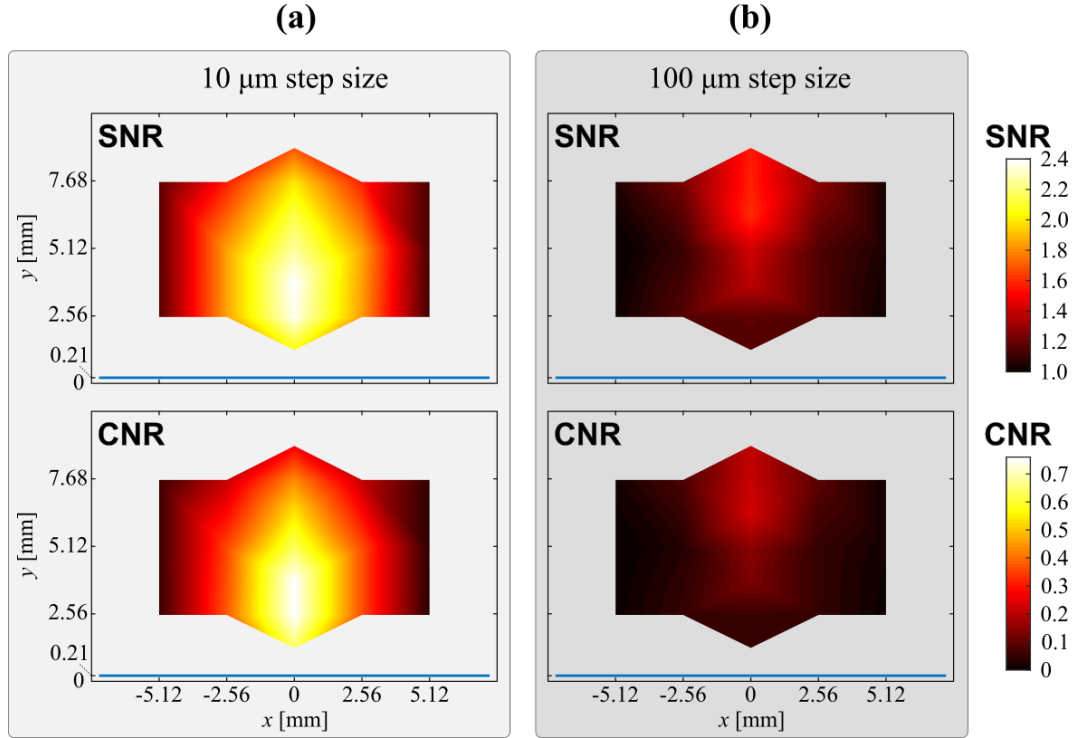


Figure 4.21: Spatial dependence of scattering SNR and CNR in an unfiltered broadband image of a hole in a random scattering medium. The acoustic field was sampled with a step size of (a) 10 μm or (b) 100 μm , and the sensor data was not frequency filtered before reconstruction.

and CNR performance maps of the ultrasound imaging system.

Effect of limited view of the sensor. For images reconstructed from fully spatially sampled sensor data with a step size of 10 μm the contrast is better near the sensor and near the centre of the sensor, Fig. 4.21a. In experimental ultrasound images a decrease in contrast at larger depths is expected due to the stronger acoustic attenuation of waves that have travelled further through tissue. However, since we did not include attenuation in the simulations of the medium, the spatial variation in image quality seen here is purely due to limited view. This means that for scatterers far from the sensor or far from the centre of the sensor a smaller proportion of the scattered ultrasound wave is detected at the finitely sized sensor. This leads to scatterers being reconstructed with lower resolution and with stronger artefacts, ultimately resulting in reduced contrast. The contrast reduction at larger depths due to limited view can also be observed in images of the hole at different depths, see

Fig. 4.22a.

Effect of spatial aliasing. For images where the sensor data was sampled with a larger step size of 100 μm , thus introducing spatial aliasing, the contrast is better far from the sensor and near the centre of the sensor scan, see Fig. 4.21b. In the aliased images of the hole at different depths, see 4.22b, the hole is invisible at depths of 1 and 2.3 mm, but visible at a depth of 6.2 mm. An increased contrast at larger depths may seem counter-intuitive, but can be explained using our knowledge about aliasing from Section 4.6.1. The sensor data set sampled with a 100 μm step size contained super-Nyquist frequencies, i.e. frequencies above 7.5 MHz, that were spatially aliased. For scatterers located near the sensor, the AOIs of the acoustic waves at the sensor plane will be overall larger, such that those signals are aliased more strongly than for scatterers far from the sensor. Similarly, signals from scatterers at a lateral position further away from the centre of the sensor are aliased more strongly than those near the centre. This results in more contrast reduction near the sensor compared to further away from the sensor, and more contrast reduction at lateral positions further away from the centre compared to lateral positions closer to the centre. In our simulations the effect of contrast reduction was so much more severe near the sensor than further away from the sensor that the scattering SNR and CNR in the spatially aliased images was worse closer to the sensor. This is an inversion of the trend observed in images obtained without spatial aliasing (Fig. 4.21a and Fig. 4.22a). The contrast reduction near the sensor due to spatial aliasing thus outweighed the contrast reduction due to limited view further away from the sensor. This is visualised in the comparison of the fully spatially sampled images in Fig. 4.22a and the spatially aliased images in Fig. 4.22b.

Effect of low-pass filtering. The image quality analysis was repeated after the sensor data for each hole position was frequency filtered with a Gaussian filter with centre frequency 1 MHz and bandwidth 10 MHz. Most of the filtered sensor data thus had frequencies between 0-6 MHz, i.e. below the temporospatial Nyquist frequency of 7.5 MHz associated with a spatial sampling interval of 100 μm . With

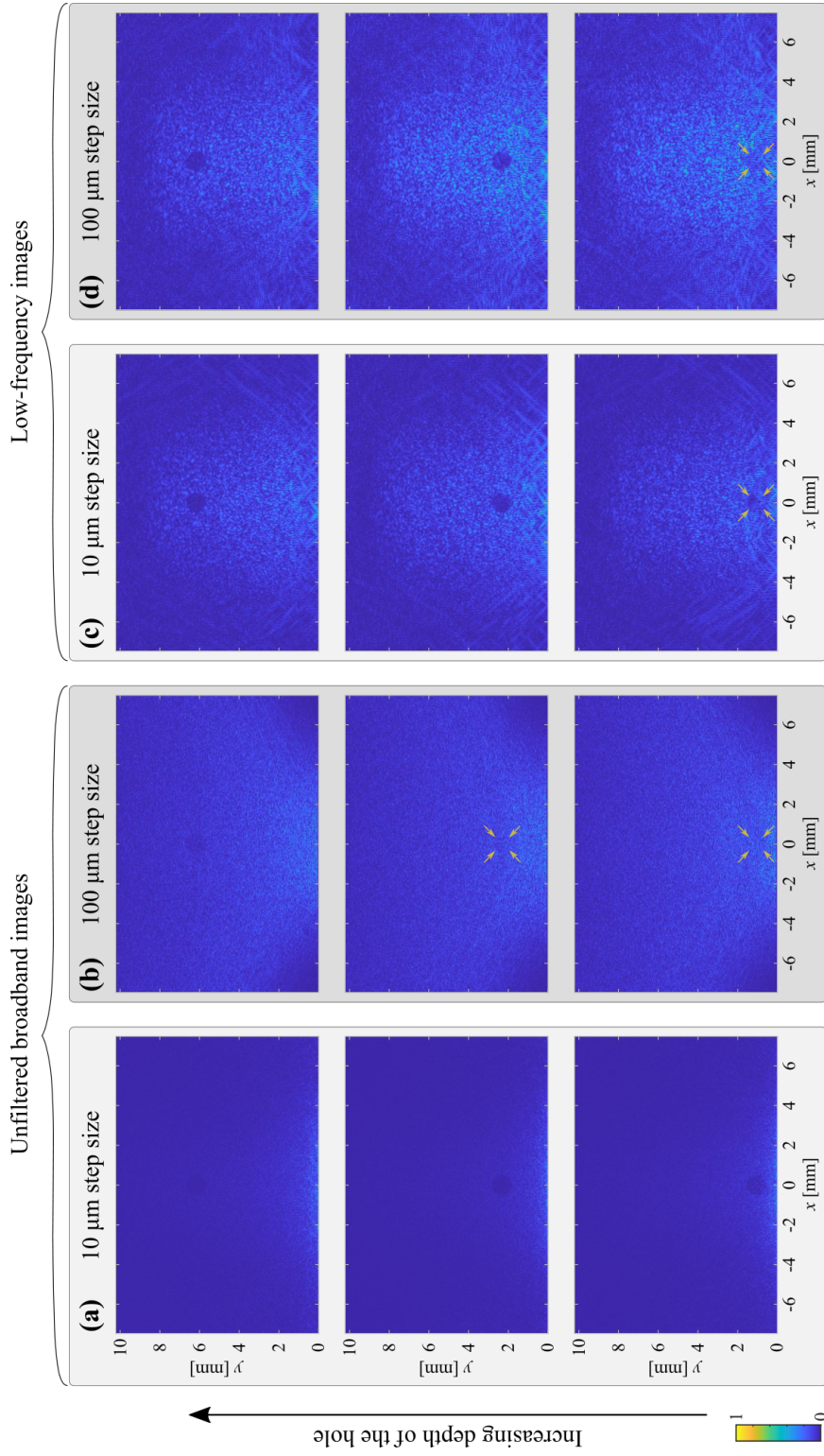


Figure 4.22: Images of a hole in a random scattering medium at different depths obtained with a sensor sampling step size of either 10 μm or 100 μm , and reconstructed without applying a frequency filter or with a low-pass frequency filter (centre frequency of 1 MHz, bandwidth of 10 MHz) applied. Unfiltered broadband images obtained with a step size of (a) 10 μm and (b) 100 μm , and low-frequency images obtained with a step size of (a) 10 μm and (b) 100 μm . Yellow arrows mark poorly visible holes. Images were individually normalised.

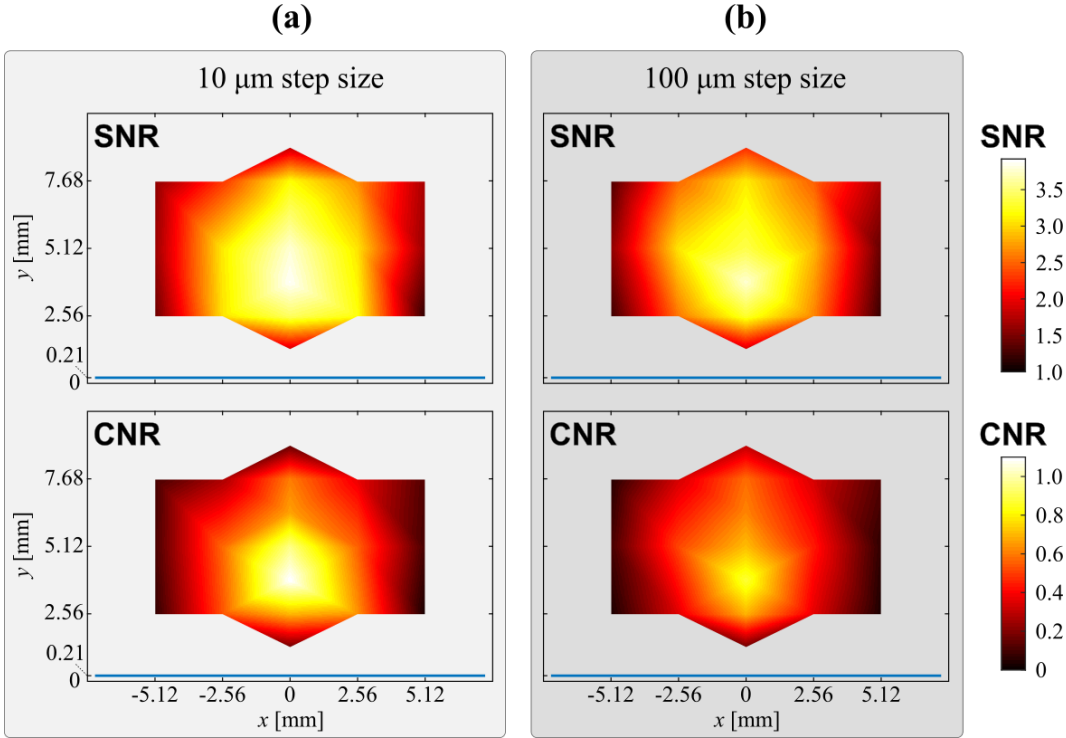


Figure 4.23: Spatial dependence of scattering SNR and CNR in a low-frequency image of a hole in a random scattering medium. The acoustic field was sampled with a step size of **(a)** 10 μm or **(b)** 100 μm , and the sensor data was filtered with a Gaussian frequency filter of centre frequency 1 MHz and bandwidth 10 MHz before reconstruction.

this frequency filter applied, the sensor data is mostly not spatially aliased even for the data acquired with a coarse spatial sampling interval of 100 μm . Both 10 and 100 μm sampled sensor data sets should thus acquire this frequency filtered data similarly well, i.e. (mostly) without aliasing. Hence, we expect little to no contrast reduction as a result of aliasing and grating lobe artefacts. This is indeed the case, as the fully spatially sampled low-frequency images in Fig. 4.22c and the spatially sampled low-frequency images in Fig. 4.22d display a similar visibility of the hole at corresponding depths. The spatial dependence of the scattering SNR and CNR look very similar for the 10 μm sampled data in Fig. 4.23a and the 100 μm sampled data in Fig. 4.23b. Differences between the differently sampled data sets are largely due to the applied Gaussian low-frequency filter including some sensor data with frequencies above the temporospatial Nyquist frequency of 7.5 MHz associated with the 100 μm sampling interval.

Effect of limited view artefacts. Since spatial aliasing affects low-frequency images less, we would expect any spatial variation in the scattering SNR and CNR to be due to the limited view of the sensor, i.e. a decrease in SNR and CNR at increasing depths, similar to what was observed for unfiltered broadband images obtained with a step size of 10 μm , as the limited view of the sensor was the only effect present there. A decrease in SNR and CNR at increasing depths is indeed observed for depths greater than 3.5 mm, see Fig. 4.23a and b. However, at depths below this, the SNR and CNR decrease with increased proximity to the sensor. This is due to limited view artefacts (or edge wave artefacts) at depths from 0-3 mm which are clearly visible in all low-frequency images in Fig. 4.22c and d (regardless of the step size). These artefacts appear to be more severe for a combination of reasons: (i) The amplitude of the plane wave source is at its maximum closest to the sensor and has not yet been attenuated due to scattering in the medium; (ii) Scattered waves from point scatterers near the sensor are detected with a higher amplitude due to lower attenuation from geometrical spreading of the wavefront; (iii) The artefacts from scatterers near the sensor are superimposed with fewer artefacts from surrounding scatterers, such that they are not mixed up into a finely grained speckle pattern as artefacts from scatterers further into the medium are; (iv) Limited view artefacts are larger in narrowband frequency images. These high amplitude limited view artefacts from point scatterers near the sensor reduce the contrast significantly in the first 1-2 mm of the image. This can be observed in the low-frequency images of the hole at 1 mm depth in Fig. 4.22c and d.

Conclusion. In this section, we studied the spatial dependency of the scattering SNR and CNR. Using a spatial sampling interval that is sufficiently small that spatial aliasing does not occur, in this case 10 μm , the effect of the limited view of the sensor on image quality was observed. As a result of the sensor's limited view, the scattering SNR and CNR are higher near the sensor, and closer to the centre of the sensor. Using a spatial sampling interval where spatial aliasing occurs, in this case 100 μm , grating lobes were generated for each scatterer in the medium leading to a position-dependent contrast reduction. This contrast reduction was shown to

be more severe near the sensor since the AOIs of the received waves are higher, leading to more severe aliasing. The effect of grating lobes due to spatial aliasing outweighed the effect of limited view leading to better scattering SNR and CNR when further away from the sensor. When a low-pass frequency filter is applied to the sensor data, such that only sub-Nyquist frequencies are contained in the signal, the images are not affected by spatial aliasing. In this case, the limited view of the sensor reduces the contrast with increasing depth, while narrowband limited view artefacts from point scatterers near the sensor reduce the contrast at small depths. It is worth noting that the effect of acoustic attenuation was not included in the simulations, which would be another factor contributing to a decrease in contrast at greater depths.

4.7 Sensor directivity

In all previous simulations in this chapter the sensor was modelled as having an omnidirectional response. This was a deliberate choice since the FP sensor has a complicated directional response that varies depending on its composition and for which there is no analytical model [106]. However, the directivity of a sensor would have an effect on the formation of artefacts and the image quality. The findings from the previous sections in this chapter are thus only valid for a general omnidirectional sensor. In this section we present preliminary simulations on the effect of the sensor directivity on grating lobe artefacts and image quality.

Modelling directivity. For the simulations in this section we used data from previous simulations sampled with a spatial sampling step of $10\ \mu\text{m}$. To introduce directivity into the model, the signal from a number of adjacent detection points was averaged. By averaging the signal from 6 or 10 adjacent detection points spaced $10\ \mu\text{m}$ apart, approximately 60 or 100 μm sized detectors were generated. Repeating this step along the sensor array at a spatial interval of 10 detection points, a downsampled and directional sensor data set with a spatial sampling interval of $100\ \mu\text{m}$ and finitely sized detectors of either 60 or 100 μm size was obtained. The downsampling was also done without averaging to obtain a sensor data set from

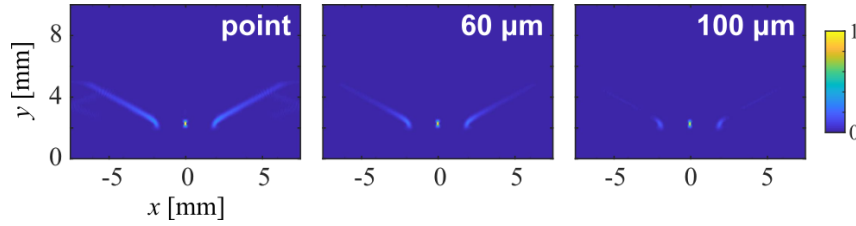


Figure 4.24: Images of a point scatterer obtained with a sensor array of point-like, 60 μm sized, and 100 μm sized detectors, with a spatial sampling interval of 100 μm , and frequency filtered with a centre frequencies of 20 MHz and a bandwidth of 2 MHz. Images were normalised individually.

omnidirectional detectors with a spatial sampling interval of 100 μm . While the 60 μm sized detectors do not exactly reproduce the directivity of the FP sensor, they provide a directional response of a similar order to the one of the FP sensor, which had an element size of approximately 64 μm (Section 3.2.2). The downsampling to a spatial sampling interval of 100 μm ensures that spatial aliasing would occur for super-Nyquist frequencies, i.e. frequencies above 7.5 MHz, resulting in the formation of grating lobe artefacts.

Effect of directivity on grating lobe artefacts. A single point scatterer of diameter 10 μm located 2.35 mm away from the sensor, and in a central position was simulated with a sound speed of 1500 m/s and a density of 5000 kg/m³. Downsampled sensor data sets with a spatial sampling interval of 100 μm were obtained as described above for sensor arrays of point-like omnidirectional, 60 μm sized, and 100 μm sized detectors. The sensor data were filtered with a Gaussian temporal frequency filter with a centre frequency of 20 MHz and a bandwidth of 2 MHz, which ensured the formation of narrowband grating lobe artefacts. For the point-like omnidirectional detectors, see Fig. 4.24, grating lobe artefacts similar to those shown in Fig. 4.14 are observed. For 60 μm sized detectors, the amplitude of the grating lobe artefacts is slightly reduced, and for 100 μm sized detectors they are significantly reduced in size and almost completely suppressed, see Fig. 4.24. This is an expected result since introducing directivity into the modelled detectors meant that waves incident at higher AOI are detected less strongly. Since these high AOI components of the field are spatially aliased, a suppression of their detection would

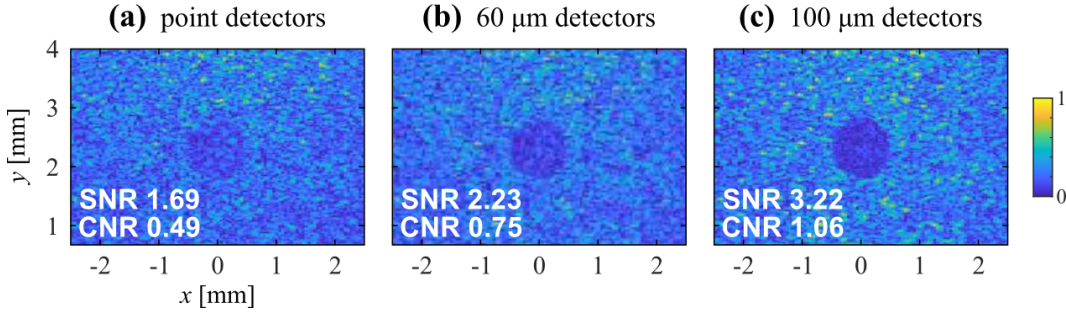


Figure 4.25: Images of a random scattering medium obtained with a sensor array of (a) point-like, (b) 60 μm sized, (c) 100 μm sized detectors, with a spatial sampling interval of 100 μm , and frequency filtered with a centre frequencies of 20 MHz and a bandwidth of 2 MHz. Images were normalised individually.

result in a reduction of aliased signals and thus a reduction in the amplitude and size of the grating lobe artefacts.

Effect of directivity on scattering SNR and CNR. A random scattering medium was simulated with the same average acoustic properties ($c_0 = 1500$ m/s, $\rho_0 = 1000$ kg/m³) and the same maximum sound speed and density fluctuations ($\Delta c = 40$ m/s, $\Delta \rho = 80$ kg/m³) as previously. A single non-scattering inclusion, the “hole”, with the same acoustic properties ($c_0 = 1500$ m/s, $\rho_0 = 1000$ kg/m³) as previously, was placed at 2.35 mm away from the sensor in the centre of the field of view. Down-sampled sensor data sets with a spatial sampling interval of 100 μm were obtained as described above for sensor arrays of point-like omnidirectional, 60 μm sized, and 100 μm sized detectors. The sensor data were filtered with a Gaussian temporal frequency filter with a centre frequency of 1 MHz and a bandwidth of 20 MHz, to approximately limit the frequency content in the simulated data to the one detected in the experimental data. The scattering SNR and CNR were determined as described in Fig. 4.3. In the image obtained with point-like detectors, see Fig. 4.25a, the scattering SNR and CNR are relatively low as previously observed. In the image obtained with 60 μm detectors the scattering SNR and CNR are improved, see Fig. 4.25b, and in the image obtained with 100 μm detectors even more significantly, see Fig. 4.25c. This is, at least in part, due to the reduction of grating lobe artefacts with increased directionality observed in Fig. 4.24, which had the effect of increasing contrast.

Conclusion. We can thus conclude that a sensor with a directional response equivalent to that of a 60 μm detector can have the effect of reducing grating lobe artefacts and improving contrast. A more directional detector can amplify these effects. However, the effect of the directivity on grating lobe artefacts and image quality likely varies spatially, and has only been studied at a single position within the field of view in this section. Increasing the directionality of the sensor will likely have other effects not studied here, e.g. it may affect the formation of limited view artefacts. Further simulations need to be carried out to fully understand and quantify the effect of directivity on the image quality. The frequency-dependent directional response of the FP sensor used for imaging (Section 3.2.2) could be measured with the method presented by Ramasawmy *et al* [106] and included in simulations.

4.8 Future work

4.8.1 Negative vs positive contrast.

Motivation. In Section 4.5 we showed that super-Nyquist frequencies contribute to grating lobe artefacts which are responsible for contrast reduction in ultrasound images of scattering media. While including super-Nyquist frequencies can improve resolution performance, it comes at the cost of the image contrast. We suggest that the reason why this is an issue with ultrasound images, but less so with photoacoustic images, is the difference in the type of contrast in both modalities.

Ultrasound vs photoacoustic contrast. Ultrasound images are characterised by a mix of specular objects, such as tissue boundaries, and scattering contrast between different tissue types. The latter scattering contrast relies on a difference in scatterer density, or a lack of scatterers in one of the regions as was the case in the random scattering medium with the non-scattering hole, which leads to a difference in the intensity distributions of two regions in the image. We will refer to this as negative contrast, i.e. the lack of or difference in scattering between two regions in the medium. In photoacoustic images, on the other hand, the contrast is created by localised optical absorption in small tissue structures, typically blood vessels. The resulting images therefore tend to have well-defined absorbing features in otherwise

non- or weakly absorbing surrounding tissue. We will refer to this as positive contrast, i.e. the creation of contrast is facilitated by a localised absorption and a lack of absorption in the surrounding medium. The simulated acoustic point scatterer phantom is of a similar positive contrast nature as blood vessels in photoacoustic images. This distinction of negative and positive contrast is important since ultrasound images typically have a mix of both types of contrast, while photoacoustic images predominantly rely on positive contrast. As discussed in Section 4.5, images relying on negative contrast experience a reduction in contrast when spatially undersampling, due to the grating lobe artefacts that contribute to image intensity everywhere in the image. Images relying on positive contrast, on the other hand, are less affected by spatial undersampling since the grating lobe artefacts appear in the background of the image and do not obtrude on the main reconstructed features.

Proposed simulations. To confirm this hypothesis on the different effects of spatial aliasing on negative *vs* positive contrast images, we suggest simulating the following: (i) A positive contrast ultrasound image of a random scattering medium and (ii) a negative contrast photoacoustic image.

The positive contrast ultrasound image of a random scattering medium can be obtained by essentially inverting the random scattering medium used previously in this chapter, i.e. having a small circular random scattering region, or "tube", inside an otherwise non-scattering medium. This is expected to show that positive contrast of a random scattering tube in water has a better scattering contrast than the negative contrast of a non-scattering hole surrounded by a random scattering medium. In the former case, grating lobe artefacts from the random scattering tube should contribute to some image intensity outside of the tube, while in the latter case, grating lobe artefacts from the random scattering medium contribute to lots of image intensity inside the hole.

A negative contrast photoacoustic image would need to be created by placing single point absorbers (blood cells) into an otherwise homogeneous non-absorbing background medium (plasma). Within this distribution of point absorbers, non-absorbing exclusions could be placed to simulate 'anti-blood vessels'. The pro-

posed negative PA phantom is similar to the hole in the random scattering medium used for ultrasound simulations in this chapter, except that scatterers are replaced with absorbers and that a discrete model instead of a continuum model should be used for the PA case. This could potentially illustrate that grating lobe artefacts due to undersampling reduce the contrast more strongly in the negative contrast image of the non-absorbing exclusion, than in a typical positive contrast photoacoustic image of a blood vessel. It is important to introduce spatial inhomogeneity within the absorbing medium on a scale similar to the imaging resolution. Only then would numerous grating lobe artefacts associated with the point absorbers be generated and overlap to reduce the contrast across the whole image. In practice, blood vessels may not necessarily exhibit the spatial inhomogeneity on a scale similar to the imaging resolution, i.e. the blood cell concentration may be high enough for the blood to be considered a continuous absorbing medium. The comparisons made in these proposed simulations are thus more theoretical and may only apply to very diluted blood in practice.

Summary. Overall these simulations could show that photoacoustic and ultrasound images are, in principle, affected in the same way by undersampling, aliasing of super-Nyquist frequencies and grating lobe artefacts, given the same spatial sampling intervals, and source and sensor bandwidths. Images relying on negative contrast will be more affected by contrast reduction due to grating lobe artefacts than positive contrast images. Since ultrasound images often include both positive and negative contrast, they could be more affected by spatial aliasing than photoacoustic images which typically rely on positive contrast only.

4.8.2 Spatial dependence of grating lobes.

In Section 4.6 we demonstrated that acoustic waves from scatterers located closer to the sensor or at a lateral position further away from the centre of the sensor have higher AOIs than from scatterers further away from the sensor or at a lateral position closer to the centre of the sensor. This was shown to result in a more severe contrast reduction due to undersampling at positions near the sensor and laterally

further away from the centre. We reasoned that the higher AOI of signals from those positions lead to more strongly aliased images, i.e. more severe grating lobe artefacts with higher relative intensity.

A simulation to demonstrate the stronger aliasing of higher AOI signals by showing the shape and position of narrowband grating lobe artefacts for different scatterer positions would strengthen this point. This can be done by simulating a point scatterer at different locations in the imaging area similar to Section 4.6.1. The simulation setup would be the same as in Section 4.5.3 where the scattered acoustic field was received with a large spatial sampling interval, e.g. 100 μm , to ensure spatial aliasing of super-Nyquist frequencies. The resulting simulated data would then be filtered with frequency filters with a super-Nyquist centre frequency, e.g. 18 MHz, and a narrow bandwidth, e.g. 2 MHz. This would generate narrowband grating lobe artefacts for point scatterers in different positions. In particular, we are interested in comparing the shape of grating lobes for point scatterers near the sensor with point scatterers further away from sensor. The hypothesis is that scatterers near the sensor, when undersampling, contribute to a greater contrast reduction due to the shape of the grating lobe artefacts, than scatterers further away from the sensor.

4.9 Conclusion

4.9.1 Summary

In this chapter, we presented a simulation platform based on the *k*-wave ultrasound simulation tool [104] to study images acquired via broadband plane-wave pulse-echo ultrasound. Point scatterers and random scattering media were simulated to explore how image quality, specifically the scattering SNR and CNR, depend on frequency. Signals with a frequency above a certain cut-off frequency were found to decrease the scattering SNR or CNR when included in the image reconstruction. We established that this is due to spatial undersampling of the acoustic field, such that high temporal frequency signals are spatially aliased when detected at larger angles of incidence. Due to spatial aliasing, signals with spatial frequencies higher than the spatial Nyquist frequency are aliased to lower spatial frequencies. For tem-

poral frequencies this means that super-Nyquist frequencies, e.g. frequencies above 7.5 MHz for a 100 μm sampling interval, are aliased to different positions to the point they were scattered from. Spatially aliased signals thus lead to the formation of grating lobe artefacts, which are a familiar concept in conventional ultrasound imaging. We have thus answered the two questions posed at the start of this chapter. The contrast reduction in ultrasound images of scattering contrast when using only ‘high’ (super-Nyquist) frequencies is due to the grating lobe formation from spatially undersampling these signals (Question 2). ‘Lower’ (sub-Nyquist) frequencies are sufficiently spatially sampled, and therefore contribute to higher image contrast in scattering media and improved image fidelity, i.e. the correct positioning of reconstructed features in images of point scatterers (Question 1). Grating lobe artefacts can be reduced in amplitude by only using sub-Nyquist frequencies, or using more broadband signals which results in broader and lower amplitude grating lobes, since each single frequency is aliased to a different position in the image. The contrast reduction due to grating lobes is more severe near the sensor and at positions laterally further away from the centre of the sensor. This is because waves scattered from these locations are detected with a higher angle of incidence which leads to more frequencies being spatially aliased and contributing to grating lobe artefacts.

4.9.2 Outlook

In this chapter, we focused on studying how the contrast in broadband plane-wave ultrasound images is reduced by spatial aliasing and the resulting formation of grating lobes. We also observed the effect of the limited view of the sensor and the resulting limited view artefacts. In general, the contrast can be limited by more factors, including acoustic attenuation of the medium, the pressure amplitude of the source and the sensitivity of the sensor. To be able to make a definitive conclusion on how the optical ultrasound system based on the FP scanner should be improved, all potentially contrast limiting factors should be investigated. The simulation platform described in this chapter forms a basis on which these factors can be studied in their frequency and spatial dependence, and the effect of all factors compared to each other.

The optical ultrasound system based on the FP scanner is so broadband that a significant amount of energy in the acoustic wave is at high (super-Nyquist) frequencies which are not sufficiently spatially sampled and thus reduce contrast. These high frequencies are, however, desirable as they provide images with higher resolution. The goal should therefore be to retain these higher frequencies to obtain high-resolution images without decreasing the contrast. In Section 4.5.3 we showed that the contrast reduction at higher frequencies is due to grating lobe artefacts whose position in the image is frequency dependent. Thus, by summing multiple frequency filtered images with different centre frequencies, i.e. frequency compounding, the amplitude of grating lobes could be suppressed and the contrast improved in the summed image. Another method to improve contrast in conventional plane wave imaging is angle compounding, which involves summing images acquired with differently angled plane waves. Both concepts of frequency and angle compounding will be explored in-depth in Chapter 5.

Chapter 5

Compounding methods for broadband plane-wave ultrasound imaging

5.1 Introduction

In Chapter 3 we found that imaging at depths greater than 5-7 mm resulted in poor SNR and contrast. In this chapter, we look at compounding methods to improve the image quality in broadband plane-wave ultrasound images.

In conventional ultrasound imaging many ways of doing compounding have been explored, usually with the aim of speckle reduction to improve contrast. Compounding methods can involve spatial movement, angular movement or frequency subdivision in transmit or receive [107]. The aim is to have a varying speckle pattern in individual images, before summing them to obtain a compound image with a smoothed out the speckle pattern. Spatial compounding involves moving the transducer, e.g. side-ways and perpendicular to the scan area, which can smooth out the speckle but also results in some loss of resolution [108]. Angle compounding is a type of spatial compounding where the transmit wave is steered to different angles [109–111]. It is easily implemented with an electronically steered linear or phased

array. The speckle pattern changes for different angle transmissions since the scatterer spacing differs when seen from different angles [107]. Frequency compounding involves either transmitting different frequency bands or splitting the received signal into frequency sub-bands, before reconstructing images from all the sub-band to compound them. This has been shown to reduce speckle due to the frequency dependence of the speckle pattern [112, 113]. However, due to the narrow bandwidth of conventional ultrasound systems the sub-bands have such small bandwidths that the spatial resolution becomes compromised. As a result, frequency compounding has not been utilised much in conventional ultrasound imaging. Other methods to reduce speckle include image post-processing methods based on filters [114]. Non-compounding methods to reduce image artefacts such as grating lobes involve the non-periodic placement of detection points. While the FP scanner system would be well suited to these methods, as the detection points can be arbitrarily chosen across the FP sensor head, they were not explored in this work. A review of these methods is included in Section 5.6.3.

In comparison to conventional ultrasound systems the optical ultrasound system based on the FP scanner is broadband and plane-wave. Hence frequency and angle compounding will be studied in-depth to be able to make full use of the broadband advantages of the FP scanner system and improve the contrast from imaging with a plane wave. Although the images produced by the FP scanner do not have the typical speckly appearance as conventional ultrasound images, they do contain speckle at a very fine grain size. The aim of compounding is thus to smooth out the fine grained speckle pattern, as well as suppress other contrast reducing effects, such as noise or artefacts, e.g. grating lobes or limited-view artefacts.

Frequency compounding. Since the optical ultrasound imaging system based on the FP scanner is much more broadband than conventional ultrasound imaging systems, frequency compounding can be more effective. Due to the broader bandwidth of the detected signal it can be split into frequency sub-bands that are not so narrowband as to excessively compromise resolution. In Chapter 4 it was found that,

due to spatial undersampling, super-Nyquist frequencies contribute to grating lobe artefacts that reduce the image contrast. It was also found that the position of these grating lobe artefacts is frequency-dependent (Section 4.5.3). These artefacts are expected to be suppressed when frequency compounding, leading to an improvement in contrast. At the same time, the images would retain the high frequency components and benefit from the high resolution these provide. If each frequency sub-band is chosen to be sufficiently broadband, the high resolution of a broadband image can be retained in the final compound image.

Angle compounding. Plane-wave ultrasound imaging using a single normal plane wave typically suffers from poor contrast. A commonly used method to improve the contrast in plane-wave ultrasound imaging is angle compounding, which uses differently angled plane-wave transmissions to obtain a set of images for compounding. For piezoelectric transducers, an angled plane wave is easily generated by introducing time delays for each transducer element and thus electronically steering the plane wave. Conventionally, plane-wave ultrasound is used for ultrafast imaging, i.e. imaging with very high frame rates. This makes compounding multiple images taken at different angles feasible. The image contrast has been shown to be greatly improved by angle compounding, giving comparable contrast at higher frame rates than B-mode imaging, see Fig. 2.2 [73]. For conventional ultrasound systems, that operate over a narrowband frequency range, the contrast improvement results from an averaging of the speckle pattern, which differs for differently angled plane wave transmissions. Although the FP scanner system used in this work was broadband, which resulted in ultrasound images without the typical large speckle grain in conventional images, the images did contain speckle at a very small grain. We would therefore still expect a contrast improvement in broadband angle compounded images from averaging out the speckle pattern. In addition, changing the transmission angle should improve the limited view problem (not to be confused with limited view artefacts), which leads to incomplete reconstruction of objects in single plane wave images. The contrast improvement can also be explained by the creation of a synthetic transmit focus at all depths and lateral positions when compounding an-

gled plane-wave images coherently. The concept of the synthetic transmit focus was first introduced by Cooley and Robinson in 1994 [115], and experimentally applied to plane wave transmissions by Montaldo *et al* in 2009 [63]. For a conventional narrowband system, Montaldo *et al* showed that coherent plane-wave angle compounding yields a similar image quality to a focused B-mode image, if the synthetic compounded focus is equivalent to the B-mode focus [63]. The same concept of a synthetic transmit focus applies to broadband plane wave transmissions, where the synthetic transmit focus should be even smaller than for narrowband transmissions.

Outline. In Section 5.2 we demonstrate that frequency compounding is feasible for a system as broadband as the FP scanner system. This is shown in simulation using the simulation platform from Chapter 4, and with experimental data obtained from the FP scanner in Chapter 3. In Sections 5.3 to 5.5, angle compounding with a broadband plane-wave ultrasound imaging system is explored. First, the reconstruction algorithm and methods were modified for imaging with angled plane waves in Section 5.3. Second, angle compounding was simulated and shown to improve image contrast for a broadband plane-wave ultrasound imaging system in Section 5.4. Finally, a system design for the optical generation of angled plane waves, which can be integrated into the FP scanner system and thus enable angle compounding, is presented and shown to be feasible in Section 5.5.

5.2 Frequency compounding

In Section 5.2.1 the frequency compounding method, distinguishing coherent and incoherent compounding, is described. In Section 5.2.2 we demonstrate for a simulated broadband ultrasound system that incoherent frequency compounding improves contrast, and that coherent frequency compounding is equivalent to filtering with the compound filter. In Section 5.2.3 the frequency compounding method used on the experimental data obtained from imaging an agar-based tissue mimicking phantom (Section 3.4.2) is detailed, and different types of compounding are compared in regard to their image quality improvement.

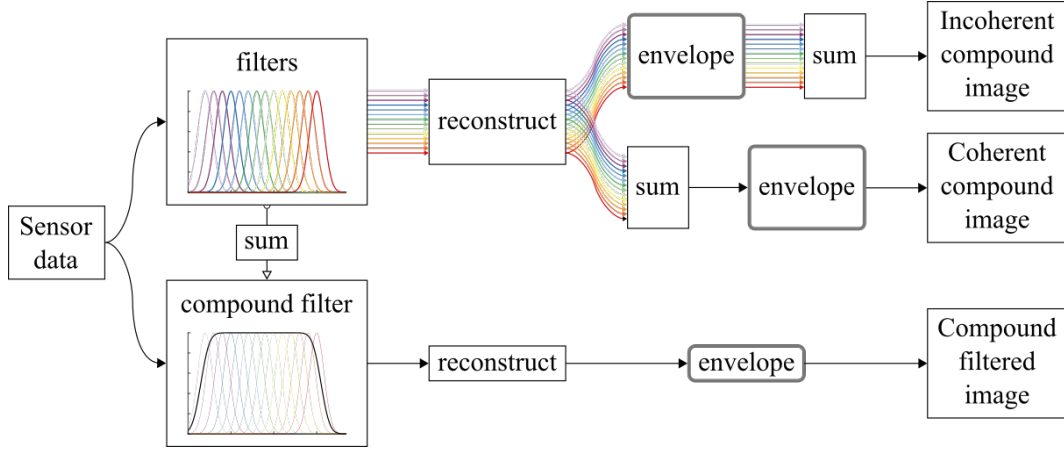


Figure 5.1: Flowchart of processing steps to obtain coherent and incoherent compound image, and compound filtered image. Steps include frequency filtering, image reconstruction, envelope detection, and the summation of images or frequency filters. The compound filter is the sum of all sub-band frequency filters.

5.2.1 Coherent vs incoherent compounding

Compounding method. Sensor data obtained from simulations of broadband plane-wave ultrasound imaging and from imaging experiments in Section 3.4.2 were used to demonstrate frequency compounding. The sensor data was filtered using Gaussian frequency filters with a given set of centre frequencies and bandwidths. Each frequency filter was applied in frequency space, i.e. the sensor data was Fourier transformed along the time axis, convolved with the frequency filter, and then inverse Fourier transformed along the time axis. Then, for each filtered sensor data set, the reconstruction algorithm was applied (Section 3.2.3) to obtain an image before applying envelope detection, here referred to as “raw image”. A coherent compound image was obtained by summing the raw images and then applying an envelope detection on the summed image, while an incoherent compound image was obtained by individually applying envelope detection to the raw images and then summing them, see Fig. 5.1.

Coherent compounding. In coherent frequency compounding, images are first reconstructed without applying envelope detection, before being summed. Since image reconstruction (excluding envelope detection) and summing are both linear operations, the order in which they are applied should not make a difference.

Coherent frequency compounding should therefore be equivalent to summing the individually frequency filtered sensor data sets before reconstructing an image using the summed sensor data. This, in turn should be equivalent to filtering with a “compound” frequency filter made up of all the frequency sub-band filters used in compounding summed together, see Fig. 5.1. The effect of coherent frequency compounding will thus depend on which frequencies are included in the compound filter, and how spatially well-sampled they are with regards to providing contrast. For example, when coherently compounding with a series of narrowband filters with a range of low centre frequencies, we expect this to be equivalent to low-pass filtering, and thus reduce the resolution and improve the contrast.

Incoherent compounding. In incoherent frequency compounding, images are first reconstructed with envelope detection applied, before being summed. Since envelope detection is a non-linear operation, the equivalence of the compound image and filtering with the compound filter which holds for coherent compounding does not apply to incoherent compounding. During incoherent compounding, the individual envelope-detected images will have established a speckle pattern and artefacts, such as grating lobes, before being compounded. The speckle patterns of more narrowband frequency filtered images have different grain sizes and positions depending on the frequency, and will smooth out when summing over images with a range of centre frequencies. The position of grating lobe artefacts is also dependent on the centre frequency as shown in Section 4.5.3. When compounding incoherently we thus expect speckle and grating lobes to average out, while the main reconstructed feature remains in the same position. The variation in the image intensity distribution in a scattering region should then decrease while maintaining its mean value, and specular objects should be displayed correctly. We would therefore expect no improvement in the scattering SNR, and an increase in the scattering CNR and the specular SNR.

5.2.2 Frequency compounding with simulated data

In this section, the concept of frequency compounding is tested on broadband simulated data without noise. This was done to ensure the frequency compounding method works as expected and discussed in the previous section, before moving on to applying frequency compounding to experimental data in the next section.

Simulation method. Sensor data was generated using the simulation platform from Chapter 4, with the random scattering medium and a non-scattering circular inclusion as the phantom (Section 4.3.1). The Gaussian frequency filters used had centre frequencies ranging from 1 to 10 MHz in 1 MHz steps, and a bandwidth of 2 MHz. The bandwidth of 2 MHz and step of 1 MHz were deliberately chosen to ensure that filters overlap at half maximum, such that the compound filter had a flat top. This way the filters had no bias towards any frequency band, or in other words, each frequency from 1 to 10 MHz was “equally used”. An incoherent and coherent compound image were generated using the compounding method described in Section 5.2.1. An image from the broadband sensor data filtered with the compound filter was generated to allow comparison with the coherent compound image.

Results. In the unfiltered image the hole feature was almost invisible, see Fig. 5.2a, which was expected, since as mentioned in Section 4.3.2, low-pass filtering with a bandwidth of 20 MHz was necessary to give an image with some contrast. Both coherent and incoherent compound image show an improvement in the scattering CNR, see Fig. 5.2b-c. The grain in the incoherent compound image is smoothed out compared to the unfiltered or coherently compounded image. The image obtained from reconstructing the sensor data filtered with the compound filter (Fig. 5.2d) was identical to the coherent compound image (Fig. 5.2c). This was verified by normalising the coherent compound image and the compound filter image and taking the difference between them, see Fig. 5.2e. This was expected since all the steps in coherent compounding, before applying envelope detection, are linear, so the coherent compound image should be identical to the compound filter image. The deviations from zero in the difference image are small (on the order of 10^{-6} less than the

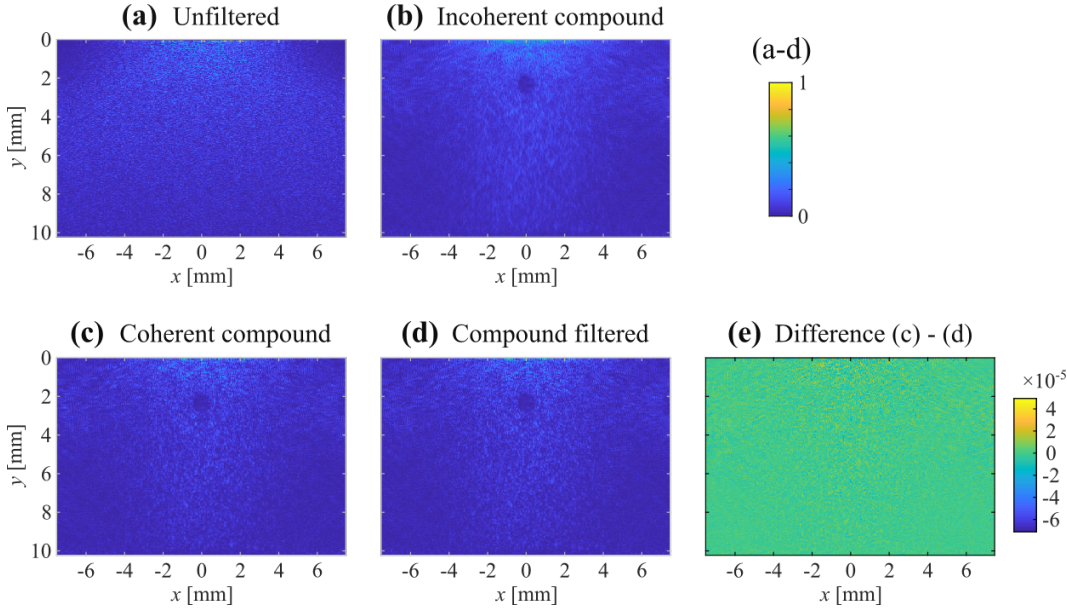


Figure 5.2: Comparison of simulated frequency compounded images. (a) Unfiltered image (22 MHz, -3dB), (b) incoherent compound image, (c) coherent compound image, (d) compound filtered image. All images were individually normalised. (e) Normalised difference between coherent compound image and compound filtered image. Compounding was carried out with Gaussian frequency filters with centre frequencies ranging from 1 to 10 MHz in steps of 1 MHz, and with a bandwidth of 2 MHz.

image) and can be attributed to floating point errors.

Conclusion. We have shown that frequency compounding improves scattering CNR when applied to broadband simulated sensor data. In the incoherent compound image this is achieved by smoothing out the grain in the image. The coherent compound image was shown to be identical to the compound filter image. The contrast improvement in the coherent compound image is therefore due to filtering out of the higher undersampled frequencies above 10 MHz. Coherent frequency compounding thus provides no benefit over simply low-pass filtering to avoid spatial aliasing.

5.2.3 Frequency compounding with FP scanner data

In the previous section it was shown that frequency compounding improves contrast when applied to broadband simulated data without noise. A good experimental data set from imaging an agar-based tissue mimicking phantom was acquired with the

FP scanner (Section 3.4.2), where the frequency compounding method used to obtain the final image was briefly described. In this section, frequency compounding will be explored in more depth using the same data set. The reasoning behind the choices of frequency filters is explained in Section 5.2.3.1. The effect of different compounding methods, i.e. coherent vs incoherent, as well as the effect of the bandwidth of the frequency filters used for compounding will be explored in Section 5.2.3.2.

5.2.3.1 Choosing frequency bands for compounding

The aim of the work in this section was to produce an image of the agar-based tissue mimicking phantom with higher contrast than the unfiltered image. First, the image quality metrics which includes contrast were defined for the agar-based tissue mimicking image. To determine which frequency filters are best to use for compounding, an exhaustive search of filters with a range of centre frequencies and bandwidths was done and thresholds for the image quality metrics defined. Frequency filtered images satisfying the thresholds were compounded to show the improvement in contrast.

Image quality definition. Image quality metrics are defined to provide a measure of how distinguishable the hole region, the surrounding scattering medium, and the features at the top and bottom boundary of the hole are. To do so, ROIs were defined for each of the three areas or features, see Fig. 5.3a. The image quality metrics were calculated as follows:

$$\begin{aligned} \text{Specular SNR} &= \frac{\mu_{\text{peaks}}}{\mu_{\text{hole}}} \\ \text{Scattering SNR} &= \frac{\mu_{\text{medium}}}{\mu_{\text{hole}}} \\ \text{Scattering CNR} &= \frac{\mu_{\text{medium}} - \mu_{\text{hole}}}{\sigma_{\text{medium}} + \sigma_{\text{hole}}} \end{aligned} \quad (5.1)$$

where μ_{peaks} is the mean peak intensity of the top and bottom features of the hole, and μ_{hole} , σ_{hole} , μ_{medium} and σ_{medium} are the mean and standard deviation of the intensity distributions in the hole and scattering medium ROIs, respectively, see

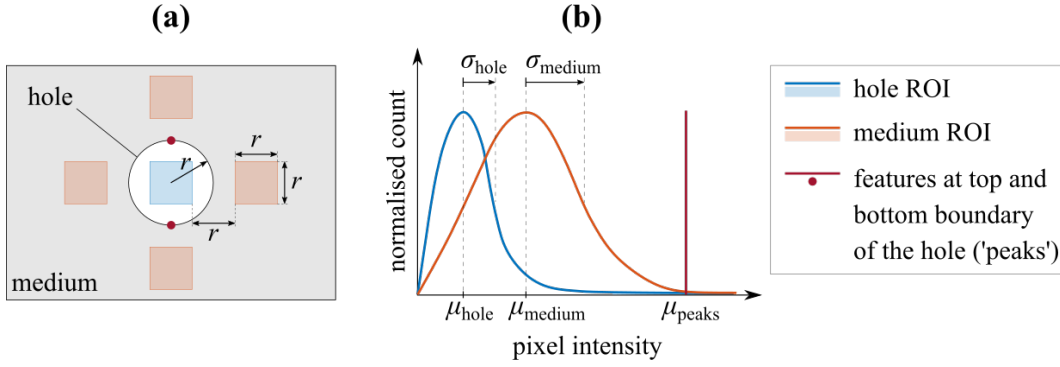


Figure 5.3: Definition of image quality metrics for the agar-based tissue mimicking phantom. (a) Schematic of the image with ROIs defined for the hole, the surrounding scattering medium, and the features at the top and bottom boundary of the hole. (b) Intensity distributions for each ROI, used to calculate means and standard deviations. Specular SNR, scattering SNR and CNR are defined in Eq. (5.1).

Fig. 5.3b. Note, that the image quality definitions for the hole and the surrounding scattering medium are identical to those defined in Section 4.4.3. Thus, the specular SNR is a measure of how much the features at the top and bottom boundary of the hole stand out from the hole. The scattering SNR is a measure of how different the hole and medium regions are on average. The scattering CNR is a measure of how distinguishable the hole and medium regions are from one another, taking into account the width of the intensity distributions. The hole is considered distinguishable for a scattering CNR of above 1.

Frequency dependent image quality. The method to determine which frequency bands to use for compounding is equivalent to the one used to obtain frequency-dependent image quality maps in Section 4.4. Gaussian frequency filters were applied to the sensor data before reconstructing the images. The filters had centre frequencies from 1 to 35 MHz and bandwidths from 1 to 40 MHz. For each filtered sensor data set an image was reconstructed and the image quality metrics, as defined in Eq. (5.1), were determined and presented as 2D maps as a function of centre frequency and bandwidth, see Fig. 5.4. For each metric, a minimum threshold was defined: specular SNR > 6 , scattering SNR > 1.25 , and scattering CNR > 0.9 . Satisfying at least one of the thresholds the image quality was considered to be ‘good enough’. This was done to narrow down the range of frequency filters that

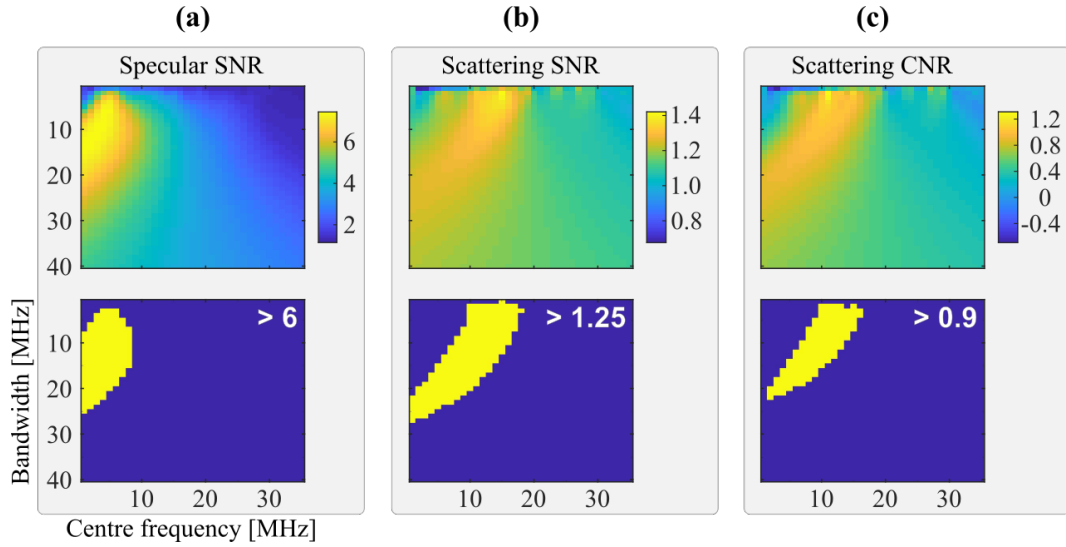


Figure 5.4: Frequency dependent image quality maps for (a) specular SNR, (b) scattering SNR and (c) scattering CNR in an agar-based tissue mimicking phantom from data acquired in Fig. 3.20. Maps of thresholded image quality metrics shown below.

are considered to give a good quality image and can be used for compounding, see Fig. 5.4.

Incoherent compounding. All images that satisfied at least one of the thresholds were incoherently compounded, see Fig. 5.5b. Compared to the unfiltered image (Fig. 5.5a), this significantly improved the scattering CNR to a value well above 1, while also improving specular SNR and scattering SNR. Since this was a rather brute force attempt to improve the image quality, the choice of filters used in compounding was further narrowed down. For example, we could only compound those images considered good enough, i.e. satisfying at least one threshold, that have the same bandwidth. In this case, we chose 10 MHz as the bandwidth as it gave the most images with continuous centre frequencies from 2 to 15 MHz that satisfied at least one threshold. The 10-MHz compound, see Fig. 5.5c, was able to improve the image quality compared to the unfiltered image (Fig. 5.5a). Crucially, the scattering CNR is above 1, which means the hole is more easily visible as the intensity distributions are distinguishable.

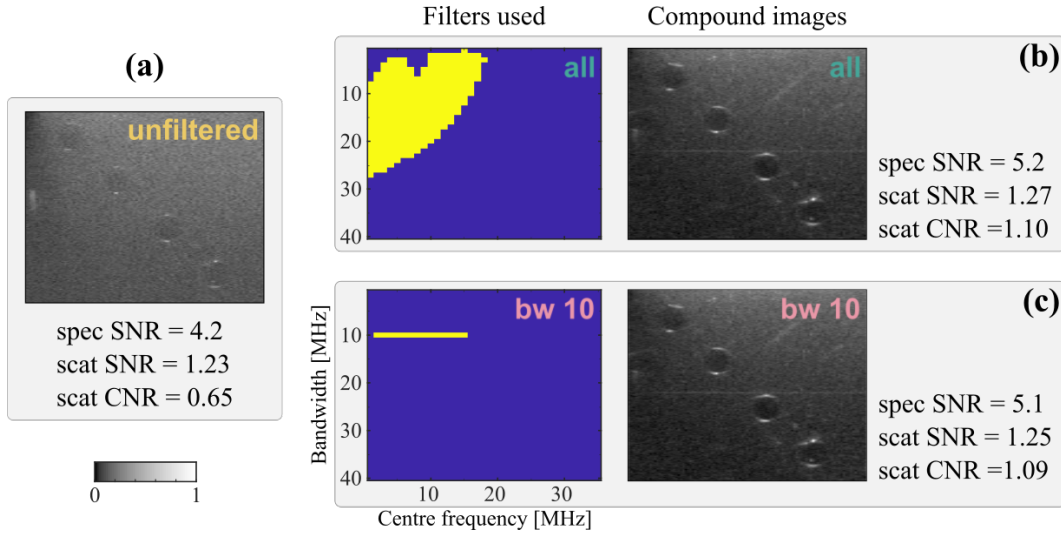


Figure 5.5: Comparison of frequency compounded images from experimental data. (a) Unfiltered image, and incoherent compound images using (b) all frequency sub-band filtered images that satisfy at least one threshold, and (c) only using 10 MHz bandwidth images that satisfy at least one threshold. Images were individually normalised and displayed with the same colour bar (grey scale brightened with *brighten(0.5)* in MATLAB)

5.2.3.2 Comparing compound methods

In this section, the different effects of coherent and incoherent compounding and the effect of the filter bandwidth on the image quality in the final compounded image are discussed.

Method. The sensor data from imaging the agar phantom was filtered with a series of filters with centre frequencies from 2 to 15 MHz and a bandwidth of either 2 MHz or 10 MHz. This was followed by either incoherent or coherent compounding. In addition to the image quality metrics defined above, the size of the feature at the top boundary of the hole was measured by taking profiles through the maximum intensity point of the feature in the axial and lateral directions, and determining the FWHM. It is important to note that the size of the feature is not a direct measure of the resolution performance, since the feature is likely made up of multiple scatterers, particularly in the lateral direction. Nonetheless, the size of the feature can be used as an indicator of the resolution performance, as both lateral and axial dimensions of the feature scale with the resolution performance. The FWHM was measured without removing the background intensity in the profile, which means

the measured value is likely an overestimate of the actual size. However, since the same was done for all images and we are only interested in image quality trends rather than absolute values, this approach should be sufficient.

Comparison. The unfiltered image was compared with the coherent and incoherent frequency compound images with narrowband or broadband filters, see Fig. 5.6. A coherent compound image is identical to the image reconstructed from sensor data filtered with the compound filter. The narrowband coherent compound image (Fig. 5.6a) is therefore equivalent to a low-pass filtered image with a cut-off frequency of 10 MHz, and thus cuts out high frequencies that are undersampled and reduce contrast. Compared to the unfiltered image, a slight contrast improvement is observed, with the scattering CNR still below 1. At the same time, however, some resolution performance was lost due to the loss of the high frequencies compared to the broadband unfiltered image. The broadband coherent compound image (Fig. 5.6b) is equivalent to a compound filtered image that is more broadband, i.e. includes higher frequencies than the narrowband coherent one (Fig. 5.6a). It suppresses some lower frequencies, peaks at 8.5 MHz and includes frequencies of up to 25 MHz. As a result, the resolution performance is largely unchanged compared to the unfiltered image, as the bandwidth was not reduced by much (Fig. 5.6c). There is a slight improvement in contrast since low frequencies with large speckle grain and thus poorer contrast are excluded, but again the scattering CNR remains below 1. The incoherent broadband compound (Fig. 5.6d) as seen before in Section 5.2.3.1 improved the scattering CNR to a value above 1, due to the averaging of frequency-dependent speckle grain and grating lobe artefacts. There is a slight decrease in resolution performance compared to the unfiltered image (Fig. 5.6c) as the broadband 10-MHz filters were less broadband than the full bandwidth, such that the individual filtered images had slightly lower resolution. When summing individual frequency sub-band images the final incoherently compounded image cannot have a higher resolution than the individual images. The incoherent narrowband compound image (Fig. 5.6e) showed the highest contrast improvement, with a scattering CNR of 1.22. This is because narrowband filters mostly included fre-

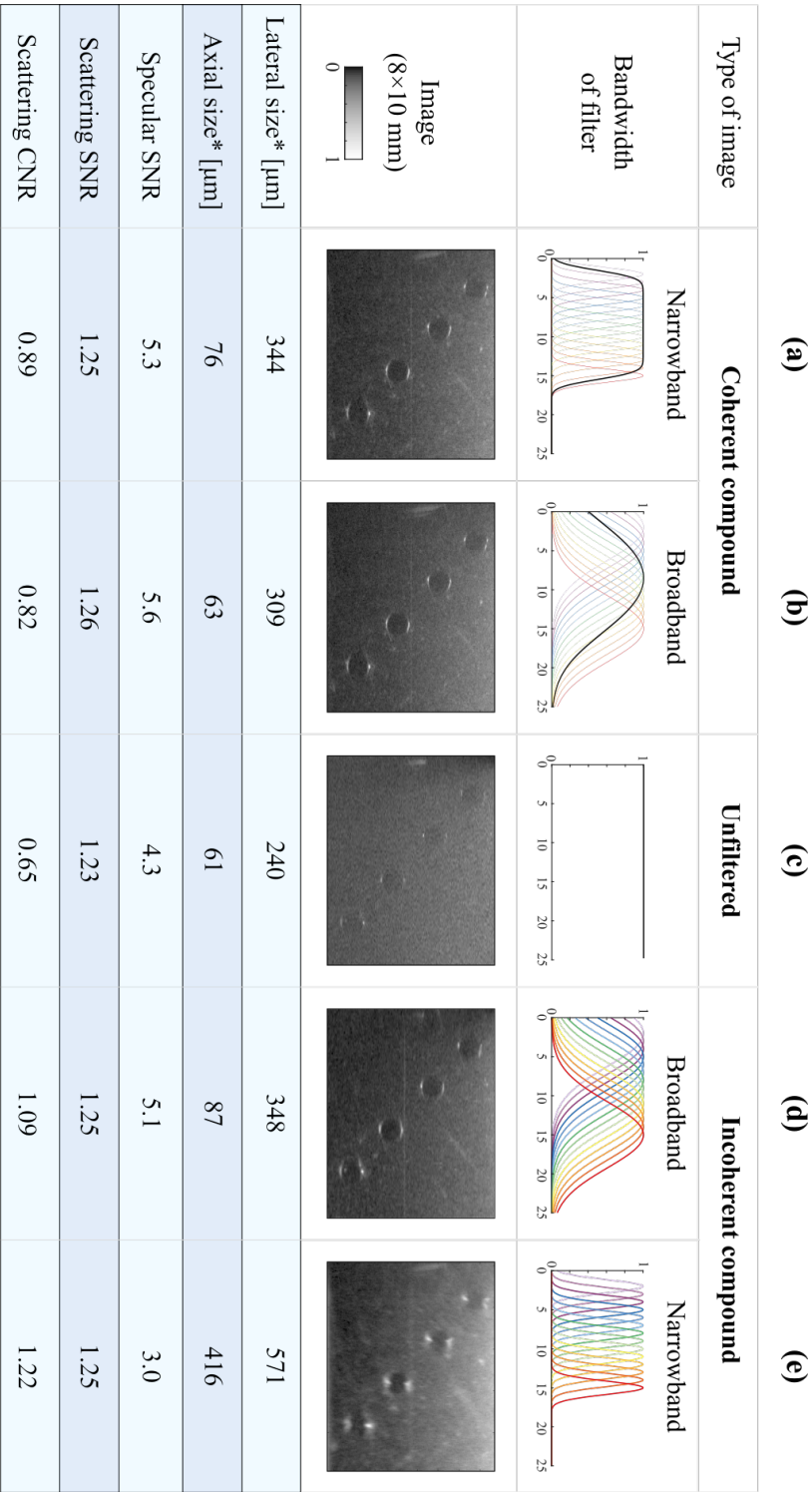


Figure 5.6: Comparison of coherently and incoherently frequency compounded images using narrowband (2 MHz) or broadband (10 MHz) frequency filters with centre frequencies ranging from 2 to 15 MHz. Coherent compound image using (a) narrowband and (b) broadband filters. (c) Unfiltered broadband image (−3 dB bandwidth of 22 MHz). Incoherent compound image using (d) narrowband and (e) broadband filters. Images were individually normalised and displayed with the same colour bar (grey scale brightened with *brighten(0.5)* in MATLAB).

quencies that were well spatially sampled and thus had no contrast reducing grating lobe artefacts resulting in good scattering SNR and CNR. However, there is a big trade off in the resolution performance, as it is drastically diminished compared to the unfiltered image (Fig. 5.6c) and even the broadband incoherent compound image (Fig. 5.6d). The reason for this is that in each individual frequency sub-band image, after applying envelope detection, the resolution is very low due to the narrow bandwidth of 2 MHz. Since the resolution cannot improve when summing incoherently, the incoherent compound has a similarly poor resolution.

Conclusion. The ideal frequency compounding method depends on what type of image is wanted. If the goal is to improve contrast, while still maintaining a high resolution, frequency compounding should be done incoherently with broadband filters. If resolution is not important, e.g. when imaging an object with no specular features, then frequency compounding incoherently with narrowband filters maximises the contrast improvement. Compounding coherently, with narrowband or broadband filters, is identical to frequency filtering, and can therefore have benefits in contrast improvement when filtering out higher, spatially undersampled frequencies. In practice, however, coherent frequency compounding does not offer any intrinsic advantage, as instead one can simply apply an equivalent low-pass filter, which is quicker and easier to do.

5.3 Angle compounding: reconstruction & methods

5.3.1 Derivation of the reconstruction algorithm

In this section, the equations for the reconstruction of an object function, in this case the scattering distribution, are derived for imaging with angled plane wave transmissions. The inverse problem was first solved by Norton and Linzer [72], and formulated by Cheng and Lu [65] for a general so-called limited-diffraction beam [116], of which a plane wave is a special case. The derivation described in this section has a slightly different approach and notation to Cheng and Lu. While Cheng and Lu started by writing down the transmit field and the receive response and convolved them to obtain the receive signal, we obtain the receive signal using a

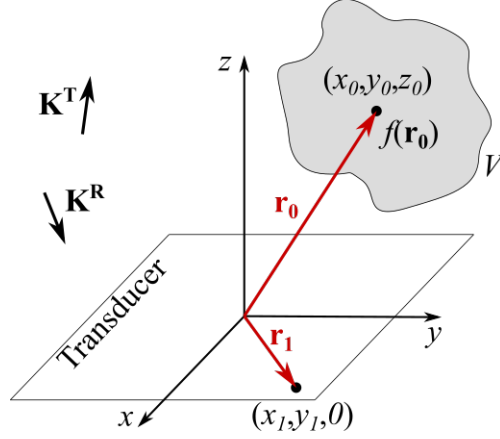


Figure 5.7: Schematic for imaging an object function $f(\mathbf{r}_0)$ contained within a volume V with the transducer located in the x - y plane. General transmit and receive wave vectors are represented by \mathbf{K}^T and \mathbf{K}^R , respectively.

Green's function approach, i.e. by convolving the object function with the Green's function. The result will be the same, but we believe this derivation to be more intuitive to understand. The reconstruction algorithm in the case of transmitting a normal plane wave was described in Section 3.2.3. Here, the equations and algorithm for the general case are derived (Section 5.3.1.1), before specifying conditions for an angled plane wave (Section 5.3.1.2).

5.3.1.1 Derivation for a general transmit field

Set-up. Let us consider an object function $f(\mathbf{r}_0)$ contained within a volume V , that is to be imaged, see Fig. 5.7. This object function could be the scattering strength, e.g. the density or compressibility of the object.

Transmit field. In this part, the expression of the transmit field as an integral over the temporal frequency will be determined. A single frequency plane wave with a given wave vector can be written as:

$$p(\mathbf{r}, t) = A e^{i(\mathbf{K}^T \cdot \mathbf{r} - \omega t)}$$

where ω is the temporal frequency and $\mathbf{K}^T = (k_x^T, k_y^T, k_z^T)$ is the transmit wavevector, and $|\mathbf{K}^T| = k = \frac{\omega}{c}$ and $k_z^T \geq 0$. A general broadband pressure field would be written

as:

$$p(\mathbf{r}, t) = \int_{k_x} \int_{k_y} \int_{\omega} A(\omega, k_x, k_y) e^{i(\mathbf{K}^T \cdot \mathbf{r} - \omega t)} d\omega dk_x dk_y$$

where the integral over ω allows for a broadband wave, while the integrals over k_x and k_y allow for wavevectors pointing in any direction. For the case of a broadband plane wave with a wavevector pointing in a given direction the pressure field can be written as:

$$p(\mathbf{r}, t) = \int_{\omega} A(\omega) e^{i(\mathbf{K}^T \cdot \mathbf{r} - \omega t)} d\omega \quad (5.2)$$

where $\mathbf{K}^T = \frac{\omega}{c} \hat{\mathbf{K}}^T$, and $\hat{\mathbf{K}}^T$ is the unit vector in the given direction of propagation. Note that $A(\omega)$ in Eq. (5.2) describes the frequency content of the pulse. Rewriting Eq. (5.2) using $\mathbf{K}^T = \frac{\omega}{c} \hat{\mathbf{K}}^T$ we get:

$$\begin{aligned} p(\mathbf{r}, t) &= \int_{\omega} A(\omega) e^{-i\omega(t - \frac{1}{c} \hat{\mathbf{K}}^T \cdot \mathbf{r})} d\omega \\ &= \int_{\omega} A(\omega) e^{-i\omega t'} d\omega \equiv \tilde{A}(t') \end{aligned} \quad (5.3)$$

where $t' = t - \frac{1}{c} \hat{\mathbf{K}}^T \cdot \mathbf{r}$. We recognise the right hand side in Eq. (5.3) as the Fourier transform of the frequency content $A(\omega)$ of the pulse, i.e. the temporal pulse shape $\tilde{A}(t')$. For example, a constant frequency spectrum $A(\omega)$ would correspond to a δ -function pulse at $t' = 0$, and a Gaussian frequency spectrum with centre frequency ω_c and bandwidth $\Delta\omega$ would correspond to an acoustic toneburst centred around $t' = 0$ with a pulse width of $\frac{2\pi}{\Delta\omega}$ and carrier frequency ω_c . In general, we can consider the acoustic pulse to be located at $t' = 0$.

Initial transmit field position. It is important to know the location of the plane wave at time $t = 0$, i.e. the time of generation, so that the pressure-time series measurement can be correctly triggered (or corrected for $t = 0$). According to our notation in Eq. (5.3), the pressure field at time $t = 0$ is given by

$$p(\mathbf{r}, 0) = \int_{\omega} A(\omega) e^{-i\omega(-\frac{1}{c} \hat{\mathbf{K}}^T \cdot \mathbf{r})} d\omega \equiv \tilde{A}\left(-\frac{1}{c} \hat{\mathbf{K}}^T \cdot \mathbf{r}\right) \quad (5.4)$$

Since we consider the pulse $\tilde{A}(t')$ to be located at $t' = 0$, Eq. (5.4) is equivalent to saying that at time $t = 0$ the pulse is located at \mathbf{r} given by $\hat{\mathbf{K}}^T \cdot \mathbf{r} = 0$. At time $t = 0$, the generated wave can thus be described as a plane wave across the origin and perpendicular to the unit wave vector $\hat{\mathbf{K}}^T$.

Propagation to a single point scatterer. Let us now consider a single point scatterer at coordinates $\mathbf{r}_0 = (x_0, y_0, z_0)$. The transmit plane wave, described in Eqs. (5.2) and (5.3), will reach the point scatterer at \mathbf{r}_0 with a time delay τ , i.e. the time when the $(t' = 0)$ -point of the pulse hits the point scatterer. By definition, the field at \mathbf{r}_0 at time τ can thus be written as $p(\mathbf{r}_0, \tau) = \tilde{A}(0)$. From Eq. (5.3) the time delay can be deduced as

$$0 = \tau - \frac{1}{c} \hat{\mathbf{K}}^T \cdot \mathbf{r}_0$$

and thus

$$\tau(\mathbf{r}_0) = \frac{\mathbf{K}^T \cdot \mathbf{r}_0}{\omega} \quad (5.5)$$

Note that $\tau(\mathbf{r}_0)$ is independent of the temporal frequency ω of the transmit wave.

Signal from a single point scatterer. The point scatterer at \mathbf{r}_0 can be treated as an acoustic point source that emits at time $t = \tau(\mathbf{r}_0)$ with the field strength scaled by the object function $f(\mathbf{r}_0)$. The field emitted by a point source is described by the Green's function of the free-space wave equation. Thus the field scattered from the point scatterer at \mathbf{r}_0 and measured at a point $\mathbf{r}_1 = (x_1, y_1, 0)$ on the sensor array is given by

$$p^{(\text{one})}(x_1, y_1, t) = f(\mathbf{r}_0) \cdot G(\mathbf{r}_0 - \mathbf{r}_1, t - \tau) \quad (5.6)$$

where (one) indicates that the field is scattered from a single point scatterer, and

$$G(\mathbf{r}_0 - \mathbf{r}_1, t - \tau) = (\text{const}) \int_{k_x} \int_{k_y} \int_{\omega} \frac{1}{k_z} e^{i\mathbf{K}^R \cdot (\mathbf{r}_0 - \mathbf{r}_1)} e^{-i\omega(t - \tau)} d\omega dk_y dk_x \quad (5.7)$$

where $\mathbf{K}^R = (k_x, k_y, k_z)$ is the receive wave vector with $|\mathbf{K}^R| = k = \frac{\omega}{c}$ and $k_z \geq 0$. Using Eq. (5.5) for the time delay $\tau(\mathbf{r}_0)$, the Green's function in Eq. (5.7) can be

rewritten as

$$G(\mathbf{r}_0 - \mathbf{r}_1, t - \tau) = (\text{const}) \int_{k_x} \int_{k_y} \int_{\omega} \frac{1}{k_z} e^{i\mathbf{K}' \cdot \mathbf{r}_0} e^{-i\mathbf{K}^R \cdot \mathbf{r}_1} e^{-i\omega t} d\omega dk_y dk_x \quad (5.8)$$

where $\mathbf{K}' = (\mathbf{K}^R + \mathbf{K}^T)$.

Signal from the whole volume. We will assume that the imaging system is linear and that scattering is weak such that multiple scattering can be ignored (Born approximation). Then, the received signal from all point scatterers within the volume V is a linear superposition of the received signal from all the individual point scatterers. Mathematically this is equivalent to integrating the single point scatterer signal from Eq. (5.6) over the volume V :

$$p(x_1, y_1, t) = \int_V f(\mathbf{r}_0) \cdot G(\mathbf{r}_0 - \mathbf{r}_1, t - \tau) d^3 \mathbf{r}_0 \quad (5.9)$$

and substituting the Green's function from Eq. (5.8) into Eq. (5.9) gives

$$p(x_1, y_1, t) = (\text{const}) \int_{k_x} \int_{k_y} \int_{\omega} \frac{1}{k_z} \left[\int_V f(\mathbf{r}_0) e^{i\mathbf{K}' \cdot \mathbf{r}_0} d^3 \mathbf{r}_0 \right] e^{-i\mathbf{K}^R \cdot \mathbf{r}_1} e^{-i\omega t} d\omega dk_y dk_x \quad (5.10)$$

We recognise the term in square brackets as the 3D spatial Fourier transform $F(\mathbf{K}')$ of the object function $f(\mathbf{r}_0)$ into the object k -space defined by $\mathbf{K}' = (k'_x, k'_y, k'_z)$. Substituting $\mathbf{K}^R \cdot \mathbf{r}_1 = k_x x_1 + k_y y_1$, Eq. (5.10) can be rewritten as

$$p(x_1, y_1, t) = (\text{const}) \int_{k_x} \int_{k_y} \int_{\omega} \frac{1}{k_z} F(\mathbf{K}') e^{-i(k_x x_1 + k_y y_1 + \omega t)} d\omega dk_y dk_x \quad (5.11)$$

Taking the 3D Fourier transform of Eq. (5.11) with respect to the aperture (x_1, y_1) and time t gives

$$P(k_x, k_y, \omega) = (\text{const}) \frac{1}{k_z} F(k'_x, k'_y, k'_z)$$

which rearranges to

$$F(k'_x, k'_y, k'_z) = (\text{const}) k_z P(k_x, k_y, \omega) \quad (5.12)$$

Equation (5.12) is a key result, as it links the 3D Fourier transform of the receive data $p(x_1, y_1, t)$, i.e. what is measured, to the 3D Fourier transform of the object function $f(x_0, y_0, z_0)$, i.e. the objective of the reconstruction.

***K*-space transformation.** It is important to note that the receive data is Fourier transformed into the receive k -space defined by $(k_x, k_y, k = \frac{\omega}{c})$, while the object function is Fourier transformed into the object k -space defined by (k'_x, k'_y, k'_z) . The receive k -space corresponds to the received pressure time-series data on a (usually) evenly spaced (x, y, ct) -grid, and the object k -space corresponds to the evenly spaced (x', y', z') -grid of the reconstructed image. To fully evaluate Eq. (5.12) in practice, we thus need to perform a mapping between the object and receive k -spaces, in general given by:

$$\begin{cases} k'_x = k_x + k_x^T \\ k'_y = k_y + k_y^T \\ k'_z = k_z + k_z^T = \sqrt{k^2 - k_x^2 - k_y^2} + \sqrt{k^2 - (k_x^T)^2 - (k_y^T)^2} \geq 0 \end{cases} \quad (5.13)$$

The requirement for $k'_z \geq 0$ is imposed to remove evanescent waves and only include propagating waves in the reconstruction.

Summary of steps. The pipeline for reconstructing an image of the object function $f(\mathbf{r}_0)$ can be summarised as follows:

1. Measure the acoustic pressure time series $p(x_1, y_1, t)$ over an aperture.
2. Apply a Fourier transform to $p(x_1, y_1, t)$ with respect to the aperture and time to obtain $P(k_x, k_y, \omega)$.
3. Multiply $P(k_x, k_y, \omega)$ with a scaling factor k_z [Eq. (5.12)] to obtain

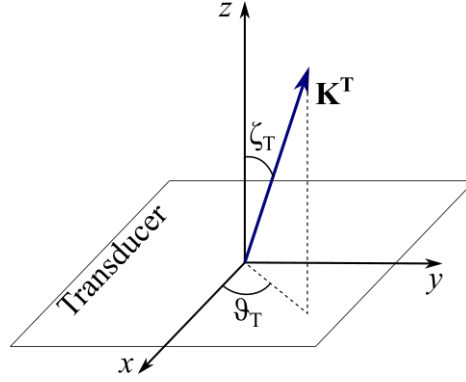


Figure 5.8: Transmit wave vector of a steered plane wave in 3D defined by steering angle ζ_T and rotation angle θ_T .

$$F(k_x, k_y, \omega).$$

4. Map $F(k_x, k_y, \omega)$ from the receive k -space to the object k -space [Eq. (5.13)] to obtain $F(k'_x, k'_y, k'_z)$.
5. Apply an inverse Fourier transform to $F(k'_x, k'_y, k'_z)$ to obtain the object function $f(x_0, y_0, z_0)$.

5.3.1.2 Special cases

For all cases of reflection ultrasound imaging, and interestingly also photoacoustic tomography, the Green's function takes the same form (with the factor of $\frac{1}{k_z}$). The only difference in the derivation is in the transmission wave vector \mathbf{K}^T and consequently the time delay τ and the object k -space vector \mathbf{K}' . The k -space mapping from Eq. (5.13) is thus the only step that will differ between modalities.

Angled plane wave. For a general steered plane wave we can define two angles: the steering angle ζ_T as the angle between the normal of the plane wave and the z -axis, and the angle θ_T as the angle of rotation in the x - y plane, see Fig. 5.8.

The transmit wave vector components can then be written as

$$\begin{cases} k_x^T = k \sin \zeta_T \cos \theta_T \\ k_y^T = k \sin \zeta_T \sin \theta_T \\ k_z^T = k \cos \zeta_T \end{cases} \quad (5.14)$$

With the transmit wave vector components defined in Eq. (5.14), the k -space mapping from Eq. (5.13) can be rewritten for the case of a steered plane wave as

$$\begin{cases} k'_x = k_x + k \sin \zeta_T \cos \theta_T \\ k'_y = k_y + k \sin \zeta_T \sin \theta_T \\ k'_z = \sqrt{k^2 - k_x^2 - k_y^2} + k \cos \zeta_T \geq 0 \end{cases} \quad (5.15)$$

Normal plane wave. This case is equivalent to the general angled plane wave case discussed above with the steering angle ζ_T set to 0. The transmit wave vector can then be simply written as $\mathbf{K}^T = (0, 0, k)$. The k -space mapping simplifies to:

$$\begin{cases} k'_x = k_x \\ k'_y = k_y \\ k'_z = \sqrt{k^2 - k_x^2 - k_y^2} + k \geq 0 \end{cases} \quad (5.16)$$

Photoacoustic tomography. In this case, there is no time delay in the generation of Green's function point source responses, which can be interpreted as the transmit wave vector being $\mathbf{K}^T = 0$. The receive and object k -spaces are identical, i.e. $\mathbf{K}' = \mathbf{K}^R$. However, a k -space mapping (or resampling) step still needs to be performed, since the sensor data is measured with an evenly sampled (k_x, k_y, ω) grid, while the object function is displayed on an evenly sampled (k_x, k_y, k_z) grid.

5.3.2 Data processing, reconstruction & compounding methods

This section describes the methods used for data processing before reconstruction and compounding after reconstruction.

Plane wave fit. In order to reconstruct an image, it is necessary to know the steering angle ζ_T and the rotation angle θ_T of the transmitted plane wave. To obtain these, the time of arrival (TOA) of the wavefront, i.e. the peak signal, at each sensor point was extracted from the sensor data. A plane (or a line in 2D) was fitted to the TOA of the wavefront using only the central part of the sensor data, since for some larger steering angles, part of the plane wave towards the edge of the imaging area was generated behind the sensor, see Fig. 5.9. For a plane wave in 2D it can be shown that the slope angle α of the wavefront's TOA in the sensor data and the steering angle ζ_T of the plane wave are related by:

$$\sin \zeta_T = \tan \alpha \quad (5.17)$$

The steering angle ζ_T can thus be calculated using the slope of the planar fit to the wavefront's TOA in the sensor data. For a plane wave in 3D, the steering angle ζ_T and rotation angle θ_T can be calculated using the relations:

$$\begin{cases} \tan \zeta_T = \sqrt{\tan^2 \alpha_x + \tan^2 \alpha_y} \\ \tan \theta_T = \frac{\tan \alpha_y}{\tan \alpha_x} \end{cases} \quad (5.18)$$

where α_x and α_y are the slope angles of the planar fit to the 3D TOA data along the x - and y -axes along the sensor.

Remove backwards propagating plane wave from signal. A backwards propagating plane wave emitted by the source is detected by the sensor, and its contribution to the sensor signal needs to be removed to avoid strong artefacts in the image. In simulation, this was done by running a forward simulation with a non-scattering medium to obtain a set of sensor data that only contains the signal from the backwards propagating plane wave. This signal was then subtracted from the sensor

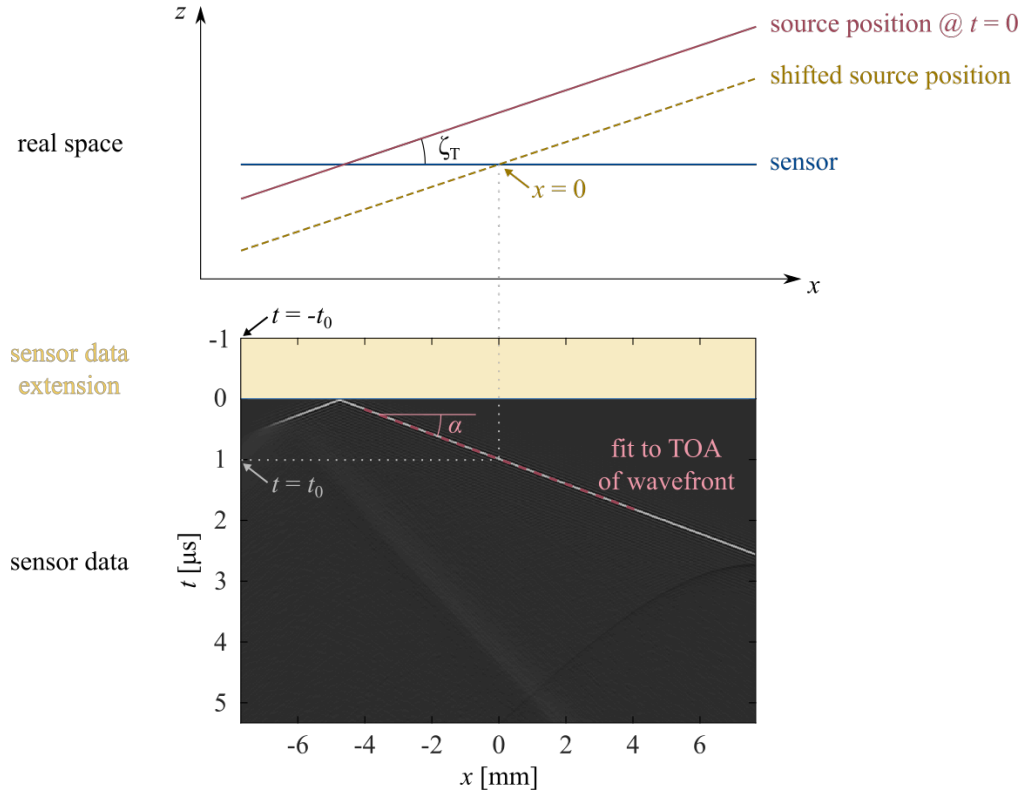


Figure 5.9: Visualisation of data processing methods for angled plane wave reconstruction in 2D. The steering angle ζ_T of the source (dark red) can be determined from the slope angle α of the time of arrival (TOA) of the wavefront in the sensor data (light red) using Eq. (5.17). The source position can be shifted *a posteriori* from its actual generation position at $t = 0$ (dark red) to a position where it intersects with the centre of the sensor at $x = 0$ (dark yellow) by extending the sensor data before $t = 0$ by an amount $t = t_0$ (light yellow), where t_0 is the TOA of the wavefront at the centre of the sensor (grey dotted line).

data acquired with the random scattering medium in place. In experimental data, the signal from the backwards propagating plane wave was removed by replacing the first few μs of data with zeros.

Compensate for source depth-offset. In both simulation and experimental demonstration, the centre of the source was offset from the sensor plane, to be able to rotate the source to a range of angles. The reconstruction algorithm for angled plane wave imaging derived in Section 5.3.1, however, requires the source to intersect with the centre of the sensor at time $t = 0$, i.e. the time at which the source is generated. To satisfy this requirement the sensor data was extended by some time before the measured $t = 0$, equal to the time it would take a plane wave to propagate from the

sensor to where it was actually generated. Conveniently, this time duration is equal to the time the plane wave was detected at the centre of the sensor, $t = t_0$ in Fig. 5.9, as this describes the same path of propagation only in the opposite direction. Thus, to shift the position of the planar source from its actual location of generation to a position where it intersects with the centre of the sensor, the sensor data was extended by a time duration of t_0 before $t = 0$, by adding zeros in front of the pressure time series, see Fig. 5.9.

Reconstruction. The reconstruction code for angled plane wave reflection imaging follows the step-by-step summary at the end of Section 5.3.1 with the k -space mapping in Eq. (5.15). For the k -space mapping, a new evenly-spaced object k -space grid is generated. This new grid needs to be at least as deep in the z -axis as the furthest object that could be imaged given the duration Δt of the acquisition. For photoacoustic tomography this depth is the same as the receive k -grid, i.e. $c\Delta t$, since there is no time delay in the photoacoustic signals being generated after excitation at $t = 0$. For normal plane wave reflection imaging the depth of the object grid only needs to be half as deep as the receive grid, i.e. $c\Delta t/2$. However, the image quality was found to benefit from making the object grid as deep along the z -axis as the receive grid, i.e. twice as deep as is theoretically necessary. Making the object grid twice as deep results in the corresponding object k -space grid being sampled twice as finely. The increase in the sampling in the object k -space allows for a more accurate mapping from the receive k -space to the object k -space, which ultimately improves the reconstruction and the final image quality. Doubling the depth of the object grid also results in a halving of the maximum k -space frequency that is supported by the object grid. This is not an issue, since that frequency is several orders of magnitude higher than the frequencies in the signal (order of GHz). We therefore chose to generate an object grid (x', y', z') as deep as the receive grid (x, y, ct) for reflection ultrasound imaging in both the normal and the angled case.

Compounding. In this work we only considered two simple compounding methods. Similar to the frequency compounding of Section 5.2, the compounding was

done either before applying envelope detection to the individual images obtained for different angles, i.e. coherent compounding, or after application of envelope detection to the individual images, i.e. incoherent compounding.

5.4 Broadband angle compounding in simulation

5.4.1 Simulation set-up

The simulation set-up for imaging with angled plane waves is largely based on the simulation platform for imaging with normal plane waves described in Section 4.3. In the following the key differences are described and explained.

Simulation grid. The simulations were run on a 2D grid with 384×265 grid points of $40 \times 40 \mu\text{m}$ size. As previously, this represents an approximately $15 \times 10 \text{ mm}$ area which is similar to the FP scanner's field of view. The grid size was increased from 10 to $40 \mu\text{m}$ to reduce the size of the grid and thus speed up the forward simulations. A grid size of $40 \mu\text{m}$ is still sufficient to fully support frequencies up to 18.75 MHz, i.e. most of the frequencies contained in the generated acoustic field (-3dB bandwidth of 22 MHz).

Medium. The medium was generated similarly to the random scattering phantom described in Section 4.3.1. The density of each grid point was randomly chosen from the range $1000 \pm 40 \text{ kg/m}^3$. Nine non-scattering circular regions with a diameter of 1.2 mm and a density of 1000 kg/m^3 were included in an evenly spaced 3×3 grid, see Fig. 5.10. The sound speed was uniformly set to 1500 m/s across the medium. A perfectly matched layer (PML) with a thickness of 20 grid points was included to absorb the acoustic field at the boundary of the simulation.

Source. The time varying pressure source had the same Gaussian profile, with a FWHM of 16 ns, as previously. Angled planar sources with steering angles from -20° to 20° were simulated. Since an angled planar source would be off-grid on a regular rectangular grid, the source needs to be represented by a number of on-grid source points located near the angled plane (or line in 2D). The pressure contributions from these on-grid source points when superimposed make up the desired

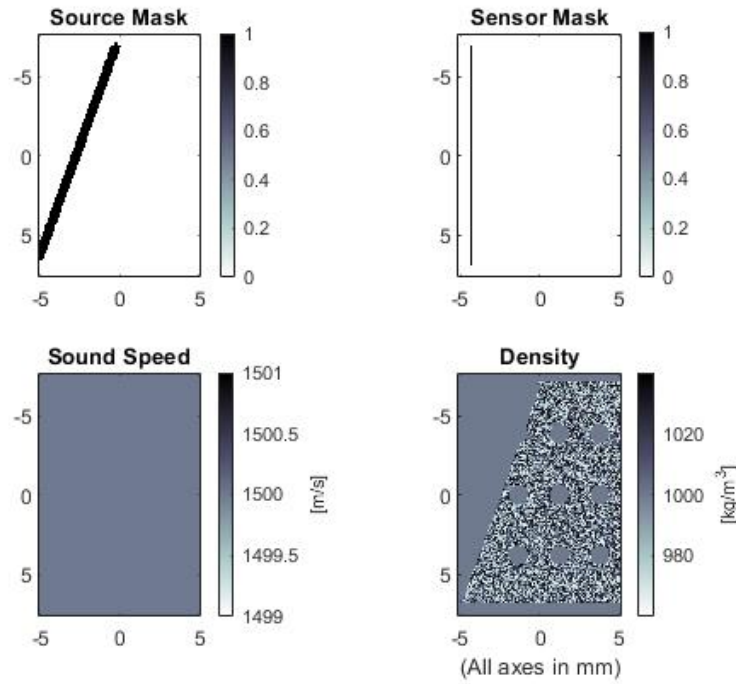


Figure 5.10: Simulation setup for 2D ultrasound imaging with an angled plane wave, including the angled source mask (here showing a 20° angled wave), the sensor mask, and the sound speed and density maps.

off-grid angled planar source. This was facilitated by the off-grid-sources package from *k-wave* [in development, unpublished], which is more accurate than representing the angled source as a stair-cased line on the grid. As a result, the source mask which includes all on-grid source points contributing to the off-grid source appears as a slightly wider line, see Fig. 5.10. The source was offset in depth by approximately 2 mm at the centre of the source to allow for the angled source to fit into the grid at all angles, without needing to expand the grid behind the sensor. This offset in depth also models the angled plane wave imaging setup used in an experimental demonstration in Section 5.5.3. The simulation therefore also tests the data processing methods used to compensate the depth-offset of the source.

Sensor. As before, the sensor was made up of individual sensor points placed at grid points along the x axis one grid point adjacent to the PML. The sensor points were equally spaced by $40\ \mu\text{m}$, i.e. as densely as the grid allows. Note that this means the scattered ultrasound field is spatially sampled sufficiently such that there

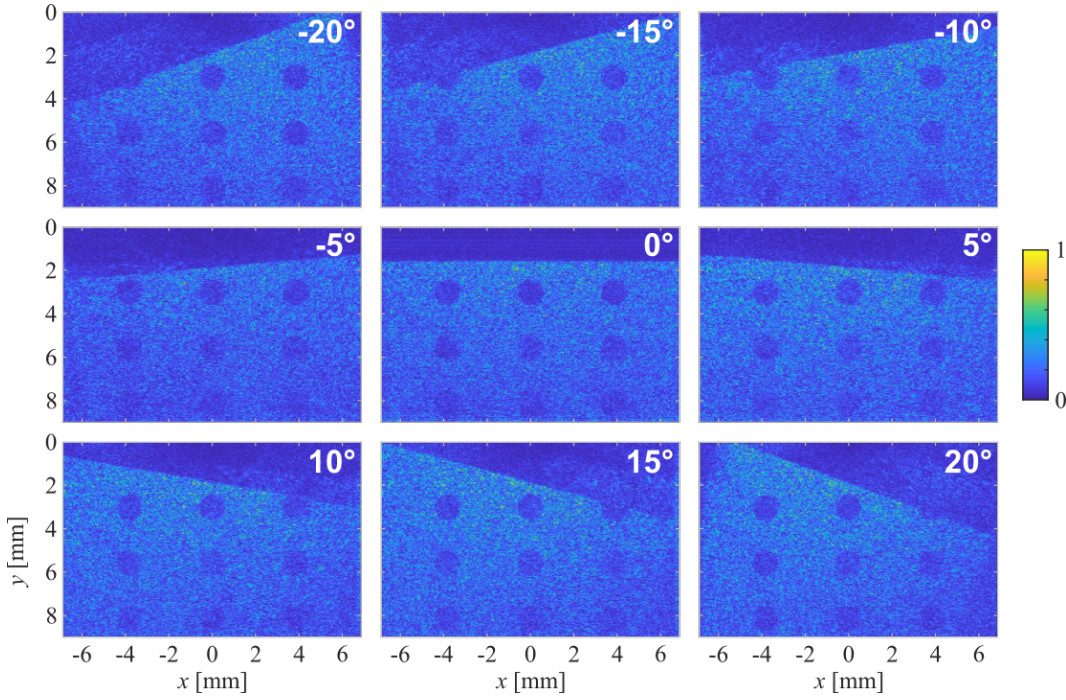


Figure 5.11: Images from the different single plane wave transmissions with steering angles from -20° to 20° . All images were individually normalised.

is no aliasing, as all frequencies that are supported by the grid are detected by the sensor. Due to the depth-offset of the source, some of the generated random scattering medium is located in between the source and the sensor. To avoid signals from forward scattered waves the medium between the source and the sensor was “removed” by setting the sound speed to 1500 m/s and the density to 1000 kg/m³.

Forward simulation. The forward simulation was run in MATLAB using a first-order k -space model [104].

Image quality. The image quality of the individual and compounded images is assessed with the same method as described in Section 4.3.1 to determine the scattering SNR and CNR for the middle hole in the first row closest to the sensor.

5.4.2 Compounding results

Individual images. Single angled plane wave ultrasound images with steering angles ranging from -20° to 20° in 1° steps were generated, see Fig. 5.11. The outline of the nine holes is visible in all 41 images (scattering SNR from 1.8-3.0), but with

low contrast (scattering CNR from 0.5-0.9). This means that the average of the intensity distributions in the hole region and the surrounding scattering region are distinct enough, but the distributions are wide due to the grain resulting in a low contrast. Also apparent in the images is the line marking the position of the source as the scattering medium was removed “behind” the source. As a result of this, the two holes in the first row closest to the sensor and on either side of the field of view have been cut off by some of the larger angled plane wave imaging simulations. This did not affect the quantitative data in this section as the image quality measurements are based on the middle hole in the first row. The line at depth 9 mm marks the end of the phantom in the simulation grid. The image grid goes beyond this as the timeseries was extended to make sure all scattering signals were received.

Compounding. Subsets of the 41 single plane wave images were compounded coherently and incoherently to obtain compounded images with a varying number of images. The maximum steering angle amplitude was either 5° , 10° or 20° , while the angle step size was either 1° , 2° , or 4° . The values for the angle parameters were deliberately chosen to generate compound images with the same number of single plane wave images compounded together, but with different spreads and steps in the steering angle. Note, that for a maximum angle amplitude of 5° and an angle step size of 4° an asymmetric spread of angles at -5° , -1° , and 3° was used. For all other configurations the transmission angles were distributed symmetrically.

Incoherent compound. The incoherently compounded images, see Fig. 5.12, look like smoothed out versions of the single plane wave images. This is because compounding after applying envelope detection averages the images causing the variation in intensity distribution to decrease in both the hole and scattering medium regions. The average in the intensity distributions, however, remain the same in the compound images as in the individual images. The scattering SNR therefore stays approximately the same (around 2.2), while the scattering CNR increases. The more images are compounded incoherently the more uniform the intensity distributions get, and the more the scattering CNR increases.

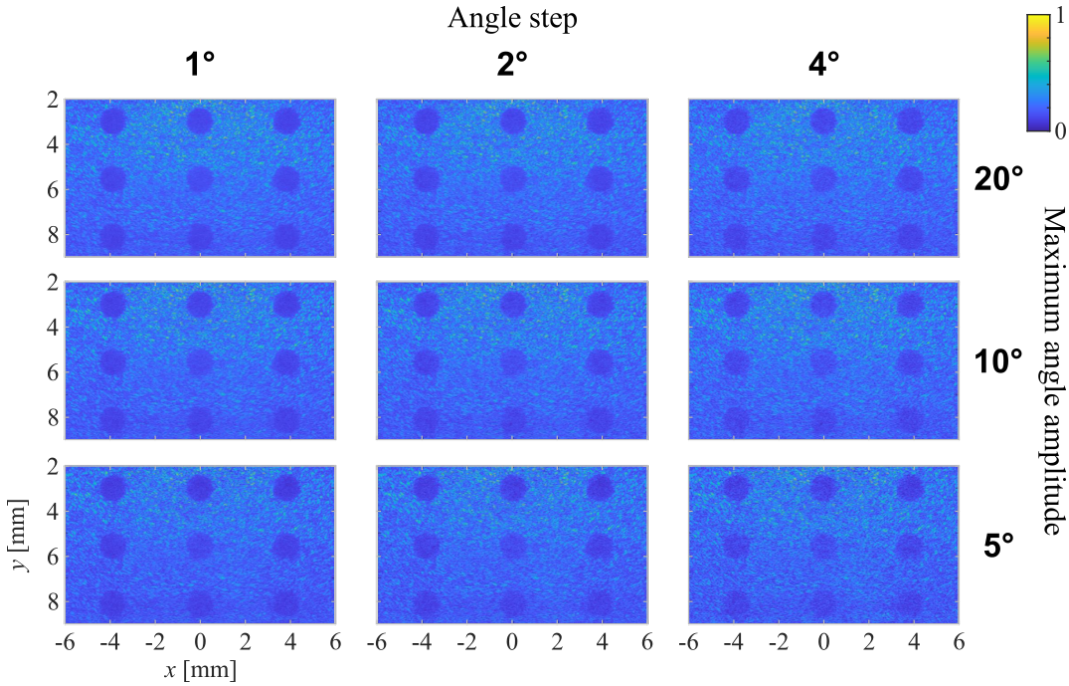


Figure 5.12: Simulated incoherent compound images from varying number of images with maximum steering angle amplitude of 5° , 10° or 20° , and angle step size of 1° , 2° , or 4° . All images were individually normalised.

Coherent compound. The coherently compounded images, see Fig. 5.13, show improvements in not only scattering CNR but also scattering SNR. Since compounding is done before application of envelope detection for coherent compound images, positive and negative image values are able to cancel out. As a result, the intensity distribution in the hole regions has decreased in its average intensity compared to the individual images. This portrays the scattering strength of the hole region more accurately, which should appear non-scattering, i.e. zero intensity, in a perfect image. The decrease in the average intensity in the hole leads to an increase in the scattering SNR. The more single plane wave images were compounded the bigger the improvement in scattering SNR and CNR.

Image quality quantified. The image quality improvement was quantified by determining the scattering SNR and CNR of the central hole nearest to the sensor for all individual and coherently and incoherently compounded images generated in this section, see Fig. 5.14. The image quality improvement trends described in the previous paragraphs can be observed in this graph: (i) Incoherent compound-

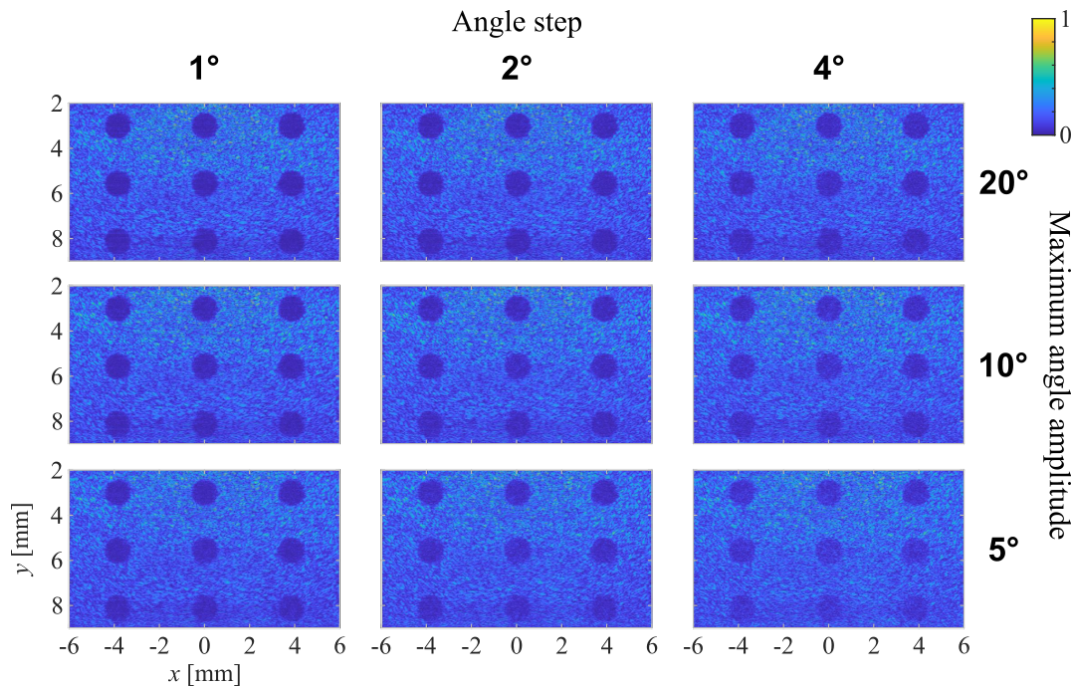


Figure 5.13: Simulated coherent compound images from varying number of images with maximum steering angle amplitude of 5°, 10° or 20°, and angle step size of 1°, 2°, or 4°. All images were individually normalised.

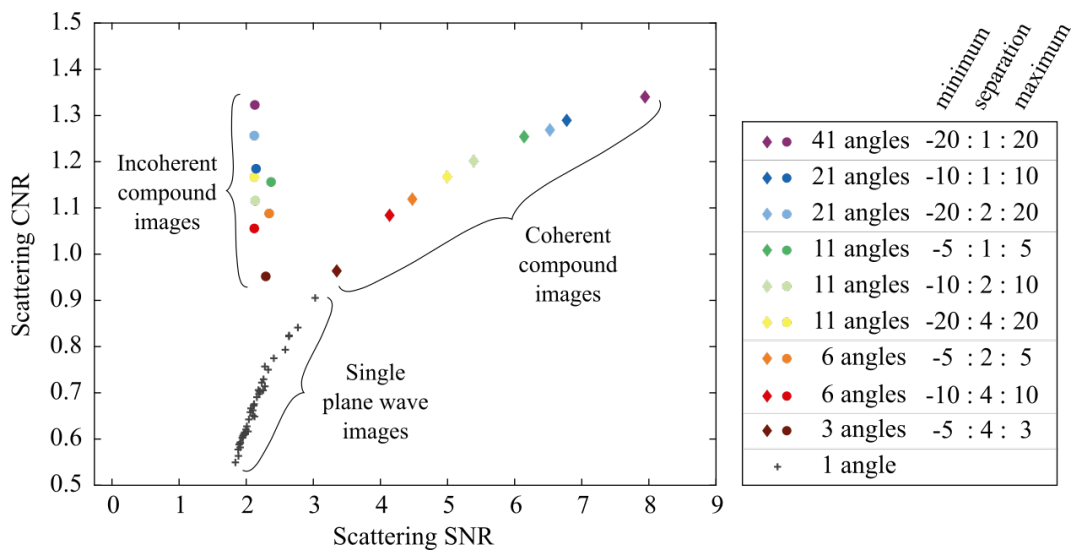


Figure 5.14: Image quality of all single plane wave, coherently compounded and incoherently compounded images.

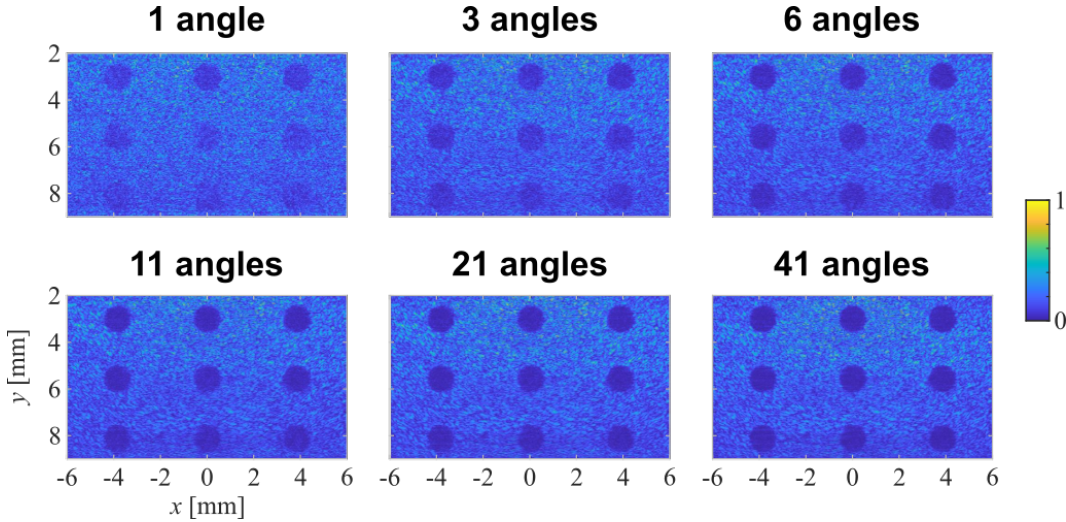


Figure 5.15: Coherent compound images with increasing number of transmission angles.

ing averages the scattering SNR while improving the scattering CNR. (ii) Coherent compounding improves both scattering SNR and CNR.

Number of angles. The more single plane wave images were compounded the bigger was the contrast improvement, see Fig. 5.14. This is visualised in Fig. 5.15 using a subset of the coherent compound images from Fig. 5.13 with different number of angles. This result is intuitive, as compounding of more angled plane waves results in a smaller synthetic transmit focus from which a better image quality is expected. The improvement seen in Fig. 5.15 resembles the one seen for conventional ultrasound images in Fig. 2.2 taken from Tanter and Fink [73]. While using a large number of angled plane wave transmissions improves the image quality, this also increases the total acquisition time of a compounded image. An important takeaway from Figs. 5.14 and 5.15 is therefore that a small number of angles was sufficient to significantly improve the contrast in a coherently compounded image. While most of the single plane wave images had a scattering CNR between 0.58 and 0.73, the coherently compounded image with three angles had a CNR of 0.96, and six angles yielded a CNR of 1.08 (the reader is reminded that a CNR of 1 means the intensity distributions of the hole and the surrounding scattering medium are considered distinguishable). This is a particularly important consideration given the FP scanner's long acquisition time for a single plane wave image. Since only few (between three

and six) single plane wave images are necessary to improve the CNR of a coherently compounded image to a value close to or above 1, the total acquisition time for the compounded image is kept to a minimum. The simulations did not include acoustic attenuation or instrument noise, which means that in practice a slightly higher number of angles may be necessary to achieve the same image quality improvements.

Spread of angles. One additional trend visible in Fig. 5.14 is that for coherent compound images with the same number of compounded images, a smaller spread of angles, i.e. a smaller maximum steering angle and consequently a smaller angle step size, yielded a better scattering SNR. For example, among the coherent compound images made up from 11 single plane wave images compounded together, the compound image with 5° maximum amplitude and 1° step has higher scattering SNR than the one with 10° maximum amplitude and 2° step which in turn has higher scattering SNR than the one with 20° maximum amplitude and 4° step. This suggests that the suppression of image artefacts within the hole region is improved when compounding with a smaller spread of angles separated by a smaller angle step. This is an interesting, counter-intuitive observation, as one would expect a coherent compound with a larger maximum steering angle to generate a smaller synthetic transmit focus. This should lead to the image of a point scatterer having a smaller reconstructed feature, i.e. a higher resolution. However, when compounding with a larger separation of angles, the artefacts from the individual single plane wave images may not cancel out as coherently as in the case of compounding with a smaller separation of angles. The increased amplitude of artefacts from single scatterers could then lead to a contrast reduction in the whole medium. It is important to note, that this trend was only observed for the 3 different spreads of angles used in these simulations and should therefore not be generalised or extrapolated to all angles. In particular, this trend breaks down in the limit of a 0° angle step, which would effectively be single plane wave imaging with a normal plane wave. This observation would need to be investigated further by testing more (and smaller) angle spread values, which could potentially reveal an optimal spread and step size.

Conclusion. Angle compounding was shown to improve the scattering SNR and CNR for broadband plane wave ultrasound images of a scattering medium. Incoherent compounding simply averaged the scattering intensity distributions of the images, leading to an averaging of the scattering SNR and an improvement in the scattering CNR. Coherent compounding cancelled out image artefacts from single plane wave images such that the scattering intensity distributions more accurately depict the scattering strength of the medium, improving both the scattering SNR and CNR. Both incoherent and coherent compounding thus smooth out the speckle grain, which is less visually apparent as for conventional more narrowband images with larger speckle grain. The more single plane wave images were compounded, the higher was the image quality improvement due to the reduced size of the synthetic transmit focus.

5.5 Angle compounding with the FP scanner

In this section, we discuss how to adapt the current FP scanner design to carry out angle compounding measurements. A design is proposed in Section 5.5.1, and to show that it could be practically implemented, critical aspects of the design were investigated: the photoacoustic generation of an angled plane wave (Section 5.5.2), and imaging with an angled plane wave (Section 5.5.3).

5.5.1 System design

In Chapter 3, the design of the optical ultrasound system based on the FP scanner featured an ultrasound transmitter coating affixed onto the FP sensor head. The main challenge is to adapt this to enable angled plane waves to be produced, since the position of the detection surface of the FP scanner, i.e. the FP sensor head, does not move. One way of achieving this is to optically scan the excitation beam to introduce a linearly increasing time delay across the wavefront. To do this, the excitation beam needs to be focused down onto a line and scanned across the transmitter coating at a uniform speed in a direction perpendicular to the line. The excitation laser would need to have a temporal pulse length that is at least as long as the duration of the scan. The speed of the excitation beam scan sets the angle of the plane

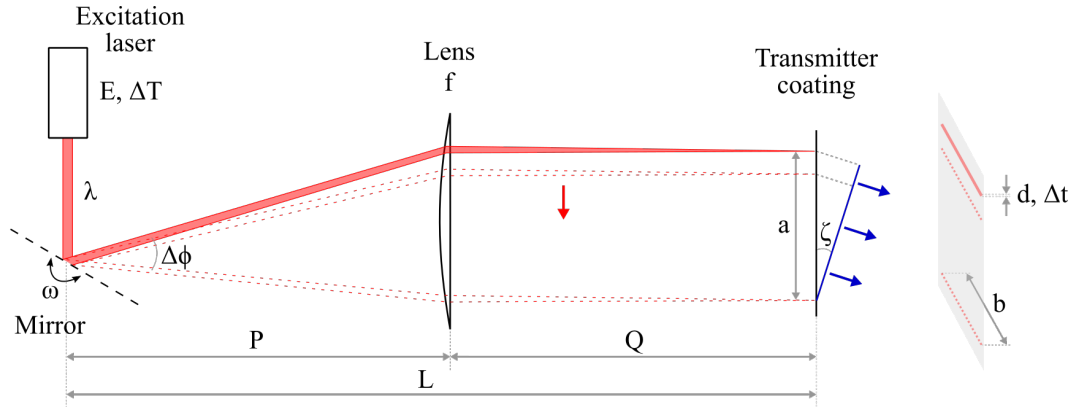


Figure 5.16: Schematic for the set-up of the photoacoustic generation of an angled plane wave. The excitation laser beam (red) is reflected by the mirror and focused down by the lens onto the transmitter coating, which generates an angled planar ultrasound wave (blue).

wave and needs to be adjustable, so the ability to scan at different speeds is necessary. A constant scan speed is required to generate a planar wave. The width of the excitation focal line determines the bandwidth of the generated ultrasound wave. An example set-up for an optical angled plane wave generation system is shown in Fig. 5.16, where an excitation laser beam is reflected off of a fast-rotating mirror and passes through an optical system that focuses the beam down onto a line across the transmitter coating. As the mirror rotates the focused excitation beam line moves along the sensor, thus photoacoustically generating an angled plane wave. The focusing optical system is shown as a simple convex lens in Fig. 5.16, but would likely need to be more complicated than this. Below is a discussion of the various technical requirements and challenges that may arise from this design.

Speed. In order to generate a plane wave with a useful steering angle, the scanning speed of the focused excitation beam on the transmitter coating needs to be very fast, of the order of the speed of sound or faster. The steering angle ζ and the mirror's rotational speed ω can be related to one another via the excitation laser pulse width ΔT . For a mirror with rotational speed ω , the rotational speed of a simply reflected beam is 2ω . In the time ΔT , the excitation line is therefore scanned with a speed of $2\omega L$ over a distance a . In the same time ΔT , the acoustic wave generated from a point source located at the first excitation point of the line scan has travelled by a

distance $a \sin \zeta$ at the speed of sound c , hence:

$$\Delta T = \frac{a}{2\omega L} = \frac{a \sin \zeta}{c} \quad (5.19)$$

which rearranges to:

$$2\omega L = \frac{c}{\sin \zeta} \quad (5.20)$$

Since this relation is inversely proportional, the smaller the angle ζ the faster the scanning speed $2\omega L$ needs to be. To generate small angles of 10° - 2° the beam would need to be scanned at speeds of 8600-43000 m/s. This can be facilitated by very fast rotating mirrors and by making the distance between the mirror pivot point and the scan surface L (or P , depending on the optical focusing system) very long. As was found in Section 5.4, angle compounded images benefit from being compiled from images obtained with different angle planes waves rotated by small angles relative to each other. The scanning speed therefore needs to be finely adjustable.

Focus. The focal width d of the focused excitation beam needs to be sufficiently small for the generated wave to be broadband. The width d and the scan speed $2\omega L$ determine how long each point on the transmitter coating is illuminated for, i.e. the effective pulse width, and thus what bandwidth the generated wave has. The effective pulse width Δt is given by:

$$\Delta t = \frac{d}{2\omega L} \quad (5.21)$$

where the excitation beam scanning speed can be substituted using Eq. (5.20), which gives:

$$\Delta t = \frac{d \sin \zeta}{c} \quad (5.22)$$

The bandwidth is inversely proportional to the effective pulse width Δt , assuming perfect thermoelastic conversion, and therefore inversely proportional to the focal line width d for a given steering angle ζ . For a simple lens as the optical focusing

system, the focal width d of the excitation beam line would be given by:

$$d = \frac{2.36}{\pi} \frac{\lambda f}{D} \quad (5.23)$$

where λ is the wavelength of the excitation beam, f is the focal length of the lens and D is the beam waist before focusing. The focal length f needs to be the same length as the distance Q between the lens and the transmitter coating, and thus of the same order of magnitude as the rotational sweep distance L (or P , depending on the optical focusing system). Since the sweep distance L (or P) is likely going to be very long to facilitate a fast sweep, the focus will be very weak leading to a wider focal line d and thus limiting the bandwidth. The focal line width d could however be further decreased by increasing the beam diameter D before focusing.

Energy. The pulse energy E of the excitation laser needs to be high enough so that every illuminated point on the transmitter coating experiences a sufficiently high effective fluence Φ to generate the pressures required for ultrasound imaging. The pulse energy E and the effective fluence Φ can be related via the irradiance I of the excitation source, i.e. the energy emitted per unit area per unit time:

$$I = \frac{E}{db\Delta T} = \frac{\Phi}{\Delta T} \quad (5.24)$$

where b is the length of the focused excitation line. Eq. (5.24) rearranges to:

$$E = db\Phi \quad (5.25)$$

Assuming a source wavelength of $\lambda = 1550$ nm, a focal length and pivot length of $f = P = 1$ m, and a beam diameter of $D = 1$ mm, using Eq. (5.23) we estimate the focal line width d to be approximately 1.2 mm. Assuming a line length of $b = 15$ mm and a required fluence $\Phi = 15$ mJ/cm², using Eq. (5.25) we estimate the required pulse energy E to be 2.6 mJ. The pulse width ΔT needs to be relatively long to be able to irradiate the whole transmitter coating during the sweep. To generate 2° to 10° angled plane waves over a sweep length $a = 15$ mm, according

to Eq. (5.19), this would require a 0.3-1.7 μs long pulse. The challenge is to find an excitation source that provides both a pulse energy on the order of mJ and flexible μs -scale pulse widths.

5.5.2 Optical generation of angled plane waves

In this section, we describe how some of the technical requirements and challenges identified in the previous section can be addressed. First, the demonstration of rapidly swept beams via a simple angle magnification method which is based on two mirrors placed quasi-parallel to one another is described (Section 5.5.2.1). Second, we describe a laser source with a variable pulse duration, repetition frequency and energy based on the amplification of a tunable continuous-wave laser source using an erbium-doped fibre amplifier combined with an acousto-optic modulator (Section 5.5.2.2).

5.5.2.1 Angle magnification system

Concept. The reflected angle of a beam off of a mirror can be increased by using multiple reflections between two quasi-parallel mirrors. We will exploit this concept to increase the scanning speed of the excitation beam. The method was first presented by Pisani *et al* [117] as a means to amplify very small rotation angles to be able to measure them. It rests on the fact that if two mirrors are placed parallel to one another, a beam reflects multiple times between them and exits at the same angle as the angle of incidence. If, however, one of the mirrors is angled by a small angle γ with respect to the other, each time the beam reflects off of this mirror it will reflect at an angle 2γ larger than the previous angle of incidence. After N reflections off of the slightly angled mirror, the beam will have incurred a change in angle of $2N\gamma$. We make use of this simple angle magnification method by placing a mirror quasi-parallel to the rotating mirror to amplify the rotation speed of the reflected beam, see Fig. 5.17. If the beam reflects N times off of the rotating mirror with rotational speed ω , its rotational speed will be $2N\omega$.

Demonstration of concept. This concept was demonstrated with a 637-nm fibre-coupled diode laser source (Thorlabs, S1FC637) and a galvanometer mirror (Cam-

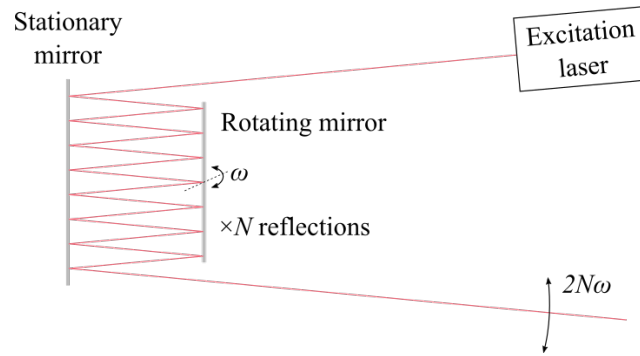


Figure 5.17: Angle magnification system to amplify the rotation speed of a laser beam reflecting off of a rotating mirror, based on work by Pisani *et al* [117].

bridge Technology, 623XH) driven by a function generator with a triangular waveform (600 mVpp, 10 kHz). The rotational speed of the beam was estimated by measuring the total deflection of the beam when projected onto a distant planar surface. Since the beam's rotational speed was very high, the total deflection appeared to the human eye as a line on the planar surface. By measuring the length of the line, dividing it by the distance between the rotating mirror and the planar surface, and multiplying it with the oscillation frequency of the mirror, the rotational speed of the mirror could be estimated. It is worth noting, that this results in an estimation of the average rotational speed across one period of oscillation. The average rotational speed of the galvanometer mirror, without angle magnification, was estimated to be 40 rad/s. With the addition of a stationary mirror for angle magnification, and setting it up to yield $N = 8$ reflections off of the rotating galvanometer mirror, the average rotational speed of the beam was measured to be 640 rad/s. This is equivalent to an angle magnification of 16 times, which is equivalent to $2N$, and serves as a check that the angle magnification system works as we expect it to.

Maximising rotational speed. There was scope to further increase the rotation speed of the beam by setting the mirrors up to yield $N = 18$ reflections off of the galvanometer mirror. For this number of reflections, the rotational speed could not be measured using the deflection method described above, as the number of reflections N on the rotating mirror changed within an oscillation period of the mirror rotation. Instead, the rotational speed was estimated by measuring the time it takes the

spot to sweep across the active element of a fast photodiode (Hamamatsu, G9801, -3dB bandwidth 300 MHz), which was connected to an oscilloscope (Tektronix, TDS2014, 100 MHz) for read-out. With knowledge of the spot size, which was determined using a beam profiler (DataRay, Beam'R2-DD), the rotational speed was then estimated. This way of estimating the rotational speed of the beam results in an instantaneous value at the position of the photodiode detector, rather than an average value like previously. For $N = 18$ reflections off of the galvanometer mirror, a maximum instantaneous beam rotational speed of 2100 rad/s was estimated, when the photodiode was positioned in the middle of the scan. A beam rotational speed of 2100 rad/s would result in the generation of a 21° angled wave assuming a distance of 1 m between the rotating mirror and the transmitter coating. The measured instantaneous rotational speed of 2100 rad/s is significantly higher than the expected average rotational speed of $2N\omega = 1440$ rad/s, which indicates that the galvanometer rotational speed varies significantly during the oscillation period, and was likely sinusoidal due to the mirror's rotational inertia. The non-uniform rotational speed of the galvanometer mirror could lead to the generation of non-planar ultrasound waves. Since only a small scan length, of e.g. 15 mm, is required over a long scan distance, of e.g. 1 m, the speed variation may be small enough to generate an almost-planar wave. It is worth noting that due to the oscillating motion of the mirror, two acoustic waves with opposite angles are generated during each period of oscillation.

Potential hardware. To avoid the potential problems that come with oscillating mirrors, rotating mirrors that rotate continuously rather than oscillate back and forth, e.g. polygon mirrors, could be used. If we consider a commercially available polygon mirror (Cambridge Technology, SA24), that provides rotational speeds ranging from 800 to 5700 rad/s, used with an angle magnification setup allowing for $2N = 8$ reflections off of it, this would be sufficient to generate angled plane waves with steering angles as small as 2° . Setting up an angle magnification system using a polygon mirror may be harder to achieve due to its continuous rotating motion which for a low number of sides may require a larger distance between the

mirrors, thus limiting the number of reflections. The advantage of using a polygon mirror would be the continuous uniform rotation speed which results in the generation of perfectly planar waves at fixed steering angles. Another alternative to the galvanometer mirrors are commercially available micro-electro-mechanical systems (MEMS) mirrors (e.g. Hamamatsu, S13989-01H), which provides fast oscillations with a high resonant frequency of 30 kHz and a wide optical deflection angle of 40° . This system would provide a mirror rotational speed of up to 21000 rad/s, which would be sufficient to generate angled waves with steering angles as small as 2° without the use of an angle magnification system. The disadvantage of such mirror systems is that they only achieve a high rotational speed at the resonant frequency, thus making it difficult to vary the rotational speed which is necessary to generate plane waves at different steering angles. Other methods of deflecting a beam, which could be explored in future, include acousto optic and electro optic deflectors, as these are not limited by inertial considerations.

Limitations. The limitation of the angle magnification concept is that the number of reflections is limited by the size of the mirrors used. However, larger sized mirrors will have higher rotational inertia and correspondingly slower rotation speeds. One possible solution is to ensure the beam going through the angle magnification system has a small waist. However, as discussed in Section 5.5.1, the beam diameter D needs to be relatively large when passing through the optical focusing system to guarantee a sufficiently small focal line width to enable the generation of broadband angled ultrasound waves. One way to facilitate the different beam diameter requirements is to send a weakly focused beam to the angle magnification system such that the beam is at its smallest diameter when passing through it, and allowing the most number of reflections possible. Once the beam exits the angle magnification system it propagates over a distance P during which its diameter expands such that the focusing system is able to create a small focal line width on the transmitter coating. We conclude, that with careful design it should be possible to scan a beam sufficiently fast using mechanical methods to optically generate plane waves with appropriate angles.

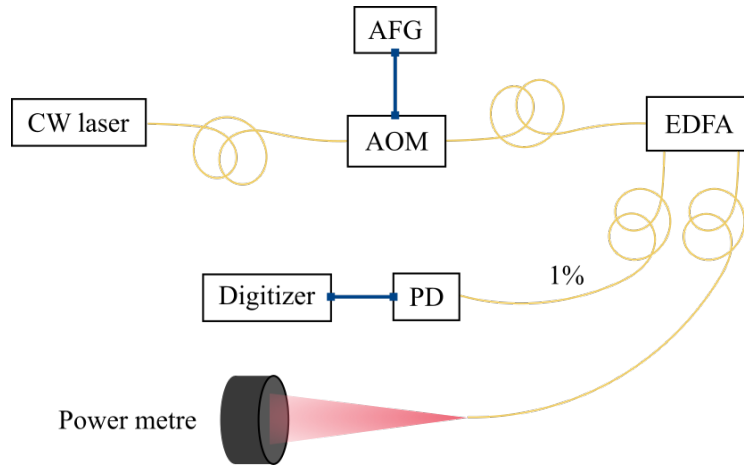


Figure 5.18: Excitation source set-up to generate variable excitation pulses, comprising a continuous-wave (CW) laser, an acousto-optic modulator (AOM), an arbitrary function generator (AFG) and an erbium-doped fibre amplifier (EDFA). Pulse duration and energy were measured with a photodiode (PD) and a power meter.

5.5.2.2 Excitation laser source

Set-up. A system to generate laser pulses with adjustable durations, repetition frequencies and energies that could be a suitable excitation source for the optical generation of angled plane waves is presented. The system comprises a continuous-wave (CW) laser, an acousto-optic modulator (AOM), an arbitrary function generator (AFG) and an Erbium-doped fibre amplifier (EDFA), see Fig. 5.18. The output of a tunable CW laser (Yenista Optics, Tunics T100s-HP) went through an AOM (Gooch & Housego, T-M040-0.5C8J-3-F2S) that was supplied rectangular voltage pulses by an AFG (Tektronix, AFG3022B) to generate optical pulses with controllable characteristics. Varying the AFG input pulse lengths and repetition frequencies accordingly varied the output optical pulse's length and repetition frequency. The pulsed output from the AOM was then coupled into an EDFA (Pritel, FA-23, 200mW) to amplify the intensity and the overall pulse energy. Varying the pump current of the EDFA varied the pulse energy of the final output. The output was measured via a 1%-monitor port and detected onto an InGaAs photodiode (Hamamatsu, G9801, -3dB bandwidth 300 MHz) which was connected to a 500-Ms/s digitizer (Tektronix, TDS520) for read-out. The time-averaged output power was measured with a laser power and energy meter (Coherent, FieldMaxII-TOP 1098580).

Pulse energy measurements. The output pulse energies were measured for the AFG producing pulse widths ranging from 60 to 500 ns. Amplified spontaneous emission (ASE) occurred when operating with low input powers (1 mW) from the CW laser. Using higher input powers (10 mW) seeded the gain sufficiently to avoid significant ASE to build up and ensure all the output energy is contained within the pulses. The highest pulse energy measured was 83 nJ for a 500-ns long pulse with a repetition frequency of 230 kHz.

Limitations. The pulse energy measurements were limited by the maximum power the EDFA could provide. Using an EDFA with a $10\times$ higher maximum power (e.g. Pritel, FA-33, 2W), would enable an improvement by a factor of 10 in the pulse energy, thus providing pulse energies of the order of mJ which was the required pulse energy for optical generation of angled plane waves in Section 5.5.1. A potential issue for longer pulse lengths that are of the order of μs , however, is that the amplified optical pulse would no longer have a rectangular shape, but may have a decaying intensity across the pulse length due to the depletion of the upper-state energy of the EDFA for longer pulses. Further characterisation measurements would be required to determine if the excitation source presented in this section is suitable for the optical generation of angled plane waves.

Conclusion. Overall, Section 5.5.2 describes the technical challenges, limitations and potential solutions to the optical generation of angled plane waves. The technical challenges with achieving a fast beam sweeping speed (Section 5.5.2.1) and a focused excitation laser with a long pulse length and sufficient pulse energy (Section 5.5.2.2) could be addressed separately. However, a practical implementation of the angle magnification and excitation amplification systems combined to optically generate angled plane waves would be technically challenging, as there are some potentially competing requirements by the two parts of the proposed system. While the angle magnification system benefits from a small beam diameter to increase the beam sweeping speed, the fluence at the focal spot would be increased for a larger beam diameter. This may put limitations on the practical implementa-

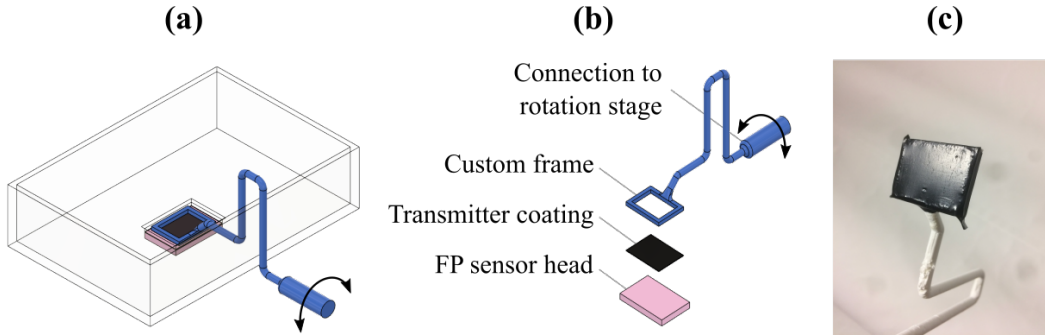


Figure 5.19: Set-up for angled plane imaging with the FP scanner and a mechanically angled transmitter coating. **(a)** Schematic of set-up, **(b)** Exploded view of custom frame (blue), transmitter coating (black) and FP sensor head (pink), **(c)** Photograph of transmitter coating mounted on custom frame.

tion of a system combining these two techniques. An exact optical system design to simultaneously focus and sweep the beam, and meet both requirements for the beam diameter is yet to be designed. With the hardware available to us at this time, the proposed solutions could not be combined into one system, however alternative hardware solutions were suggested which could overcome this limitation.

5.5.3 Imaging with an angled transmitter coating

In this section, images from angled plane wave transmissions are obtained by manually angling the transmitter coating. The aim was to show that using the FP scanner for imaging with angled plane waves is feasible, before implementing the optical generation of angled plane waves described in the previous section. This also entailed testing the data processing and reconstruction steps described in Section 5.3.2 of experimental data.

Set-up. The only difference compared to the set-up for normal plane wave imaging described in Section 3.2 is the placement of the transmitter coating. All other elements of the FP scanner system remain identical. The transmitter coating was mounted onto a custom 3D-printed frame between the FP sensor and the imaging object, see Fig. 5.19a. The frame was designed with an arm that connects to a manual rotation stage to allow for angling of the coating, see Fig. 5.19b. The transmitter coating was stretched across the frame using the same ethanol-soaking and shrink-fit method used for fitting it onto the FP sensor heads in Section 3.2.1.

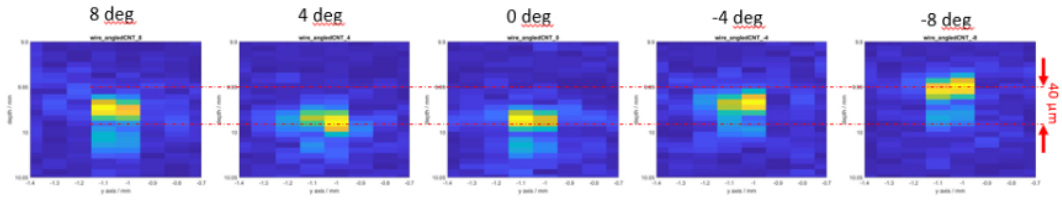


Figure 5.20: Single plane wave ultrasound images of a 27 μm tungsten wire acquired with steering angles from -8° to 8° . Each frame is shown over the same field of view with dimensions of 0.7×0.15 mm to demonstrate the registration issue.

The transmitter coating was additionally fixed in place using superglue to ensure that it remains stretched throughout the imaging experiment, see Fig. 5.19c. To allow inclining of the coated frame relative to the sensor, the imaging object had to be placed sufficiently far from the sensor so that the coated frame was able to rotate freely to the desired maximum steering angles ($\pm 10^\circ$). The excitation laser beam was transmitted through the FP sensor head, as previously, but had to also pass through a layer of water (order of 3-5 mm) before being completely absorbed by the transmitter coating. The loss in pulse energy due to the absorption of the 1064-nm beam by water was negligible, such that the generated angled planar wave had peak pressures and a bandwidth similar to the ones generated for the normal plane-wave imaging system characterised in Section 3.3.1. The measured timeseries had to be accordingly modified to account for the offset of the coated frame with respect to the FP sensor plane and to be able to apply the reconstruction algorithm described in Section 5.3.2.

Tungsten wire. A 27- μm diameter tungsten wire was imaged for five different angles of the transmitter coating ranging from -8° to 8° , with a sensor sampling step size of 100 μm . Between acquisitions at different angles, the transmitter coating was rotated in 4° steps. This experiment would help characterise how well-registered different angled frames of the wire were, i.e. check that the depth-offset compensation and the angled plane wave fitting methods described in Section 5.3.2 are sufficiently accurate. The image of the wire shifted by up to 40 μm in depth between the five different frames acquired, see Fig. 5.20. This is likely due to small

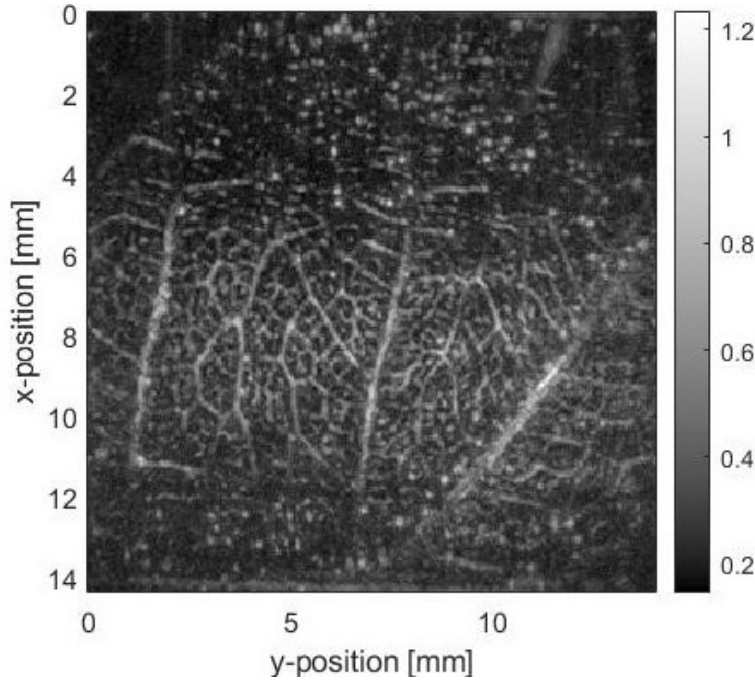


Figure 5.21: Single plane wave ultrasound image of a polymer leaf phantom with a steering angle of approximately 3° , shown as a MaxIP in the xy plane.

inaccuracies in the fitting of the plane wave position, since the high peak pressure saturates the sensor leading to some uncertainty as to where exactly the peak of the wavefront is. One possible way to address this is by introducing a time-offset variable and optimising the image quality (the resolution in the case of these tungsten wires) to automatically find the exact time of arrival of the plane wavefront. It is important to note that the registration issue is not intrinsic to angled plane wave imaging, but is a result of the method of mechanically angling and offsetting the transmitter coating. Hence the registration issue is expected to be less severe when imaging with all-optically generated angled plane waves as no depth-offsetting is required.

Polymer leaf. A similar polymer leaf to the one imaged in Section 3.4.1 was imaged with an angled plane wave, see Fig. 5.21. The leaf's structures were resolved, as previously, with features at the top and bottom of the image being broken up due to the curving of the leaf away from the sensor. This shows that the generation of an angled plane wave through a transmitter coating mounted on a frame and the reconstruction algorithm for angled planar transmissions work well for 3D imaging.

Agar-based tissue mimicking phantom. An agar-based phantom, similar to the one described in Section 3.4.2 was imaged with angled plane waves, however no image is shown as sample features were not visible in the acquired images. This is partly due to issues of reliable fabrication of this phantom (trapped air bubbles) and the additional distance of the phantom from the sensor due to the angled transmitter coating frame being in the way (the distance of the phantom to the sensor was approximately 8 mm compared to a distance of 0 mm in the non-angled case). As a result, the image quality of a single plane wave image is so poor that compounding would unlikely improve the visibility of the phantom features. It is worth highlighting that this is not an intrinsic problem of angle compounding, but only an issue with the practical implementation of angled plane wave imaging using a manually angled transmitter coating. Imaging with an all-optically generated angled plane wave should not require a depth offset between the FP sensor head and the imaging object.

Conclusion. In this Section 5.5, we explored the implementation of an angle compounding system with the FP scanner. A possible design for a modified FP scanner system capable of optically generating angled plane waves was described in Section 5.5.1. The system is based on the optical generation of angled plane waves by scanning an excitation beam across an ultrasound transmitter coating to introduce the necessary time delay for an angled wavefront. The technical requirements and challenges of such a system were identified. Some of the key challenges of this approach were addressed in Section 5.5.2, including a method for a fast scan of the excitation beam, and an excitation light source capable of generating laser pulses with adjustable durations and energies. Possible hardware options were discussed which could enable the optical generation of angled plane waves in future. Finally, imaging with an angled plane wave was demonstrated in Section 5.5.3 with a mechanically angled transmitter coating. This showed that the reconstruction method and algorithm work for angled plane wave imaging, while highlighting the issue of registration between frames taken with different steering angles. Overall, Section 5.5 shows that the concept of angle compounding with the FP scanner is fea-

sible, and that any technical challenges with the optical generation of angled plane waves and imaging with angled plane waves can be addressed. The next steps to develop the angle compounding system based on the FP scanner are described in Section 5.6.2.

5.6 Future work

5.6.1 Frequency compounding

Frequency compounding with a point scatterer. In Section 5.2, frequency compounding was demonstrated with simulated and experimental data for scattering media phantoms. Incoherent frequency compounding was shown to improve contrast at the cost of spatial resolution. This was a consequence of the averaging of frequency-dependent grating lobe artefacts and speckle that occurs during incoherent frequency compounding. This point could be further demonstrated by imaging a single point scatterer and applying incoherent frequency compounding to its image to illustrate the effect of averaging of the frequency-dependent artefacts and the increase in the size of the point spread function. In simulations, this could be realised with a point scatterer, similar to those simulated for the investigation of narrowband grating lobe artefacts in Section 4.5.3, or in experiments this could be done by imaging a wire in water.

Quantifying the effect of frequency compounding. The effect of the bandwidth of the sub-band frequency filters on the image quality in the random scattering medium was shown for only two bandwidths in Section 5.2.3.2. By varying the filter bandwidth over a range of values the correlation between the filter bandwidth, the image contrast and the spatial resolution can be quantified. This could potentially be useful in determining what filter bandwidth should be used for a desired contrast and resolution performance. The frequency compounding approach could also be expanded to include a non-continuous or non-overlapping frequency bands, which could be chosen depending on the image quality requirements for the final compound image.

5.6.2 Angle compounding

Broadband angle compounding with a point scatterer. In images where there is no speckle, e.g. a medium of few point scatterers or specular reflectors, how does broadband angle compounding improve the image quality? Angle compounding does not suppress grating lobe artefacts, as they do not depend on the angle of the transmitted plane wave but only on the spacing of the sensor detection points, and should therefore be in the same position for all single plane wave images. Limited view artefacts (also known as edge wave artefacts) should equally only depend on the size of the sensing aperture, not the angle of transmission. The image quality improvement from broadband angle compounding in media with few scatterers could be investigated with a simulation of angle compounding with a single point scatterer or small finitely sized scatterer. This would enable a comparison of the image artefacts between images obtained from single angled plane wave transmissions and the coherently or incoherently compounded images. For finitely sized scatterers this should illustrate the improvement of the limited view problem (not to be confused with limited view artefacts) which leads to incomplete reconstruction of objects from a single transmission angle.

Demonstrating angle compounding with the FP scanner. In Section 5.5, a system design for all-optical generation of angled plane waves was described. The system relies on specific hardware for a sufficiently fast scan of the excitation beam with sufficiently long and high-energy pulses, as described in Sections 5.5.2.1 and 5.5.2.2. The system for optical generation of angled plane waves needs to be characterised. We suggest to first optically generate a wave from a stationary excitation beam incident on the transmitter coating, with the pulse energy and the pulse width equivalent to the effective values experienced by a point on the transmitter coating during a fast scan of the excitation beam. After implementing a suitably fast optical scanning system of the excitation beam, an angled wave can be optically generated and characterised for its peak pressure, planarity and bandwidth as was done for a normal plane wave in Section 3.3. If the angled wave is sufficiently planar, high in peak pressure and broadband, it can be used to demonstrate imag-

ing with an optically generated angled wave. The reconstruction algorithm needs to be modified to allow for better co-registration of different single plane wave images, before compounding the images. All-optical angle compounding can then be demonstrated with resolution targets, scattering structures, tissue mimicking phantoms, and *ex vivo* tissue samples. Compared to a single angle plane wave image, angle compounding with the FP scanner would have an increased acquisition time by a factor equal to the number of angles, making the total acquisition time for an angle compounded image very long. This limitation can be addressed by decreasing the acquisition time of a single plane wave image. As discussed in Section 3.5, this can be done by using a higher pulse repetition frequency laser and parallelising the sensor read-out by the use of multiple interrogation beams [93] or wide-field illumination and a camera-based sensor array [94].

5.6.3 Other compounding ideas

In Section 4.5.3, grating lobes were identified as a source of contrast reduction for signals at higher, super-Nyquist frequencies. The grating lobes were a result of the spatial undersampling of the acoustic field with a regular sensor detection array. The contrast reduction from grating lobes could be mitigated with frequency compounding, as shown in Section 5.2, but cannot be addressed with angle compounding. Alternative methods to reduce the effect of grating lobes could involve addressing the root of the problem, which is the spatially periodic (under)sampling at the sensor array.

Pitch non-uniformity. One way to suppress grating lobe artefacts is to sample the acoustic field at irregularly spaced sensor points. Non-periodic sensor locations have been extensively studied to design sparse arrays, usually with the goal to reduce the number of elements in receive to enable 3D ultrasound imaging with a 2D sensor array [118–124]. The reduction of elements resulted in non-periodical spacing between the elements, which in turn lead to in the reduction of the grating lobe level in both transmit and receive. The suppression of grating lobes has been demonstrated with sparse arrays via the random removal of elements [118, 119],

Gaussian distributed random elements [120], spiral patterns [121, 122], and patterns designed for minimal redundancy [123]. While periodic sparse arrays have also been shown to reduce grating lobes by employing different element spacings in transmit and receive to offset the respective grating lobes [125, 126], this approach is not applicable to the optical ultrasound system based on the FP scanner as there are no grating lobes in transmit. More recently, a deep learning approach has been demonstrated to fill in the detection gaps in periodic sparse arrays which reduced grating lobes [127]. The concept of pitch non-uniformity has been demonstrated in transmit using an optical ultrasound generation [128]. Image artefacts including grating lobes were reduced with a non-uniform point source distribution of a synthetic source aperture. Due to the reciprocity of ultrasound, all methods employing pitch non-uniformity to reduce grating lobes in transmit should also work when applied in receive by sampling at non-uniformly spaced sensor points. The advantage of the FP scanner system is that the detection points can be arbitrarily chosen across the FP sensor head by optically scanning the interrogation beam.

Pitch compounding. Multiple images could be obtained with the acoustic field sampled at regularly spaced sensor points but with different step sizes. Since the grating lobe are at different position depending on the sensor sampling step size, they would be at different positions in the differently sampled images. Compounding these images coherently or incoherently should therefore average or partially cancel the grating lobe artefacts in the final compounded image.

Both suggestions of sensor pitch non-uniformity and pitch compounding should first be tested by imaging a single point scatterer, either in simulation or experimentally using a wire in water, before verifying the contrast improvement on a scattering medium.

5.7 Conclusion

Frequency compounding. The feasibility of frequency compounding was shown for a broadband optical ultrasound imaging system based on the FP scanner, in sim-

ulation and with experimental data from imaging an agar-based tissue mimicking phantom. The coherent frequency compound image was shown to be equivalent to filtering with the compound filter, i.e. the filter obtained from summing all sub-band filters. Coherent frequency compounding therefore does not provide any advantage over simply frequency filtering the data. Incoherent frequency compounding was shown to improve contrast at the expense of spatial resolution. The resolution performance of the full bandwidth image could be largely retained by compounding incoherently with broadband frequency filters (10 MHz). Using a narrowband frequency filters (2 MHz) for incoherent compounding, diminished the resolution while significantly improving the contrast. The bandwidth of the filters thus determined the trade-off between the resolution performance and the contrast improvement, with broadband filters being favourable for the resolution and narrowband filters favouring contrast.

Angle compounding. The reconstruction algorithm for angled plane wave ultrasound imaging was described along with processing methods to implement with simulated and experimental data. Angle compounding was simulated for a broadband ultrasound system and was shown to improve the scattering CNR by smoothing out the scattering intensity distributions, i.e. the fine-grain speckle pattern contained in the broadband optical ultrasound images. Coherent angle compounding was shown to also improve scattering SNR by more accurately representing the scattering distributions for every region of the image. The contrast improvement scaled with the number of angles, and depended on the spread and separation of the angles. For the same number of angled transmissions, a smaller spread and separation of angles yielded a bigger contrast improvement. A system design for the optical generation of angled plane waves, that can be integrated into the FP scanner system, was presented and the requirements and challenges were discussed. Angled plane waves are proposed to be generated photoacoustically by scanning a focused line across the ultrasound transmitter coating. An angle magnification system and a source amplification set-up were tested to show the feasibility of including them in the FP scanner system for sufficient scan speeds and excitation energy. Finally,

imaging with an angled plane wave was demonstrated with a mechanically angled transmitter coating mounted on a custom-designed rotating mount between the FP sensor head and the imaging object. The set-up was used to image a tungsten wire at multiple angles to assess the registration issue in 2D over multiple frames, and a polymer leaf skeleton phantom to test the reconstruction and processing methods in 3D. The next steps to develop the angle compounding system based on the FP scanner were detailed.

Frequency vs angle compounding. The two compounding methods explored in this chapter work in distinctly different ways. Yet, they both improved the image quality, specifically the scattering CNR, and in the case of coherent angle compounding, also the scattering SNR. Frequency compounding is preferentially done incoherently, while angle compounding is most effective when done coherently. While frequency compounding works by smoothing out frequency-dependent speckle patterns and grating lobe artefacts, the contrast improvement in angle compounding stems from a reduction of speckle and the improvement of the limited view of the sensor.

Chapter 6

Dual-mode imaging with the FP scanner

The overall aim of this thesis was to develop a dual-mode photoacoustic and ultrasound imaging system based on the planar FP scanner. As the FP scanner was originally developed for photoacoustic imaging [1], the majority of the work has been focused on developing the ultrasound imaging modality of the FP scanner (Chapter 3), understanding its limitations in image quality (Chapter 4), and exploring methods to improve image quality (Chapter 5). In this chapter, we return to the overall goal and present a dual-mode imaging system based on the FP scanner. Since the dual-mode system is largely similar to the ultrasound imaging system presented in Chapter 3, this chapter will focus on the differences between the two systems, see Fig. 6.1.

Dichroic transmitter coating. The main difference in the dual-mode system compared to the optical ultrasound system is the material of the ultrasound transmitting layer used to coat the FP sensor head for optical ultrasound generation. To allow for excitation of both PA and US modes, the US transmitter coating needs to be dichroic, i.e. transparent to the PA excitation light while being absorbing to the US generation light, see Fig. 6.1b. The FP scanner system can then be used sequentially for PA imaging the same way it was previously developed without a transmit-

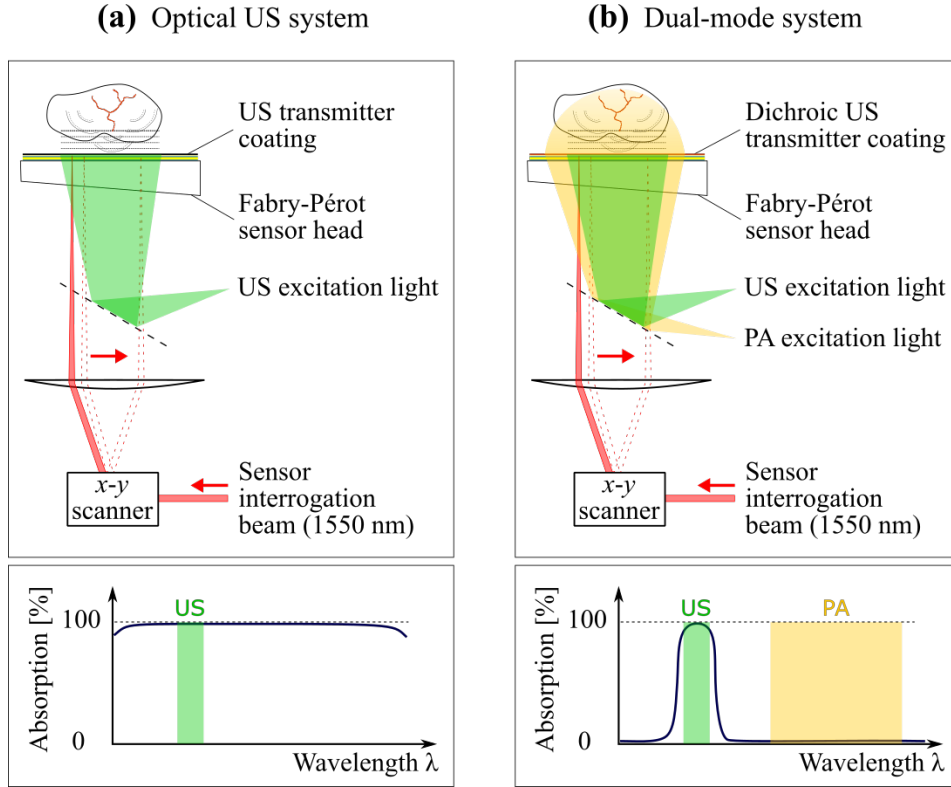


Figure 6.1: Schematic of system set-ups with example optical absorption spectra for US transmitter coatings. **(a)** Optical US imaging system using a transmitter coating with a broadband absorption for optical US generation, and **(b)** Dual-mode imaging system using dichroic transmitter coating with narrowband absorption for optical US generation and broadband transmission for PA generation. Figure adapted from [129] © 2019 SPIE.

ter coating [1], and for optical US imaging the same way as described in Chapter 3. The transmitter coating is ideally highly absorbing at a narrow wavelength range for optical US generation and transparent over a wide wavelength range for PA excitation, see Fig. 6.1b. In this work, selective absorption was achieved with a transmitter coating made from a AuNP-PDMS composite [17].

Outline. Details of the AuNP-PDMS transmitter coating's absorption spectrum, and the fabrication and excitation method are described in Section 6.1. Dual-mode imaging experiments of phantoms are presented in Section 6.2, including a discussion on crosstalk between the two modalities. The chapter is summarised in Section 6.4 with an outlook into potential future work on dual-mode imaging.

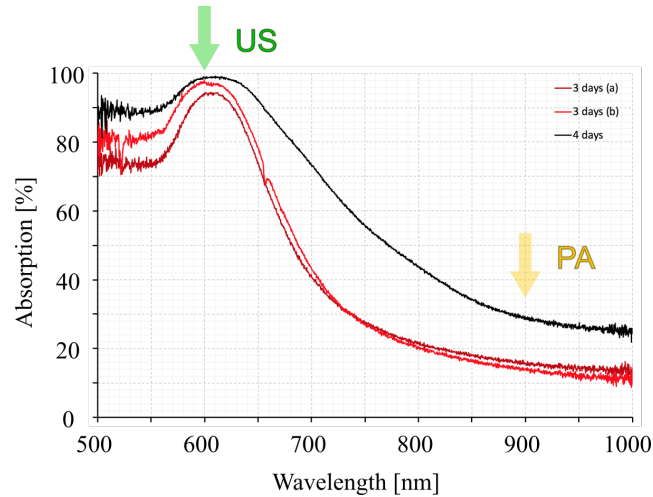


Figure 6.2: Absorption spectra of three AuNP-PDMS composite samples prepared by Sacha Noimark with different amounts of immersion time in Gold-salt solution. Excitation wavelengths for US and PA mode marked with arrows. Figure adapted from [129] © 2019 SPIE.

6.1 Dichroic transmitter coating

AuNP-PDMS coating. AuNP-loaded PDMS films were prepared by Sacha Noimark by first making pure PDMS films using the method described in Section 3.2.1. One side of the PDMS film was then covered with tape, before immersing it in a gold-salt solution for AuNP to accumulate in the PDMS [17]. This accumulation is meant to only occur at the exposed surface, in order to generate a single monopolar US pulse. By varying the amount of time the PDMS film spends in the gold solution, the absorption spectrum can be shifted. Finally, planar FP sensor heads were coated with the AuNP-PDMS films using the same ethanol-soaking and shrink-fit method used for CNT-PDMS films in Section 3.2.1.

Absorption spectrum. Using a spectrophotometer, the absorption spectra for three different AuNP-PDMS samples were measured by Sacha Noimark, see Fig. 6.2. A dependence of the absorption spectrum on the amount of immersion time in the gold-salt solution can be observed (3 days vs 4 days). All samples were strongly absorbing at 600 nm, which was used for optical ultrasound generation, and partially transparent at 900 nm, which was used for PA excitation. 900 nm is a suitable wavelength for PA imaging, due to its long penetration depth in tissue and preferen-

tial absorption by blood. For the imaging experiments a AuNP-PDMS coating with a 3-day immersion time was used.

Excitation. For excitation of both modes a tunable (410–2100 nm) fibre-coupled optical parametric oscillator laser system (Innolas, SpitLight 600 OPO) was used, providing 7-ns duration laser pulses. The laser beam had a pulse energy of 11 mJ at 600 nm and 6 mJ at 900 nm, a Gaussian beam profile with diameter of approximately 20 mm, and a pulse repetition frequency of 30 Hz.

6.2 Imaging experiments

6.2.1 Phantom imaging

The dual-mode imaging capability of the system was demonstrated by imaging two phantoms with both US and PA modes.

Method. Images obtained using the two modes were taken sequentially in separate raster scans, e.g. first US, then PA. For both modes the acoustic signals were acquired by raster scanning the sensor interrogation beam over a 15×15 mm area in steps of 100 μm , with a spot size of 64 μm . The sensor bandwidth was 30 MHz (-3 dB). The temporal sampling interval was 4 ns for the polymer leaf skeleton, and 8 ns for the ink-filled tube phantom. No signal averaging was used for any of the acquisitions. The sensor data from the US mode was frequency filtered with a Gaussian filter of centre frequency 10 MHz and bandwidth 15 MHz to filter out high-frequency environmental noise. From the detected acoustic pressure-time series the reconstruction algorithm described in Section 3.2.3 was used to recover 3D US images of the imaging targets. For the PA mode, 3D images were reconstructed using a reconstruction algorithm based on similar k -space methods [65, 72], described in Section 5.3. Images are presented as maximum intensity projections (MaxIP) or mean intensity projections (MeanIP) through the whole 3D image volume or through slices of the volume.

Polymer leaf skeleton. The same polymer leaf imaged with the optical ultrasound system in Section 3.4.1 was imaged again with the dual-mode system, see Fig. 6.3a.

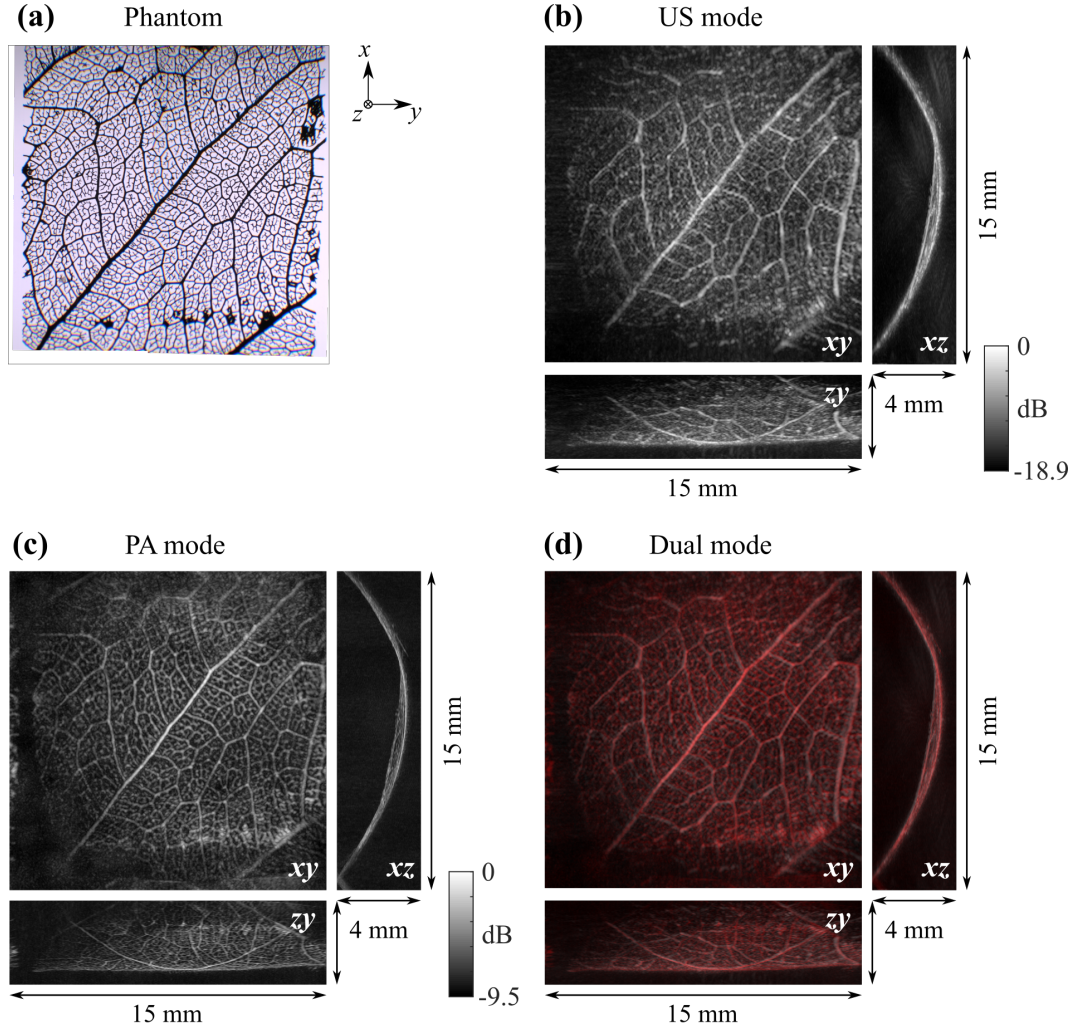


Figure 6.3: Dual-mode imaging of a polymer leaf phantom to demonstrate 3D imaging capability of the dual-mode system. (a) Photograph of the polymer leaf phantom with structures from 60 to 200 μm diameter. (b) Maximum intensity projection through the 3D optical US image. (c) Maximum intensity projection through the 3D PA image. (d) Dual-mode image obtained from overlaying the US image (grey) and the PA image (red). Figure adapted from [129] © 2019 SPIE.

The reconstructed 3D US and PA images are presented as MaxIPs through the whole 3D image volume in the xy , xz and zy planes, see Fig. 6.3b-c. Both the US and PA mode portrayed the leaf with high resolution. A dual-mode image was obtained by overlaying the images of the two modes, see Fig. 6.3d. Perfect overlap of the leaf skeleton features was observed in the dual-mode image. This is because the polymer leaf is simultaneously a strong acoustic scatterer as well as strong optical absorber. Both modes, therefore, highlighted the same structures, which overlap due to the inherent co-registration of the images. Since the US image (Fig. 6.3b)

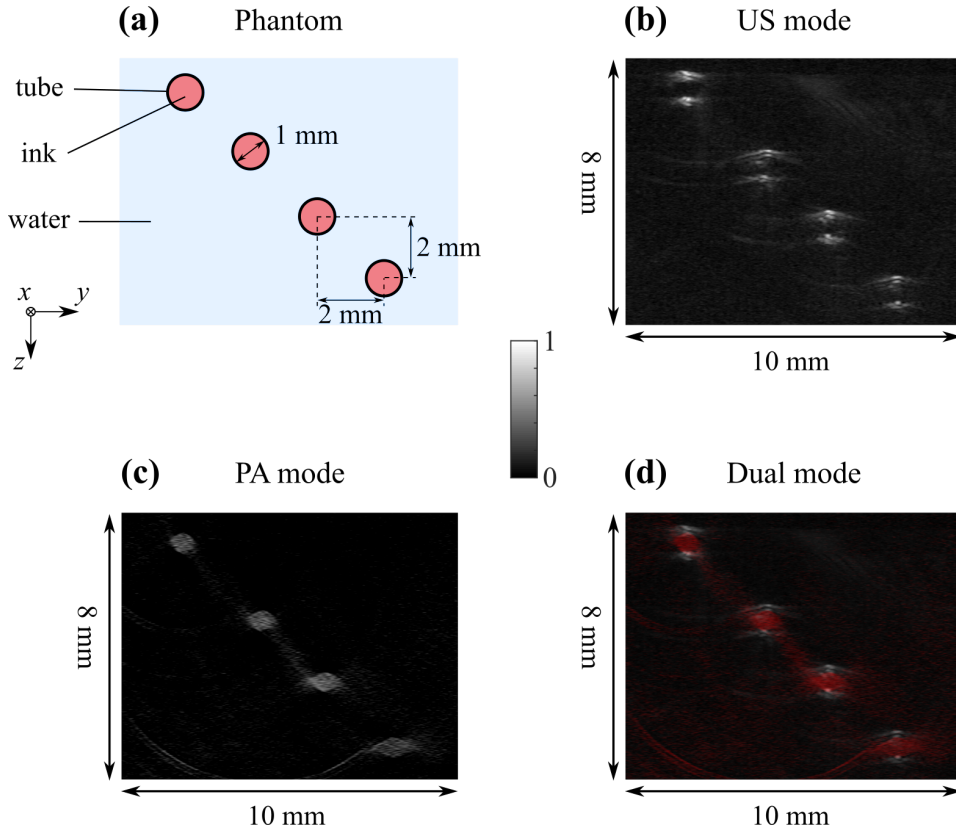


Figure 6.4: Dual-mode imaging of ink-filled tube phantom to demonstrate complementary contrast provided by the dual-mode system. **(a)** Schematic of the phantom comprising polyethylene tubes filled with India ink. **(b)** Maximum intensity projection through a 2 mm slice of the 3D optical US image. **(c)** Mean intensity projection through a 2 mm slice of the 3D PA image. **(d)** Dual-mode image obtained from overlaying the US image (grey) and the PA image (red). All images were individually normalised. Figure adapted from [129] © 2019 SPIE.

has a higher dynamic range than the PA image (Fig. 6.3c), it appears less sharp on a log compressed scale, as a larger range of magnitudes is displayed on the same grey scale. When viewing both images on a linear scale (see Fig. E.1 in Appendix E) they appear approximately equally sharp. The US image may have a slightly lower resolution performance due to the Gaussian frequency filter of centre frequency 10 MHz and bandwidth 15 MHz applied to the US data before reconstruction.

Ink-filled tube phantom. A phantom designed to demonstrate the complementary contrast that US and PA can provide was imaged. For this purpose, polyethylene tubes of 1 mm diameter were filled with diluted India ink (1:700) and immersed in water, see Fig. 6.4a. The ink concentration made for an absorption coefficient

similar to blood at around 900-1000 nm (0.57 mm^{-1}). The reconstructed 3D US image is presented as a MaxIP, while the PA image is presented as a MeanIP, see Fig. 6.3b-c. Both projections were taken in the xz -plane over a slice of thickness 2 mm through the 3D image volume. In the US image the top and bottom point of each tube are visible as a strong specular reflection resembling point-like scatterers, see Fig. 6.4b. On close inspection two features can be seen for each top/bottom point, corresponding to the wall thickness of the tube, which leads to two separate reflections. In the PA image the ink filled region of the tubes is clearly visible as filled-in circles resembling vessel-like absorbers, see Fig. 6.4c. Some arc artefacts can be seen in the bottom left half of the image. These were caused by the coating not being completely transparent at 900 nm and generating a weak, planar optical US wave when operating in the PA mode. The scattered signals from this “parasitic” wave did not reconstruct into the point-like reflectors as in the US mode due to the different reconstruction algorithm applied in PA mode. In the overlaid dual-mode image the point-like reflectors and the vessel-like absorbers corresponding to each ink-filled tube line up well, see Fig. 6.4d. The dual-mode image has thus indeed provided complementary contrast in US and PA modes.

6.2.2 Mode crosstalk

Since the AuNP-PDMS coating is not completely absorbing at 600 nm, a small fraction of the US excitation light will be transmitted through the coating and generate weak PA signals within the target. And vice versa, since the coatings are not completely transparent at 900 nm, a small fraction of the PA excitation light will be absorbed in the coating and generate a weak planar ultrasound wave. This means that some weak ‘parasitic’ PA signals will be detected in the pressure time series of the US mode, and some weak ‘parasitic’ US signals will be detected in the pressure time series of the PA mode. For a given scattering and absorbing point source the time of arrival of the PA signal is approximately half the time of arrival of the pulse-echo US signal. These parasitic signals will, however, not reconstruct coherently since the reconstruction algorithms of the two modes differ in their dispersion relation. For example, in the US image volume of the polymer leaf a blurry and

faint structure at approximately half the depth of the leaf is visible (not shown in Fig. 6.3 as it is cropped out in depth), which corresponds to the parasitic PA signals being reconstructed incoherently by the US reconstruction algorithm. In the PA image, at approximately double the depth of the polymer leaf, nothing was visible. This suggests that the parasitic US signals were completely ‘washed out’ by the PA reconstruction. In practice, biological tissues are less strongly scattering and less strongly optically absorbing, meaning that the parasitic signals are likely to have a low SNR and should not appear in the reconstructed images.

This crosstalk effect could potentially be useful for an imaging situation where the imaging ROI is separated from the sensor by a distance that is larger than the depth of the ROI. In this case the time of arrival of the PA and US signals are completely separated, such that any blurry structures from the parasitic crosstalk images don’t overlap with the actual images. Then it is possible to reconstruct images for both modes by using the two different reconstruction algorithms with the sensor data acquired in one of the modes. The polymer leaf imaged in Section 6.2.1 fulfilled the depth criterion, as it was approximately 3 mm deep and positioned 4 mm away from the sensor. In the US mode enough of the excitation light was transmitted through the AuNP-PDMS coating to generate appreciable PA signals that can be used to reconstruct a PA image of the leaf, see Fig. 6.5c. In the PA mode enough of the excitation light was absorbed in the AuNP-PDMS coating to generate a weak planar US wave from which a noisy but spatially accurate US image of the leaf was reconstructed, see Fig. 6.5b.

6.3 Future work

6.3.1 Simultaneous-excitation dual-mode imaging

The dual-mode imaging system based on the planar FP scanner presented in this chapter was designed to acquire images of the two modes sequentially. This leads to a doubling of the acquisition time for a dual-mode image compared to a single US or PA image. Given an acquisition time for a single image of approximately 20 minutes, acquiring a dual-mode image would take approximately 40 minutes. This

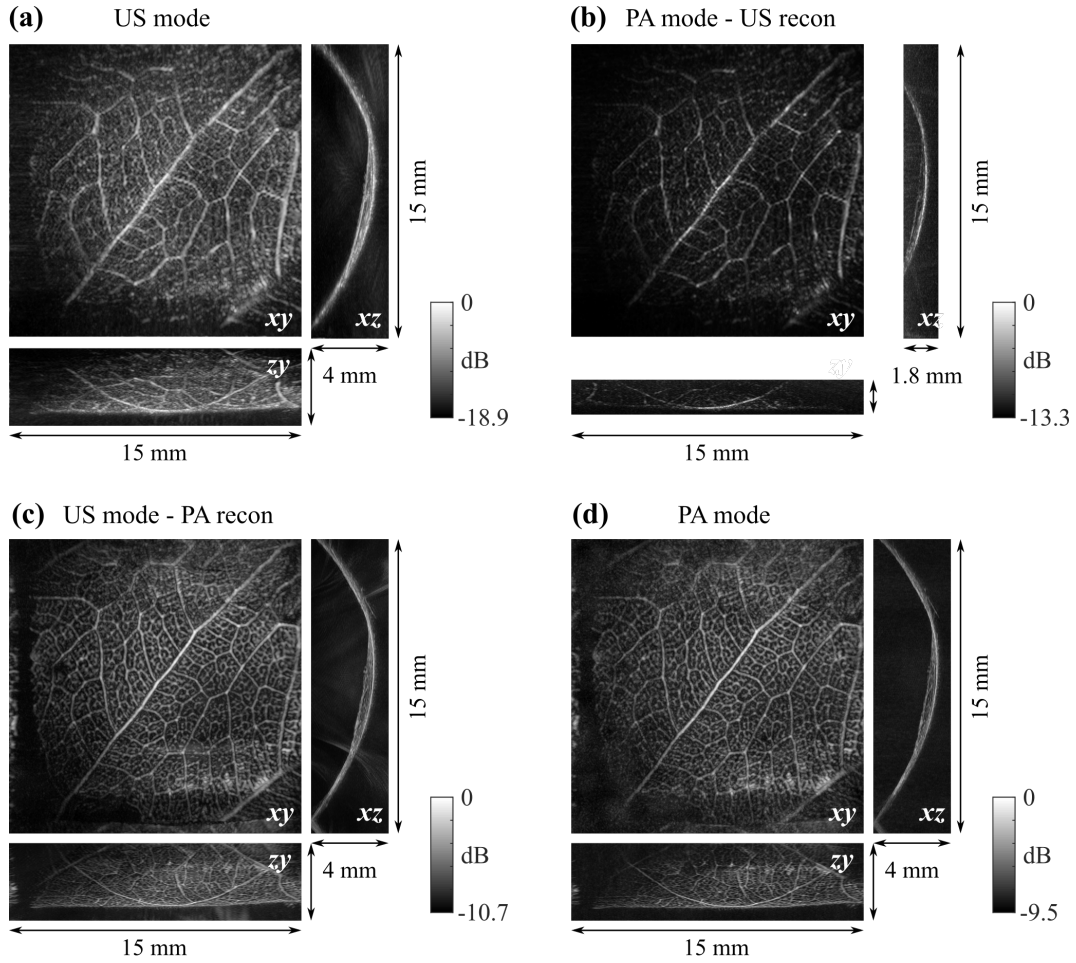


Figure 6.5: Crosstalk reconstructions compared to normal reconstructions from dual-mode acquisition data of polymer leaf. (a) US image, (b) US reconstruction of PA mode data, (c) PA reconstruction of US mode data, (d) PA image. Linear scale version shown in Fig. E.1.

long dual-mode acquisition time could limit the clinical applications of the system. Preferably, images of both modes are acquired simultaneously to reduce the total acquisition time. This can be done using the same excitation laser pulse to generate both US and PA signals simultaneously.

Simultaneous excitation using AuNP-PDMS. The simultaneous excitation of US and PA signals was demonstrated in this chapter for a AuNP-PDMS film used as a dichroic transmitter coating. The AuNP-PDMS coating was neither completely absorbing in the US mode, nor completely transparent in the PA mode (Fig. 6.2). This was shown to result in PA signals being detected in the US mode, and scattered

US waves detected in the PA mode, both of which were sufficient to reconstruct appreciable crosstalk images (Fig. 6.5). The leaf phantom imaged in this experiment had an ROI that was approximately 3 mm deep and positioned 4 mm away from the sensor, such that the signals from the two modes were separated in time. However, in a general imaging setup the imaging ROI does not usually fulfil this depth criterion. The signals from both modes will then overlap in the detected pressure time series, which would result in noise and blurry artefacts in images of both modes. If, however, the intensity of these crosstalk artefacts is low compared to actual image features, simultaneous excitation could be used to obtain an US and PA image from a single excitation pulse. We propose to test the severity of crosstalk artefacts in simulation.

Simulation of crosstalk artefacts. A first simulation could be of a single point source that is both an acoustic scatterer and an optical absorber, i.e. it appears in both image modes. To simulate simultaneous excitation the received pressure-time series from both US and PA modes simply need to be summed, optionally with weights to model the different amount of energy transmitted and absorbed in the dichroic coating. By using the summed sensor data to reconstruct images with either mode's reconstruction algorithm, the intensity of the crosstalk artefacts relative to the main reconstructed feature of the point source can be measured. The simulation can then be expanded to include a large number of scatterers and optical absorbers across the field of view, with some structures providing either acoustic or optical contrast. For example, the random scattering medium with a non-scattering hole inclusion, used in simulations in Chapter 4, could be modified to include optically absorbing features, e.g. point absorbers or small vessels, across the medium. This would test the effect of PA crosstalk artefacts on the image contrast of the US image.

Coded ultrasound generation. In the case that crosstalk artefacts severely impact the image quality of a single-excitation dual-mode image, we propose a method to make the US and PA signals in the combined time series separable. This would involve coding the optical ultrasound generation through a transmitter coating with

a spatially varying absorption profile in depth. In a simple example, this could be achieved by layering partially absorbing and non-absorbing layers to construct a layered dichroic transmitter coating. Using a single monopolar excitation pulse this would generate a non-monopolar, coded ultrasound pulse from the light absorbed in the layered coating, while still generating monopolar PA signals as previously. The US and PA signals could then be separated by deconvolving the received signal with the temporal shape of the coded ultrasound pulse, which would extract signals from acoustic scatterers as if the excitation light pulse were a monopolar pulse. The more complicated the coded US signal is the more likely will the deconvolution be able to separate the signals. This concept can be tested in simulation to try out increasingly complex coded US signals.

6.3.2 Temporal separation of PA and US signals

An alternative solution to separating the PA and US signals could be to offset them in time. This could be done by placing an optically and acoustically transparent stand-off pad between the FP sensor and the medium to delay the time-of-arrival of the back-scattered US waves. While simple, this approach would increase the distance of the imaging object from the sensor which can reduce the image quality as seen in Section 3.4. The PA and US signals could also be generated by two different excitation lasers pulsing with a slight time delay, of e.g. 20 μs , to ensure all signals from one mode are detected before signals of the other mode are generated.

6.4 Conclusion

The planar FP scanner was modified for dual-mode PA and US imaging. The FP sensor head was coated with a dichroic transmitter coating made from a AuNP-PDMS composite, replacing the US transmitter coating made from a CNT-PDMS composite used in the optical ultrasound scanner developed in Chapter 3. The dichroic transmitter coating allowed for wavelength-selective absorption enabling optical generation of planar US waves from light absorbed in the coating, and excitation of PA waves from light transmitted through the coating. The dual-mode imaging system based on the FP scanner was demonstrated to provide high-resolution

high-fidelity 3D dual-mode US and PA images of scattering structures, providing complementary contrast from optically absorbing and acoustically scattering structures. Simultaneous excitation of US and PA signals using a single excitation pulse was shown to yield appreciable images of both modes in preliminary imaging experiments with a strongly scattering and strongly absorbing phantom. Simulations and experiments to explore the potential of simultaneous excitation for dual-mode imaging were proposed.

Chapter 7

Conclusion

The aim of this thesis was to develop a dual-mode photoacoustic and ultrasound imaging system based on the planar FP scanner for detection and optical ultrasound generation of broadband planar waves in absorbing coatings. This was motivated by the need to add the morphological contrast of tissues to photoacoustic images, which ultrasound images could provide. For high-resolution superficial imaging applications the planar FP scanner was identified as a suitable ultrasound detector together with PDMS composite absorbers for optical ultrasound generation. Since photoacoustic imaging with the FP scanner had previously been demonstrated by Zhang *et al* [1], this work was primarily focused on developing the ultrasound modality before demonstrating dual-mode imaging with the scanner. To develop an ultrasound imaging system based on the FP scanner a number of challenges had to be overcome. These included the engineering challenge of combining the FP scanner with optically generated ultrasound, limitations in image quality and ways of overcome these.

In Chapter 3, an optical ultrasound imaging system based on the planar FP scanner was developed. Optical ultrasound generation was achieved by coating the sensor head of the FP scanner with an ultrasound transmitting film made of a CNT-PDMS composite absorber and exciting it with nanosecond laser pulses to generate plane-wave ultrasound pulses. The FP scanner was used to detect the scattered acoustic

field in reflection mode. The optically generated plane waves were characterised for their peak pressure, planarity and bandwidth. The heat generated during optical ultrasound generation was shown to not impact the acoustic sensitivity of the FP scanner. The system provided high-resolution high-fidelity 3D ultrasound images of scattering structures, tissue mimicking phantoms and *ex vivo* tissues. The work in this chapter is the first demonstration of an all-optical plane-wave ultrasound imaging system based on the planar FP scanner for detection and optical ultrasound generation.

In Chapter 4, limitations in the image quality of a broadband plane-wave ultrasound imaging system were investigated by undertaking numerical simulations. A simulation platform was developed based on a time-domain pseudospectral forward model and a continuum model to represent acoustic scattering media. The effect of the frequency content of the detected signals and the effect of spatial aliasing on the image quality were studied. Spatial undersampling was found to limit image contrast in broadband plane-wave ultrasound images. Spatially aliased high frequencies created grating lobe artefacts which contributed to image grain across the field of view, and lowered the image contrast. A broadband system that includes low frequencies that are sufficiently spatially sampled was shown to reduce the impact of grating lobes, and thus contribute to higher image contrast and improve image fidelity. The detrimental effect of spatial aliasing on image contrast was found to be more severe near the sensor and at lateral positions further away from the centre of the sensor. The work in this chapter is, to our knowledge, the first attempt at simulating ultrasound imaging for a broadband plane-wave system.

In Chapter 5, compounding methods to improve the image quality of the optical ultrasound imaging system were explored in simulations and experimentally. Incoherent frequency compounding was shown to be effective for broadband plane-wave ultrasound images, improving contrast at the expense of spatial resolution. The more broadband the individual filters used in incoherent frequency compounding, the more the resolution performance can be retained while still improving contrast.

Angle compounding was explored for a broadband plane-wave ultrasound system. In simulations, image contrast was shown to be improved particularly when compounding coherently due the smoothing of the fine-grain speckle pattern. Preliminary work was done to explore the feasibility of angle compounding with the FP scanner system. This involved presenting a possible system design where angled plane waves are optically generated by scanning a focused excitation beam across an absorbing film. An angle magnification system and a source amplification set-up were tested to show that sufficient scanning speed and excitation energy could be achieved with the appropriate hardware. Scattering structures were imaged with an angled ultrasound transmitter coating to test the reconstruction algorithm and identify registration problems between frames. The work in this chapter is the first demonstration applying ultrasound compounding techniques to a broadband plane-wave system.

In Chapter 6, a dual-mode photoacoustic and ultrasound imaging system based on the planar FP scanner was demonstrated. A dichroic transmitter coating made from a AuNP-PDMS composite enabled wavelength-selective absorption of light. Absorption at one wavelength generated planar ultrasound waves, while transmission at another wavelength suitable for absorption in blood allowed for excitation of photoacoustic waves. The system obtained high-resolution high-fidelity 3D dual-mode photoacoustic and ultrasound images of scattering structures, providing complementary contrast from optically absorbing and acoustically scattering structures. The crosstalk between the two modes of the system could be exploited in some circumstances to generate images for both modes from a single excitation pulse. The work in this chapter is the first demonstration of a dual-mode photoacoustic and ultrasound imaging system based on the planar FP scanner and a dichroic transmitter coating.

Overall, this thesis represents a body of work centred on the development of a broadband plane-wave ultrasound imaging system based on the planar FP scanner and PDMS composites for optical ultrasound generation. Possible clinical applications

of this system are high-resolution imaging of the skin and superficial lymph nodes. The system can be modified for endoscopic use by placing both the sensor [35] and the transmitter coating [57] at the distal end of a fibre bundle, and delivering the interrogation and excitation light through the bundle. This would have the advantage of a higher element density compared to endoscopic piezoelectric arrays. These modifications would also make the system MRI compatible since separating the galvanometer mirrors from the sensor head makes it completely free of electronics and metallic components. With the demonstration of dual-mode photoacoustic and ultrasound imaging, the system was shown to obtain high-resolution dual-mode images, potentially capable of adding complementary morphological ultrasound contrast to photoacoustic vascular images.

Appendices

Appendix A

Reconstruction code for normal plane-wave ultrasound imaging

```
function F = kspacePlaneRecon_US(p, dy, dz, dt, c, varargin)
%KSPACEPLANERECON_US 3D planar FFT reconstruction for plane wave ultrasound
%                      reflection imaging
%
% DESCRIPTION:
%   adapted from kspacePlaneRecon (which is for photoacoustic imaging).
%
% USAGE:
%   F_xyz = kspacePlaneRecon_US(p_tyz, dy, dz, dt, c)
%   F_xyz = kspacePlaneRecon_US(p_tyz, dy, dz, dt, c, ...)
%
% INPUTS:
%   p_tyz      - pressure time-series recorded over an evenly spaced
%               array of sensor points on a line (indexed as t, y, z)
%   dy, dz     - spatial step [m]
%   dt         - time step [s]
%   c          - acoustically-homogeneous sound speed [m/s]
%
% OPTIONAL INPUTS:
%   Optional 'string', value pairs that may be used to modify the default
%   computational settings.
%
%   'DataOrder' - String input which sets the data order (default =
%                 'tyz'). Valid inputs are 'tyz' and 'yzt'.
%   'Interp'     - String input controlling the interpolation method
```

```

%           used by interp3 in the reconstruction (default =
%           '*nearest').
%   'Plot'      - Boolean controlling whether a plot of the reconstructed
%                 estimate of the initial acoustic pressure distribution
%                 is produced (default = false).
%   'PosCond'   - Boolean controlling whether a positivity condition is
%                 enforced on the reconstructed estimate of the initial
%                 acoustic pressure distribution (default = false).
%
% OUTPUTS:
%   F_xyz       - image (indexed as x, y, z)
%
% ABOUT:
%   author      - Bradley Treeby and Ben Cox
%   date        - 2nd July 2009
%   update      - 21st June 2017 (Ben - mod for pwUS)
%   last update - 6 July 2021 (Khoa - corrections for pwUS,
%                               rename output & tidy comments &
%                               explicitly distinguish between
%                               receive and object k space)
%
% define defaults
num_req_inputs = 5;
data_order = 'tyz';
interp_method = '*nearest';
positivity_cond = false;

% replace with user defined values if provided
if nargin < num_req_inputs
    error('Incorrect number of inputs.');
```

```

elseif ~isempty(varargin)
    for input_index = 1:2:length(varargin)
        switch varargin{input_index}
            case 'DataOrder'
                data_order = varargin{input_index + 1};
                if ~strcmp(data_order, 'tyz') && ~strcmp(data_order, 'yzt')
                    error('Unknown setting for optional input DataOrder.');
```

```

                end
            case 'Interp'
                interp_method = varargin{input_index + 1};
            case 'PosCond'
                positivity_cond = varargin{input_index + 1};
            otherwise
                error(['Unknown optional input ' varargin{input_index}]);
        end
    end
end

```

```

        end
    end

    % reorder the data to p(t, y, z) if needed
    if strcmp(data_order, 'yzt')
        p = permute(p, [3, 1, 2]);
    end

    % mirror the time domain data about t = 0 to allow the cosine transform in
    % the t direction to be computed using an FFT
    p = [flip(p, 1); p(2:end, :, :)];

    % extract the size of mirrored input data
    [Nt, Ny, Nz] = size(p);

    % update command line status
    disp('Running k-Wave planar reconstruction...');
    disp([' grid size: ' num2str((Nt+1)/2) ' by ' num2str(Ny) ' by ' ...
        num2str(Nz) ' grid points']);
    disp([' interpolation mode: ' interp_method]);

    % create a computational grid that is evenly spaced in w, ky, and kz (the
    % receive k-space), where the kx component is w/c, so Nx = Nt and dx = dt*c
    kgrid_rec = kWaveGrid(Nt, dt*c, Ny, dy, Nz, dz);

    % from the grid for kx, create a computational grid for w using the
    % relation dx = dt*c; this represents the initial sampling of p(w, ky, kz)
    w = c .* kgrid_rec.kx;

    % calculate the scaling factor using the value of kx, where
    % kx = sqrt( (w/c).^2 - kgrid.ky.^2 - kgrid.kz.^2 )
    sf = sqrt( (w./c).^2 - kgrid_rec.ky.^2 - kgrid_rec.kz.^2 );

    % compute the FFT of the input data p(t, y, z) to yield p(w, ky, kz) and
    % scale with sf to give F(w, ky, kz)
    F = sf .* fftshift(fftn(ifftshift(p)));

    % remove unused variables
    clear sf;

    % exclude the inhomogeneous part of the wave
    F(abs(w) < (c * sqrt(kgrid_rec.ky.^2 + kgrid_rec.kz.^2))) = 0;

    % create a new computational grid that is evenly spaced in kx', ky' and kz'
    % (the object k-space)
    kgrid_obj = kWaveGrid(Nt, dt*c, Ny, dy, Nz, dz);

```

```

% remap the computational grid for kx' onto w using the dispersion relation
%  $w/c = (kx'^2 + ky'^2 + kz'^2)/(2*kx')$ 
% This gives an w grid that is evenly spaced in kx'. This is used for the
% interpolation from F(w, ky, kz) to F(kx', ky', kz'). Only real w is taken
% to force kx' (and thus x) to be symmetrical about 0 after interpolation.
w_new = c .* kgrid_obj.k.^2 ./ (2 * kgrid_obj.kx) ;
w_new(kgrid_obj.kx==0) = 0;

% compute the interpolation from F(w, ky, kz) to F(kx', ky', kz'); for a
% matrix indexed as [M, N, P], the axis variables must be given in the
% order N, M, P
F = interp3(kgrid_rec.ky, w, kgrid_rec.kz, F, kgrid_obj.ky, w_new, ...
            kgrid_obj.kz, interp_method);

% remove unused variables
clear kgrid_rec kgrid_obj w;

% set values outside the interpolation range to zero
F(isnan(F)) = 0;

% compute the inverse FFT of F(kx', ky', kz') to yield F(x, y, z)
F = real(fftshift(ifftn(ifftshift(F))));

% remove the left part of the mirrored data which corresponds to the
% negative part of the mirrored time data
F = F( ((Nt + 1) / 2):Nt, :, :);

% correct the scaling - the forward FFT is computed with a spacing of dt
% and the reverse requires a spacing of dz = dt*c, the reconstruction
% assumes that p0 is symmetrical about z, and only half the plane collects
% data (first approximation to correcting the limited view problem)
F = 2 * 2 * F ./ c;

% enforce positivity condition
if positivity_cond
    disp(' applying positivity condition...');
    F(F < 0) = 0;
end

end

```

Appendix B

Mapping of optically generated ultrasound from a CNT-PDMS film

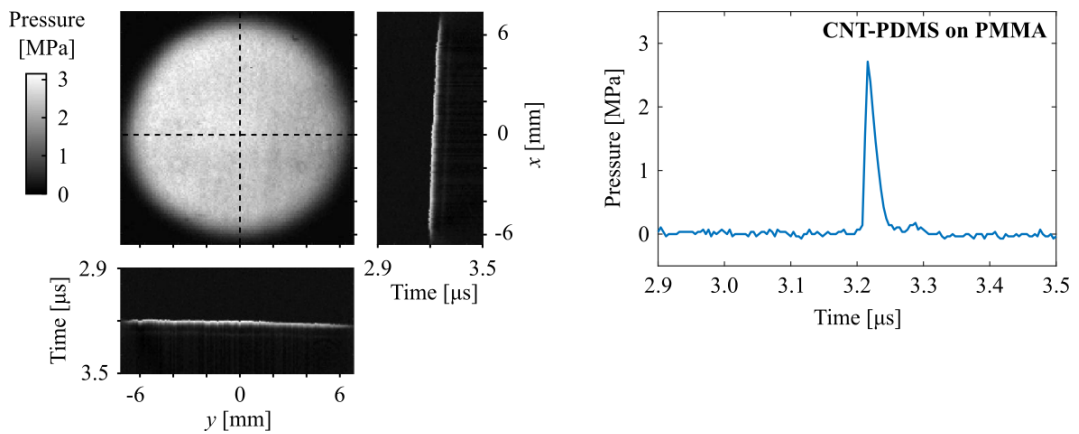


Figure B.1: Map of peak pressure distribution in xy plane, profiles through the wavefront in x and y , and pressure time series at the centre of the sensor produced by a CNT-PDMS composite transmitter coating on a PMMA slab. Figure adapted from [83] © 2021 IEEE.

Appendix C

Pulse duration variation of excitation laser

In Section 3.3.1.3, the non-linear propagation of optically generated ultrasound pulses was studied by varying the incident fluence on the CNT-PDMS transmitter coating. This was done by inserting ND filters with a range of optical densities to attenuate the excitation light. An alternative method to vary the fluence is to change the Q-switch (QS) delay on the excitation laser (Quantel Laser, Ultra 50) to vary its pulse energy. The pulse energy of the excitation laser is increased by decreasing the QS delay.

Measurement for non-linear propagation. The QS delay was varied from 296 to 143 μs , resulting in pulse energies from 1 to 20 mJ. Similar to Section 3.3.1.3, the generated ultrasound waves were detected after a propagation distance of 8.5 mm at a single interrogation point on the reference FP sensor with a temporal sampling interval of 4 ns. The pressure time series were Fourier transformed to obtain frequency spectra. Ultrasound waves with peak pressure from 40 kPa to 2.3 MPa were generated, which should exhibit varying degrees of non-linear propagation. A shorter QS delay, giving larger pulse energy and thus generating higher peak pressures, yielded acoustic pulses that were narrower and sharper towards the front edge, resulting in broader frequency spectra, see Fig. C.1. This result may initially indi-

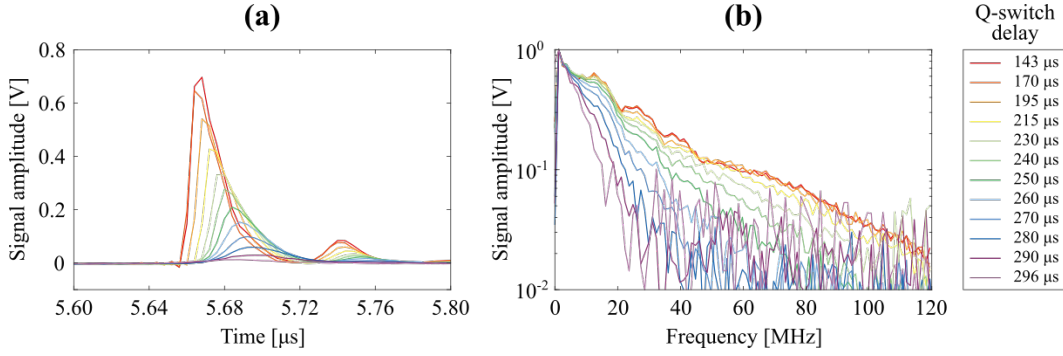


Figure C.1: Non-linear propagation demonstrated with LUS from CNT on PMMA for a range of QS delays to vary the fluence. Detected at 8.5 mm distance in water with broadband reference FP sensor. **(a)** Pressure time series in the centre of the excitation beam with a temporal sampling step of 4 ns and over 100 averages, and **(b)** corresponding normalised frequency spectra.

cate that non-linear propagation was detected for higher pressure amplitude pulses. However, it relies on the assumption that the optical pulse duration remained identical for all QS delays.

Pulse duration variation. In this paragraph we show that changing the QS delay of the excitation laser changes the optical pulse duration. This was demonstrated by generating optical ultrasound pulses with long QS delays which gave peak pressures in the range of 10 to 150 kPa. These low pressures ensured linear propagation of the acoustic waves meaning the acoustic pulse shape remained largely unchanged during propagation (neglecting frequency dependent acoustic attenuation, which if all pulses had the same frequency content would affect them equally regardless of peak pressure amplitude). Assuming a linear conversion of optical energy to pressure, the acoustic pulse shape can be taken as a measure for the optical pulse duration. Since the acoustic pulse shape changed with the different QS delays, see Fig. C.2, the optical pulse duration must also depend on the QS delay. Longer QS delays appeared to give a longer optical pulse which lead to lower acoustic bandwidth. Thus the variation of the acoustic pulse shape in Fig. C.1 cannot be attributed solely to non-linear propagation, but is in part owed to the change in pulse duration with different QS delays.

Conclusion. While the Q-switch delay on the excitation laser provides a convenient

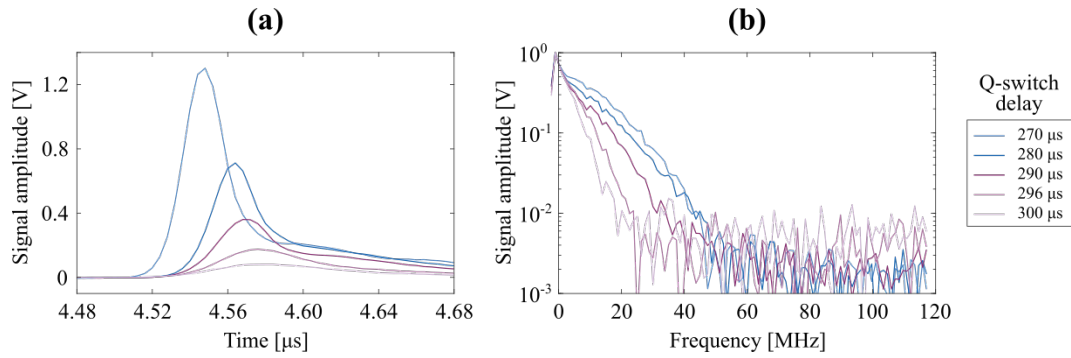


Figure C.2: Acoustic pulse shape variation of LUS from CNT on PMMA for a range of long QS delays to ensure linear acoustic propagation, demonstrating optical pulse duration variation. LUS detected at 6.8 mm distance in water with broadband reference FP sensor. **(a)** Pressure time series in the centre of the excitation beam with a temporal sampling step of 4 ns and over 100 averages, and **(b)** corresponding normalised frequency spectra.

method to vary the pulse energy, it also changes the optical pulse duration. This is an important detail to keep in mind when using the Q-switch delay. It is not a suitable tool to vary the pulse energy if the pulse shape and the frequency content of the optical ultrasound generation are to remain constant for all measurements.

Appendix D

Screenshots from clinical ultrasound scanner

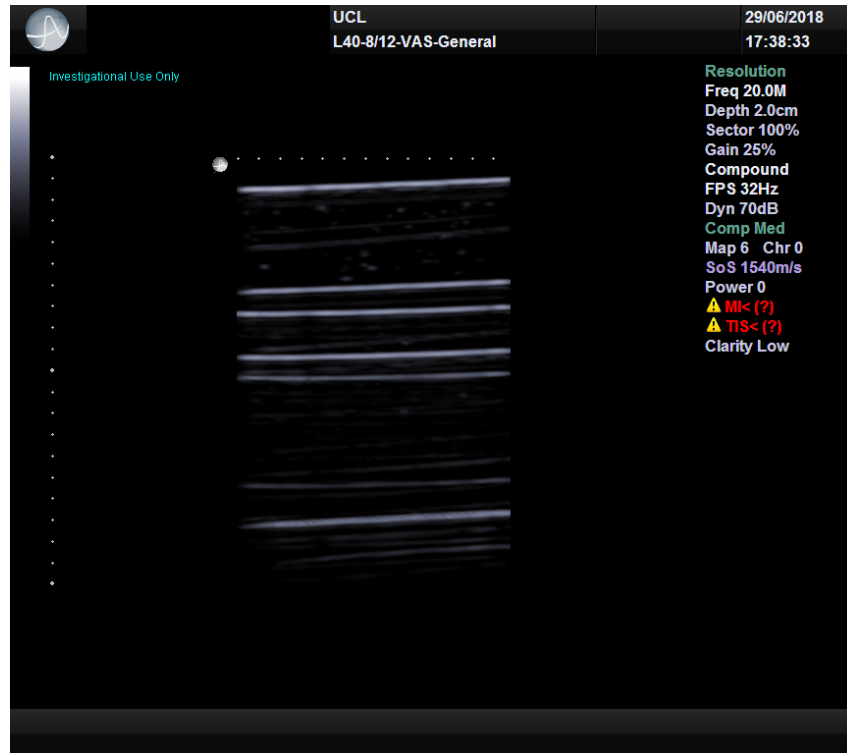


Figure D.1: Screenshot from clinical scanner imaging a layered gel-wax phantom corresponding to Fig. 3.19b.

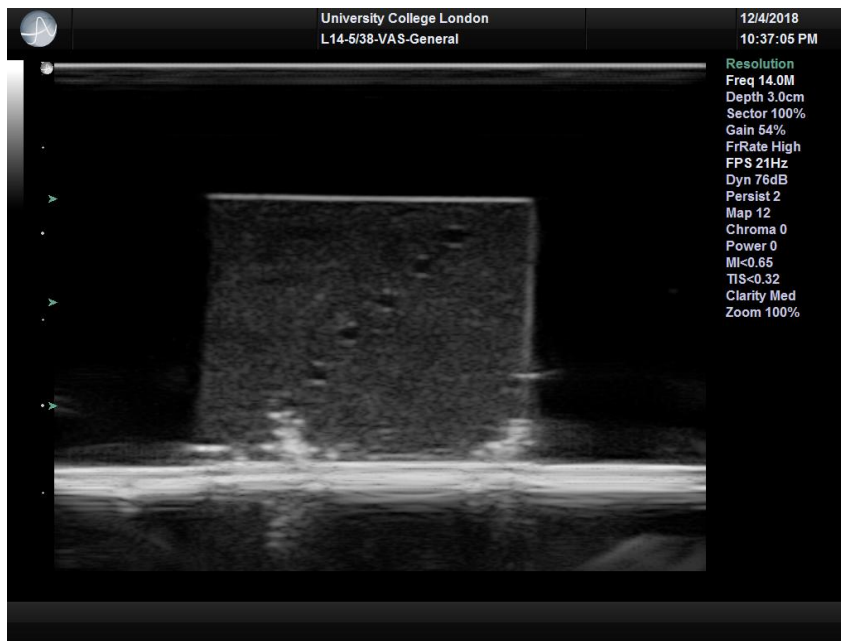


Figure D.2: Screenshot from clinical scanner imaging an agar-based scattering phantom corresponding to Fig. 3.20b.

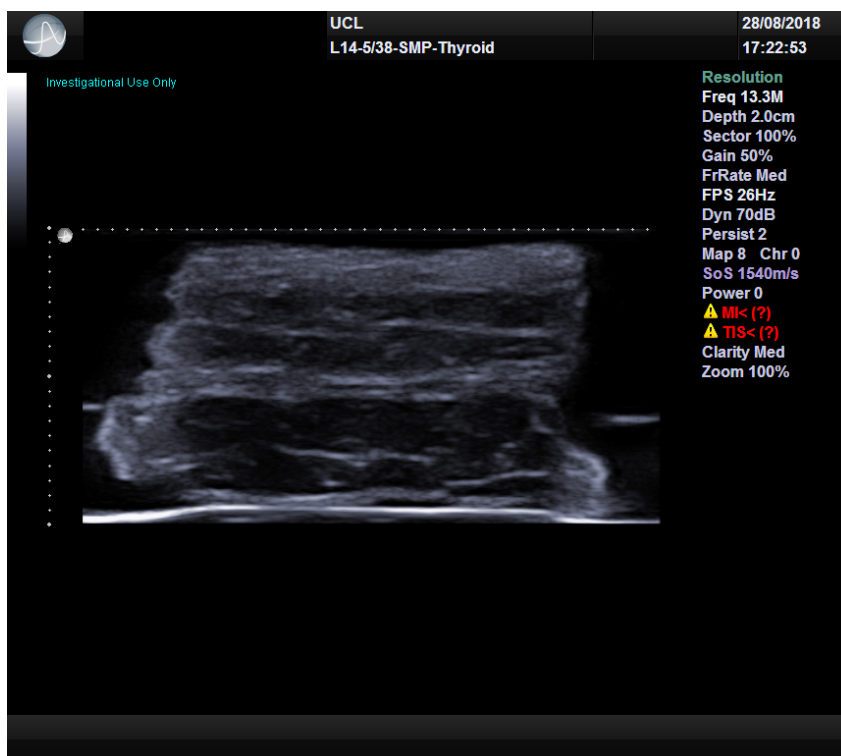


Figure D.3: Screenshot from clinical scanner imaging an *ex vivo* pork belly corresponding to Fig. 3.21b.

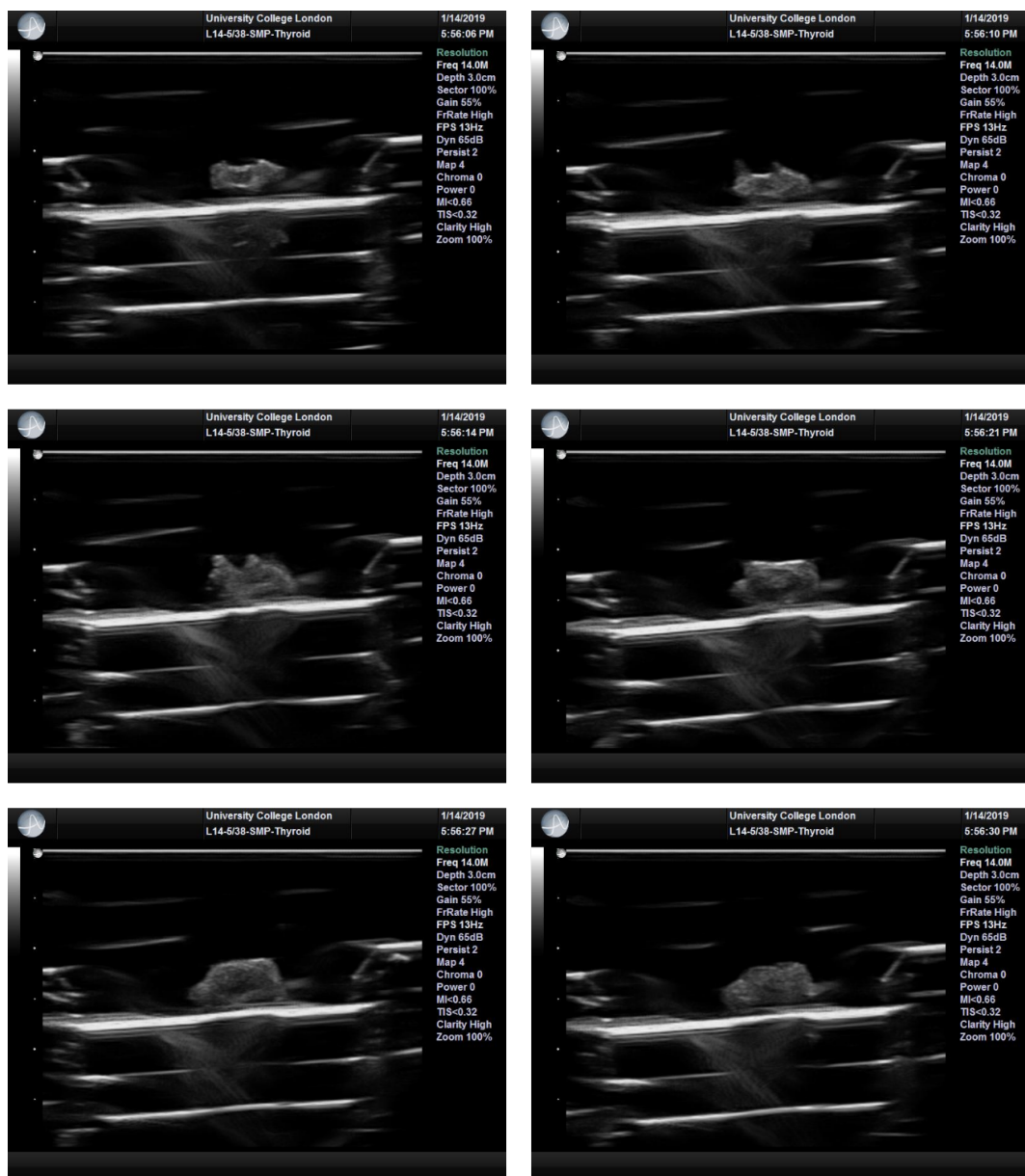


Figure D.4: Screenshots from clinical scanner imaging an *ex vivo* human lymph node corresponding to Fig. 3.23d.

Appendix E

Dual-mode images on linear scale

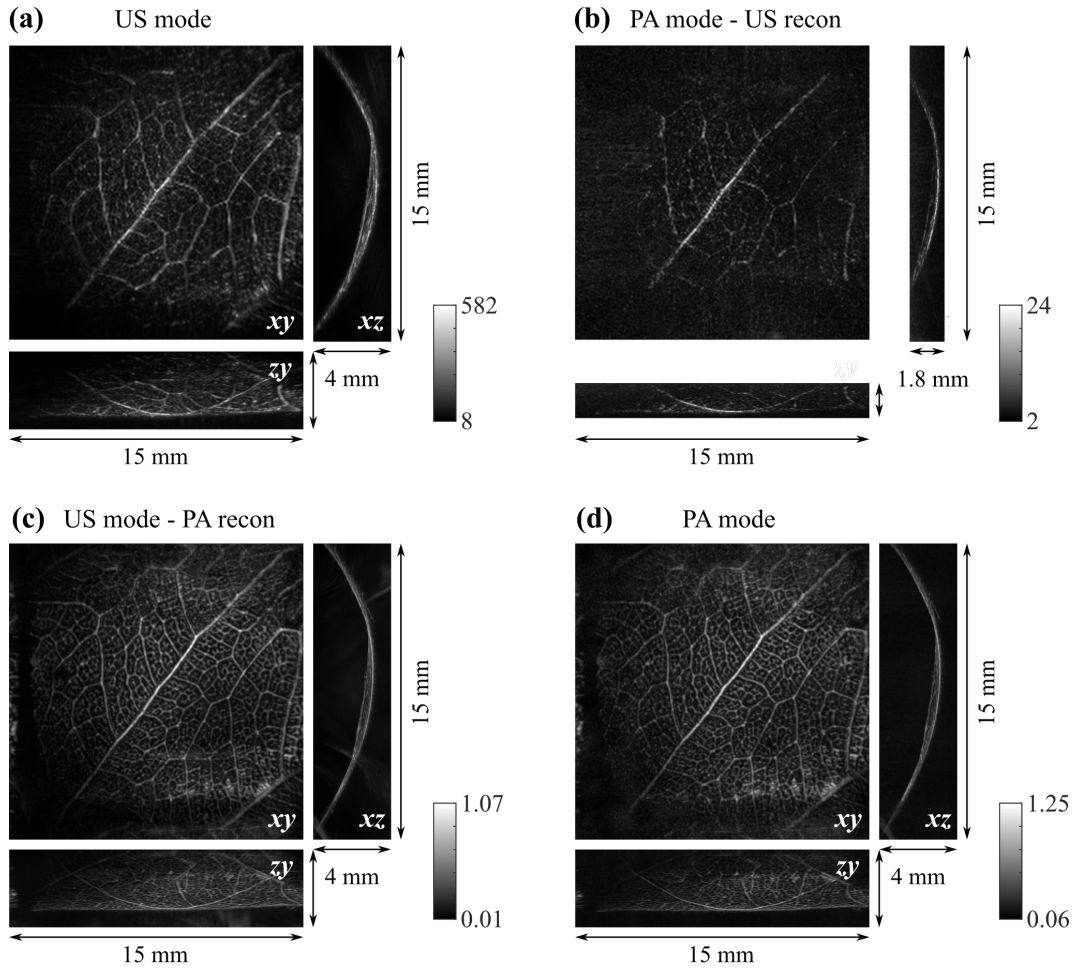


Figure E.1: Crosstalk reconstructions compared to normal reconstructions from dual-mode acquisition data of polymer leaf. (a) US image, (b) US reconstruction of PA mode data, (c) PA reconstruction of US mode data, (d) PA image.

Publications

Journal paper

K. Pham, S. Noimark, N. Huynh, E. Zhang, F. Kuklis, J. Jaros, A. Desjardins, B. Cox, and P. Beard, “Broadband all-optical plane-wave ultrasound imaging system based on a Fabry-Perot scanner,” *IEEE Transactions on Ultrasonics, Ferroelectrics, and Frequency Control*, vol. 68, no. 4, pp. 1007–1016, 2021.

Conference presentations

K. Pham, N. T. Huynh, E. Zhang, S. Noimark, A. Desjardins, B. Cox, and P. Beard, “High-resolution three-dimensional all-optical ultrasound imaging system based on a Fabry-Perot scanner,” in *6th International Symposium on Laser Ultrasonics*, Nottingham, United Kingdom, 2018.

K. Pham, S. Noimark, N. T. Huynh, E. Zhang, A. Desjardins, B. Cox, and P. Beard, “Dual mode photoacoustic and ultrasound imaging system based on a Fabry-Perot scanner,” in *SPIE Photons Plus Ultrasound: Imaging and Sensing*, San Francisco, CA, USA, 2019.

Bibliography

- [1] E. Zhang, J. Laufer, and P. Beard, “Backward-mode multiwavelength photoacoustic scanner using a planar Fabry-Perot polymer film ultrasound sensor for high-resolution three-dimensional imaging of biological tissues,” *Appl. Opt.*, vol. 47, no. 4, pp. 561–77, 2008.
- [2] P. Beard, “Biomedical photoacoustic imaging,” *Interface focus*, vol. 1, no. 4, pp. 602–31, 2011.
- [3] J. Laufer, P. Johnson, E. Zhang, B. Treeby, B. Cox, B. Pedley, and P. C. Beard, “In vivo preclinical photoacoustic imaging of tumor vasculature development and therapy,” *Journal of biomedical optics*, vol. 17, no. 5, p. 056016, 2012.
- [4] A. P. Jathoul, J. Laufer, O. Ogunlade, B. Treeby, B. Cox, E. Zhang, P. Johnson, A. R. Pizzey, B. Philip, T. Marafioti, M. F. Lythgoe, R. B. Pedley, M. A. Pule, and P. Beard, “Deep in vivo photoacoustic imaging of mammalian tissues using a tyrosinase-based genetic reporter,” *Nature Photonics*, vol. 9, pp. 239–246, 2015.
- [5] J. J. Niederhauser, M. Jaeger, R. Lemor, P. Weber, and M. Frenz, “Combined ultrasound and optoacoustic system for real-time high-contrast vascular imaging in vivo,” *IEEE Transactions on Medical Imaging*, vol. 24, no. 4, pp. 436–440, 2005.
- [6] R. G. M. Kolkman, P. J. Brands, W. Steenbergen, and T. G. van Leeuwen,

- “Real-time in vivo photoacoustic and ultrasound imaging,” *Journal of Biomedical Optics*, vol. 13, no. 5, p. 050510, 2008.
- [7] P. J. van den Berg, R. Bansal, K. Daoudi, W. Steenbergen, and J. Prakash, “Preclinical detection of liver fibrosis using dual-modality photoacoustic/ultrasound system,” *Biomedical Optics Express*, vol. 7, no. 12, p. 5081, 2016.
- [8] X. L. Deán-Ben, E. Merčep, and D. Razansky, “Hybrid-array-based optoacoustic and ultrasound (OPUS) imaging of biological tissues,” *Applied Physics Letters*, vol. 110, no. 20, p. 203703, 2017.
- [9] M. Kuniyil Ajith Singh, N. Sato, and T. Agano, “Acousticx: Handheld led-based multispectral photoacoustic/ultrasound imaging system,” *Nature Methods*, 11 2017.
- [10] M. Kuniyil Ajith Singh, M. Dantuma, F. Kalloor Joseph, S. Manohar, and W. Steenbergen, “Breast imaging using an LED-based photoacoustic and ultrasound imaging system: a proof-of-concept study,” *Proceedings of SPIE*, no. March 2021, p. 89, 2021.
- [11] J. Joseph, B. Ma, and B. T. Khuri-Yakub, “Applications of Capacitive Micro-machined Ultrasonic Transducers: A Comprehensive Review,” *IEEE Transactions on Ultrasonics, Ferroelectrics, and Frequency Control*, vol. 69, no. 2, pp. 456–467, 2022.
- [12] D. Ren, Y. Sun, J. Shi, and R. Chen, “A review of transparent sensors for photoacoustic imaging applications,” *Photonics*, vol. 8, no. 8, 2021.
- [13] S. Vaithilingam, T. J. Ma, Y. Furukawa, I. O. Wygant, X. Zhuang, A. De La Zerda, Ö. Oralkan, A. Kamaya, S. S. Gambhir, R. B. Jeffrey, and B. T. Khuri-Yakub, “Three-dimensional photoacoustic imaging using a two-dimensional CMUT array,” *IEEE Transactions on Ultrasonics, Ferroelectrics, and Frequency Control*, vol. 56, no. 11, pp. 2411–2419, 2009.

- [14] J. Chen, M. Wang, J. C. Cheng, Y. H. Wang, P. C. Li, and X. Cheng, “A photoacoustic imager with light illumination through an infrared-transparent silicon CMUT array,” *IEEE Transactions on Ultrasonics, Ferroelectrics, and Frequency Control*, vol. 59, no. 4, pp. 766–775, 2012.
- [15] A. K. Ilkhechi, C. Ceroici, Z. Li, and R. Zemp, “Transparent capacitive micro-machined ultrasonic transducer (CMUT) arrays for real-time photoacoustic applications,” *Optics Express*, vol. 28, no. 9, p. 13750, 2020.
- [16] S.-L. Chen, “Review of laser-generated ultrasound transmitters and their applications to all-optical ultrasound transducers and imaging,” *Applied Sciences*, vol. 7, no. 1, p. 25, 2016.
- [17] S. Noimark, R. J. Colchester, R. K. Poduval, E. Maneas, E. J. Alles, T. Zhao, E. Z. Zhang, M. Ashworth, E. Tsolaki, A. H. Chester, N. Latif, S. Bertazzo, A. L. David, S. Ourselin, P. C. Beard, I. P. Parkin, I. Papakonstantinou, and A. E. Desjardins, “Polydimethylsiloxane composites for optical ultrasound generation and multimodality imaging,” *Advanced Functional Materials*, vol. 28, no. 9, pp. 1–16, 2018.
- [18] S. Rajagopal, T. Sainsbury, B. E. Treeby, and B. T. Cox, “Laser generated ultrasound sources using carbon-polymer nanocomposites for high frequency metrology,” *J. Acoust. Soc. Am.*, vol. 144, no. 2, pp. 584–597, 2018.
- [19] S. Noimark, R. J. Colchester, B. J. Blackburn, E. Z. Zhang, E. J. Alles, S. Ourselin, P. C. Beard, I. Papakonstantinou, I. P. Parkin, and A. E. Desjardins, “Carbon-nanotube-PDMS composite coatings on optical fibers for all-optical ultrasound imaging,” *Advanced Functional Materials*, vol. 26, pp. 8390–8396, dec 2016.
- [20] A. G. Bell, “On the production and reproduction of sound by light,” *Am. J. Sci.*, vol. 20, pp. 305—24, 1880.
- [21] B. Cox, J. G. Laufer, S. R. Arridge, and P. C. Beard, “Quantitative spec-

- troscopic photoacoustic imaging: a review,” *J. Biomed. Opt.*, vol. 17, no. 6, p. 061202, 2012.
- [22] S. L. Jacques, “Optical properties of biological tissues: a review,” *Physics in Medicine and Biology*, vol. 58, no. 11, pp. R37–R61, 2013.
- [23] J. A. Guggenheim, T. J. Allen, A. Plumb, E. Z. Zhang, M. Rodriguez-Justo, S. Punwani, and P. C. Beard, “Photoacoustic imaging of human lymph nodes with endogenous lipid and hemoglobin contrast,” *Journal of Biomedical Optics*, vol. 20, no. 5, p. 050504, 2015.
- [24] B. Dong, C. Sun, and H. F. Zhang, “Optical detection of ultrasound in photoacoustic imaging,” *IEEE Transactions on Biomedical Engineering*, vol. 64, no. 1, pp. 4–15, 2017.
- [25] G. Wissmeyer, M. A. Pleitez, A. Rosenthal, and V. Ntziachristos, “Looking at sound: optoacoustics with all-optical ultrasound detection,” *Light: Science and Applications*, vol. 7, no. 53, 2018.
- [26] H. Lamela, D. Gallego, and A. Oraevsky, “Optoacoustic imaging using fiber-optic interferometric sensors,” *Opt. Lett.*, vol. 34, pp. 3695–3697, Dec 2009.
- [27] G. Paltauf, R. Nuster, M. Haltmeier, and P. Burgholzer, “Photoacoustic tomography using a mach-zehnder interferometer as an acoustic line detector,” *Appl. Opt.*, vol. 46, pp. 3352–3358, Jun 2007.
- [28] H. Li, B. Dong, Z. Zhang, H. F. Zhang, and C. Sun, “A transparent broadband ultrasonic detector based on an optical micro-ring resonator for photoacoustic microscopy,” *Scientific Reports*, vol. 4, no. 4496, 2014.
- [29] W. J. Westerveld, M. Mahmud-Ul-Hasan, R. Shnaiderman, V. Ntziachristos, X. Rottenberg, S. Severi, and V. Rochus, “Sensitive, small, broadband and scalable optomechanical ultrasound sensor in silicon photonics,” *Nature Photonics*, vol. 15, pp. 341–345, may 2021.

- [30] K. O. Hill and G. Meltz, "Fiber bragg grating technology fundamentals and overview," *Journal of Lightwave Technology*, vol. 15, pp. 1263–1276, 1997.
- [31] G. Wissmeyer, D. Soliman, R. Shnaiderman, A. Rosenthal, and V. Ntziachristos, "All-optical optoacoustic microscope based on wideband pulse interferometry," *Opt. Lett.*, vol. 41, pp. 1953–1956, May 2016.
- [32] A. Rosenthal, M. Ángel Araque Caballero, S. Kellnberger, D. Razansky, and V. Ntziachristos, "Spatial characterization of the response of a silica optical fiber to wideband ultrasound," *Opt. Lett.*, vol. 37, pp. 3174–3176, Aug 2012.
- [33] A. Rosenthal, M. Omar, H. Estrada, S. Kellnberger, D. Razansky, and V. Ntziachristos, "Embedded ultrasound sensor in a silicon-on-insulator photonic platform," *Applied Physics Letters*, vol. 104, no. 021116, 2014.
- [34] J. A. Guggenheim, E. Z. Zhang, and P. C. Beard, "A method for measuring the directional response of ultrasound receivers in the range 0.3 MHz to 80 MHz using a laser generated ultrasound source," *IEEE Transactions on Ultrasonics, Ferroelectrics, and Frequency Control*, no. April, pp. 1–8, 2017.
- [35] R. Ansari, E. Z. Zhang, A. E. Desjardins, and P. C. Beard, "All-optical forward-viewing photoacoustic probe for high-resolution 3D endoscopy," *Light: Science & Applications*, vol. 7, no. 75, 2018.
- [36] K. P. Köstli, M. Frenz, H. Bebie, and H. P. Weber, "Temporal backward projection of optoacoustic pressure transients using Fourier transform methods," *Physics in Medicine and Biology*, vol. 46, no. 7, pp. 1863–1872, 2001.
- [37] P. Kruizinga, B. Cox, N. De Jong, P. Beard, A. F. Van Der Steen, and G. Van Soest, "Plane wave ultrasound imaging with a broadband photoacoustic source," *IEEE International Ultrasonics Symposium*, pp. 1414–1416, 2012.
- [38] R. M. White, "Generation of Elastic Waves by Transient Surface Heating,"

Journal of Applied Physics, vol. 34, no. 3559, 1963.

- [39] T. Lee, H. W. Baac, Q. Li, and L. J. Guo, “Efficient Photoacoustic Conversion in Optical Nanomaterials and Composites,” *Advanced Optical Materials*, vol. 6, no. 24, 2018.
- [40] S. Kang, Y. Yoon, J. Kim, and W. Kim, “Thermoelastic response of thin metal films and their adjacent materials,” *Applied Physics Letters*, vol. 102, no. 2, 2013.
- [41] T. Lee and L. J. Guo, “Highly Efficient Photoacoustic Conversion by Facilitated Heat Transfer in Ultrathin Metal Film Sandwiched by Polymer Layers,” *Advanced Optical Materials*, vol. 5, no. 2, pp. 1–9, 2017.
- [42] F. Schneider, J. Draheim, R. Kamberger, and U. Wallrabe, “Process and material properties of polydimethylsiloxane (pdms) for optical mems,” *Sensors and Actuators A: Physical*, vol. 151, no. 2, pp. 95–99, 2009.
- [43] E. J. Alles, J. Heo, S. Noimark, R. J. Colchester, I. P. Parkin, H. W. Baac, and A. E. Desjardins, “Acoustical characterisation of carbon nanotube-loaded polydimethylsiloxane used for optical ultrasound generation,” *IEEE International Ultrasonics Symposium Proceedings*, 2017.
- [44] Y. Hou, S. Ashkenazi, S.-w. Huang, and M. O’Donnell, “Improvements in optical generation of high-frequency ultrasound,” *IEEE Transactions on Ultrasonics, Ferroelectrics, and Frequency Control*, vol. 54, no. 3, pp. 682–686, 2007.
- [45] D. Thompson, D. Gasteau, and S. Manohar, “Spatially compounded plane wave imaging using a laser-induced ultrasound source,” *Photoacoustics*, vol. 18, no. 100154, 2020.
- [46] B. Y. Hsieh, J. Kim, J. Zhu, S. Li, X. Zhang, and X. Jiang, “A laser ultra-

- sound transducer using carbon nanofibers-polydimethylsiloxane composite thin film,” *Applied Physics Letters*, vol. 106, no. 2, 2015.
- [47] W. Y. Chang, W. Huang, J. Kim, S. Li, and X. Jiang, “Candle soot nanoparticles-polydimethylsiloxane composites for laser ultrasound transducers,” *Applied Physics Letters*, vol. 107, no. 16, 2015.
- [48] J. Tian, Q. Zhang, and M. Han, “Distributed fiber-optic laser-ultrasound generation based on ghost-mode of tilted fiber bragg gratings,” *Opt. Express*, vol. 21, pp. 6109–6114, Mar 2013.
- [49] Y. Hou, J. S. Kim, H. Sheng-Wen, S. Ashkenazi, L. J. Guo, and M. O’Donnell, “Characterization of a broadband all-optical ultrasound transducer - from optical and acoustical properties to imaging,” *IEEE Transactions on Ultrasonics, Ferroelectrics, and Frequency Control*, vol. 55, no. 8, pp. 1867–1877, 2008.
- [50] S. Link and M. A. El-Sayed, “Spectral Properties and Relaxation Dynamics of Surface Plasmon Electronic Oscillations in Gold and Silver Nanodots and Nanorods,” *Journal of Physical Chemistry B*, vol. 103, no. 40, pp. 8410–8426, 1999.
- [51] S. Bodian, R. J. Colchester, T. J. Macdonald, F. Ambroz, M. Briceno de Gutierrez, S. J. Mathews, Y. M. M. Fong, E. Maneas, K. A. Welsby, R. J. Gordon, P. Collier, E. Z. Zhang, P. C. Beard, I. P. Parkin, A. E. Desjardins, and S. Noimark, “CuInS 2 Quantum Dot and Polydimethylsiloxane Nanocomposites for All-Optical Ultrasound and Photoacoustic Imaging,” *Advanced Materials Interfaces*, vol. 8, p. 2100518, oct 2021.
- [52] I. Lewis-Thompson, S. Zhang, S. Noimark, A. E. Desjardins, and R. J. Colchester, “PDMS composites with photostable NIR dyes for multi-modal ultrasound imaging,” *MRS Advances*, no. 0123456789, 2022.
- [53] J. R. Fincke, C. M. Wynn, R. Haupt, D. Rivera, J. R. Fincke, C. M. Wynn,

- R. Haupt, X. Zhang, D. Rivera, and B. Anthony, “Characterization of laser ultrasound source signals in biological tissues for imaging applications biological tissues for imaging applications,” *Journal of Biomedical Optics*, vol. 24, no. 2, 2018.
- [54] C. Sheaff and S. Ashkenazi, “A polyimide – etalon thin film structure for all-optical high-frequency ultrasound transduction,” *IEEE Transactions on Ultrasonics, Ferroelectrics and Frequency Control*, vol. 59, no. 10, pp. 2254–2261, 2012.
- [55] R. J. Colchester, E. Z. Zhang, C. A. Mosse, P. C. Beard, I. Papakonstantinou, and A. E. Desjardins, “Broadband miniature optical ultrasound probe for high resolution vascular tissue imaging,” *Biomedical Optics Express*, vol. 6, no. 4, pp. 1502–1511, 2015.
- [56] R. J. Colchester, C. Little, G. Dwyer, S. Noimark, E. J. Alles, E. Z. Zhang, C. D. Loder, I. P. Parkin, I. Papakonstantinou, P. C. Beard, M. C. Finlay, R. D. Rakhit, and A. E. Desjardins, “All-Optical Rotational Ultrasound Imaging,” *Scientific Reports*, vol. 9, no. 1, p. 5576, 2019.
- [57] E. J. Alles, N. Fook Sheung, S. Noimark, E. Z. Zhang, P. C. Beard, and A. E. Desjardins, “A reconfigurable all-optical ultrasound transducer array for 3d endoscopic imaging,” *Scientific reports*, vol. 7, p. 1208, April 2017.
- [58] E. J. Alles, E. C. Mackle, S. Noimark, E. Z. Zhang, P. C. Beard, and A. E. Desjardins, “Freehand and video-rate all-optical ultrasound imaging,” *Ultrasonics*, vol. 116, no. April, p. 106514, 2021.
- [59] H. W. Baac, J. G. Ok, A. Maxwell, K. T. Lee, Y. C. Chen, A. J. Hart, Z. Xu, E. Yoon, and L. J. Guo, “Carbon-nanotube optoacoustic lens for focused ultrasound generation and high-precision targeted therapy,” *Scientific Reports*, vol. 2, pp. 1–8, 2012.
- [60] J. Ylitalo and H. Ermert, “Ultrasound synthetic aperture imaging: monostatic

- approach,” *IEEE Transactions on Ultrasonics, Ferroelectrics, and Frequency Control*, vol. 41, no. 3, pp. 333–339, 1994.
- [61] J. A. Jensen, S. I. Nikolov, K. L. Gammelmark, and M. H. Pedersen, “Synthetic aperture ultrasound imaging,” *Ultrasonics*, vol. 44, pp. e5–e15, 2006. Proceedings of Ultrasonics International (UI’05) and World Congress on Ultrasonics (WCU).
- [62] L. Demi, “Practical guide to ultrasound beam forming: Beam pattern and image reconstruction analysis,” *Applied Sciences*, vol. 8, no. 9, 2018.
- [63] G. Montaldo, M. Tanter, J. Bercoff, N. Benech, and M. Fink, “Coherent plane-wave compounding for very high frame rate ultrasonography and transient elastography,” *IEEE Transactions on Ultrasonics, Ferroelectrics, and Frequency Control*, vol. 56, no. 3, pp. 489–506, 2009.
- [64] D. Garcia, L. L. Tarnec, S. Muth, E. Montagnon, J. Porée, and G. Cloutier, “Stolt’s f-k migration for plane wave ultrasound imaging,” *IEEE Transactions on Ultrasonics, Ferroelectrics, and Frequency Control*, vol. 60, no. 9, pp. 1853–1867, 2013.
- [65] J. Cheng and J.-y. Lu, “Extended high-frame rate imaging method with limited-diffraction beams,” *IEEE Trans. Ultrason. Ferroelectr. Freq. Control*, vol. 53, no. 5, pp. 880–899, 2006.
- [66] G. Matrone, A. S. Savoia, G. Caliano, and G. Magenes, “The delay multiply and sum beamforming algorithm in ultrasound b-mode medical imaging,” *IEEE Transactions on Medical Imaging*, vol. 34, no. 4, pp. 940–949, 2015.
- [67] B. Berthon, P. Morichau-Beauchant, J. Porée, A. Garofalakis, B. Tavitian, M. Tanter, and J. Provost, “Spatiotemporal matrix image formation for programmable ultrasound scanners,” *Physics in Medicine and Biology*, vol. 63, no. 3, 2018.

- [68] E. J. Alles, E. C. Mackle, S. Noimark, and A. E. Desiardins, “Direct model-based inversion for improved freehand optical ultrasound imaging,” in *2021 IEEE International Ultrasonics Symposium (IUS)*, pp. 1–4, 2021.
- [69] R. van Sloun, R. Cohen, and Y. Eldar, “Deep learning in ultrasound imaging,” *Proceedings of the IEEE*, vol. 108, pp. 11–29, Jan. 2020.
- [70] S. Rothl ubbers, H. Stroh m, K. Eickel, J. Jenne, V. Kuhlen, D. Sinden, and M. G nther, “Improving image quality of single plane wave ultrasound via deep learning based channel compounding,” in *2020 IEEE International Ultrasonics Symposium (IUS)*, pp. 1–4, 2020.
- [71] Y. Qi, Y. Guo, and Y. Wang, “Image quality enhancement using a deep neural network for plane wave medical ultrasound imaging,” *IEEE Transactions on Ultrasonics, Ferroelectrics, and Frequency Control*, vol. 68, no. 4, pp. 926–934, 2021.
- [72] S. J. Norton and M. Linzer, “Ultrasonic reflectivity imaging in three dimensions: Exact inverse scattering solutions for plane, cylindrical, and spherical apertures,” *IEEE Transactions on Biomedical Engineering*, vol. BME-28, no. 2, pp. 202–220, 1981.
- [73] M. Tanter and M. Fink, “Ultrafast Imaging in Biomedical Ultrasound,” *IEEE Trans. Ultrason. Ferroelectr. Freq. Control*, vol. 61, no. 1, pp. 102–119, 2014.
- [74] P. Subochev, A. Orlova, M. Shirmanova, A. Postnikova, and I. Turchin, “Simultaneous photoacoustic and optically mediated ultrasound microscopy: an in vivo study,” *Biomedical Optics Express*, vol. 6, no. 2, p. 631, 2015.
- [75] J. Xia, C. Huang, K. Maslov, M. A. Anastasio, and L. V. Wang, “Enhancement of photoacoustic tomography by ultrasonic computed tomography based on optical excitation of elements of a full-ring transducer array,” *Physiology & behavior*, vol. 38, no. 16, pp. 3140–3143, 2013.

- [76] D. Cui, Z. Zhang, and Y. Shi, "Optically-excited simultaneous photoacoustic and ultrasound imaging based on a flexible gold-PDMS film," *Journal of Innovative Optical Health Sciences*, vol. 13, no. 4, pp. 1–10, 2020.
- [77] T. Berer, H. Grun, J. Bauer-Marschallinger, P. Burgholzer, K. Passler, R. Nuster, and G. Paltauf, "Dual mode photoacoustic/acoustic microscopy with optical generation and detection," *IEEE International Ultrasonics Symposium, IUS*, pp. 4–7, 2012.
- [78] R. Nuster, N. Schmitner, G. Wurzinger, S. Gratt, W. Salvenmoser, D. Meyer, and G. Paltauf, "Hybrid photoacoustic and ultrasound section imaging with optical ultrasound detection," *Journal of Biophotonics*, vol. 6, no. 6-7, pp. 549–559, 2013.
- [79] G. Wurzinger, R. Nuster, N. Schmitner, S. Gratt, D. Meyer, and G. Paltauf, "Simultaneous three-dimensional photoacoustic and laser-ultrasound tomography," *Biomedical Optics Express*, vol. 4, no. 8, p. 1380, 2013.
- [80] B. Y. Hsieh, S. L. Chen, T. Ling, L. J. Guo, and P. C. Li, "All-optical transducer for ultrasound and photoacoustic imaging by dichroic filtering," *IEEE International Ultrasonics Symposium, IUS*, vol. 20, no. 2, pp. 1410–1413, 2012.
- [81] B. Y. Hsieh, S. L. Chen, T. Ling, L. J. Guo, and P. C. Li, "All-optical scan-head for ultrasound and photoacoustic imaging-Imaging mode switching by dichroic filtering," *Photoacoustics*, vol. 2, no. 1, pp. 39–46, 2014.
- [82] G. Li, Z. Guo, and S.-L. Chen, "Miniature all-optical probe for large synthetic aperture photoacoustic-ultrasound imaging," *Optics Express*, vol. 25, no. 21, p. 25023, 2017.
- [83] K. Pham, S. Noimark, N. Huynh, E. Zhang, F. Kuklis, J. Jaros, A. Desjardins, B. Cox, and P. Beard, "Broadband all-optical plane-wave ultrasound imaging

- system based on a Fabry-Perot scanner,” *IEEE Transactions on Ultrasonics, Ferroelectrics, and Frequency Control*, vol. 68, no. 4, pp. 1007–1016, 2021.
- [84] W. F. Beach, *Encyclopedia of Polymer Science and Technology*. Hoboken, NJ, USA: Wiley, 2004.
- [85] B. T. Cox and P. C. Beard, “The frequency-dependent directivity of a planar Fabry-Perot polymer film ultrasound sensor,” *IEEE Trans. Ultrason. Ferroelectr. Freq. Control*, vol. 54, no. 2, pp. 394–404, 2007.
- [86] E. Martin, E. Z. Zhang, J. A. Guggenheim, P. C. Beard, and B. E. Treeby, “Rapid spatial mapping of focused ultrasound fields using a planar Fabry-Pérot sensor,” *IEEE Transactions on Ultrasonics, Ferroelectrics, and Frequency Control*, vol. 64, no. 11, pp. 1711–1722, 2017.
- [87] F. A. Duck, “Hazards, risks and safety of diagnostic ultrasound,” *Medical Engineering and Physics*, vol. 30, no. 10, pp. 1338–1348, 2008.
- [88] E. Maneas, W. Xia, O. Ogunlade, M. Fonseca, D. I. Nikitichev, A. L. David, S. J. West, S. Ourselin, J. C. Hebden, T. Vercauteren, and A. E. Desjardins, “Gel wax-based tissue-mimicking phantoms for multispectral photoacoustic imaging,” *Biomedical Optics Express*, vol. 9, no. 3, p. 1151, 2018.
- [89] V. L. Newhouse, N. M. Bilgutay, J. Saniie, and E. S. Furgason, “Flaw-to-grain echo enhancement by split-spectrum processing,” *Ultrasonics*, vol. March, pp. 59–68, 1982.
- [90] T. J. Allen, M. Berendt, D. Lin, S. U. Alam, N. T. Huynh, E. Zhang, D. J. Richardson, and P. C. Beard, “High pulse energy fibre laser as an excitation source for photoacoustic tomography,” *Opt. Express*, vol. 28, pp. 34255–34265, Nov 2020.
- [91] E. J. Alles, R. J Colchester, and A. E. Desjardins, “Adaptive All-Optical Ul-

- trasound Imaging Through Temporal Modulation of Excitation Light,” *IEEE International Ultrasonics Symposium, IUS*, vol. 2018-October, 2018.
- [92] R. K. Ing, F. Gires, and M. Fink, “Focusing and beamsteering of laser generated ultrasound,” in *IEEE Ultrasonics Symposium*, pp. 539–544, 1989.
- [93] N. Huynh, O. Ogunlade, E. Zhang, B. Cox, and P. Beard, “Photoacoustic imaging using an 8-beam Fabry-Perot scanner,” in *Proceedings of SPIE*, vol. 9708, p. 97082L, 2016.
- [94] T. J. Allen, E. Zhang, and P. C. Beard, “Fully parallelised read-out of a Fabry-Perot ultrasound sensor using an InGaAs camera for fast photoacoustic imaging (Conference Presentation),” in *Proceedings of SPIE*, 2020.
- [95] L. L. Foldy, “The multiple scattering of waves. i. general theory of isotropic scattering by randomly distributed scatterers,” *Phys. Rev.*, vol. 67, pp. 107–119, Feb 1945.
- [96] L. Y. L. Mo and R. S. C. Cobbold, “A stochastic model of the backscattered doppler ultrasound from blood,” *IEEE Transactions on Biomedical Engineering*, vol. BME-33, no. 1, pp. 20–27, 1986.
- [97] B. A. J. Angelsen, “A theoretical study of the scattering of ultrasound from blood,” *IEEE Transactions on Biomedical Engineering*, vol. 27, pp. 61–67, 1980.
- [98] L. Mo and R. Cobbold, “A unified approach to modeling the backscattered doppler ultrasound from blood,” *IEEE Transactions on Biomedical Engineering*, vol. 39, no. 5, pp. 450–461, 1992.
- [99] B. Lim, P. A. J. Bascom, and R. S. C. Cobbold, “Particle and voxel approaches for simulating ultrasound backscattering from tissue,” *Ultrasound in Medicine & Biology*, vol. 22, no. 9, pp. 1237–1247, 1996.
- [100] P. A. Bascom and R. S. Cobbold, “On a fractal packing approach for un-

- derstanding ultrasonic backscattering from blood,” *Journal of the Acoustical Society of America*, vol. 98, no. 6, pp. 3040–3049, 1995.
- [101] G. E. Topholme, “Generation of acoustic pulses by baffled plane pistons,” *Mathematika*, vol. 16, no. 2, p. 209–224, 1969.
- [102] J. Jensen, “Field: A program for simulating ultrasound systems,” *Medical and Biological Engineering and Computing*, vol. 34, pp. 351–352, 01 1996.
- [103] A. Rodriguez-Molares, O. M. H. Rindal, O. Bernard, H. Liebgott, A. Austeng, and L. Løvstakken, “The ultrasound toolbox,” *2017 IEEE International Ultrasonics Symposium (IUS)*, pp. 1–1, 2017.
- [104] B. E. Treeby and B. T. Cox, “k-Wave : MATLAB toolbox for the simulation and reconstruction of photoacoustic wave fields,” *Journal of biomedical optics*, vol. 15, no. April 2010, pp. 1–12, 2010.
- [105] K. Pham, “PhD Project code.” <https://github.com/k-pham/phd-project-code>, 2021.
- [106] D. R. Ramasawmy, E. Martin, J. A. Guggenheim, E. Z. Zhang, P. C. Beard, B. E. Treeby, and B. T. Cox, “Analysis of the directivity of glass-etalon fabry–pérot ultrasound sensors,” *IEEE Transactions on Ultrasonics, Ferroelectrics, and Frequency Control*, vol. 66, no. 9, pp. 1504–1513, 2019.
- [107] R. S. C. Cobbold, *Foundations of Biomedical Ultrasound*. Oxford University Press, 3 ed., 2008.
- [108] F. S. Foster, M. S. Patterson, M. Arditi, and J. W. Hunt, “The conical scanner: A two transducer ultrasound scatter imaging technique,” *Ultrasonic Imaging*, vol. 3, pp. 62–82, 1981.
- [109] M. Berson, A. Roncin, and L. Pourcelot, “Compound scanning with an electrically steered beam,” *Ultrasonic Imaging*, vol. 3, no. 3, pp. 303–308, 1981.

- [110] D. P. Shattuck and O. T. von Ramm, "Compound scanning with a phased array," *Ultrasonic Imaging*, vol. 4, no. 2, pp. 93–107, 1982. PMID: 7201697.
- [111] S. K. Jespersen, J. E. Wilhjelm, and H. Sillesen, "Multi-angle compound imaging," *Ultrasonic Imaging*, vol. 20, no. 2, pp. 81–102, 1998. PMID: 9691367.
- [112] P. A. Magnin, O. T. von Ramm, and F. L. Thurstone, "Frequency compounding for speckle contrast reduction in phased array images," *Ultrasonic Imaging*, vol. 4, pp. 267–281, 1982.
- [113] G. E. Trahey, J. W. Allison, S. W. Smith, and O. T. von Ramm, "A quantitative approach to speckle reduction via frequency compounding," *Ultrasonic Imaging*, vol. 8, pp. 151–164, 1986.
- [114] J. Bamber and C. Daft, "Adaptive filtering for reduction of speckle in ultrasonic pulse-echo images," *Ultrasonics*, vol. 24, no. 1, pp. 41–44, 1986.
- [115] C. R. Cooley and B. S. Robinson, "Synthetic focus imaging using partial datasets," *IEEE Transactions on Ultrasonics, Ferroelectrics, and Frequency Control*, pp. 1539–1542 vol.3, 1994.
- [116] J. A. Stratton, *Electromagnetic Theory*. New York, USA: McGraw-Hill, 1941.
- [117] M. Pisani and M. Astrua, "Angle amplification for nanoradian measurements," *Applied Optics*, vol. 45, no. 8, pp. 1725–1729, 2006.
- [118] D. Turnbull and F. Foster, "Beam steering with pulsed two-dimensional transducer arrays," *IEEE Transactions on Ultrasonics, Ferroelectrics, and Frequency Control*, vol. 38, no. 4, pp. 320–333, 1991.
- [119] B. Diarra, M. Robini, P. Tortoli, C. Cachard, and H. Liebgott, "Design of optimal 2-d nongrid sparse arrays for medical ultrasound," *IEEE Transactions on Biomedical Engineering*, vol. 60, no. 11, pp. 3093–3102, 2013.

- [120] R. E. Davidson, J. A. Jensen, and S. W. Smith, “Two-dimensional random arrays for real time volumetric imaging,” *Ultrasonic Imaging*, vol. 16, pp. 143–163, 1994.
- [121] A. Ramalli, E. Boni, A. S. Savoia, and P. Tortoli, “Density-tapered spiral arrays for ultrasound 3-d imaging,” *IEEE Transactions on Ultrasonics, Ferroelectrics, and Frequency Control*, vol. 62, no. 8, pp. 1580–1588, 2015.
- [122] E. Roux, A. Ramalli, P. Tortoli, C. Cachard, M. C. Robini, and H. Liebgott, “2-d ultrasound sparse arrays multidepth radiation optimization using simulated annealing and spiral-array inspired energy functions,” *IEEE Transactions on Ultrasonics, Ferroelectrics, and Frequency Control*, vol. 63, no. 12, pp. 2138–2149, 2016.
- [123] M. Karaman, I. O. Wygant, O. Oralkan, and B. T. Khuri-Yakub, “Minimally redundant 2-d array designs for 3-d medical ultrasound imaging,” *IEEE Transactions on Medical Imaging*, vol. 28, no. 7, pp. 1051–1061, 2009.
- [124] A. Trucco, “Thinning and weighting of large planar arrays by simulated annealing,” *IEEE Transactions on Ultrasonics, Ferroelectrics, and Frequency Control*, vol. 46, no. 2, pp. 347–355, 1999.
- [125] G. Lockwood, P.-C. Li, M. O’Donnell, and F. Foster, “Optimizing the radiation pattern of sparse periodic linear arrays,” *IEEE Transactions on Ultrasonics, Ferroelectrics, and Frequency Control*, vol. 43, no. 1, pp. 7–14, 1996.
- [126] G. Lockwood and F. Foster, “Optimizing the radiation pattern of sparse periodic two-dimensional arrays,” *IEEE Transactions on Ultrasonics, Ferroelectrics, and Frequency Control*, vol. 43, no. 1, pp. 15–19, 1996.
- [127] V. Kumar, P.-Y. Lee, B.-H. Kim, M. Fatemi, and A. Alizad, “Gap-filling method for suppressing grating lobes in ultrasound imaging: Experimental

- study with deep-learning approach,” *IEEE Access*, vol. 8, pp. 76276–76286, 2020.
- [128] E. J. Alles and A. E. Desjardins, “Source Density Apodization: Image Artifact Suppression through Source Pitch Nonuniformity,” *IEEE Transactions on Ultrasonics, Ferroelectrics, and Frequency Control*, vol. 67, no. 3, pp. 497–504, 2020.
- [129] K. Pham, S. Noimark, N. T. Huynh, E. Zhang, A. Desjardins, B. Cox, and P. Beard, “Dual mode photoacoustic and ultrasound imaging system based on a Fabry-Perot scanner (Conference Presentation),” in *Proceedings of SPIE*, 2019.